UNIVERSITY OF CAMERINO

SCHOOL OF ADVANCED STUDIES

Chemical and Pharmaceutical Sciences and Biotechnologies Area
Ph.D. Curriculum in Chemical Science
XXXVI Cycle

Investigation of Lignocellulosic Waste-Derived Hard Carbons and Binders as Electrode Materials for Li-ion and Na-ion Batteries

Doctoral Thesis

Ph.D. Candidate

Luca Bottoni

Supervisor

Prof. Francesco Nobili

.

Academic Years 2020/2021 – 2022/2023

UNIVERSITY OF CAMERINO

SCHOOL OF ADVANCED STUDIES

Chemical and Pharmaceutical Sciences and Biotechnologies Area
Ph.D. Curriculum in Chemical Science
XXXVI Cycle

Investigation of Lignocellulosic Waste-Derived Hard Carbons and Binders as Electrode Materials for Li-ion and Na-ion Batteries

Doctoral Thesis

Ph.D. Candidate

Luca Bottoni

Supervisor

Prof. Francesco Nobili

.

Academic Years 2020/2021 – 2022/2023

"Se ecco trona, da che parte pioe"

Preface

The present doctoral thesis reports the results obtained during the three-year PhD course with curriculum in Chemical Sciences at the University of Camerino (Italy), under the supervision of Prof. Francesco Nobili. Part of the reported results are obtained during a six-months research internship at the University of Basque Country – UPV/EHU (Spain), under the supervision of Prof. Teófilo Rojo and Prof. Verónica Palomares. The research work reported in this thesis was the subject of some of the conference proceedings and scientific publications listed below.

Conferences

- **SYNC 2022 – Symposium for YouNg Chemists** 20-23 June 2022, Roma (Italy);
- **GEI 2022 – Giornate dell'Elettrochimica Italiana** 11-15 September 2022, Orvieto (Italy);
- **GEI 2023 – Giornate dell'Elettrochimica Italiana** 17-21 September 2023, Cefalù (Italy);

Scientific Publications

- H. Darjazi, A. Staffolani, L. Sbrascini, **L. Bottoni**, R. Tossici, F. Nobili. *Sustainable Anodes for Lithium- and Sodium-ion Batteries Based on Coffee Ground-derived Hard Carbon and Green Binders*, Energies (2020), 13(23), 6216, https://doi.org/10.3390/en13236216;

- L. Sbrascini, A. Staffolani, **L. Bottoni**, H. Darjazi, L. Minnetti, M. Minicucci, F. Nobili. *Structural and Interfacial Characterization of a Sustainable Si/Hard Carbon Composite Anode for Lithium-Ion Batteries*, ACS Applied Materials & Interfaces (2022), 14, 29, 33257-33273, https://doi.org/10.1021/acsami.2c07888;

- S. Gabrielli, M. Caviglia, G. Pastore, E. Marcantoni, F. Nobili, **L. Bottoni**, A. Catorci, I. Bavasso, F. Sarasini, J. Tirillò, C. Santulli. *Chemical, Thermal and Mechanical Characterization of Licorice Root, Willow, Holm Oak, and Palm Leaf Waste Incorporated into Maleated Polypropylene (MAPP)*, Polymers (2023), 14(20), 4348, https://doi.org/10.3390/polym14204348;

- H. Darjazi, **L. Bottoni**, H.R. Moazami, S.J. Rezvani, L. Balducci, L. Sbrascini, A. Staffolani, A. Tombesi, F. Nobili. *From Waste to Resources: Transforming Olive Leaves to Hard Carbon*

as Sustainable and Versatile Electrode Material for Li/Na-ion Batteries and Supercapacitors, Materials Today Sustainability (2023), 21, 100313, https://doi.org/10.1016/j.mtsust.2022.100313;

- **L. Bottoni**, H. Darjazi, L. Sbrascini, A. Staffolani, S. Gabrielli, G. Pastore, A. Tombesi, F. Nobili. *Electrochemical Characterization of Charge Storage at Anodes for Sodium-Ion Batteries based on Corncob Waste-derived Hard Carbon and Binder*, ChemElectroChem (2023), e202201117, https://doi.org/10.1002/celc.202201117;

Abstract

In the present thesis work, the valorization of lignocellulosic waste has been pursued through the production of Hard Carbon active material and binders that can be used as electrode materials for both lithium- and sodium-ion batteries.

In order to suppress the ever-rising greenhouse gases emissions, energy transition toward clean energy sources is mandatory. In this context, the development of rechargeable batteries to store electricity produced by renewable energy sources is fundamental and therefore is attracting great attentions in the last decade. However, the huge increase in the global demand of lithium-ion batteries mainly driven by transport electrification is posing serious concerns associated with the future availability of the so-called "critical raw materials", motivating the investigation of an alternative, MWh-scalable battery technology composed of low-cost and sustainable materials. In this context, sodium-ion batteries can potentially fulfill these requirements, although the cost-competitiveness of these systems strictly depends on the achievable energy density and the electrode materials cost. At anode side, biomass-derived Hard Carbons are appealing candidates thanks to their good electrochemical performance coupled with technical aspects of low-cost and sustainability of the synthesis. Also the development of bio-based binders and eventually aqueous electrode processing is beneficial for the breakdown of the electrode manufacturing process.

In this regard, an abundant and widely distributed agricultural by-product such as corncob has been used as raw material for both the production of Hard Carbon and for the extraction of cellulose for the synthesis of the sodium carboxymethylcellulose. Moreover, the bio-based electrode was used to study the sodium storage mechanism into Hard Carbon, which is fundamental to understand the structure-capacity relationship and open the path to the structural design and optimization of the electrochemical performance of Hard Carbons. The bio-based anode was deeply characterized at materials level as well as the electrochemical performance and interfacial properties. The results show that the corncob-derived anode possess good specific capacity with a promising capacity retention and good rate capability in sodium-ion system as a consequence of the high reaction kinetic and interfacial stability. Moreover, the sodium storage arises from the capacitive-controlled adsorption on surface active sites in the sloping region, while the diffusion-controlled intercalation is the predominant process approaching the low-voltage plateau. Additionally, the corncob waste-derived electrode has been evaluated also in Li-ion system both as active materials, investigating the capabilities of Hard Carbon to replace the graphite in some specific applications, and also as buffer matrix for SnO_2, an interesting high-energy density anode material for lithium-ion batteries, whose development is hindered by the rapid capacity fading as a consequence of the huge volume changes during lithiation and de-lithiation. In the first application, corncobs electrodes show the same features

experimented in sodium analogue, i.e. good specific capacity, long cycling stability and rate capability, while in the second application, the corncob-derived HC reveals that the mitigation of capacity fade is remarkable whit low content of SnO_2 and 2% of vinylene carbonate is added to the electrolyte, promoting the formation of a thin and stable electrode/electrolyte, which increases the capacity retention.

Parallelly, forestry scraps, another abundant and renewable sources of lignocellulosic materials, have been used to produce Hard Carbons and to isolate cellulose and lignin, which are in turn processed for the preparation of binders. The obtained bio-based materials have been characterized and then combined for the fabrication of anode electrodes for sodium-ion batteries. Particular emphasis has been given to the extraction and valorization of lignin as binder material for Hard Carbon anodes. The lignin extractions have been conducted using an organsolv method with two different bio-based solvents, γ-Valerolactone and Dihydrolevoglucosenone, observing that the first is more selective respect to the latter toward delignification of the biomass. The electrochemical performances of the obtained electrodes were investigated in Na half-cells. When Cyrene extracted lignin is used as binder, the electrodes show impressively long cycling stability, which can be ascribed to the high hydrogen bonding ability of the binder. The long cycling stability as well as the coulombic efficiency is enhanced when Cyrene extracted lignin is used also in $Na_3(VO)_2(PO_4)_2F$ cathode electrode. Finally, the best Hard Carbon anode have been employed with $Na_3(VO)_2(PO_4)_2F$ cathode in full-cell application, evaluating the electrochemical performance in terms of specific capacity and capacity retention especially at high-current rates, where this kind of cathode find its most important application. The obtained specific capacities at different current rates are good and have been confirmed also when the commercial CMC is replaced with Cyrene extracted lignin as binder at anode side. Additionally, in order to evaluate an alternative strategy for the anode preconditioning respect to the electrochemical presodiation with metallic sodium, sodium mesoxalate $Na_2C_3O_5$ has been evaluated as sacrificial salt to overcome the drawback of low initial coulombic efficiency of Hard Carbon, although unsuitable results have been preliminary obtained.

TABLE OF CONTENTS

TABLE OF FIGURES

INDEX OF TABLES

1. INTRODUCTION

Nowadays, climate change is a global and complex challenge that could lead to potentially catastrophic impacts on ecosystems. The term *climate change* refers to the long-term shifts in temperature and weather patterns (rainfall, snow or wind).[1] These climate shifts may be natural and can be mainly attributed to small changes of solar energy arises from small variations in Earth's orbit. However, natural factors cannot explain the warming trend occurring over the last century.[2,3] According to data from NASA's Goddard Institute for Space Studies (NASA/GISS), the Earth's surface average temperature in 2022 was 0.89 °C above the average baseline period from 1950 to 1980 (**Figure 1**), with an increase rate of 0.08 °C/decade and the past eight years being the consecutive warmers ones since 1880.[4] In addition to global warming, many other aspects of climate are changing such as melting rate of ice sheets and glaciers, sea levels rising, shifts in plants blooming times, expansion of deserts, relocation or extinction of animal species and more frequent extreme weather events. Therefore, many evidences coming from the analysis of indirect measures of climate and the study of the changes in the earth's orbit around the sun demonstrate that it is *extremely likely* that human activities are driving the climate change.[5]
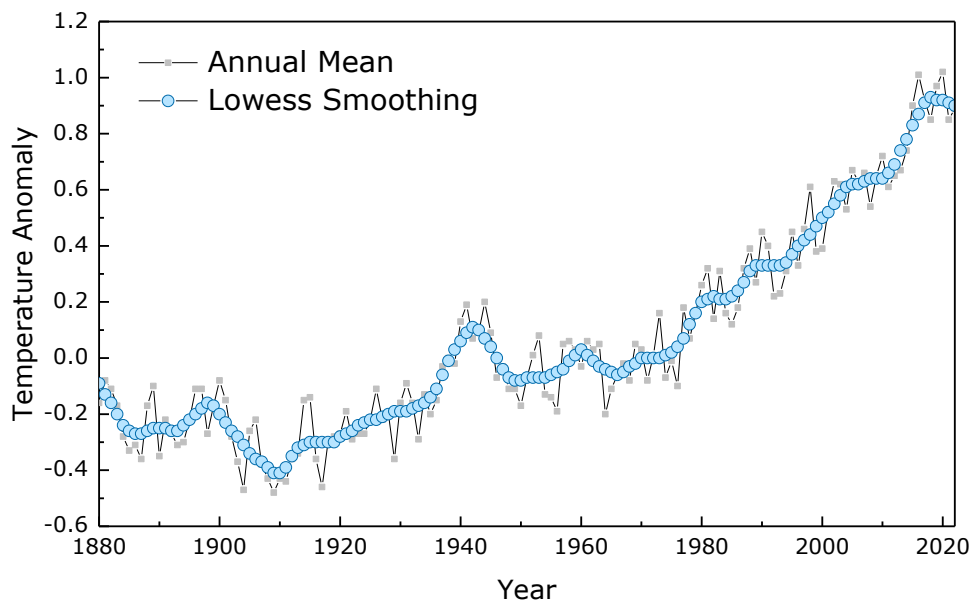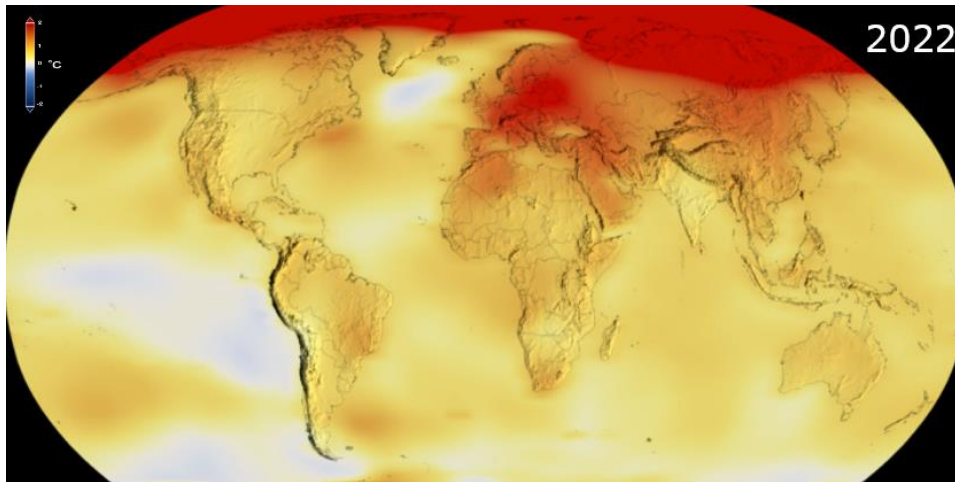
Figure 1 *(a) Earth's surface average temperature anomalies between 1880 and 2022; (b) Color-coded map of global average surface temperature in 2022: normal temperatures are shown in white, higher-than normal temperatures are shown in red and lower than normal temperatures are shown in blue. Data Source: NASA/GISS*[6]

Among the human activities, the *Intergovernmental Panel on Climate Change (IPCC)* considers the Green House Gas (GHG) emissions as the main cause of the observed climate change.[7] Green House Gases are gases that absorbs and re-emit the infrared radiation keeping the Earth' temperature at an average of 14° C. The natural greenhouse effect is caused by the presence in the atmosphere of water vapor (H_2O), carbon dioxide (CO_2), methane (CH_4) and nitrous oxide (N_2O) and is vital for life. However, human activities are changing the natural earth's greenhouse effect increasing the concentrations of greenhouses gases in the atmosphere, promoting the global warming. The main GHGs whose concentrations are rising are CO_2, CH_4, N_2O and fluorinated gases which includes HFCs (hydrochlorofluorocarbons), perfluorocarbons (PFCs), sulfur hexafluoride (SF_6) and nitrogen trifluoride (NF_3). These gases differ in terms of warming effect and their longevity in the atmosphere. As shown in **Figure 2**, the global net anthropogenic emissions have continued to rise during the period 1990-2019 reaching an historic high of 59 ± 6.6 $GtCO_2$-eq in 2019, about 12 % higher than 2010 and 54 % higher than 1990. Growth in emissions has persisted across all the major groups of GHGs even if at different rates. Carbon dioxide is the primary GHG emitted by human activities, accounting for around the 74 % of the

total emissions in the period 1990-2019, mostly generated through fossil fuel combustion for energy production.[8]
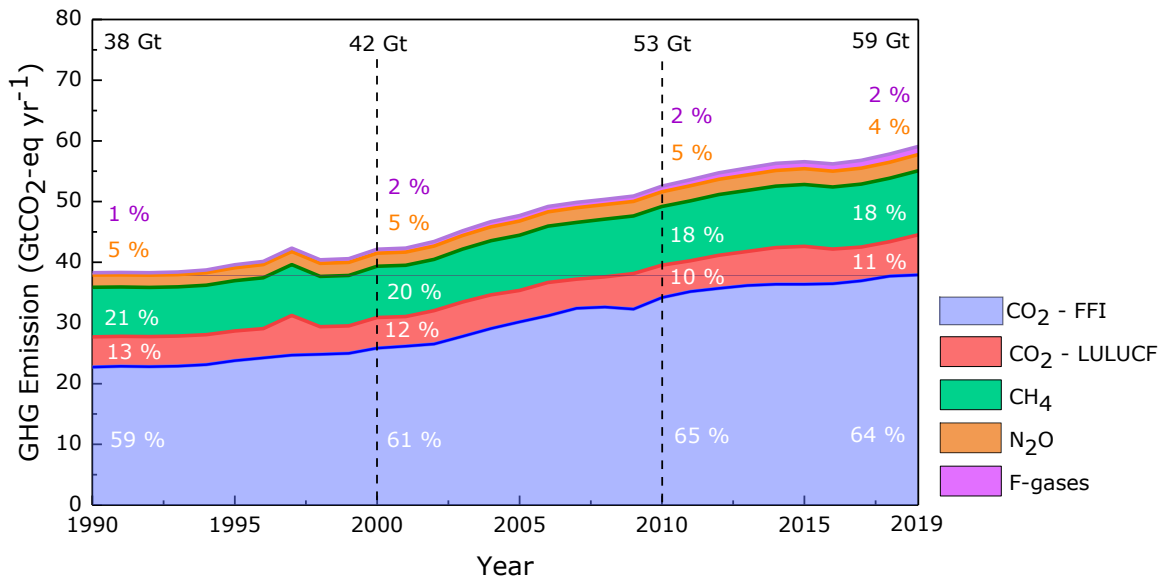
Figure 2 *(a) Global net anthropogenic emissions 1990-2019 (GtCO₂-eq yr⁻¹). Legend: CO₂ – FFI (carbon dioxide from fossil fuel combustion and industrial processes; CO₂ – LULUCF (net carbon dioxide from land use, land-use change and forestry); F-gases (fluorinated gases HFCs, PFCs, SF₆, NF₃). Data Source (IPCC-WGIII)*[8]

Therefore, in order to achieve the targets of Paris Agreement, which "would reduce the risks and impacts of climate change" mainly through "holding the increase in the global average temperature to well below 2°C above pre-industrial levels and pursuing efforts to limit the temperature increase to 1.5°C above pre-industrial levels",[9] important changes in policies and technologies must be adopted toward a Net-Zero Emission scenario by 2050, which mainly included the complete transformation of how the energy is produced, transported and consumed. The *International Energy Agency (IEA)* in the World Energy Outlook 2022 (**Figure 3**) showed the total energy supply by fuel in 2021 and the projections to 2030 and 2050 in the Stated Policies scenario (STEPS), which corresponds to the energy supply with the current policy settings, and in the Net Zero Emission scenario (NZE), which design the roadmap to cap the temperature increase to 1.5 °C. It is clear that the NZE scenario requires a profound transition from fossil fuels toward renewable energy sources which cannot be guaranteed with the current policy settings as shown in STEPS projections. Clean energy shall account for around the 30 % of total supply in 2030 and 70 % in 2050, respectively. Simultaneously, unabated fossil-fuels which directly provided around 80 % of energy in 2021 shall undergo a huge decline to around 18 % in 2050, in which a proportion is used with carbon capture, utilization and storage (CCUS) technologies. Moreover, despite global population and economy growth, the total energy supply

is projected to decline by 15 % between 2021 and 2050: this trend is mainly driven by efficiency benefits of switching from the traditional use of biomass, technical gains in energy consuming equipments and building envelopes and efficiency benefits of electrification.[10]
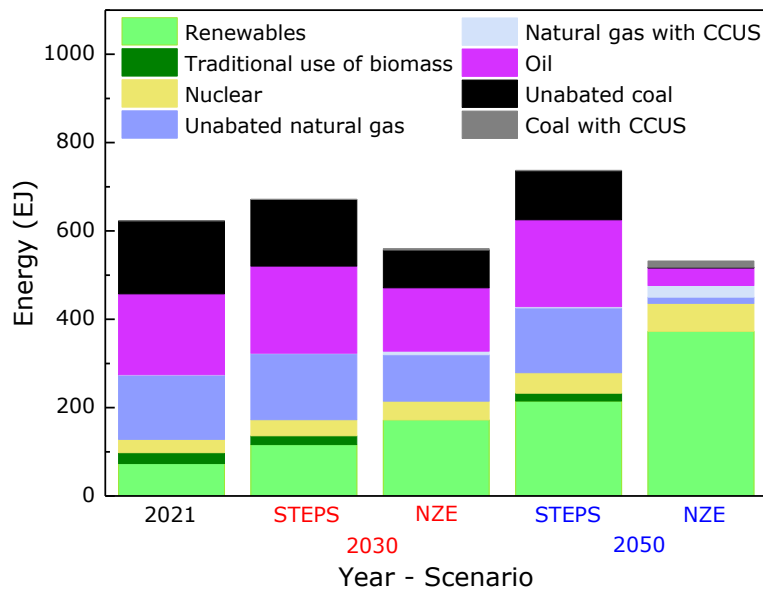
Figure 3 *Comparison of total energy supply by fuel in different years and scenarios. Legend: EJ (Exajoule); CCUS (Carbon Capture, Utilization and Storage); STEPS (Stated Policies Scenario); NZE (Net Zero Emissions scenario). Data source (IEA)[10]*

Therefore, the energy transition requires huge efforts by all governments that must provide feasible step-by-step plans to reach their net zero goals, building confidence among investors, industry, citizens and other countries. These plans must include long-term objectives, facilitating an ordered and progressive transition, coupled with measurable short-term targets and policies. Nevertheless, cooperation is the key word to face this challenge: all stakeholders must play their part through coordinated actions and plans.[11]

1.1 ELECTRICITY AND ELECTROCHEMICAL ENERGY STORAGE

Electrical energy is the world's fastest-growing form of end-use energy thanks to its versatility for many applications and the intrinsic behavior that can be quickly and efficiently transported over long distances. Therefore, global electricity generation will increase significantly from around 28300 TWh in 2021 to around 73200 TWh in 2050 according to the NZE scenario.[10] However the electricity sector is the first sector that shall be decarbonized since it is responsible for around the 35 % of CO_2 emissions in 2021. Fortunately, the decarbonization of the electricity sector is under way: the emission carbon intensity of global electricity generation reached an

historic low of 436 g_{CO2} kWh^{-1} in 2022. This record is mainly due by the replacement of fossil fuels with renewable energy sources, which reached a 29 % of share in 2022 and is projected to reach around 90 % in 2050.[12] Among the renewable sources (**Figure 4**), generation from solar photovoltaic (PV) and wind are the predominant sources of the increase, with the solar undergoing the world's fastest-growing form of renewable energy and going to be the dominant energy source in the future followed by wind power.[10]
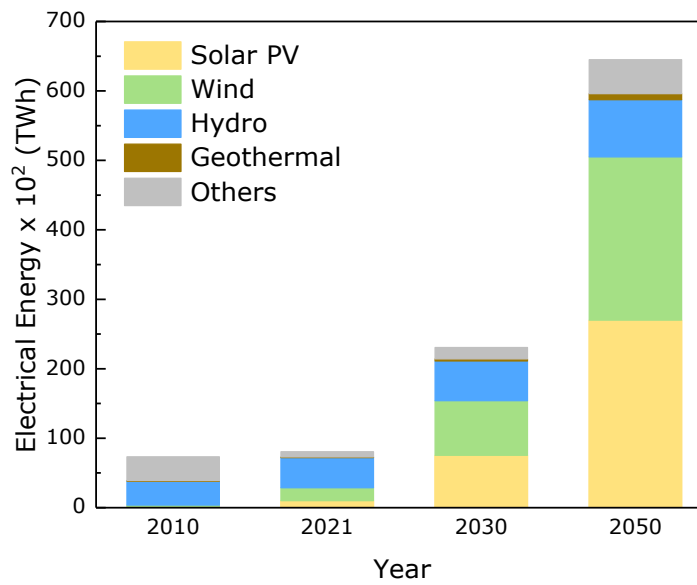
Figure 4 *Comparison of renewable electricity generation by source 2010-2050. Data source (IEA)[10]*

However, renewable energy sources cannot be easily integrated into the grid. Firstly, renewable energy is by nature intermittent and unpredictable, leading to an irregular electricity supply; additionally, the electricity demand fluctuates both in time and regions, producing on- and off-peaks periods.[13] Therefore, the only way to introduce stability into the electrical grid relies into the creation of hybrid systems combining different types of renewable technologies, with different time of low and high generations, together with energy storage systems (ESS) with the aim to store electricity when there is an excess of supply and compensate it during on-peak period. In addition, energy storage fulfils other functions such as improvement of power capability and overall efficiency of the power system. There are different ways to store energy and the selection of a technology is mainly based on its reliability, efficiency, flexibility, cost and environmental impact.[14] Among them, electrochemical energy storage systems (EESSs) are a class of storage devices able to store and release electrical energy by exploiting redox reactions that can be divided into several types as shown in **Figure 5 a**:
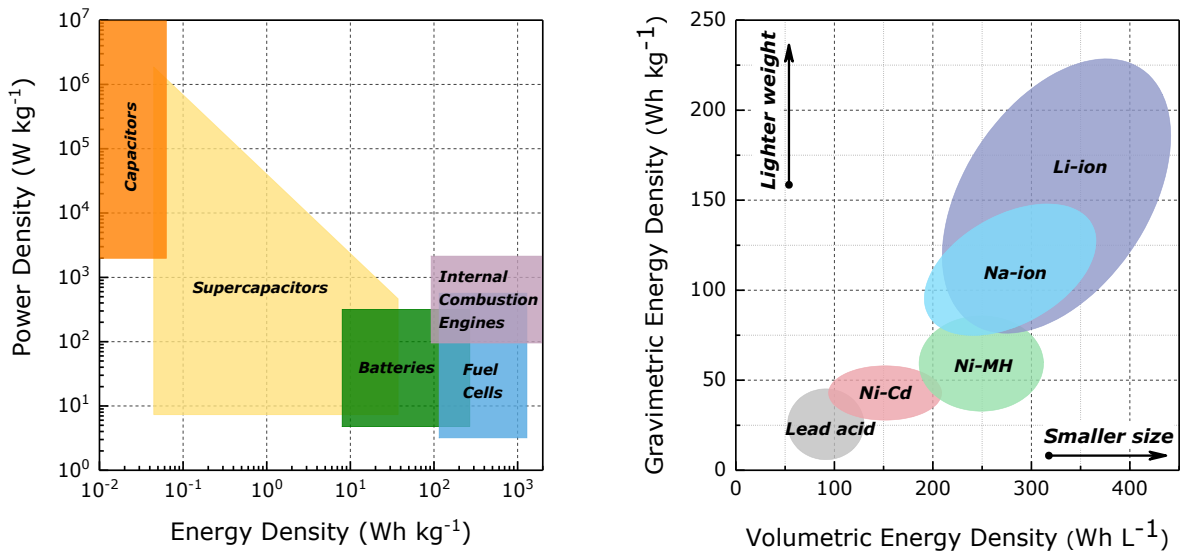
Figure 5 *Ragone plot showing a) different EESSs in comparison to internal combustion engines b) different types of batteries.*

These technologies differ each other in terms of power and energy density where fuel cells possess the highest energy density while capacitors and supercapacitors the highest power densities. However, efficiency, life span, technological maturity, feasibility of scale-up and economic and environmental costs of the systems are crucial requirements for practical applications in large-scale systems. Knowing that single technology cannot fulfill all the requirements for all different applications,[15] nowadays, the most realistic options to store electricity generated by clean energy sources, especially solar PV and wind, are secondary batteries.[16,17] Secondary batteries are a family of batteries that, contrarily to primary batteries, can be recharged. As displayed in **Figure 5 b**, there are different types of secondary batteries which possess different energy densities together with its own advantages and limitations. Generally, their relatively high energy densities and acceptable power densities in combination with other properties make them ideal devices for the grid and the most promising devices to substitute internal combustion engines. However, most of the parameters such as nominal voltage, cycle life, stability, energy and power densities largely depend on the cell chemistry comprising the battery.[18]

Lead-acid battery (Pb-acid) is the oldest rechargeable battery and a successful product for more than a century, especially in automotive industry as SLI battery (Starting, Lighting and Ignition) and motive power traction. The wide use of lead-acid battery is mainly due to the low cost compared to other secondary batteries as well as electrical efficiency (75-80 %), relatively high cell-voltage (> 2.0 V), good charge retention and high-rate performances. Its main

disadvantages rely in the limited energy density (typically 30-40 Whkg^{-1}) and deterioration in long-term storage in discharge condition.

Nickel-Cadmium battery (Ni-Cd) is another type of battery with a long history: the first Ni-Cd battery was created in 1899 and now it is available in different cell designs to suit the variety of applications. Overall, Ni-Cd cell is a very reliable and long-life battery (> 2000 cycles), with a very good charge retention properties and withstand both severe mechanical, thermal and electrical abuses. However, even if it has a higher energy density (ranging from 30 to 60 Whkg^{-1}), the higher cost respect to Pb-acid batteries disallow it to dominate the industrial applications market, while representing a niche-market product for long time where higher rate performances and longer cycle life are required.

Nickel-metal hydride (Ni-MH) battery is a more recent technology in which the principal difference with Ni-Cd is that the cadmium has been replaced with hydrogen present as an hydride of a metal alloy for the negative active material. Hence, it can achieve higher energy density (up to 90 Whkg^{-1}) and more environmental sustainability while maintaining long-cycle life, high charge retention and excellent thermal properties. Therefore, Ni-MH batteries have dominated for a decade the market of portable electronic devices, mainly replacing primary alkaline batteries, although Ni-MH batteries became famous as enabling device for hybrid electric vehicles (HEVs), where the power density is the main purpose of the battery facing high current pulses during both charge (regenerative braking) and discharge (assistance in acceleration at startup).[19]

Nevertheless, the rechargeable alkali-ion batteries towed by the lithium-ion battery technology represent the most important EESSs since its development in 1970, providing excellent performances as energy storage for a wide range of applications, including portable electronic devices, electric transportation and renewable energy-based grid.[20]

1.2 LITHIUM-ION BATTERIES

The history of lithium-ion batteries (LIBs) obviously starts from the key features of lithium: it is the lightest metal in the periodic table (6.94 a.m.u), has a small ionic radius (0.76 Å), has the lowest electrochemical potential (-3.04 V vs SHE) and has an high theoretical capacity (3860 mAh g^{-1} or 2061 mAh cm^{-3}).[21,22] These characteristics made lithium metal as an appealing anode material, motivating the research toward lithium-based batteries. In the 1970s, the first primary Li cells were developed and commercialized for small applications such as medical implants, watches and military applications. The huge success of these primary batteries opened the interest to develop lithium-based rechargeable systems. Therefore, over the same period, different contributions lead to the discovery and development of several inorganic compounds, especially transition-metal chalcogenides, that react reversibly with alkali ions, the so-called

"intercalation/insertion compounds", leading to the commercialization of the first rechargeable Li battery by Exxon Company. The battery is based on the discovery of *Prof.* Whittingham and consists of a lithium metal anode, lithium perchlorate in dioxolane as electrolyte and titanium disulfide as cathode material.[23] However, safety issues and operational faults hindered the commercial success of this system. It was soon realized that the problems were associated with the lithium metal anode and especially with its dendrite growth upon cycling, which could cause in the worst case short circuit and thermal runaway.[24] Therefore, the main approach to solve the safety issues was the replacing of metallic lithium with a second intercalation material at anode side, representing the breakthrough toward the first conceptualization of the so-called "rocking-chair batteries", where the lithium ions shuttle between cathode and anode hosts during charge and discharge processes. The concept was later demonstrated in the early 1980s, especially by Scrosati et al.,[25] while Besenhard,[26] Basu[27] and Yazami[28] and their co-workers parallelly developed the use of carbon materials, in particular graphite, as anode intercalation materials which were able to intercalate Li ions with outstanding reversibility.[29] To overcome the higher potential of graphite respect to lithium metal, metal oxides, having higher oxidation potential, were investigated at cathode side.[30] In 1981 *Prof.* Goodenough et al.[31] proposed the use of $LiCoO_2$ as high voltage and high energy cathode, opening the route to *Prof.* Yoshino et al. to patent in 1985 a prototype of lithium-ion battery using a carbonaceous material anode and $LiCoO_2$ cathode. Few years of improvements were required to reach the first commercialization of the first Lithium-Ion Battery in 1991 by Sony Corporation.[24] Nowadays, despite a progressive optimization, lithium-ion batteries still rely on the same technology of three decades ago, with the main components being the cathode, anode, electrolyte, separator and the current collectors (**Figure 6**).
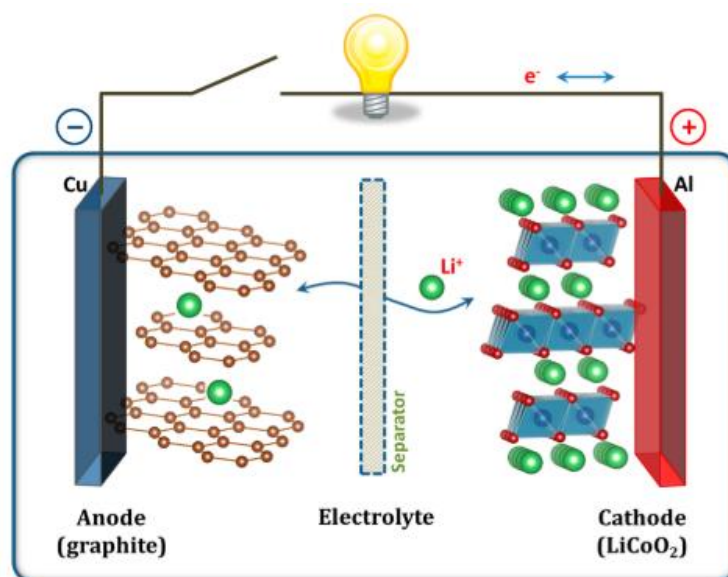
Figure 6 *Schematic illustration of a typical Li-ion battery.[32]*

The positive and negative electrodes represent the heart of the cell since they provide the active surface at which redox half-reactions take place. The electrodes are coated into current collectors (Cu for anodes and Al for cathodes), which act as a rigid and electronically support for the active materials by means of a polymeric binder. Externally, electrodes are directly connected through an electric circuit, while inside the cell, anode and cathode are physically separated by a microporous separator, which prevent short circuit coming from direct contact; additionally, electrodes are immersed into the electrolyte, which provides the Li^+ ions conduction between electrodes in order to restore the charge balance during charge and discharge processes.

The working mechanism of a Lithium-ion cell is shown in **Figure 7**:
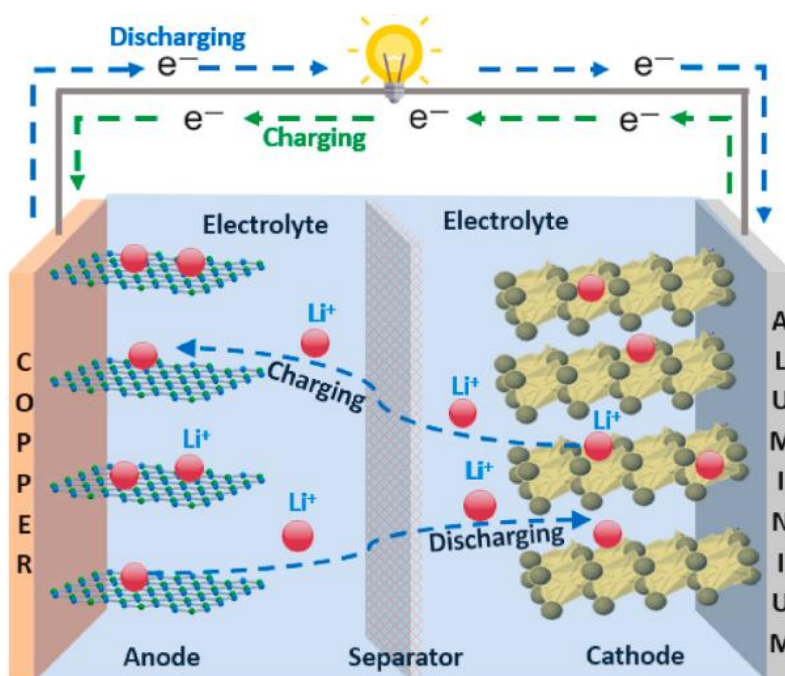
Figure 7 Schematic representation of working mechanism of a LIB.[33]

During discharge, the spontaneous electrochemical reaction takes place where the negative electrode is oxidized releasing electrons and lithium ions. Concurrently, Li^+ dissolve into the electrolyte and flow to positive electrode while electrons flow to the same electrode through the external circuit, producing an electric current. At the positive electrode side, a reduction reaction occurs where lithium ions from the electrolyte combine with incoming electrons filling up the cathode host matrix. During charge, the process is reversed: positive electrode undergoes oxidation, thus Li^+ ions are extracted to go to be reduced at negative electrode, while electrons flow through the external circuit. This inversion is possible by the action of an external power supply which applies a voltage higher than the spontaneous cell voltage, forcing an electric current to flow in the opposite direction respect to the spontaneous redox reactions.[34] It is

common practice to name cathode the positive electrode and anode the negative one, regardless the direction of the charge/discharge process.

The overall reactions that occur in a state-of-the-art LIB composed by graphite anode and $LiCoO_2$ cathode during discharge and charge processes can be summarized by **Equations 1-6** reported below:

Discharge:

Anode	$Li_xC_6 \rightarrow 6C_{(graphite)} + xLi^+ + xe^-$	**Eq. 1**
Cathode	$Li_{1-x}CoO_2 + xLi^+ + xe^- \rightarrow LiCoO_2$	**Eq. 2**
Overall	$Li_{1-x}CoO_2 + Li_xC_6 \rightarrow LiCoO_2 + 6C_{(graphite)}$	**Eq. 3**

Charge:

Anode	$6C_{(graphite)} + xLi^+ + xe^- \rightarrow Li_xC_6$	**Eq. 4**
Cathode	$LiCoO_2 \rightarrow Li_{1-x}CoO_2 + xLi^+ + xe^-$	**Eq. 5**
Overall	$LiCoO_2 + 6C_{(graphite)} \rightarrow Li_{1-x}CoO_2 + Li_xC_6$	**Eq. 6**

Nowadays, LIBs represent the most important secondary batteries thanks to their high energy densities (up to 260 Whkg^{-1} and 770 Whl^{-1})[35] and power densities (up to 3000 Wkg^{-1}) with high round trip efficiency, long cycle life (500-10000 cycles), good rate capability, low self-discharge (around 1-5 % per month) and broad range of working temperatures (charge between 0-45 °C and discharge between -40-65 °C).[36] These properties coupled with a considerable abatement of pack costs from 1000 US\$ kWh^{-1} in 2010 to around 200 US\$ kWh^{-1} in 2020 and a target of 160 US\$ kWh^{-1} in 2025,[37,38] allowed LIBs to be the technology of choice in wide range of applications, ranging from portable electronic devices (smartphones, laptops, smartwatches, tablets) to electrified vehicles (bikes, scooters and cars), drones and satellites as well as stationary energy storage.[39]

For many years the research has been focused mainly on the development of LIBs with higher performance in terms of energy and power densities, cycle life, costs and safety through the use of new electrode materials and architecture, electrolytes, binders as well as modules and cells design. However, the huge increase in the global demand of LIBs mainly driven by the electric vehicles (EVs) market,[40] which will reach around 4.7 TWh in 2030 (around six-fold the demand of 2022),[41] is posing serious concerns associated with the future availability of the so-called "critical raw materials" by European Commission, which includes common LIBs elements such as cobalt, copper, graphite, lithium, manganese and nickel.[42] Despite lithium content is usually in the range 5-7% in LIBs,[43] the unpredictability about its availability, considering also that high-grade lithium reserves are oddly distributed on Earth crust (mainly in Argentina, Australia, Chile and China),[41] is expected to increase its price, giving uncertainty about the suitability of

LIBs for large-scale applications in stationary ESS. Indeed, as shown in **Figure 8**, stationary energy storage is a less demanding application respect to the transportation and portable electronics sectors in terms of energy and power densities while low cost, long cycle life and high safety are the main requirements.

Figure 8 *Radar map of specific requirements for batteries employed in different applications. Data source (Bresser et al.).[34]*

In this context, the needs and concerns aforementioned have motivated the investigation of an alternative, MWh-scalable battery technology composed of cheap, abundant and environmentally friendly materials to match the performance and economical success of LIBs.[44]

1.3 SODIUM-ION BATTERIES

The history of sodium as charge carrier for energy storage begun at the end of 1960s with the invention of sodium-sulfur (Na-S) battery by Ford Company. Na-S is a high-temperature battery with a tubular design comprising molten sulfur as positive electrode and molten sodium as negative electrode separated by a solid ceramic alumina that works as electrolyte. This battery has an operating voltage of around 2 V, an appreciable energy density ($\sim$140 Whkg^{-1}) and efficiency (80-90 %), long shelf life (3500-5000 cycles) and does not suffer from self-discharge. Additionally, the battery is a low-cost device made with eco-friendly materials that can be recycled. However, safety issues arising from the intrinsic features of Na-S system limited its practical applications, especially in transportation, the sector for which it has been developed. Nevertheless, companies shifted Na-S batteries toward peak leveling in stationary applications, in which it has been the electrochemical energy storage system leader until 2010. In 1985, a

derivative of this battery was invented in South Africa, the so-called ZEBRA (Zeolite Battery Research Africa) in which sulfur is replaced with $NiCl_2$ and a secondary liquid electrolyte $NaAlCl_4$ has been added to enhance the Na^+ conduction. Compared to Na-S, ZEBRA has similar performance, but it has higher cell voltage (2.6 V), a wider range of working temperatures (250-350 °C), higher efficiency (90-95 %) and a higher-level of safety.[45] As well as Na-S, ZEBRA has been applied in the stationary sector, but mainly for backup power application (70-80 % of the market) while load leveling represent an emerging market segment.[34]

In the same years of the development of sodium-based high temperature batteries, the research over LIBs intrinsically carried on those of sodium analogues due to the similar nature of the alkali metals. In the early 1980s, the ability of TiS_2 to electrochemically intercalate Na was demonstrated,[46] while parallelly the family of layered metal oxides Na_xMO_2 was pioneered by Delmas and co-workers, focusing the attention on electrochemical Na^+ intercalation and structural modifications, but also leading to the classification of Na-layered oxides which is still used.[47] In the late 1980s, the collaboration between Allied Corp. (USA), Showa Denko K.K. (Japan) and Hitachi, Ltd. (Japan) produced the firsts Na-containing full-cells based on Na-Pb alloy//γ-NaxCoO₂, which showed good cyclability. However, the need for a pre-sodiation process for Pb-negative electrode combined with the higher energy density of contemporaneous Li-ion system Carbon//$LiCoO_2$, promoted the decline for research in sodium-ion systems and the commercialization of the latter. Nevertheless, at the turn of 1980s and 1990s, studies conducted to investigate the sodium-carbon interaction for metallurgy purposes led Doeff et al. to explore the electrochemical insertion of sodium into carbons.[48] Later, the first rejuvenated interest in sodium-ion batteries came in 2000 with the discovery of sodium intercalation into hard carbons by Stevens and Dahn,[49] with performance close to those of graphite in LIBs. In the following years the published research on Na-ion batteries started to increase progressively, while the growth became exponential since 2008.[47]

Nowadays, sodium-ion batteries (SIBs) are considered a complementary technology to LIBs and particularly appealing to become the device of choice for large-scale stationary energy storage installations [17,44,50,51] mainly thanks to more than 1000 times higher abundance Na resources than those of Li[52] and wider global distribution,[13] which reflect in lower cost of Na-containing raw materials (0.27 \$kg^{-1} for Na_2CO_3 vs 43.60 \$kg^{-1} for Li_2CO_3 in July 2023).[53] Moreover, the feasibility to use aluminum as current collector for both cathode and anode electrodes decrease materials cost (1.75 \$kg^{-1} for Al vs 4.77 \$kg^{-1} for Cu)[54] and weight. Although the cost of SIBs is theoretically expected to be lower respect to LIBs, the cost analysis must be addressed carefully considering a realistic mass production level of SIBs and that battery cost is not only determined by materials cost.[34] Moreover, cost-energy analysis (\$ kWh^{-1}) is clearly influenced by energy density of the battery: in this context SIBs require high energy density materials to reduce both materials and processing costs per kWh.[55] Nowadays, the cost-competitiveness of SIBs in terms of \$ kWh^{-1} can be considered achieved only respect to $LiFePO_4$ (LFP) based LIBs.[54]

Nevertheless, SIBs provide some other important advantages. About the safety, the main advantage relies in the use of aluminum current collectors which allow the storage at fully discharge state without affecting the cell performance, making handling and transportation safer. Additionally, several abuse and self-heating tests have shown that SIBs offer higher thermal stability and abuse tolerance respect to LIBs.[55] Another important aspect is that SIBs offer, in principle, higher sustainability since do not require critical raw materials such as Li, Co, Cu and natural graphite.[42] Finally, an important technical advantage relies in the feasibility to fully use the same manufacturing processes and cell designs of LIBs, providing easily conversion of LIB's giga-factories, as well as the presence of well-established supply chains for most precursors and cell components, which facilitate the large-scale production of Na-ion systems respect to other battery technology.

Despite LIBs and SIBs share the same "rocking chair" working principle, involving the reversible shuttling of alkali ions between anode and cathode upon charge and discharge, there are some differences between these systems. The larger ionic radius of Na^+ (1.02 Å) when compared to Li^+ (0.76 Å) affects the transport properties and phase stability,[56] while the higher standard potential of -2.71 V for Na^+/Na and the heavier molecular weight of Na in contrast with Li (with a redox potential of -3.01 V and a molecular weight of 6.9 $gmol^{-1}$), prevent higher theoretical specific capacity and energy density.[21] Nevertheless, the mass of the charge carrier represents a small fraction of the overall mass of the cell components, thus the gap in energy density can be in practice mitigated by selecting high capacities host structures along with high operating potential interval between cathode and anode (i.e. high cell output voltage).[57] In this context, considering that the energy density of $C/LiFePO_4$ 18650 size commercial LIBs is around 130 $Whkg^{-1}$, a same size and fully developed Na-ion battery can reach 160 $Whkg^{-1}$ at best, making it suitable for replacing LFP batteries.[58] However, another important consequence of the dissimilarities between Li and Na is that the materials used in LIBs cannot be transferred straightforward to SIBs: prominent examples are electrochemical behaviors of hard carbon and graphite in Li and Na cells, followed by the differences observed in layered oxides cathodes for Li and Na.[59] Therefore, the development of advanced sodium-ion systems requires huge efforts in materials developments.

As for LIBs, there are different SIB cell chemistries being developed with different markets and applications. **Table 1** summarizes the main sodium-ion batteries cell chemistries proposed by different companies with their reported or estimated performance:

Table 1 *Summary of SIB cell chemistries under development. Data source (Hasa et al.)[59]*

Cell Chemistry	Companies	Energy Density Wh kg⁻¹	Power Density W kg⁻¹	Cycle Life
NLO//Hard Carbon	Faradion (UK)	120-160	> 1000	> 1000
	AMTE (UK)	135-140	> 1000	> 1000
NLO//Soft Carbon	HiNa Battery (China)	120-145	Rate > 5C	> 4500
PWA//Hard Carbon	CATL (China)	160		
NVPF//Hard Carbon	Tiamat Energy	80-100	> 5000	> 4000
PBA//Hard Carbon	Altris AB (Sweden)	100-120		
PBA(Fe)//PBA(Mn)	Natron Energy (USA)	25-40	> 60000	2000-5000

Legend: NLO: Sodium Layered Oxide; PWA: Prussian-White Analogue; PWB: Prussian-Blue Analogue; NVPF: Sodium Vanadium Fluorophosphate;

Most of the companies are focusing their products to penetrate LFP-type lithium-ion batteries market, which includes low- and large- scale stationary energy storage, low-speed mobility, industrial traction and UPS (Uninterruptible Power Supply) power. The latter and the grid frequency regulation included in the stationary applications can be target especially by Tiamat Energy and Natron Energy products, which are designed for high-power applications. However, future improvements are expected in sodium-ion cell chemistry and engineering, which can open new market opportunities including electric mobility and even possibly consumer electronics.[55,59]

1.4 CELL COMPONENTS

The main components that make up the cell are the electrodes and the electrolyte. Electrodes active materials chemistry govern the cell energy since the stoichiometry of the redox processes and the mass of active materials determine the charge that can be exchanged, while the difference between the redox potentials of cathode and anode determines the cell voltage. On the other hand, the electrolyte properties regulated by salt and solvents influence the electrochemical behavior of the cell,[34] especially affecting the formation and stability of the electrode/electrolyte interphase. The cell assembly is then completed by separators, casing and electrical terminals. The electrode architecture comprises also the presence of another key

component, the binder, which is responsible, to some extent, for the performance of the cell, especially the cycle life.[60]

An overview of the abovementioned components in Li- and Na-ion batteries is provided in **Subsections 1.4.1**, **1.4.2**, **1.4.3** and **1.4.4**.

1.4.1 Anode Materials

The anode accepts Li^+/Na^+ ions during charge and release them during discharge. Attractive anode materials may have working potential as low as possible with respect to Li^+/Li and Na^+/Na redox couples and may have high reactivity towards alkali metals in order to achieve a high specific capacity. Ideally, this reaction may not promote modifications and structural damages in order to offer a long cycle life. According to the mechanism of interaction between anode material and alkali ions, they can be divided into different classes: insertion, conversion and alloying materials. Each type of anode possesses advantages and drawbacks over the others, and their characteristics are summarized in the following subsections.

One of the most important behavior of anode (and, to a minor extent, cathode) relies in the formation of a solid passivation layer on the electrode-electrolyte interface, called Solid Electrolyte Interphase (SEI). This reaction mainly occurs during the first charge, when the redox potential of the electrodes used in a battery lies outside the electrochemical stability window of the electrolyte, undergoing to an irreversible reduction at anode surface, which causes the typical initial loss of efficiency. Structurally, the SEI in LIBs is similar to that in SIBs: it has a complex and disordered structure composed of a porous organic outer layer which is permeable to both Li^+/Na^+ and electrolyte solvent molecules, plus an inorganic inner layer which allows Li^+/Na^+ transport. Unlike it could be imagined, a complete and stable SEI formation is beneficial for the (electro)chemical stability of the battery since it acts as ion conductor and electron insulator, thus allowing Li^+/Na^+ transport while preventing further electrolyte decomposition; on the other hand, an unstable and evolving SEI continually consume electrolytes along with active ions, leading to an increase in battery resistance, gradual capacity fade and low power density,[61] eventually promoting also thermal runaway events.[62] Therefore, battery performances are strongly affected by SEI composition and properties, especially thickness, morphology, chemical and mechanical stability. In this context, the lack of stable electrode-electrolyte interface in SIBs remains a key obstacle especially in successful SIB operation and commercialization.[63]

1.4.1.1 Insertion Materials

Insertion materials have been extensively studied as anode materials for both LIBs and SIBs since the insertion reactions are considered the most reversible charge storage mechanisms for

alkali-ion batteries. This kind of reactions involves the topotactic incorporation of Li^+/Na^+ into the crystal lattice of the host material, thereby modifying its stoichiometry, followed by the extraction of the guest ion which restore the original stoichiometry of the host. The reaction is generally characterized by no irreversible changes in the crystal structure of the host material, limited volume changes as well as minimal loss of energy and charge.[64] Usually the term "insertion" is randomly replaced with the term "intercalation", however, to be precise, the latter should be referred to a particular type of insertion in which the host material possess a layer-type crystal structure.[65] Based on insertion reaction, carbonaceous materials are the most important family of compounds investigated for lithium and sodium batteries.[56]

Graphite

Among the carbon material, graphite, the most stable among the allotropic forms of carbon, is currently the anode of choice for LIBs.[55] Graphite structure is composed of sp^2-hybridized graphene layers stacked together by weak Van Der Waals forces produced by the delocalized π-orbital.[66] The layers are mostly stacked in the thermodynamically stable ABA sequence with an hexagonal form (**Figure 9 a**), while the less stable ABC sequence, with a rhombohedral symmetry (**Figure 9 b**), is a less important polymorph since account for around the 14 % of natural graphite.[67] The weakness of the inter-planar van der Waals interactions, which provides a suitable interlayer distance of 3.35 Å, combined with the nature of inter-planar π-bands consisting of C $2p_z$ orbitals, easily enable the intercalation of electron donors species such as alkali metals, forming the so-called graphite intercalation compounds (GICs).[68]
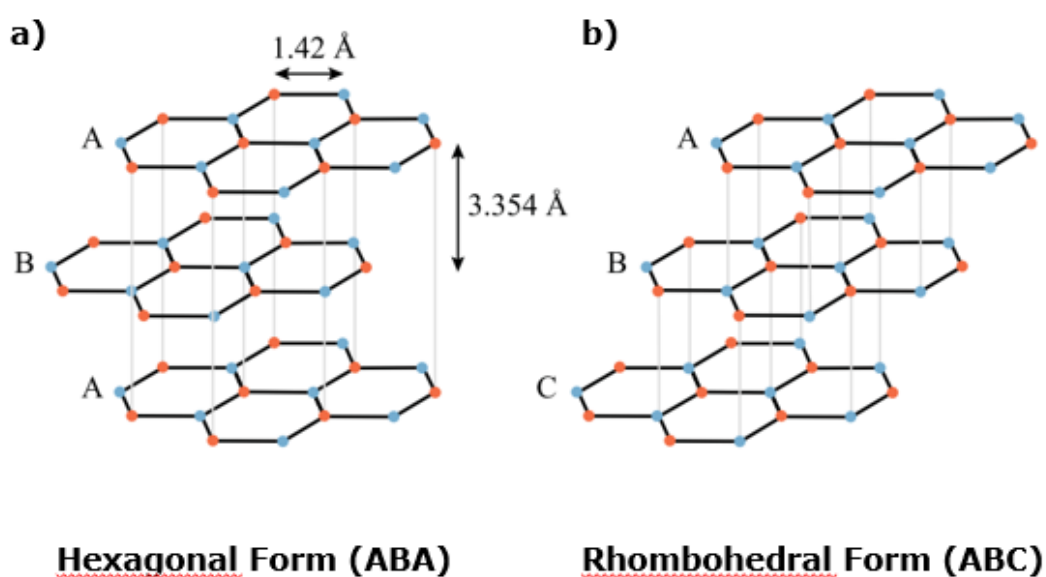
Figure 9 *Stacking arrangements of graphite: a) hexagonal and b) rhombohedral structures.*[67]

The intercalation of Li^+ in graphite occurs through a concentration-dependent process called "staging mechanism". According to this model, the intercalation of Li^+ proceeds in discrete steps, called stages, characterized by progressive incorporation of lithium into a sequence of graphite layers separated by layers without any intercalant species, in which the order *n* defines the number of graphene planes between two intercalated layers (**Figure 10 a**).[69] During electrochemical intercalation of Li^+ into graphite (**Figure 10 b**), pontential profile provides information about the sequential formation of the different stages through the presence of well-defined two-phase plateaus, meaning that both phases simultaneously exist over the course of the plateaus, while well-defined chemical compounds are present at the beginning and end of the plateaus.[70] Although different electrolytes, graphite types and testing conditions may lead to different stage transformations, the structural transitions stage III -> stage II and stage II -> stage I have been widely reported ,whereas there are some standing debates regarding higher stage such as stage IV.[71] Overall, the final formation of Stage 1, accompanied by a sliding of the single planes with respect to each other and an increase of the interlayer distance to 3.70 Å, leads to a stoichiometry of LiC_6 and provides a theoretical capacity of 372 mAh g^{-1}.[69,72] The electrochemical intercalation of lithium occurs through the previous mentioned reaction described in **Equation 4**.
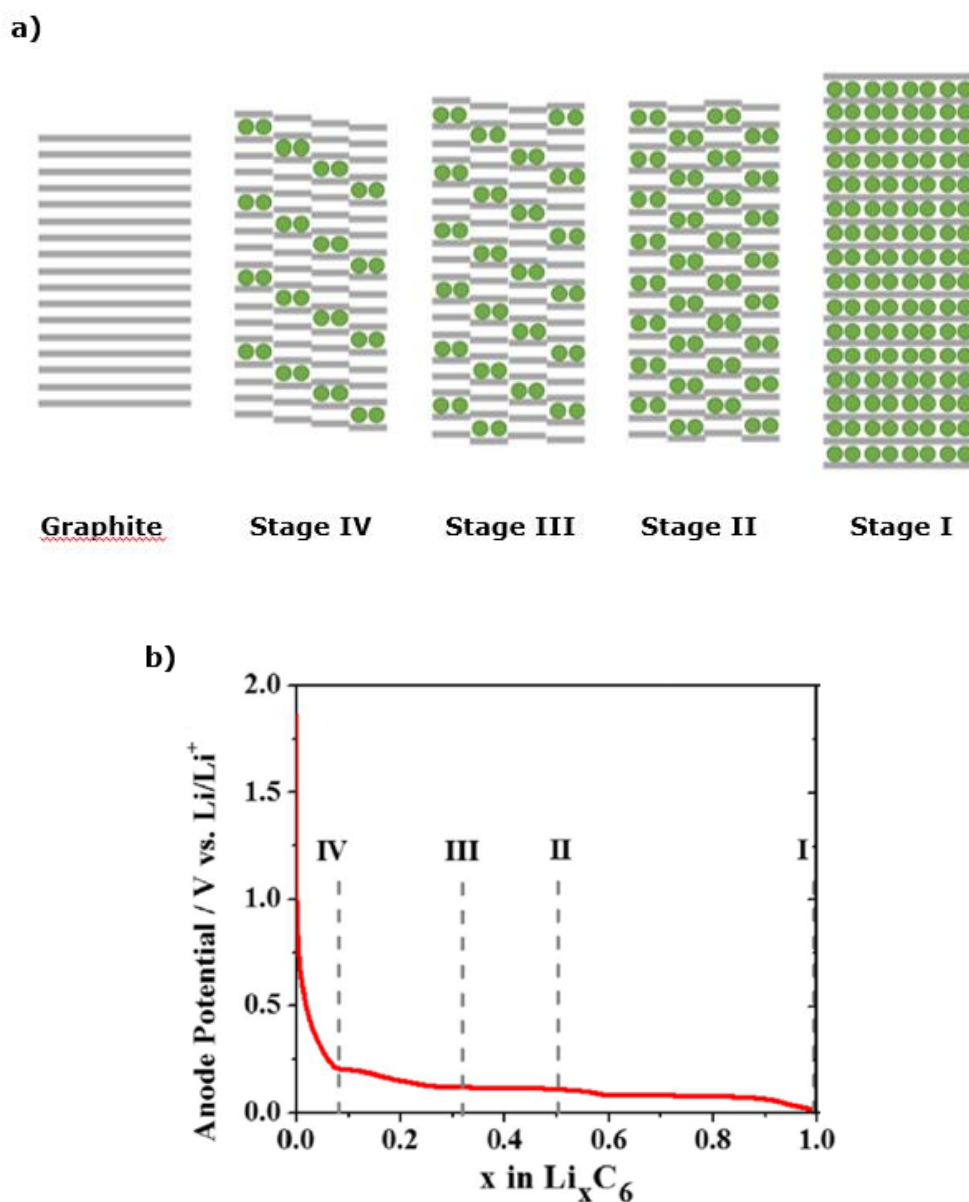
Figure 10 *a) Classical representation of staging mechanism;[73] b) charge profile as a function of lithiation state in a Li-graphite half-cell, with stages marked.[74]*

However, the electrochemical intercalation of Na$^+$ ions into graphite at room temperature is very poor, hindering the use of graphite as anode material for SIBs. The higher ionic radius of sodium compared to lithium is not the main obstacle for intercalation, since larger alkali metal ions (i.e. K$^+$, Rb$^+$ and Cs$^+$) have been reported to form GICs. The reasons should be found into the lowest thermodynamic stability of Na-GICs, which additionally require redox-potentials below 0 V vs Na$^+$/Na due to the very weak binding ability between sodium and graphite.[69,75] Attempts to improve electrochemical activity of graphite in SIBs involved the use of ether-based electrolytes, which enable the co-intercalation of solvated Na$^+$ ions, with which the best results obtained up

to now reached 150 mAh g^{-1}.[76] Nevertheless, these performance are far from that obtained with LIBs analogues.[77]

Despite its wide LIBs market share, the production of high purity natural graphite has an important drawback which can be identified in its considerable environmental impact. Recently Engels et al. estimated a global warming potential (GWP) of 9.6 kg CO_2-eq per kg of graphite produced.[78] According to their study, large part of the environmental impact (~ 74 %) arises from the energy required to perform all the production steps. Briefly, the production of graphite involves the mining and the extraction of the flake graphite through flotation; subsequently, a spheronization step is used to obtain spherical graphite particles with low surface area and narrow particle size distribution followed by a purification step through acid leaching in order to remove the impurities. Finally, an high energy-intensive coating step is conducted at high temperatures to increase the electrical conductivity of the material.

Hard Carbon

Due to the inadequate performance of graphite in SIBs, different types of alternative anode materials have been investigated so far. Among them, disordered and non-graphitizable carbon materials, called Hard Carbons (HCs), represent the state of the art anode material for SIBs[44,56,79] thanks to their promising high storage capacity, relatively low cost, wide availability, and low operating voltage of ~ 0.1 V *vs.* Na$^+$/Na.[80] As illustrated in **Figure 11**, HCs have complex structures composed by arrangements of non-planar and twisted graphene sheet fragments stacked in the short-range due to the Van Der Waals forces, forming micro-nanocrystallites. Ideally, the graphene layers are composed by sp^2 carbon atoms arranged in hexagons. However, the presence of non-sp^2 carbons or vacancies locally disrupt the hexagons network, inevitably generating structural defects; in addition, the presence of heteroatoms is another important source of crystalline defects. In the long-range, the graphene layers and crystallites are randomly oriented, creating both open and closed pores with different sizes and shapes.[81]
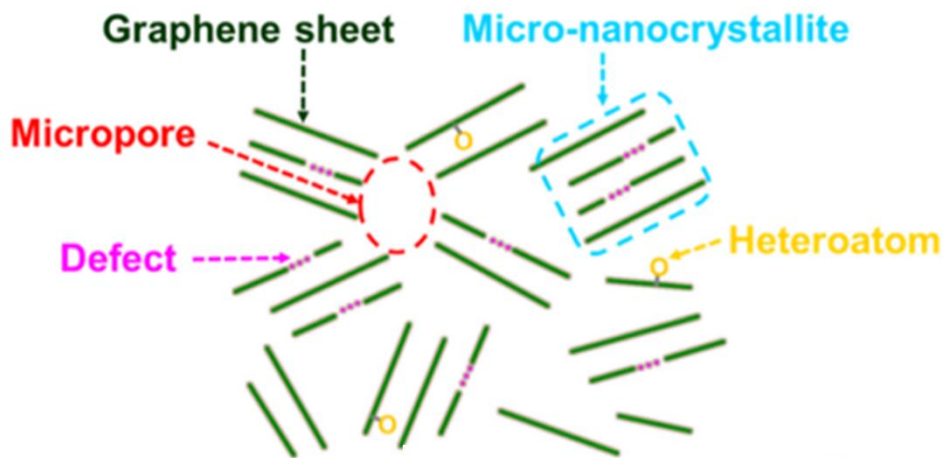
Figure 11 *Schematic illustration of Hard Carbon structure.*[82]

While extraordinary improvements have been achieved in HCs performance during the last years, the sodium storage mechanism of HCs is still not completely elucidated.[83] Typically, the sodium storage mechanism in HCs involves two distinct voltage regions in the galvanostatic profile: a sloping potential region (up to 0.1 V *vs.* Na^+/Na) and a low potential plateau (<0.1 V *vs.* Na^+/Na).[84] However, the assignment of these regions to a specific sodium storage mechanism is still under debates mainly due to the complexity of HC structure, which additionally varies from sample to sample. Despite the versatile structure of HCs, the sodium storage processes can be grouped into three categories: 1) Na^+ adsorption at surface sites, which can be divided into open pores and defect sites (edges, heteroatoms, vacancies, etc.); 2) Na^+ intercalation between graphene layers; 3) Na^+ fill of nanopores and formation of quasi metallic clusters.[85,86] Different models of interaction have been proposed so far, with four prevailing models depicted in **Figure 12**.[83] In 2000, Steven et al. proposed the model of "intercalation-adsorption" for HCs, suggesting a similar interaction mechanism between HC and Na^+ and Li^+: at high potential the intercalation of Na^+ ions between graphene layers occurs, while at low potential Na^+ fill the nanopores, resulting in a voltage plateau close to sodium deposition.[87] This model was verified one year later by the same group[88] and more recently by Komaba et al.[89] By contrast, in 2012 Cao et al. suggested the model of "adsorption-intercalation", meaning that the adsorption of Na^+ ions into surface active sites occur in the high-potential, while low-potential plateau corresponds to intercalation between layers.[90] Subsequently, structural and experimental characterizations verified this model.[91–96] In 2015, Bommier et al. put forward the so-called "three-stage model", which basically is consistent with the "adsorption-intercalation model" but with an additional process of pore filling at the end of the plateau region.[97] This model was confirmed in 2018 by Jin and co-workers.[98] Finally, Zhang et al. present the "adsorption-filling model", where the sodium storage is governed by the adsorption of Na^+ at defect sites and

surface of graphitic nanodomains in the sloping region, while the plateau capacity is due to the nanopore filling.[99] Lately, Li et al. supported this model.[100]
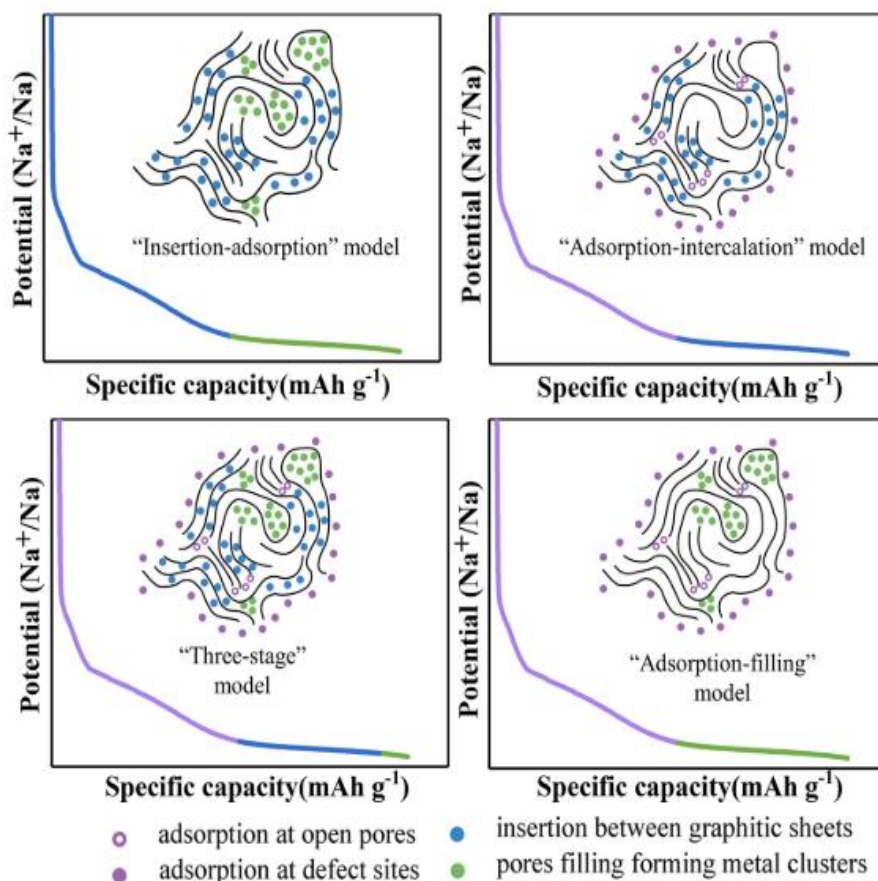
Figure 12 Four different models of sodium storage mechanism proposed for Hard Carbon.[83]

Although there may not be only one correct sodium storage model for hard carbon anodes, generalized correlation between the sodium storage behaviors and the different microstructures as well as graphitic domains of hard carbons would represents a breakthrough toward the preparation of high-performance HCs with high specific capacities, initial coulombic efficiency (ICE), capacity retention and rate capability.[94] In this way, key strategies can be applied such as graphitic structure regulation, morphological engineering and heteroatom doping.[86] Therefore, more extensive studies are required.

HCs are generally synthesized from several carbon-rich precursors, either synthetic either natural, performing a solid-phase pyrolysis generally in the temperature range 600-1500 °C,[101,102] while hydrothermal carbonization is a less common synthetic procedure.[103] Often, the carbonization process is accompanied by pre- or post-treatments with the aim of removing impurities or modifying the morphology and structure of HC. During the synthesis, several reactions occur according to the synthetic conditions and precursor composition: this means that the properties of HCs are strongly affected by these factors.[104] The thermal decomposition is a

complex process with several concurrent reactions.[81] At low-temperatures (below 200 °C), dehydratation/depolymerization reactions release water,[105] while a great amount of gases (H_2O, CO_x, CH_4) is released at around 400 °C, promoting the formation of the typical microporous structure of HCs. This first-stage lead to the formation of a solid residue called char. The char is not able to graphitize due to the highly crosslinked structure, or coming from the precursor either from the crosslinking reactions occurring during this first pyrolysis stage.[86] At higher temperatures (500-1000°C), the release of oxygen- and nitrogen-based functional groups and the removal of hydrogen from the structure leads to the formation of hard carbon (interlayer space d_{002} comprise between 3.7 and 4.0 Å). Higher temperatures (> 2000°C) lead to glassy carbon formation ($3.4 \leq d_{002} \leq 3.6$ Å) (**Figure 13**).[106]
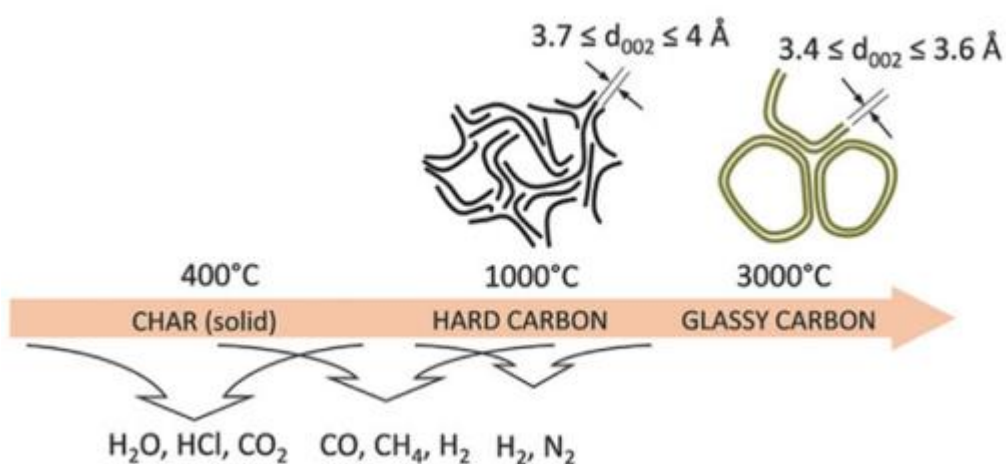
Figure 13 *Schematic illustration of structural transformation during pyrolysis of carbon-rich precursors.*[86]

Despite Hard Carbons are the most important anode materials for SIBs, there are two important challenges that must be faced: low ICE and poor rate capabilities.[107] Generally, the approaches used to improve HCs performance rely in the structural and morphological design and surface engineering. First of all, the low ICE is considered the main obstacle of HC anodes, since it dramatically decreases the energy density of the battery by irreversibly consuming active Na^+ from cathode during the first charge mainly for the formation of the SEI and also by a small irreversibility of sodiation/de-sodiation reaction. Huge efforts have been done so far for improving ICE, including pre-sodiation and electrolyte optimization as well as HCs structural design and surface engineering strategies.[108] Another important drawback of HCs are the poor rate capabilities, which mainly arises to the slow kinetic of the sodium intercalation.[109] In this case, general approaches to enhance the ionic transport relies into the increasing of the graphite interlayer distance as well as the creation of an open porous structure, while surface heteroatom doping is a general strategy to provide more active sites for adsorption.[110]

Beyond the electrochemical performance, important features that make Hard Carbons appealing candidates for SIBs are closely related to their sustainability, the feasibility of large-scale production and low-cost. As already mentioned, Hard Carbons have been successfully synthesized from both synthetic and natural precursors, which can be grouped into three main families: raw biomass, bio- and synthetic polymers. Nowadays, biomass is the most explored precursor for HC production (~ 45 %), followed by bio-polymers and synthetic polymers, which contribute for around 35 % and 20 % of the investigated precursors, respectively.[106] Although another class of precursor is composed by pitches, this class of hydrocarbons has not been taken into account since it easily tend to graphitize during pyrolysis, thus requiring important pre-treatments to obtain HCs.[111]

Raw biomass is a cheap, renewable a widely distributed precursor for HC production.[112] Technically, biomass is an organic solid product of non-fossil nature obtained from natural or anthropogenic processes.[113] It can be classified into different groups, among them, the so-called lignocellulosic biomass represent the most abundant natural biomass in the world, thus making it an appealing feedstock for the production of high-value materials such as those for energy storage. Lignocellulosic biomasses are materials mainly composed of cellulose, hemicellulose and lignin arranged in three-dimensional structures forming plant cell walls (**Figure 14**).[114] The lignocellulosic biomasses are largely composed by lignocellulosic wastes, which refers to plant or plant-based biomass not used for food, feed and industrial applications (buildings, energy crops, etc.). Therefore, it mainly includes agricultural by-products/residues and forestry wastes, which represent either abundant and renewable feedstocks for the conversion into other products (organic fertilizer, biochemicals, biofuels, etc.), or a considerable environmental problem if are not properly managed.[115] In fact, the combination of the large quantities produced with a traditional management which usually involves the landfilling and open-air burning, produces various adverse impacts for the environment.[116] Therefore, the exploitation of lignocellulosic waste for the production of value-added materials such as active material for batteries is not only beneficial for the improvements of the environmental sustainability of battery industry, but also for the agroforestry waste management itself.[114,117]
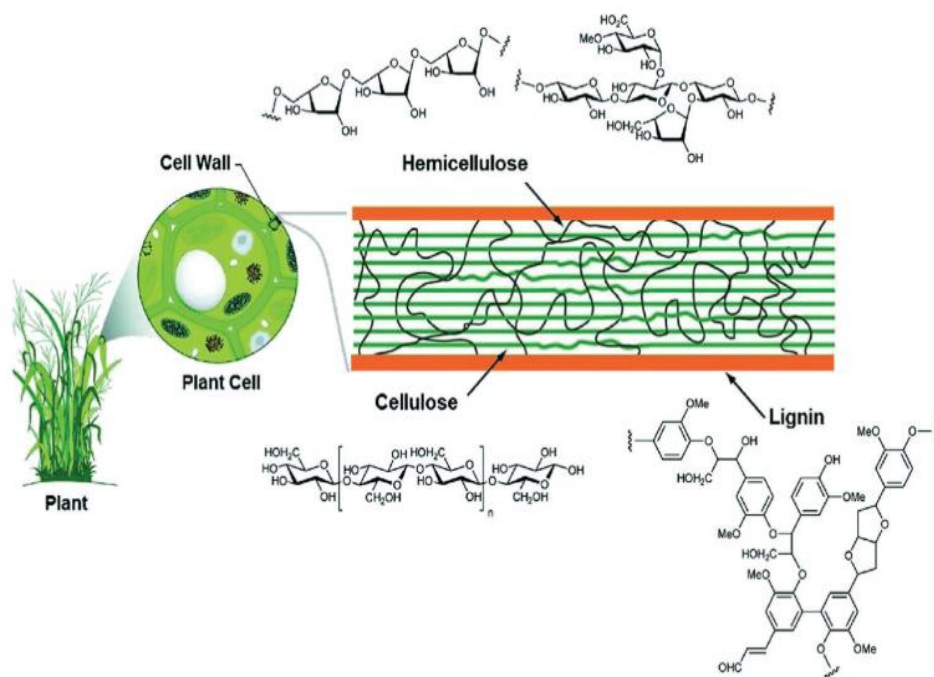
Figure 14 *Lignocellulosic composition of cell walls and the chemical structure of each subunit (cellulose, hemicellulose and lignin).*[105]

In this context, several lignocellulosic waste materials have been investigated as precursors for SIBs such as wood,[118] peanut shells,[119] pinecone,[120] sugarcane bagasse,[121] olive leaves[122] and lotus stem.[123] These lignocellulosic material differs each other for the chemical composition as well as along with the macro and micro-architecture of the raw biomass, which facilitate unique properties of the resulting HC materials. Although lignocellulosic precursors are the most interesting material to produce hard carbon due to their chemical composition, availability and low cost,[81] important disadvantages rely in the low carbon-yield after pyrolysis (~ 20 %) and in the presence of a significant amount of inorganic impurities, which may negatively affect the electrochemical performance, requiring a supplementary washing step generally with acids.[106] Another important drawback of lignocellulosic waste precursors and, in general, of the raw biomass, is the large compositional variability within the different biomass, which inevitably lead to different HC structure and electrochemical performance. This aspect is particularly crucial in the context of an industrial level production and must be carefully addressed. One interesting approach to mitigate the large variability of the structures and electrochemical performance of the biomass-derived HCs, is the use of biopolymers extracted from biomass as potential high-quality precursors since they combine the more homogenous chemical composition respect to raw biomass with the cost-effectiveness, non-toxicity and sustainability typical of natural compound.[105] In fact, biopolymers are produced or derived by natural sources such as plants, microbes and animals. Typical biopolymers used for HCs are cellulose,[124] lignin,[125,126] starch,[127,128] chitosan and chitin.[129] However, they offer low carbon yield (in the range 20-40 %) and the need of pre-treatments to extract the target polymer, which can dramatically reduce

the sustainability of the synthesis. Nonetheless, a recent LCA study support the environmental sustainability of a cellulose-derived HC.[130]

Finally, synthetic polymers is another important class of HCs precursors, which generally offer very high yield (~ 40-50%) and flexibility to tuning carbon microstructure and morphology by controlling the chemical composition of the precursor.[131] The most common synthetic precursors are phenolic resins,[132,133] PAN[134] and PANI.[135] The synthetic-polymers-derived HCs offers the best electrochemical performance, however, the high costs and the toxicity for humans and environment of both monomers and gases produced during pyrolysis represent the main disadvantages of these precursors.[106]

An important aspect of Hard Carbon production is the environmental sustainability of the synthesis, which is a key point in determining the overall sustainability of SIBs. Indeed, Peters et al. revealed that the anode active material production has the highest contribution (24 %) to the total GWP of a layered oxide cathode-based Na-ion battery.[136] Moreover, they found that this value is largely determined by the Hard Carbon precursor, which account for more than two-thirds of the anode GWP. If the sugar precursor considered in this study is replaced with organic waste or petroleum coke, the GWP can be significantly lowered. More recently, Peters and co-authors confirms these results in another LCA study,[137] including in the analysis also waste tyres and phenolic resin precursors. They concluded that, overall, the best precursor for HC is the organic waste apple pomace while resin-derived HC has an high environmental impact mainly arises to feedstock production. Compared to graphite, apple pomace-derived HC requires three-times less GHG emission (2.7 kg CO_2-eq per kg of Hard Carbon[137] vs 9.6 kg CO_2-eq per kg of graphite)[78] highlighting the sustainability potential arises from biomass waste derived HC.

1.4.1.2 Conversion Materials

Conversion materials are a family of compounds able to store ions through a reversible redox reaction between the alkali metal ion and a transition metal, resulting in the formation of a metallic phase and an alkali oxide/sulfide/phosphide/nitride/fluoride according to the general reaction in **Equation 7**:

$$M_b X_c + (c \cdot n)A^+ + (c \cdot n)e^- \rightleftarrows bM^0 + cA_n X$$ **Eq. 7**
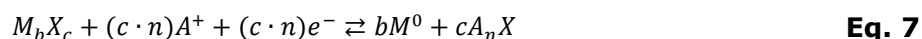
Where M is a transition metal (TM), X is a non-metal (O, P, N, F, S, H) and A is lithium or sodium. This reaction involves multiple electron exchange per TM leading to high theoretical specific capacity.[138] **Figure 15** shows the conversion reaction mechanism: during the alkali incorporation reaction, the electrochemical driving force promotes the reduction of the starting material to a metallic state M^0, which nucleates forming amorphous or crystalline nanoparticles embedded in an amorphous-like matrix $A_n X$.[139] This mechanism leads to the formation of two new phases, i.e. the electrically conductive metallic phase and the other non-metallic and

electrically insulating A_nX phase. Although the A_nX species are usually thermodynamically stable and therefore their decomposition is extremely difficult, the reversibility of the process is ensured by the presence of nanosized metal particles M^0 that catalyze A-X bond breaking leading to the formation of amorphous like $M_bX_c{}^*$, which has lost the original crystal structure.[64,140]
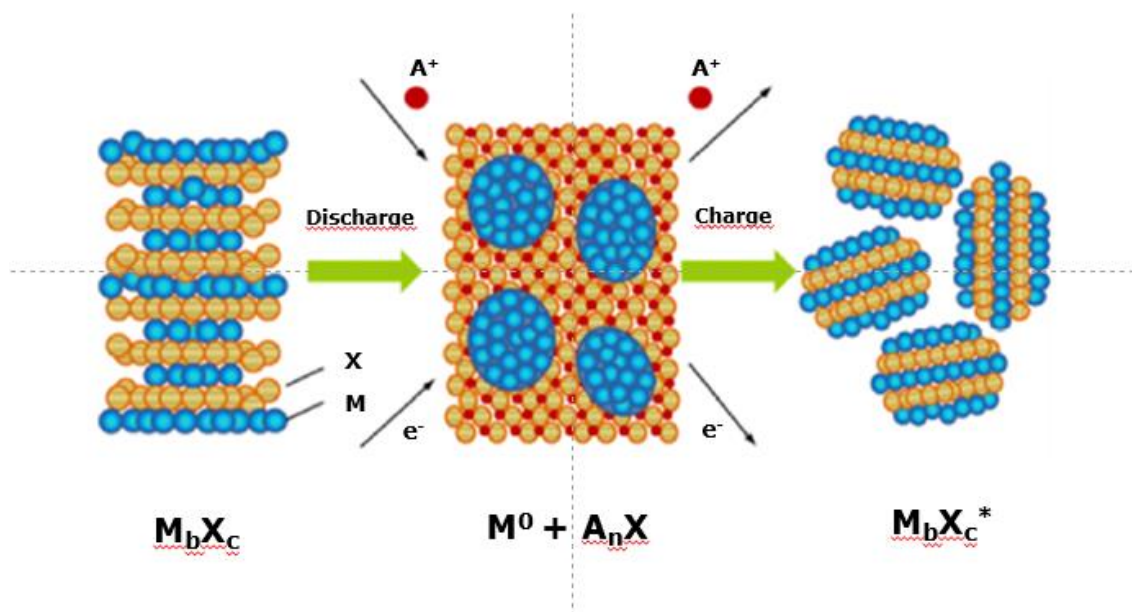
Figure 15 *Schematic illustration of the conversion reaction mechanism and structural rearrangements with alkali ions.*[141]

An important aspect that makes conversion materials appealing candidates for next-generation LIBs and SIBs is that the working potential can be tuned choosing the appropriate combination of TM and counter-anion since the ionicity of the M-X bond increases the potential of the reaction.[142] In this context, the family of conversion anode materials includes a wide range of transition metal oxides, sulfides, phosphides, fluorides, nitrides, hydrides, etc., which display a broad range of working potentials vs. Li^+/Li and Na^+/Na (generally between 0.5 and 1.5 V). Among them, binary and ternary oxides of 3d TMs (e.g. Cr, Mn, Fe, Co, Ni and Cu) are the most explored compounds for both LIBs and SIBs,[138,140] while TMs sulfides represent the most interesting alternatives.

Nevertheless, conversion materials suffer of three major shortcomings which are hindering their commercialization, considering also that their causes are complex, multiples and not well understood. The first drawback is the inconsistent cycling stability, which mainly originates from the aggregation of metallic particles during phase conversion that gradually increase in size upon cycling and in turn make the active material kinetically inaccessible; additionally, the large volume variations that accompany charge and discharge processes lead to loss of cyclable active material through mechanical stresses followed by electrode active material pulverization and dissolution; finally, a small irreversibility inherently associated with the conversion reaction

contributes to the capacity fading.[143] On the other hand, the low-initial coulombic efficiency (generally in the range 50-80 %) can be mainly attributed to the electrolyte decomposition together with the incomplete back conversions to the initial M_bX_c and/or to intermediate phases that can permit less Li/Na storage. Lastly, the most serious drawback is the low round-trip energy efficiency, which is due to the voltage hysteresis between charge and discharge profiles: charge occurs at a higher voltage compared to discharge, indicating that the amount of energy retrieved back is less than the energy stored in each cycle. The origin of voltage hysteresis is based on kinetic and thermodynamic factors and appears to be highly dependent on the nature of the anionic species, although it is still not well clarified.[139] Currently, strategies to improve the electrochemical performances of conversion-based electrode materials relies in the mitigation of the negative effects of volume variations and in the improvements of the electronic conductivity and Li^+/Na^+ ionic diffusion through particle size and morphology control coupled with the inclusion of carbon material to form composites. Finally, composition control can play an important role to reduce the voltage hysteresis since several transition metals can be combined to different anionic species to achieve suitable performance.[143,144]

1.4.1.3 Alloying Materials

Alloying materials are another class of important anode materials which electrochemically react with alkali ions generating an alloy or an intermetallic compound through the general reaction in **Equation 8**:[64]

$$M + xA^+ + xe^- \rightleftarrows A_xM \qquad \textbf{Eq. 8}$$

Where M is generally an element of group IV and V or its compounds while A is lithium or sodium.[145] The reaction leads to the formation of Li/Na-rich intermetallic compounds with multiple electron exchange, thus delivering very high theoretical capacities which can be from two to more than ten time higher than that of other carbonaceous anodes.[146] As shown in **Figure 16**, the alloying reaction mechanism generally involves phase transformation from M to A_xM through intermediate phases and leads to drastic structural changes and frequent amorphization.[64,147]
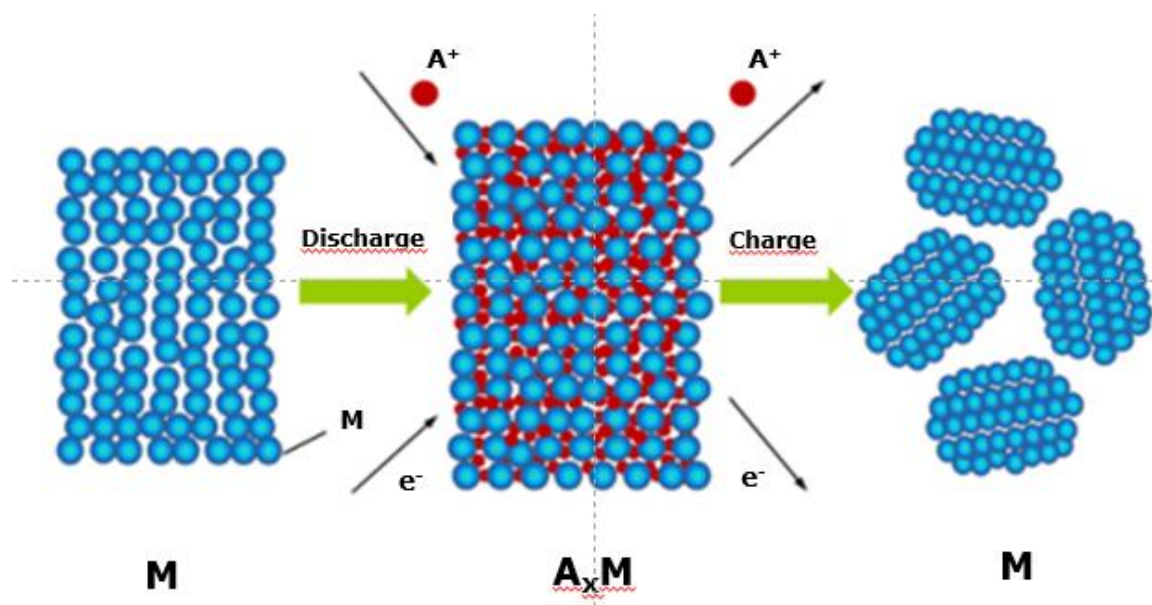
Figure 16 *Schematic illustration of alloying reaction mechanism with alkali ions.*[141]

The very high specific capacities of alloying-type anodes combined with their ability to work at a relatively low potential versus Li$^+$/Li or Na$^+$/Na as well as wide distribution, low-cost and safety of most of the investigated alloying elements, make alloying-based materials as appealing candidates for next-generation LIBs and for SIBs.

However, these materials suffer either from a low-initial coulombic efficiency due to SEI formation, either from a severe capacity fade upon cycling, which represent the key obstacles toward their implementation and commercialization; additionally, some of them (i.e. Si and P), show poor electrical conductivity.[146] The rapid capacity drop is the result of different reasons, among them, the huge volumetric variations accompanying alloying and de-alloying processes is the most important: large volume changes lead to electrode cracking and pulverization followed by loss of contact between active particles and current collector; additionally this phenomenon induce a continuous SEI breaking and re-formation and aggregation of alloy particles during cycling, accelerating the loss of reversible capacity. Finally, other irreversible processes contribute to progressive capacity loss, such as the permanent trapping of ions into the host alloy and the reaction of ions with the oxide layer on the surface of metal particles. Different approaches have been studied to mitigate the effects of the volume changes. One strategy relies in the dispersion of the active material particles in a matrix, which can be electrochemically active or not, with the aim of buffering the volume changes, providing a fast ions and electrons exchange and preventing particle aggregation by working as a spacer.[148] Another approach is the reduction of particle size and morphology tailoring, which can significantly improve the resistance toward mechanical stress and can also decrease the electronic and ionic transport distances, providing faster diffusion paths.[138,149]

Among the alloying-type anode material for LIBs, silicon (Si) is undoubtedly the most interesting material thanks to its very high theoretical specific capacity of 3579 mAh g^{-1} and low operating voltage (~ 0.2 V vs. Li$^+$/Li). The alloying reaction with lithium proceeds until a stoichiometry of Li$_{15}$Si$_4$ at room temperature,[150] leading to a huge volume expansion (up to 400 %). Apart from the very high theoretical capacity, silicon possesses other advantages such as high relative abundance (Si is the 2nd most abundant element on the Earth's crust), low cost and environmental sustainability.[151,152] However, the electrochemical performance of Si in Na-ion systems are quite lower: in a theoretical study, Si was predicted to electrochemically react with sodium to form the final phase of Na$_{0.76}$Si, limiting the theoretical capacity to 725 mAh g^{-1}.[153] Nevertheless, experimentally reported specific capacities are around 250 mAh g^{-1}: it is believed that this deviation from the theoretical value is mainly due to the slow diffusion kinetic of Na in Si.[154,155]

On the other hand, tin (Sn) has received a much greater attention as a possible alloying anode in SIBs although it has been extensively studied also for Li-system. The formation of alkali-rich phases can reach stoichiometries of Li$_{22}$Sn$_5$ in LIBs and Na$_{15}$Sn$_4$ in SIBs, corresponding to theoretical capacities of 994 mAh g^{-1} and 847 mAh g^{-1}, respectively. Additionally, Sn reacts with sodium at relatively low potential (~ 0.2 V vs Na$^+$/Na).[156,157] As an alloying-type material, the main drawback of Sn is the huge volume changes upon cycling, which are lower than those of Si, but it can still reach expansions up to 259 % for LIBs and 420 % for SIBs, hindering the practical application of pure Sn.[146,158] As for Si, synthesis of Sn-composites, nanosizing and morphology control are well accepted strategies to improve the cycling performance, although the use of metallic tin is still far from commercialization.[159] Beyond pure tin, tin oxide (IV) is another potential next generation anode material especially for LIBs due to its high theoretical capacity of 1494 mAhg^{-1} for Li$^+$ ions storage, its low operating voltage of 0.6 V vs. Li$^+$/Li as well as availability and environmental benignity.[160] The lithiation mechanism of SnO$_2$ is described by two stage reactions, where the first is a conversion-type reaction to form Li$_2$O and elemental Sn (**Eq. (9)**), accounting for a capacity of 711 mAhg^{-1}, followed by alloying-type reaction (**Eq. (10)**), which contributes for a capacity of 783 mAhg^{-1}.[161]

$$SnO_2 + 4Li^+ + 4e^- \rightleftarrows 2Li_2O + Sn \qquad \textbf{Eq. 9}$$

$$Sn + xLi^+ + \rightleftarrows Li_xSn \; (0 < x < 4.4) \qquad \textbf{Eq. 10}$$
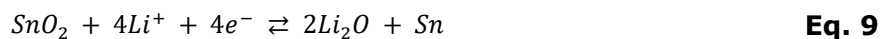
Earlier, the conversion reaction of **Eq. (9)** was considered as completely irreversible with no capacity contribution, while recently findings revealed that this reaction could be partially reversible and will have significant amount of capacity contribution, strongly depending on the structure of the electrode.[162] As for the others, the large volume variations accompanying charge and discharge reactions are the main obstacle toward its commercialization, where the strategies brought into play are basically the same: nano-structuring, morphology control and

compounding with porous carbonaceous materials. In particular the last strategies has been largely demonstrated to be beneficial both for the overall conductivity of the electrode and also for the mitigation of the large volume changes of SnO_2.[159,160,162]

1.4.2 Cathode Materials

Cathodes are materials able to release Li^+ or Na^+ ions during charge and accept them during discharge. Generally, the cathode is the key component limiting the performance of the battery and the most expensive part.[163] Current LIB/SIB chemistries require lithium/sodium-containing compounds as positive-electrode materials to supply alkali ions to the negative electrode.[34] Suitable compounds should display specific properties such as high capacity, chemical stability, low toxicity and safety, and a high working potential vs. Li^+/Li or Na^+/Na redox couples. Cathodes are generally intercalation-type materials and are classified according to their crystal structure: layered oxides, spinel oxides and olivine phosphates are the common crystal structures for Li-cathodes, while the most viable cathode families for SIBs can be divided into layered oxides, prussian blue analogues and polyanionic compounds.

1.4.2.1 Layered Oxides – LIBs and SIBs

Lithium layered transition metal oxides of general formula Li_xTMO_2 (x ≤ 1, TM = Transition Metal) are the most employed cathode materials for LIBs.[164] These cathode materials have Li and TM located in octahedral sites of the cubic close-packed (ccp) oxygen array, forming alternating layers between oxygen planes. This structure has an ABCABC stacking sequence defined as O3-type structure since the Li^+ ions occupy the octahedral sites (O refers to octahedral) and there are three MO_2 layers per unit cell (**Figure 17**). The two-dimensional framework for reversible lithium insertion/extraction is provided by MO_2 layers, while a fast Li^+ diffusion is guarantee through the interconnected lithium-ion sites arises from the edge-shared LiO_6 octahedral.[165]
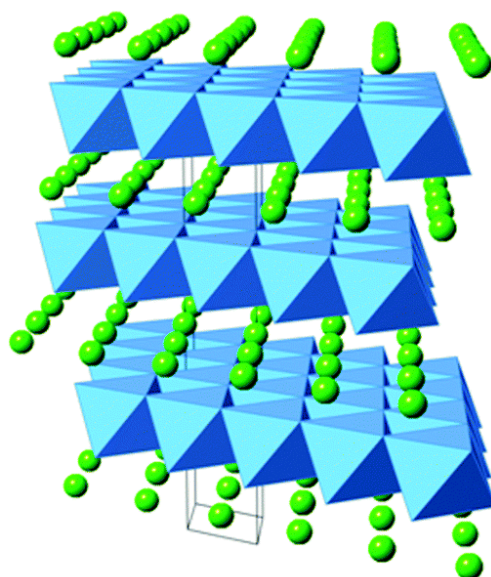
Figure 17 *Crystal structure of layered LiMO$_2$ cathodes. Green spheres represent Li$^+$ ions, while MO$_6$ octahedra are colored in blue.*[166]

The main layered cathodes studied for LIBs are lithium cobalt oxide LiCoO$_2$ (LCO), lithium nickel oxide LiNiO$_2$ (LNO) and lithium manganese oxide LiMnO$_2$ (LMO). Among them, LCO was the first positive-electrode materials studied and commercialized by Sony in 1991.[34,166] LCO has a theoretical capacity of 274 mAh g^{-1}, a redox potential of $\sim$ 4 vs. Li$^+$/Li, long cycle life and good cycling performance. However, important limitations are attributed to the high cost, low thermal stability and fast capacity fade at high current rates or during deep cycling (i.e., delithiation above 4.2 V, meaning approximately 50% or more Li extraction). In fact, although the high theoretical capacity, only 0.5 lithium ions per formula unit can be reversibly inserted/extracted leading to a practical capacity of around 140 mAh g^{-1}. This considerable limitation in practical capacity has been attributed to lattice distortion from hexagonal to monoclinic symmetry which deteriorates cycling performance. Therefore, different types of metals have been studied as Co partial substitutes or dopants with the aim to improve LCO thermal stability and electrochemical performance even during deep cycling.[167] Among them, the family of LiNi$_{1-y-z}$Mn$_y$Co$_z$O$_2$ (NMC) compounds with different stoichiometric ratios received great attention as possible replacements for LCO, providing an higher reversible capacity ($\sim$160-200 Ah kg^{-1}) together with a lower Co content (hence resulting in cheaper and more sustainable cathode materials).[168] The reason for mixing Ni, Co and Mn relies in the physical features that each metal provides, with the main aim of improving structural and chemical stability as well as lowering the cost.[169] Nowadays, successful designs of NMC cathodes based on trade-offs in terms of composition and morphology allowed that these nickel-rich layered oxides are installed in most EVs, such as Kia, Toyota, Volkswagen, Ford, Mercedes, Volvo and Fiat.[170]

Analogous to LIBs, the cathode of general formula NaxTMO$_2$ built with edge-sharing MO$_6$ and NaO$_6$ octahedral layers have attracted great attention due to their high specific capacity and tunable electrochemistry based on the TM redox center.[171] According to the classification proposed by Delmas et al.,[172] layered oxides can be classified into O3, O2, P2 and P3 structures (**Figure 18**), where O and P denote the Na$^+$ polyhedral coordination environment, i.e. Octahedral and Prismatic trigonal coordination, respectively, while the characters 2 and 3 correspond to the number of MO$_2$ stacked layers within each unit cell. In addition, when an in-plane distortion is present, it is denoted with the prime symbol ('), such as that O'3 and P'3.[173,174] Among the Na$_x$TMO$_2$ family, O3 and P2 phases are the most employed crystal structures.[171]
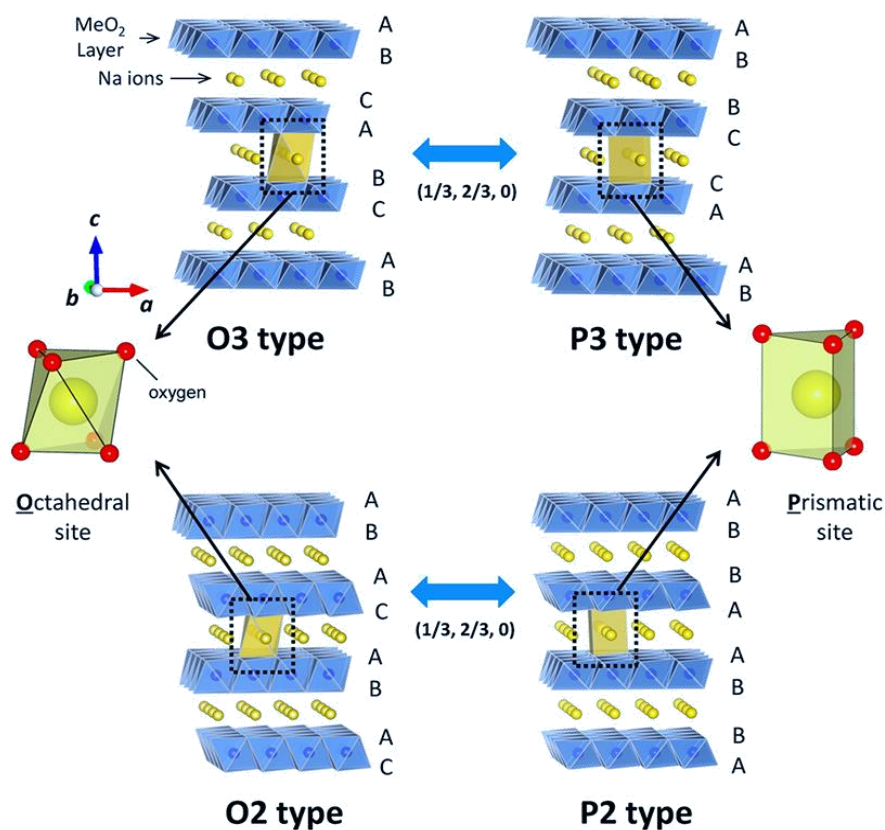
Figure 18 Classification of Na$_x$MO$_2$ layered structures and phase transition processes upon Na extraction.[173]

Generally, depending on the sodium content, the formation of a crystal structure is favored over the others. O3-phase materials typically have high Na content (x close to 1),[56] thus enabling high specific capacities and energy densities, but suffering from poor rate capabilities due to relatively small interlayer spacing and complex Na diffusion channels through interstitial sites, and also unsatisfactory cycling stabilities due to multiple phase transitions occurring during cycling.[175] In fact, generally, sodium extraction from O3-structures is known to induce phase transitions as a result of the vacancies generated during sodium extraction, forming energetically stable prismatic sites for Na$^+$ by gliding the MO$_2$ layers without M-O bonds breaking. As a result, a new phase with oxygen stacking of ABBCCA, classified as P3-type, is formed. On the other

hand, the transition O3→P2 requires high energy to promote M-O bond break and reformation, hence it is a forbidden transition at room temperature.[174]

In contrast, P2-type phase is structurally stable with sodium content in the range 0.7 > x > 0.6,[173] typically displaying enhanced cycling stability as a result of lower phase transitions coupled with superior rate performance due to large Na diffusion channels with straight pathways between prismatic sites. However, the lower Na contents result in lower capacities in full-cell configuration.[175] Also the P2-phase is not inert toward phase transition: the large prismatic sites of P2-phase are stabilized by Na^+ ions upon $Na_{0.46}TMO_2$,[56] while further desodiation leads to phase shift toward a new O2-type phase where octahedral sites are created as a consequence of the gliding of MO_2 layers, with oxide layers stacked in an ABACAB fashion. Overall, the P2-phase displays better electrochemical performance respect to O3-phase because of its structural integrity and lower diffusion barrier and high ionic conductivity.[173,174] Nonetheless, the use of bi-phasic materials, which combine both the P2 and O3 type phases into a single material, has attracted significant attention in recent years as a potential solution to combine the cycling stability of P2-type materials with the Na content of O3-type oxides.[175] In any case, as for LIBs, binary and ternary systems with more than one TM (TM = Co, Mn, Ni, Ti, Fe, Cr, Al, V) are generally more appealing than single transition metal Na_xTMO_2 since the use of more TMs can allow to enhance structural stability and, when an electrochemical active TM is introduced, increases energy density through the operating voltage or the specific capacity by inducing reversible oxygen redox activity or by the new transition metal-based redox processes. Additionally, a better pathway and a faster Na^+ diffusion can be provided by more Na^+ vacancies due to ions with a higher valence state (such as Ti^{4+}), improving the rate performance of the cathode material.[176] In this context, Faradion has already patented and installed in its battery packs a mixed phase layered oxide cathode of O3/P2-Na_x(Ni, Mn, Mg, Ti)O_2.[59]

1.4.2.2 Spinel Oxides - LIBs

A restricted family of compound of general formula LiM_2O_4 (M=Ti, V and Mn) crystallizes in the spinel structure (**Figure 19**), in which Li^+ and $M^{3+/4+}$ ions occupy the tetrahedral 8a and octahedral 16d sites, respectively, while the oxygen ions are located on the 32e sites forming a cubic close-packed array.[165] Half of the octahedral sites are occupied by M ions which form a 3D-framework of edge-sharing MO_6 octahedra, which is the lithium transport pathway for Li^+ conductivity. Since the octahedral 16c sites remain empty, the Li^+ conduction occurs from one 8a tetrahedral site to another 8a tetrahedral site via a neighboring empty 16c octahedral site as it offers the lowest energy barrier.[169,177]
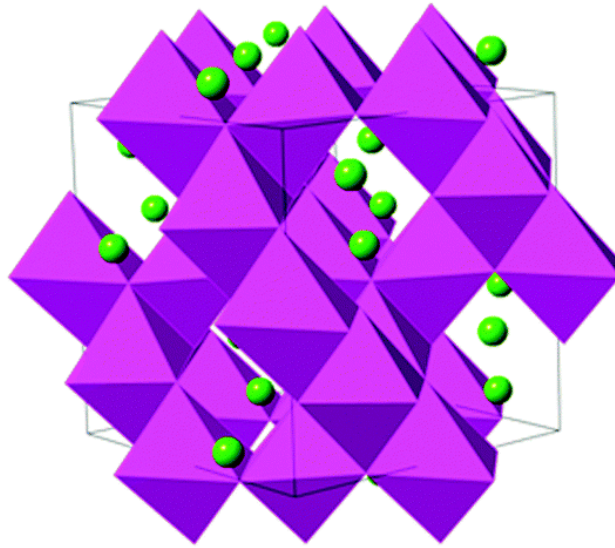
Figure 19 *Crystal structure of spinel cathode LiM$_2$O$_4$. Green spheres represent Li$^+$ ions, while MO$_6$ octahedra are colored in violet.*[166]

Among the spinel-type, LiMn$_2$O$_4$ with a theoretical capacity of 148 mAh g^{-1} and a limited practical capacity of 120 mAh g^{-1} is an important cathode material for LIBs which is still used in cathode blends of many EV batteries thanks to its excellent rate performance as well as low cost and environmentally benignity compared to Co-containing cathodes.[178] However, despite its strong edge-shared [Mn$_2$]O$_4$ octahedral lattice and structural robustness, LiMn$_2$O$_4$ undergoes failure upon cycling, particularly at high temperatures.[177] This capacity fade can be mainly attributed to the manganese dissolution and to the Jahn-Teller distortion effect.[179] The first is the result of the disproportion of manganese species at the particles surface in the presence of trace amounts of acidic H$^+$ in the electrolyte according to the **Equation 11**:

$$2Mn^{3+}_{(solid)} \rightarrow Mn^{4+}_{(solid)} + Mn^{2+}_{(solution)}$$ **Eq. 11**

where Mn^{2+} species are soluble in the electrolyte, leading to the leaching of TM redox centers and thus resulting in a progressive capacity loss. On the other hand, the Jahn-Teller distortion effect aggravates the situation, since the transition from cubic to tetragonal crystal symmetry, as the concentration of Mn^{3+} increases in the spinel lattice, leads to large volume changes causing poor electrochemical performance.[169]

As for layered oxides, the partial substitution of Mn with other metal cations forming LiM$_x$Mn$_{2-x}$O$_4$ solid solutions (M = Ni, Cu, Cr, etc.) is an important strategy to improve the cycling of LMO, at the expense of a decrease in the initial capacity. In particular, the substitution of 25 % Mn with Nickel in LMO spinel provides an effective stoichiometry for Mn to stay in the 4+ valence state, thus reducing the Jahn-Teller effect associated to the presence of Mn^{3+} ions, while still

possessing a high capacity associated to a high-voltage plateau at 4.7 V associated to the oxidation/reduction of Ni^{2+}/Ni^{4+} couple, with an overall 2e$^-$ transferred per single half-cycle.[180]

1.4.2.3 Polyanionic Compounds – LIBs and SIBs

Another important class of cathode materials are the polyanionic compounds, which contain a series of tetrahedron units $(XO_4)^{n-}$ or their derivatives $(X_mO_{3m+1})^{n-}$ (X= P, S, Si, As, Mo or W) with strong covalent-bonded TMO_x polyhedra. Compared to layered oxide cathodes, the strong X-O bonding in polyanion-type compounds can promote ionicity character in M-O bonding, leading to higher energy difference between its antibonding orbitals and vacuum state, hence resulting in higher redox potential. This is the so-called "inductive effect" in polyanion-type electrode materials. Furthermore, the strong X-O covalent bonds greatly improve the stability of the oxygen in the lattice, thus increasing the safety of such class of materials.[181,182] One of the most important group of polyanionic-type electrode materials for both LIBs and SIBs are phosphates: olivine-type-structured $ATMPO_4$ (where A = Li, Na and TM = Fe, Mn, Co, Ni) and NASICON-structured $A_xTM_2(PO_4)_3$ (where A = Li, Na and TM = V, Ti) represent the main phosphate compounds investigated for both lithium and sodium rechargeable batteries.[181]

In LIBs, the olivine-type structure compounds are the most investigated phosphates-type cathode materials, among them, $LiFePO_4$ (LFP) is the most representative one, since it is widely used in commercial lithium-ion batteries for EVs and stationary energy storage systems.[183] The olivine $LiTMPO_4$ consists of a slightly distorted hexagonal close-packed (hcp) oxygen array, where Li and TM are located in half of the octahedral sites and P atoms in one-eighth of the tetrahedral sites, generating TMO_6 octahedra with a distorted geometry.[184] The tetrahedral PO_4 groups share a common edge with one TMO_6 octahedron and two edges with LiO_6 octahedra. The lattice displays a strong 2D-dimensional character, with Li$^+$ ions able to be inserted and removed in the 1D tunnel-like structure as displayed in **Figure 20**:[185]
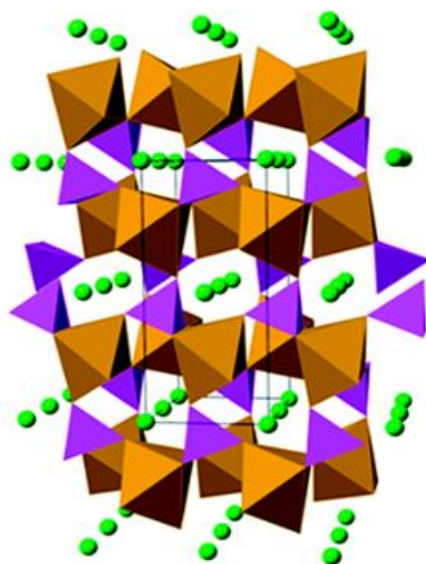
Figure 20 *Crystal structure of olivine cathode LiMPO₄. Green spheres represent Li⁺ ions, M-O polyhedra in brown, while PO₄ tetrahedra in purple octahedra are colored in violet.*[166]

LFP has a theoretical capacity of 170 mAh g^{-1} and a working potential around 3.5 vs Li⁺/Li,[186] the latter being advantageously constant during the redox processes associated with Li⁺ (de)insertion. Moreover, the redox potential can be tuned according to the TM used. The olivine-type family displays other interesting properties, such as high structural and thermal stability, which can be translated in long cycle life and high safety level, as well as low cost and low toxicity.[184] However, the most important limitation of olivine-type materials is given by their low electronic conductivity, which can be generally overcome by using thin carbon coatings on the surface of the material's particles.[177]

In SIBs, polyanionic compounds and in particular Na-containing phosphates are one of the major classes of cathode materials investigated so far. Inspired by the huge success of LiFePO₄, the sodium analogue NaFePO₄ was explored as possible Na⁺ host, however, this material crystallizes in two different structures: triphylite-type and maricite-type. The former possesses analogous structure to LFP with 1D-pathways for sodium diffusion, while the second lacks diffusion channels for Na⁺ transport. This means that triphylite NaFePO₄ has excellent electrochemical performance in SIBs, while maricite NaFePO₄ is electrochemically inactive. Conventional synthetic routes are not suitable for obtaining triphylite since the more thermodynamically stable crystal structure is maricite. The only way to obtain triphylite is performing chemical or electrochemical Li⁺/Na⁺ cation exchange from LiFePO₄, but this method is reported to be very complicated and not suitable at industrial scale.[187]

On the other hand, polyanionic compounds of the NASICON-type (Na Super Ionic CONductor) have attracted great attentions due to their 3D open framework with superior ionic conductivity.

The general structure presents TMO_6 octahedra connected to three PO_4 tetrahedral units each, forming the basic unit called "lantern". Each lantern is linked with other six lanterns, composing a 3D framework with large interstitial space that can accommodate from 0 to 5 alkali cations per formula, depending on the oxidation state of TM and X element.[188] Several NASICON materials have been investigated, demonstrating satisfactory rate capability and cycling stability.[189] Among them, NASICON-phosphates represent the most important family since they combine the fast ionic diffusion typical of NASICON with the high structural stability and easy producibility typical of phosphates.[190]
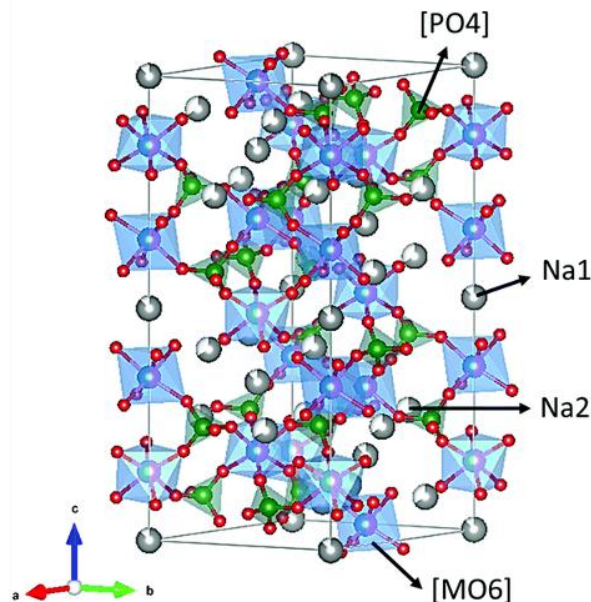
Figure 21 *Crystal lattice of the NASICON-type structure, depicting MO_6 octahedra (blue), PO_4 tetrahedra (green) and Na atoms (red).*[189]

Among the most promising NASICON-type compounds, vanadium-based NASICON-phosphates are considered promising cathode for SIBs thanks to the high specific capacities given by the multi-electron transfer of vanadium redox couples V^{5+}/V^{4+} and V^{4+}/V^{3+} operating at high potential, while the redox couple V^{3+}/V^{2+} can be in principle used as anode redox center since it works at relatively low potential.[188] As example, the famous NASICON $Na_3V_2(PO_4)_3$ (NVP) was found to possess great sodium storage capability and versatility, showing two redox potentials at 3.4 V and 1.6 V, corresponding to V^{4+}/V^{3+} and V^{3+}/V^{2+} redox reactions, with can be applied both as cathode and anode with relative theoretical capacities of 117 mAhg^{-1} and 50 mAhg^{-1}, respectively.[191] When NVP is used as cathode, two moles of Na per formula unit are extracted with an impressively flat voltage plateau, providing ultrahigh rate performance.[188] Even if the main drawback for this cathode material is the poor electronic conductivity, it has been generally overcome reducing particle and/or using carbon-coatings.[44,190]

In order to increase the energy density of the material, improving the output voltage of the cathode materials through the introduction of a highly electronegative anion is considered an

effective approach to increase the redox potential: as already mentioned, highly electronegative anion can weaken the covalent bond between TM−O, which can lead to a larger energy difference between antibonding orbitals and vacuum state and hence result in a higher redox potential. F$^-$ is the most widely explored anion, especially for vanadium-based phosphates: replacing one $(PO_4)^{3-}$ of NVP with 3F$^-$ leads to the fluorophosphate $Na_3V_2(PO_4)_2F_3$ (NVPF), which has proven to exhibits superior performance, with a theoretical capacity up to 130 mAhg^{-1} with a stable high operating voltage of 3.9 V. NVPF is one of the representative members of the sodium−vanadium fluorophosphate family, which comprises all the compounds of general formula $Na_3(VO_{1-x})_2(PO_4)_2F_{1+2x}$ ($0 \leq x \leq 1$) where the oxidation state of vanadium alters as the fluorine content changes: when x is 1, the compound is the above-mentioned $Na_3V_2(PO_4)_2F_3$ and the valence of V is +3, while when x is 0, the compound is $Na_3V_2O_2(PO_4)_2F$ and the valence of V is +4. Intermediate compounds are V^{4+}/V^{3+} mixed-valence phases.[192] All the $Na_3(VO_{1-x})_2(PO_4)_2F_{1+2x}$ phases exhibit two high reaction voltages at 3.6 and 4.1 V vs. Na$^+$/ Na and capacities in the range 120–130 mAhg^{-1}.[189,193] However, there is an ongoing debate regarding the vanadium redox activity in this family of compounds: the endmember $Na_3V_2(PO_4)_2F_3$ is believed to have the V^{3+} electrochemically active, thus involving the V^{4+}/V^{3+} redox couple during charge and discharge,[194] while authors who work with mixed valent V^{3+}/V^{4+} compounds found either that V^{3+} is active[195] or inactive,[192,196] thus in the latter the V^{5+}/V^{4+} redox couple is involved. Finally, the other extreme of this family, $Na_3(VO)_2(PO_4)_2F$ (NVOPF) with vanadium in 4+ valence state, has a crystal structure comprises bi-octahedra $(V_2O_{10}F)$ and (PO_4) tetrahedra with two Na$^+$ diffusion sites Na1 and Na2 at (8h) and (8i), respectively (**Figure 22**).[197]
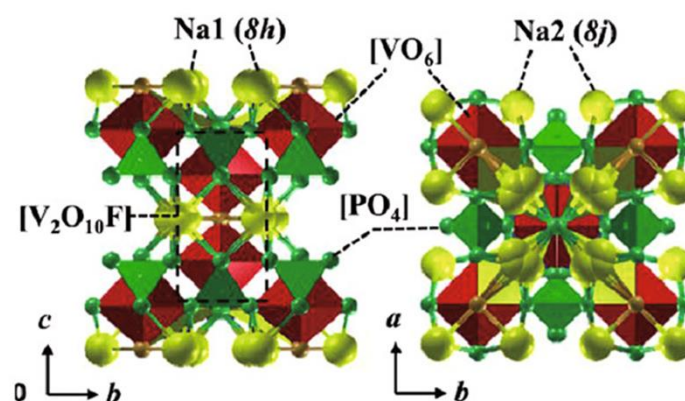
Figure 22 3D crystal structure of $Na_3V_2O_2(PO_4)_2F$.[197]

The NVOPF involves the redox transition between V^{4+} and V^{5+}, with two sodium extracted per mole of cathode according to the **Equation 12**:[196]

$$Na_3(VO)_2(PO_4)_2F \rightleftarrows Na(VO)_2(PO_4)_2F + 2Na^+ + 2e^-$$ **Eq. 12**
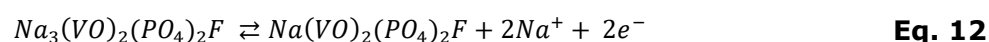
Overall, all the materials belonging to this family have a great potential for the practical application in SIBs, especially for those purpose requiring high power density and long cycle life: as already mentioned in **Table 1**, Tiamat Energy (France) employs NVPF as cathode in its cell chemistries, reporting a power density higher than 5000 Wkg^{-1} for more than 4000 cycles.[59] Concerning the endmember NVOPF, full cell performance still need to be carefully evaluated to fulfill the requirements for commercial application, considering also that it was found that this material has a lower electronic conductivity respect to NVPF and to the mixed valence phase with V^{3+} and V^{4+}.[192,193] Nevertheless, cation doping, carbon coating and nano structuring are considered effective strategies to overcome these issues.[197]

1.4.2.4 Prussian Blue Analogues – SIBs

For the last forty years, Prussian Blue Analogues (PBAs) have been widely studied as promising cathode materials for SIBs thanks to their excellent redox activity, low cost and highly reversible phase transitions during insertion/extraction of alkali metal ions.[198] Nowadays, PBAs are the cathodes of choice for the first-generation SIBs cell chemistries of Natron Energy (USA) and Altris AB (Sweden).[59] PBAs are a family of compounds of general formula Na$_x$TM[TM'(CN)$_6$]$_y\square_{1-y}$·zH$_2$O, where TM and TM' represent transition metals bonded by C≡N− bridge in a 3D open structure able to host Na$^+$ ions, while $\square$ represents the vacancy caused by the removal of an TM'(CN)$_6$ group, which are spontaneously occupied by coordination or interstitial water.[199] According to the amount of redox active sites, PBAs can be divided into single and dual-electron transfer types, with theoretical specific capacities of 85 mAhg^{-1} and 170 mAhg^{-1}, respectively. The former have the advantages of negligible structural distortion and high ionic conductivity, allowing in principle long cycle-life and fast-charge, while the latter are more suitable for higher energy density application thanks to the higher output voltage and capacities.[198] Usually, the crystal structures of PBAs vary between cubic, monoclinic and rhombohedral, mainly depending on the amount of vacancies and crystal water.[200] Upon cycling, PBAs undergo phase transitions during sodium extraction/insertion (**Figure 23**), which are generally reversible for high-quality PBAs, although the exact mechanisms has not been clarified yet.[198,200]
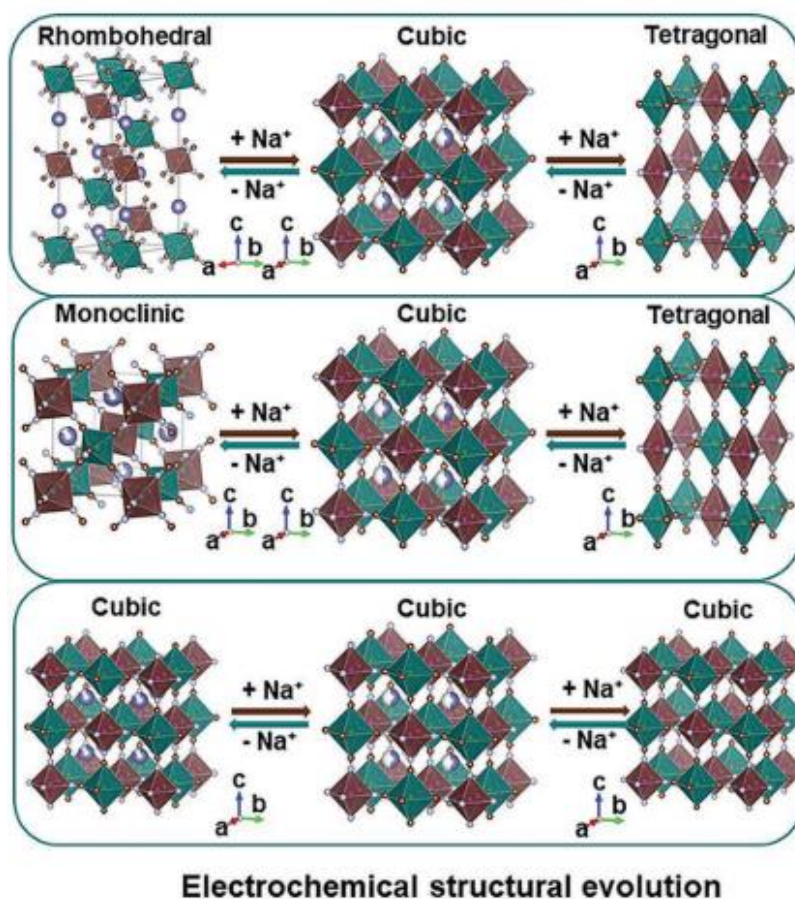
Figure 23 *Illustration of PBAs structural evolution upon sodium extraction/insertion.*[198]

The main disadvantage of PBAs is the severe capacity fading strongly correlated with the crystal structure collapse, which can be ascribed to the negative effect of vacancies, crystal water and the interfacial side reactions between active material and electrolyte, as well as cathode material dissolution and electrolyte decomposition. Researchers have proposed different approaches to elongate the cycle life of PBAs, including material crystallinity enhancement, elemental substitution and the utilization of carbonaceous composites. However, despite PBAs reached the practical application, additional efforts are required to improve the electrochemical performance of this class of compounds.

1.4.3 Binder

The binder is another key component of battery electrodes although is generally employed in small amounts (between 2-5%). The function of the binder is to glue the active material and the conductive agent with the current collector, thus ensuring physical and electrical contact within the electrode components, avoiding the capacity loss and increasing the cycle life.[60] An ideal binder should meet some important requirements, among them, those related to the electrode

processing are the most important: firstly, the binder should be uniformly dissolved/dispersed in high concentration in the solvent, while the latter should be as greener as possible to drastically reduce the environmental impact of electrode production. Other important properties for binders are appreciable thermal stability, high chemical and electrochemical stability, excellent mechanical properties, good conductivity as well as low-cost, safety and environmentally friendly behaviors.[201] Polyvinylidene fluoride (PVdF) is the state-of-the-art binder for commercial LIBs thanks to its excellent adhesion capability and its chemical stability towards the common electrolyte solvents. Moreover, PVdF has a wide ESW, appreciable mechanical strength and a thermal stability in the range of temperatures between −40°C and +150°C.[202] However, this binder has some important limitations, especially the need to be dissolved in the expensive, non-recyclable, toxic and volatile solvent N-methyl-2-pyrrolidone (NMP) during the electrode slurry processing.[201,203] Furthermore, PVdF has low flexibility, which is an important constraint especially for alloying and conversion materials and an insulating nature, restricting the Li^+ and electrons transports.[202,204] To complicate the situation, in February 2023 the European Chemicals Agency (ECHA) published a proposal to restrict the manufacture of per- and poly-fluoroalkyl substances (PFASs), which includes the PVDF.[205] Currently, the European Commission is discussing about the PFASs ban, posing serious concerns for the electrode manufacture. Therefore, new types of F-free binders have been proposed in the last years, especially aiming to drastically reduce the environmental impact and costs of electrode processing. In this context, alternative binders should be identified according to processability, chemical composition and bio-based nature.[203] Considering these criteria, aqueous binders are the desired materials, among them, bio-based polymers are the holy grail binder for both LIBs and SIBs. In this regard, the most important alternative to PVdF is the sodium salt of carboxymethylcellulose (Na-CMC), which is gradually replacing PVdF at anode side.[60]

Carboxymethyl cellulose is a water-soluble cellulose derivative obtained by replacing the H of hydroxyl group with carboxymethyl groups ($-CH_2-COO-$) at the 2-, 3- and 6- positions of anhydroglucose unit (AGU) (**Figure 24**).[206] The amount of hydroxyl group replaced by carboxymethyl moieties per AGU determines the CMC degree of substitution (DS):[207] theoretically, a maximum DS of 3 can be reached,[208] although commercial CMCs for battery applications have DS between 0.4 and 1.5. The CMC properties strongly depend upon DS and distribution of substituents along the chain since the water solubility is provided by the carboxymethyl groups, thus, a DS greater of 0.4 or almost with high uniformity in the distribution pattern is fundamental.[209] Also the molecular weight and particle size affect CMC properties.
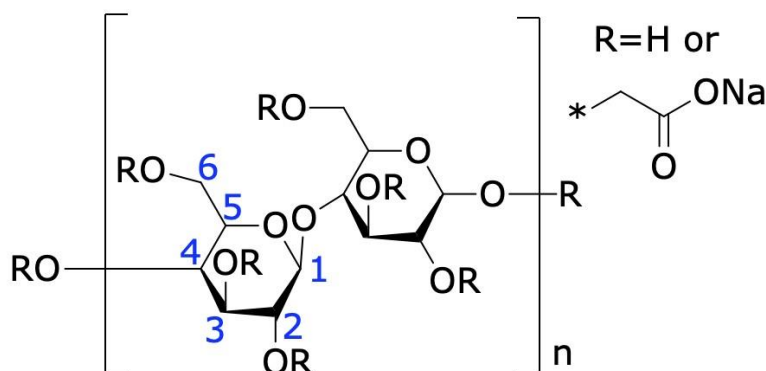
Figure 24 *Chemical structure of Na-CMC.*

Overall, Na-CMC has good mechanical, adhesive and emulsifying behaviors,[202] which has shown excellent compatibility especially with carbonaceous anode materials for both LIBs and SIBs.[210] Sometimes, CMC is used in combination with styrene-butadiene-rubber (SBR) to improve the mechanical flexibility, especially with alloying and conversion materials which are characterized by huge volume variations during cycling.[203]

Other important green binders already investigated are the sodium salt of alginic acid (Na-Alg), a water-soluble biopolymer extracted from brown algae,[211,212] polyacrylic acid (PAA) and its salts,[213,214] which can be dissolved in a series of environmentally friendly organic solvents such as ethanol, and also chitosan (CS), a derivative of chitin extracted from shells of shrimps, lobsters and crabs, which can be dissolved in water in the presence of diluted acetic acid (i.e. 1% solution).[215] Together with CMC, all these binders are characterized by the high concentration of functional groups able to form strong hydrogen bond with the active material,[60] ensuring high adhesion that maintain the electrode integrity for the long cycle life of the battery. Moreover, the chemical structure of these binders open the possibility to the development of novel binders through cross-linking reactions and self-healing capability for high-performance SIBs.[210]

Recently, lignin, the second most abundant biopolymer has attracted great attention due to the large abundance worldwide, especially as byproduct of paper industry. Overall, global lignin industry produces around 50 million tons per year of which the 95 % is disposed or used as low-quality fuel while only the 5% is reused for value-added applications.[216,217] Lignin is one of the main constituents of plant cell walls, providing rigidity and strength to the cell wall through the covalent bonds with cellulose and hemicellulose, forming the so-called lignin-carbohydrate complex (LCC). Chemically, lignin is an heterogenous aromatic polymer biosynthesized by enzymatic dehydrogenation of three monlignols monomers, p-coumaryl alcohol, coniferyl alcohol

and sinapyl alcohol (**Figure 25 a**), which undergo radical polymerization forming characteristic lignin linkages, which basically are ether bonds and carbon-carbon bonds.[218] The polymerization creates an high level of crosslinks and branches, building the typical amorphous 3D network of lignin, which is composed by three types of phenylpropanoid subunits: p-hydroxyphenyl (H), guaiacyl (G) and sinapyl (S) residues (**Figure 25 b**), where specific proportions of them varies between different plant species.[219]
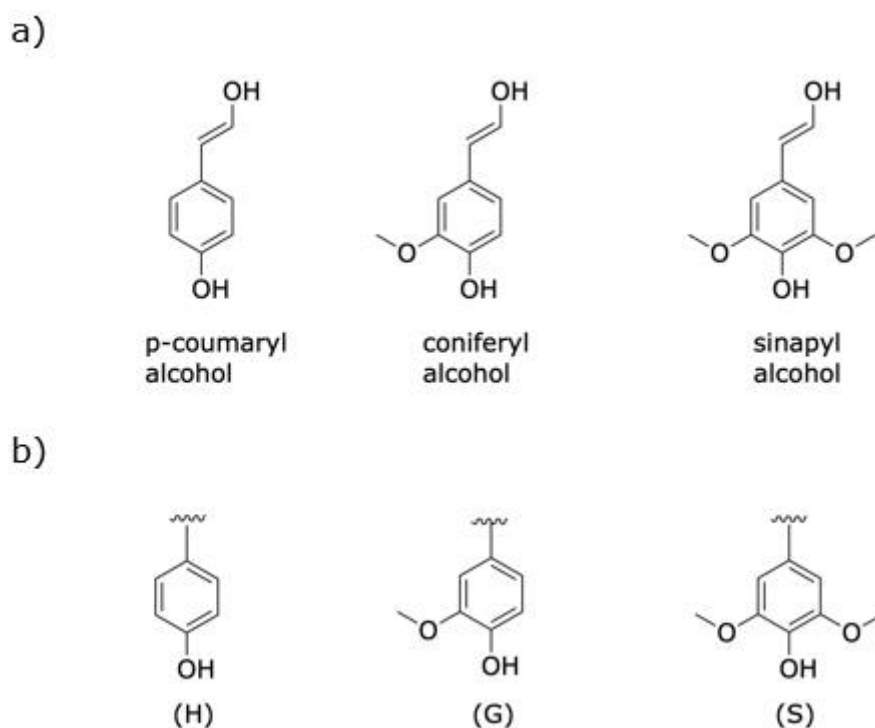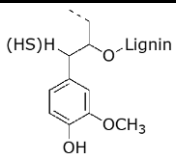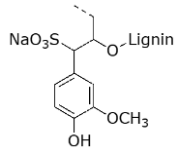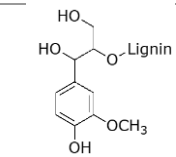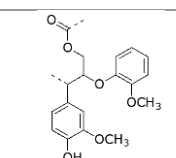
Figure 25 *Molecular structure of a) monolignols monomers and b) hydroxyphenyl (H), guaiacyl (G) and syringyl (S) subunits.*

The exact molecular structure of lignin as well as some physical and chemical properties depends on its origin and also on the extraction method. There are four common extraction methods of lignin, although there are other types of lignin isolated from biorefinery processes, which separate lignocellulosic components through acid, alkali or enzymatic hydrolysis of carbohydrates.[220] Recently, the extraction with deep eutectic solvents (DES) has attracted great attentions due to the high purity of lignin obtained.[221,222] Since the extraction involves the partial depolymerization of "native lignin" to isolate the so-called "technical lignin", the chemical structure, molecular weight, solubility, thermal properties, etc. depends upon the process conditions and reagents used.[223] **Table 2** compares some properties of the lignin obtained from the main different methods.

Table 2 *Comparison of structures and properties of four main lignin.*[220,224]

Method	Lignin Structure	Reagents	Impurities (%)	Mw	Solubility
Kraft	(HS)H O–Lignin, OCH₃, OH	Na₂S/NaOH	Sulphur: 1.0-3.0 Ash: 0.5-3.0 Carbohydrates: 1.0-2.3	1.5-5 (up to 25)	Alkali aqueous solution, some organic solvents
Sulfite Pulping	NaO₃S O–Lignin, OCH₃, OH	Na₂SO₃/NaHSO₃	Sulphur: 3.0-8.0 Ash: 4.0-7.0 Carbohydrates: N/A	1-50 (up to 150)	Aqueous solution
Soda Pulping	HO, HO, O–Lignin, OCH₃, OH	NaOH	Sulphur: 0 Ash: 0.7-3.0 Carbohydrates: 1.5-3.0	0.8-3 (up to 15)	Alkali aqueous solution
Organosolv	O, OCH₃, OCH₃, OH	Organic solvents	Sulphur: 0 Ash: 1.7 Carbohydrates: 1.0-3.0	0.5-5	Alkali aqueous solution, some organic solvents

The lignin can be divided into sulfur-containing lignin, obtained from Kraft and sulfite pulping processes, and sulfur-free lignin, extracted with soda pulping and organosolv method, respectively. Generally, sulfur-based lignins have higher molecular weight and impurities, while sulfur-free lignins are more pure with a lower molecular weight. Regarding the solubility, all the technical lignins are soluble in alkali aqueous solution (pH > 12), while kraft and organosolv lignin are also soluble in some organic solvents.[220,224]

Lately, lignin has attracted great interest to produce fuels, fertilizers, polymers, carbon materials and fine chemicals. In the energy storage sector, lignin has been identified as an excellent precursor for Hard Carbon synthesis since it combines the low cost and large distribution proper of natural compound with the desired properties for HCs production, such as very high carbon content (around 60 %), high aromaticity and several oxygen-containing functional groups.[225] On the other hand, the use of lignin as binder in electrode materials was not so much explored:[226] few studies were done using lignin as binder in electrode materials for LIBs[216,217,227,228] and SIBs.[229] Nevertheless, lignin can be in principle a good binder thanks to its aromatic skeleton that can provide structural rigidity and thermal stability while the highly crosslinked structure can ensure robust adhesiveness.[220,224] However, the main issue to the use

of lignin as binder is related to the solubility of low molecular weight lignin into the common electrolyte solvents,[217] which require that this fraction must be removed. Considering the typical large distribution of lignin molecular weights obtained with current extraction methods, the removal of low molecular weight lignin can drastically decrease the suitable fraction for binder application, obstacling the practical application. Therefore, huge efforts are required to assess the feasibility of using lignin as binder material for rechargeable batteries, paying attention to the electrochemical behavior and stability upon cycling.

1.4.4 Electrolyte

The electrolyte is another major key component of a battery since it provides the migration of Li^+ and Na^+ ions between the two electrodes upon charge and discharge. A good electrolyte must meet some important requirements: 1) high ionic conductivity and low electronic conductivity to minimize the internal resistance of the cell, 2) wide electrochemical stability window (ESW) to tolerate the voltage between anode and cathode, 4) high thermal stability to guarantee high level of safety, 4) high chemical stability to ensure no side reactions with electrodes, 5) low-cost and non-toxicity.[230] For both LIBs and SIBs, several types of electrolytes have been investigated over the years, either liquid and solid, among them, the most widely studied and commercially employed are liquid ones. Nonetheless, solid electrolytes are rapidly emerging as a potential alternative because they can allow to improve the energy density of the cell, either being lighter respect to liquid analogues either because they have a wider ESW, allowing the use of high-voltage cathodes, as well as opening the field of metallic anodes.[231] Additionally, they can ensure an higher level of safety since flammable organic solvents will be no longer present.[35] However, the main problems of solid-state electrolytes relies in the low ionic conductivity, poor electrode/electrolyte interfacial compatibility and thus limited kinetics of the charge transfer, which dramatically limits the power performance of the solid-state batteries ant their practical application in commercial devices.[232]

Typically, liquid electrolytes contain an alkali metal salt dissolved in organic solvents with eventually the presence of additives.[233] The salt provides the alkali ions needed to shuttle the charge between anode and cathode. It must possess a very hindered negative counter-ion, so that its contribution to the ion diffusion is negligible with respect to that of Li^+ or Na^+. For LIBs, several salts such as $LiPF_6$, $LiClO_4$, $LiAsF_6$ and $LiBF_4$ have been investigated, while equivalent salts have been studied for SIBs, especially $NaPF_6$, $NaClO_4$ and $NaBF_4$.[234] Regarding the solvent, an ideal electrolyte solvent should meet the following requirements: 1) at least one component must have an high dieletric constant to be able to dissolve the salt; 2) be fluid (low viscosity) over a wide range of temperatures to allow for rapid ion transfer; 3) be safe, cheap and non-toxic. Generally, a mixture of organic solvents is employed to achieve the above-mentioned criteria. The nature of battery prevents the use of any protic solvents since protons would be

readily reduced at negative electrode while corresponding anions would be oxidized at the positive electrode. Thus, the organic polar aprotic solvents relevant to the field of alkali-ion batteries include two main families: ethers and esters.[235] The most common are displayed in **Figure 26**. For Li-ion batteries, the most widely used electrolyte is 1M LiPF$_6$ dissolved in a 1:1 v/v mixture of EC:DMC, commercially known as LP30, while for Na-ion batteries, better full-cell performance have been observed with 1M NaPF$_6$ dissolved in 1:1 v/v mixture of EC:PC or EC:DEC.
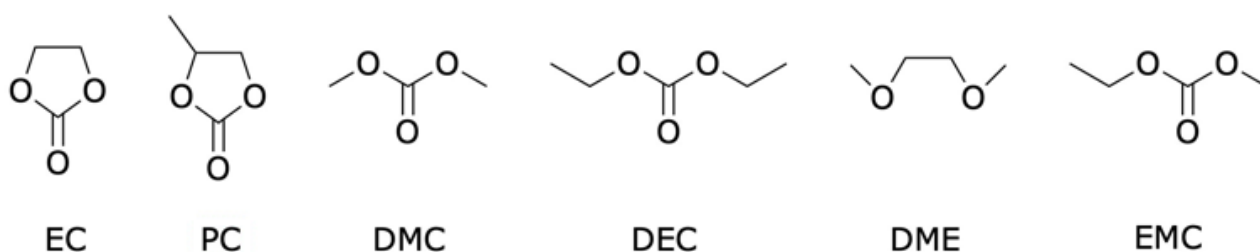
Figure 26 Structures of common electrolyte solvents used for LIBs and SIBs.

As already mentioned in **Section 1.4.1**, the performance of the battery are strongly influenced by the interfacial stability electrode-electrolyte, especially at anode side where the SEI is formed.[63] Nonetheless, a passivation layer is formed also on the cathode surface, which is called Cathode Electrolyte Interface (CEI), of which the precise structure and composition is still under debate.[236] Since the properties of the passivation layer largely depends on the nature of the electrolyte, chemical composition of LIBs electrolytes have been optimized during the years, achieving very stable SEI with few cycles of formation,[237] while worse results have been obtained for SIBs, considering also that the SEI itself in sodium-ion systems is generally more unstable and tends to dissolve in electrolyte solvents.[238] In this context, electrolyte additives are used to enhance the formation of a stable SEI, preventing dissolution and excessive growth. These compounds are added in small amounts with the aim to be consumed during the formation of the passivation layer, providing a composition with higher stability. Among the different additives, the most employed for both LIBs and SIBs are vinylene carbonate (VC) and fluoroethylene carbonate (FEC).[239]

Regarding the affinity of Hard Carbon with common liquid electrolytes, the electrode-electrolyte compatibility is generally limited, as demonstrated by the characteristic low ICE and poor rate performance. Indeed, the excessive and continuous SEI formation leads to thick and irregular interphase with poor mechanical stability, which reflects in high SEI impedance, reduced cycling stability and reaction kinetics. Also, the binder plays a crucial role in determining the electrode-electrolyte compatibility mainly affecting the decomposition of the electrolyte. In particular, the hydrogen bonding ability of the binder can reduce the exposure of surface oxygen-containing functional groups toward the electrolyte, inhibiting the decomposition of the latter.[240] In this

context, bio-based binders such as CMC and lignin can provide better H-bonding ability respect to the conventional PVDF.

1.5 AIM OF THE WORK

In the present thesis work, the goal of sustainability and circular economy are pursued by investigating lignocellulosic waste as feedstock for the production of electrode materials for lithium- and sodium-ion batteries, trying to achieve suitable performance coupled with the reduced environmental impact coming from the valorization of bio-waste. Taking into account that the two main sources of lignocellulosic waste are agricultural by-products and forestry residues and just Italy produces around 20 millions tonnes/year of crop waste and 2 millions tonnes/year of forestry residues,[241] one agricultural by-product and different forestry residues have been used to produce Hard Carbon and binder materials for alkali-ion batteries. Although the optimization of materials synthesis and cell configurations is out of the aim of this work – hence it has not been fully explored –, the methodologies and electrodes proposed are aimed to keep the whole work as greener as possible. Overall, the work has been divided in two experimental chapter, one dedicated to the agricultural waste corn cob, while the other focused on the forestry residues.

Chapter 2

Corncob, the core of an ear of maize, represent an abundant and readily available lignocellulosic waste considering that the maize has the largest production globally with an estimate production of 1026 million tons per year and the corncob account for around the 22 % of its weight.[242] The average lignocellulose composition of corncob is in the range 33-43 % cellulose, 26-36 % hemicellulose and 17-21% lignin,[243] while the carbon content account for around the range 47 % of the weight.[244] Considering these interesting data, corncob has been used as raw material for both the production of Hard Carbon and for the extraction of cellulose for the synthesis of the aqueous binder material sodium carboxymethylcellulose. Moreover, considering the debate still ongoing over the sodium storage mechanism of HCs and the huge attempts done to elucidate it through advanced in-situ and ex-situ characterization techniques,[83] herein, the fundamental insight of the sodium storage behavior has been expanded through an electrochemical approach, which has not been deeply investigated so far. Finally, the performance of the corncob waste-derived electrode has been evaluated also in Li-ion half-cells with two different purposes. Firstly, as active materials, exploring a potential alternative to the well-established graphite considering the looming issues related to the supply of this material, which has been recently added as a critical raw material from the European Commission especially due to the monopoly of China, which produces more than 70 % of natural graphite.[245] In this context, the electrochemical

tests were performed focusing the attention where the graphite is less performing, i.e. rate capability and high-current rate performance,[72] thus investigating the capabilities of Hard Carbon to replace the graphite in some specific applications, decongesting the pressure over the graphite supply chain. Secondly, corncob-derived HC has been evaluated as buffer matrix for SnO_2, an extensively studied next-generation anode material for both lithium-ion and sodium-ion batteries, whose development is hindered by the rapid capacity fading typical of this type of material as a consequence of the huge volume changes during lithiation and de-lithiation.[162] Taking into account that the creation of SnO_2/carbon composites is one of the best strategies to improve the cyclability of tin (IV) oxide, the electrochemical measurements were conducted with the aim to screen the effects of electrode parameters and electrolytes over the electrochemical performance, expanding the efforts for the development of this anode material.

Chapter 3

Beyond the agricultural by-products, the conversion of forestry waste to value-added materials and their application into electrochemical energy storage systems is another important task to promote the circular economy and improve the sustainability of both wood and batteries supply chains as well as the maintenance of forest areas. In fact, during wood processing into timber or other valuable wood products, approximatively 50 % of lignocellulosic waste is produced, which is typically used for heat generation or landfilled directly in the forest.[246] In this context, taking into account that the forest scraps represent another abundant and renewable sources of cellulose, hemicellulose and lignin, five different forestry trees scraps were collected and exploited to produce Hard Carbons and to isolate cellulose and lignin, which are in turn processed for the preparation of Na-CMC and lignin binders, respectively. In details, regarding the Hard Carbon, although the effects of the composition of the lignocellulosic raw material over the structure and the electrochemical performance of Hard Carbon have been investigated, there is not a single consensus regarding the best precursors for Hard Carbon production between high-lignin content or high-cellulose content biomasses. Additionally, the inorganic impurities present in the biomass matrix play a crucial role over the structure and the performance of HCs.[247] Herein, a short comparison between the structure and the electrochemical performance of high-lignin content or high-cellulose content biomasses have been conducted. After that, the best Hard Carbon has been evaluated in full-cell configuration with vanadium fluorophosphate cathode material in order to preliminary assess the practical feasibility of the system. Moreover, since the low initial coulombic efficiency of Hard Carbon obstacle their practical application in sodium-ion batteries,[248] the use of a sacrificial salt for the preconditioning of the anode material have been investigated as a proof of concept, conducting some preliminary experiments. Simultaneously, the lignin and cellulose fractions, the latter which has been converted into carboxymethylcellulose, were extracted and characterized, especially in terms of yields and purity. Forestry-waste derived Hard Carbons and the obtained bio-based binders were combined

in anode electrode for sodium-ion batteries, testing their performance in Na half-cell. Special attention has been given in the development of lignin as binder material, taking into account its poor valorization, currently limited to 5% of total industrial production.[224]

2. CORNCOB WASTE-DERIVED HARD CARBON AND BINDER

Herein, corncobs are used as raw materials both for the preparation of HC with a simple one-step thermal treatment and as cellulose source, which is then converted to sodium carboxymethylcellulose (Na-CMC). Apart for an additional way to reuse lignocellulosic waste, the in-house synthesis of CMC binder can be advantageous since the DS can tuned accordingly to the active material used, enhancing the electrode stability. Then, Hard Carbon and Na-CMC are combined and used for the fabrication of composite SIB anodes. The electrochemical performances of the corncob-waste derived electrode and the mechanisms of sodium storage into HC are investigated in Na half-cells. Moreover, taking into account the good electrochemical performance obtained in SIBs, particularly at high current rates and upon rate capability, corncob-derived HC and CMC composite electrodes are tested also in Li half-cells. Finally, the synthesized Hard Carbon is preliminary evaluated as a buffer matrix for SnO_2, conducting tests toward the optimization of electrode formulation, pressure as well as the effect of electrolyte additives upon cycling stability.

2.1 EXPERIMENTAL SECTION

In this section, the details about synthetic procedures, electrode processing, structural, chemical, morphological and electrochemical characterizations are summarized.

2.1.1 Synthesis of Corncob Derived Hard Carbon

The corncobs utilized in the experiment were collected from a market food of Marche region (Italy). The corncobs were smashed and dried at 80 °C for 1 day in an oven. Therefore, the dried corncobs were carbonized in a horizontal cylindrical furnace at 950 °C for 2 h under argon flow after a heating ramp of 10 °C/min. The sample was cooled down inside the furnace, under argon flow as well. Finally, the resultant material was ground in an automatic ball mill for 4 h at 300 rpm in a steel jar (ball to powder ratio 1:50 in weight). The fabricated corncobs-derived hard carbon was denoted as CCDHC.

2.1.2 Isolation of Cellulose and Synthesis of Corncobs Derived CMC

The raw materials were first ground and dried to remove the excess of water, then three subsequent treatments were preliminary conducted, each followed by a washing step with deionized water until neutral pH. The first treatment was with an aqueous solution of NaOH (3% w/w) at 100 °C for 4 h under vigorous agitation. The second one was a bleaching with an aqueous solution of NaClO (0.1% w/w) at 85 °C for 5 h, using NaOH as buffer (pH ≈12).[249] The third one consisted in a mild acid hydrolysis with 3 M HCl for 1 h at room temperature. Next, for the etherification reaction, the cellulose (dried product) was preliminary immersed in an aqueous solution of NaOH (15% w/w) and stirred for 1h at room temperature. At the same time, the mixture of chloroacetic acid and ethanol (96% v/v) was added to the batch and stirred for 2 h at 70 °C. The alkali excess was neutralized with some drops of 3 M HCl. The Na-carboxymethyl cellulose was obtained by filtration, followed by washing with ethanol and drying. The NaOH:ClCH$_2$COOH molar ratio was 1.6. The synthesized corncobs-derived CMC was labelled as CC-CMC

2.1.3 Material Characterization

Infra-Red spectra of the extracted cellulose, CC-CMC, and standard CMC (ST-CMC) (Sigma Aldrich) powders were recorded by means of a Perkin-Elmer Spectrum Two FTIR spectrometer within the wave number range of 400 to 4000 cm^{-1}. Thermogravimetric analysis (TGA) of CC-CMC was carried out using a Perkin-Elmer STA 6000 Thermal Analyzer. The nitrogen flow rate was set to 50 mL min^{-1} and an alumina crucible was used to hold the sample. After equilibration, the powder was heated up to 900 °C at a rate of 10 °C min^{-1}. The thermogram of synthesized CC-CMC was compared with that of a commercial analogue (Sigma-Aldrich). ^{1}H-Nuclear Magnetic Resonance spectroscopy (NMR) was used to estimate the degree of substitution (DS) of CMC, according to the method proposed by Klosiewict.[250] The method involves the measurement of the ratio of two spectral integrals, A/B, where A is one half of the integral of the carboxymethyl signals in the region between 4.0-4.5 ppm, and B is the integral representing an area of one proton in an anhydroglucose unit. The values of B are obtained using one-sixth of the total integral of the major C-H signals between 3-4 ppm. Before the analysis, the CC-CMC sample was dissolved in deuterium oxide at a concentration of 15 mg/ml heating to 70 °C for 2h. The spectra were recorded using a Varian Mercury 400 spectrometer operating at 400 MHz. The chemical shifts were quoted in ppm and calibrated from the residual protons signal of deuterated solvent as internal standard. The goodness of the estimation method was assessed applying it to a reference Na-CMC with a DS of 0.90 declared by the manufacturer.

Scanning Electron Microscopy (SEM) and Energy Dispersive X ray analysis (EDX) of the CCDHC sample were acquired using a FESEM Cambridge Stereo scan 360 electron microscope equipped with QUANTAX EDX detector (at an accelerating voltage of 15 kV). The structure of the CCDHC powder was characterized by X-ray diffraction (XRD) (Bragg–Brentano geometry, Cu-Kα, λ = 1.54059Å) and Raman spectroscopy (Horiba IHR 320, wavelength 532 nm). The interplanar spacing (d_{002}) was calculated according to the Bragg's Law **Eq. (13)**:

$$d_{002} = \lambda \: / \: 2 sin \: (\theta_{002})$$ **Eq. 13**

with λ = 0.154 nm. The crystallite size along c-axis (staked plane height) L_c was estimated according to the Scherrer's Equation **Eq. (14)**:

$$L_c = K\lambda \: / \: \beta_{002} cos(\theta_{002})$$ **Eq. 14**

where K is a shape factor which corresponds to 0.9 and β is the full width at half maximum of (002) peak.[251] Moreover, the average width of graphene domain L_a was also estimated using Raman technique according to the **Eq. (15)**:

$$L_a = (2.4E^{-10}) \: \lambda^4 \: (I_G \: /I_D)$$ **Eq. 15**

where λ is the wavelength of laser source (532 nm) and I_G/I_D is the intensity ratio between the G band over the D band. Pore characteristics of CCDHC were evaluated by N_2 adsorption/desorption measurement at 77 K and CO_2 adsorption measurement at 273 K using a Micromeritics ASAP 2020 instrument. Prior to both the adsorption/desorption measurements, the CCDHC sample had been outgassed for 12 h at 150 °C. The specific surface area was calculated by the BET model over the classical range p/p^0 = 0.05 - 0.3.

2.1.4 Electrode Processing and Cell Assembling

Negative electrodes were firstly made with CCDHC as the active material, Super-P carbon (Imerys) as the conductive agent, and CC-CMC as the binder. CCDHC:Super-P:CC-CMC (85:10:5 w/w) slurries were prepared in high purity deionized water, coated onto Cu foil using the doctor blade technique (thickness of wet coating = 100 μm), and left to dry at room temperature. After calendaring, circular electrodes (9 mm diameter) were cut and further dried at 120 °C under vacuum for 12 h. The loading of active material was around 1.5 mg cm^{-2} for all the electrodes. On the other hand, composite electrodes SnO_2/CCDHC were obtained firstly mixing the SnO_2 nanoparticles (< 100 nm, Sigma-Aldrich) with the CCDHC carbon matrix through an automatic ball mill for 1 h at 300 rpm in a steel jar (ball to powder ratio 1:50 in weight); then, SnO_2/CCDHC powder was mixed with Super-P and Na-CMC (DS=0.90, Sigma-Aldrich) in the formulation

SnO$_2$/CCDHC:Super-P:Na-CMC (80:10:10 w/w). For parameters optimization, different laminates were prepared, varying the pressures applied (no pressure vs. 3.14 ton cm^{-2} vs. 6.29 ton cm^{-2}) and the ratio between the SnO$_2$ and CCDHC (1:3 vs. 1:1 vs. 3:1). Slurries were prepared in high purity deionized water, coated onto Cu foil using the doctor blade technique (thickness of wet coating = 150 μm), and left to dry at room temperature. Circular electrodes (9 mm diameter) were cut and further dried at 120 °C under vacuum for 12 h. The loading of active material was between 1.2 and 1.7 mg cm^{-2} for all the electrodes. For the Na half-cells, three-electrode Swagelok-type cells were assembled in an argon-filled glove box (Jacomex GP-campus, oxygen and moisture content less than 0.8 ppm) using CCDHC as working electrode and metallic sodium (Sigma-Aldrich) as reference and counter electrodes. A 1 M solution of NaClO$_4$ (Sigma-Aldrich) in ethylene carbonate (EC)/ polycarbonate (PC) (1:1 in volume) (Sigma-Aldrich) was selected as the electrolyte (400 μl) and 12 mm glass fiber disks (Whatman GF/A) as separator. For the Li half-cells, three-electrode cells were assembled using both CCDHC and SnO$_2$-CCDHC as working electrodes and metallic lithium (Sigma-Aldrich) as reference and counter electrodes. A 1 M solution of LiPF$_6$ in ethylene carbonate (EC)/ dimethyl carbonate (DMC) (1:1 v/v), commercially knowns as LP30 (Solvionic), was selected as the electrolyte (400 μl) and 12 mm glass fiber disks (Whatman GF/A) as separator. For SnO$_2$/CCDHC electrochemical tests, LP30 was also used in formulations including additives, i.e., 2% VC, 5% VC and 10% FEC (Solvionic). After the assembly, all the cells were removed from the glove box for the electrochemical characterization.

2.1.5 Electrochemical Characterization

All electrochemical tests were carried out using a VMP-2Z multichannel electrochemical workstation by Bio-Logic Science Instruments (France). Cyclic voltammetry of the CCDHC electrodes in Na half-cell was carried out at different scanning rates ranging from 0.10 mV s^{-1} to 1.00 mV s^{-1} in the voltage range 0.01 to 2 V. Galvanostatic charge/discharge and rate capability tests of the electrodes in both Li- and Na- half cells were collected with the voltage ranging between 0.01 and 2 V. For all the experiments of CCDHC/CC-CMC, 1C rate was assumed as 300 mA g^{-1} with respect to active material mass. In addition, C-rate capability of the CCDHC electrode was evaluated in the C/5 to 5C range (5 cycles at every rate). In order to evaluate the interfacial behavior of electrodes, electrochemical impedance spectroscopy (EIS) was carried out at the first cycle and then at each tenth cycle at E = 0.5 V, with an AC amplitude of 5 mV, in a frequency range 100 kHz > f > 10 mHz. Additionally, to deeply understand the interfacial and the sodium storage behaviors of CCDHC, staircase potentiostatic impedance spectroscopy (SPEIS) was carried out during sodiation and desodiation. The impedance measurements were carried out at 5th cyle, setting potential step of 100 mV from 1.00 to 0.01 V, applying the same pulse of 5 mV amplitude as for EIS each tenth cycle, in the frequency range 100 kHz to 50 mHz. The SPEIS data analysis was performed by Distribution of Relaxation Times (DRT) and Equivalent Circuit

Model (ECM) methods. For the SnO$_2$/CCDHC composite, galvanostatic charge/discharge tests of the electrodes in Li- half cells were collected in the voltage range 0.01-3 V. For all the experiments of SnO$_2$/CCDHC, 1C rate was assumed as 500 mA g^{-1} with respect to active material mass. According to the nature of counter and refence electrodes used, the potentials are given vs. Na$^+$/Na redox couple (E° = -2.7 V vs. SHE) or vs. Li$^+$/Li redox couple (° = -3.0 V vs. SHE).

2.2 RESULTS AND DISCUSSION

2.2.1 Synthesis, Chemical and Structural Characterization of the Corncob Derived Carboxymethylcellulose Binder

Carboxymethyl cellulose has been synthesized from corncob food waste as raw material by the procedure detailed in the Experimental Section. The NaOH alkaline pretreatment and subsequent NaClO bleaching were used to dissolve lignin and hemicellulose,[252] while HCl treatment was aimed to isolate the crystalline part of cellulose.[253] Then, the extracted cellulose was submitted to alkalinization with NaOH and etherification with monochloroacetic acid. According to the scheme proposed by Shui et al. in alkalization, the cellulose is converted to sodium cellulosate, as shown in **Eq. (16)**, while in etherification, monocholoroacetic acid is firstly converted to sodium monochloroacetate **Eq. (17)** and then undergoes to nucleophilic substitution at chloride site, forming Na-CMC **Eq. (18)**:[254]

$$[C_6H_7O_2(OH)_3]_n + nNaOH \rightarrow [C_6H_7O_2(OH)_2ONa]_n + nH_2O \qquad \textbf{Eq. 16}$$

$$ClCH_2COOH + NaOH \rightarrow ClCH_2COONa + H_2O \qquad \textbf{Eq. 17}$$

$$n[C_6H_7O_2(OH)_2OCH_2COONa] + nNaCl \qquad \textbf{Eq. 18}$$
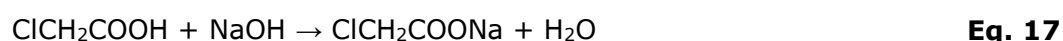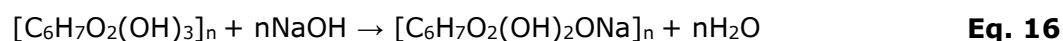
The final product has been labelled as CC-CMC. The reference commercial product is hereafter labelled as ST-CMC.

FT-IR spectra of the extracted cellulose, CC-CMC and ST-CMC are reported in **Figure 27 a**. The wide peaks around 3340 cm^{-1} and 2890 cm^{-1} in all samples can be assigned to the stretching vibration of O-H groups in glycosidic units and the C-H group stretching, respectively, indicating the cellulose backbone. The presence of a strong absorption band at ~1597 cm^{-1} in the CC-CMC sample corresponds to the carboxyl stretching COO$^-$, confirming the carboxymethylation.[255,256] The peaks at about 1422 and 1319 cm^{-1}, present in both CMC samples, are related to the -CH$_2$-scissoring and -OH bending vibration, respectively.[257] The peak at ~1040 cm^{-1} is attributed to the C-O stretching of ether and alcohol in glucose units in all samples.[254]

In order to investigate the thermal stabilities of synthesized CC-CMC and commercial ST-CMC, TGA was carried out (**Figure 27 b**). The thermal degradation pattern of CC-CMC has a similar

trend than the reference compound. In both samples, the first degradation step around 100 °C is associated with the evaporation of water. The main weight loss ($\sim$ 41%) for CC-CMC starts at an onset temperature of 230 °C and continues until 305 °C. This step can be mainly related to the decarboxylation of cellulose[258] followed by the onset of breaking down of cellulose chains into lower molecular weight fractions. The cellulose backbone decomposition is the main process evidenced in the range 305-600 °C,[259] with a weight loss of around 25%. Above 600 °C, the residual liquid and solid char evolve into a gaseous fraction leaving around 10% of ash content. Since the physical-chemical properties of CMC are affected by the degree of substitution (DS), the DS was estimated using ^{1}H-NMR spectroscopy. **Figure 27 c** illustrates ^{1}H-NMR spectrum of CC-CMC in D_2O. The CMCs spectral lines in the range 4.5-3.0 ppm are very complicated, making the assignment of ^{1}H chemical shifts and the extrapolation of structural information very difficult. The DS value of the CC-CMC sample has been estimated as 0.59, in agreement with Shui et al.[254] which used the same $NaOH/ClCH_2COOH$ molar ratio for the etherification. The DS value of ST-CMC has been estimated as 0.84 (vs. 0.9 declared by the manufacturer), thus assessing a quite good reliability of the analytical method. Due to the lower DS of CC-CMC sample, an higher hydrophobicity and thus lower water solubility is expected compared to ST-CMC.
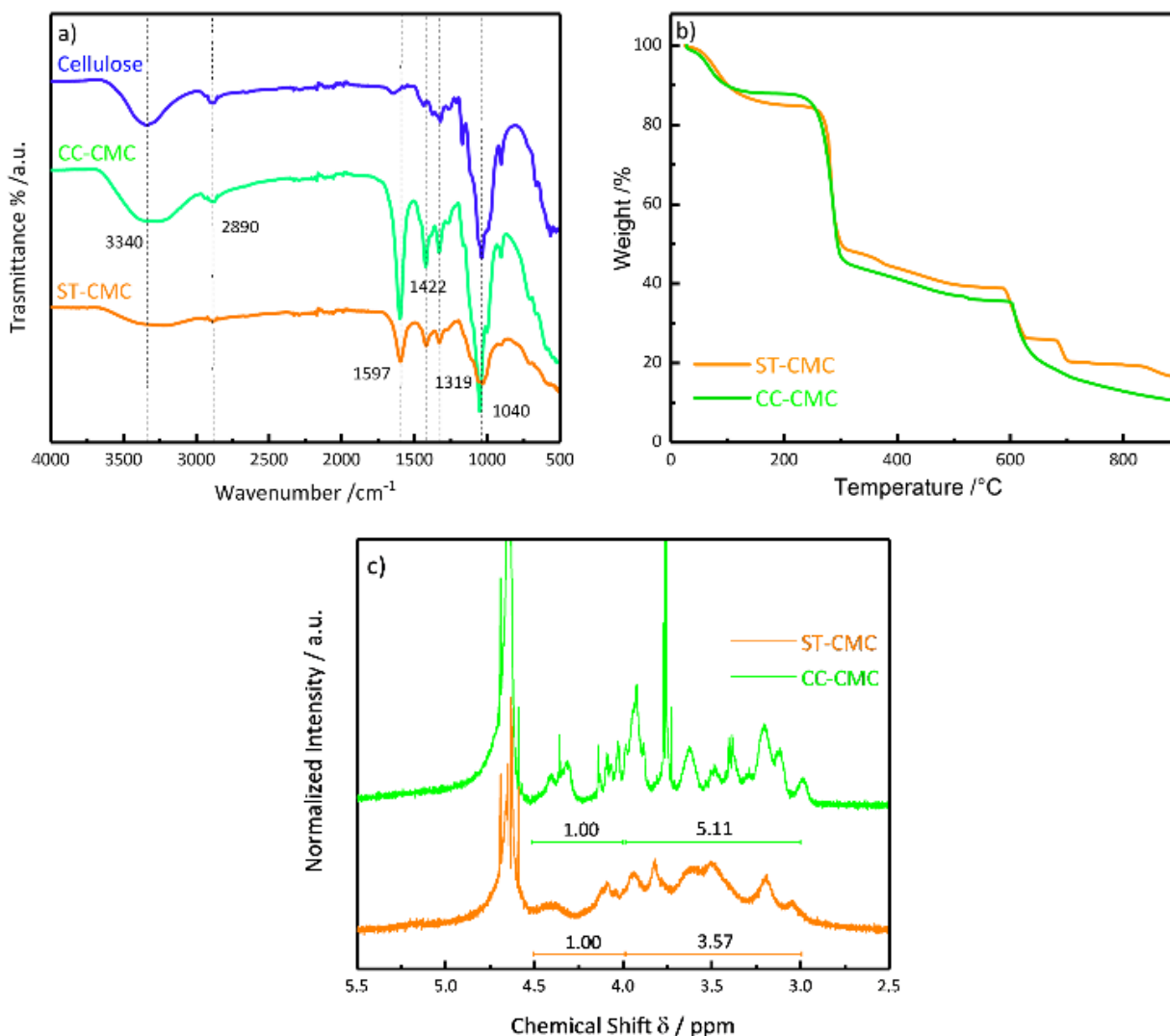
Figure 27 *Chemical Characterization of CMC. (a) FT-IR spectra of Cellulose, CC-CMC, and ST-CMC; (b) TGA data of CC-CMC, and ST-CMC; (c) NMR spectra of CC-CMC and ST-CMC.*

2.2.2 Structural and Morphological Characterizations of the Corncob-Derived Hard Carbon

The SEM image in **Figure 28** shows that the CCDHC is characterized by blocklike morphology with irregular particles size in the micrometer range.[260] The elemental composition estimated by EDX analysis reveals that, apart from carbon (95.9 at%) and oxygen (1.6 at%), there are residual potassium impurities (2.5 at%), which is originated from the biomass matrix.
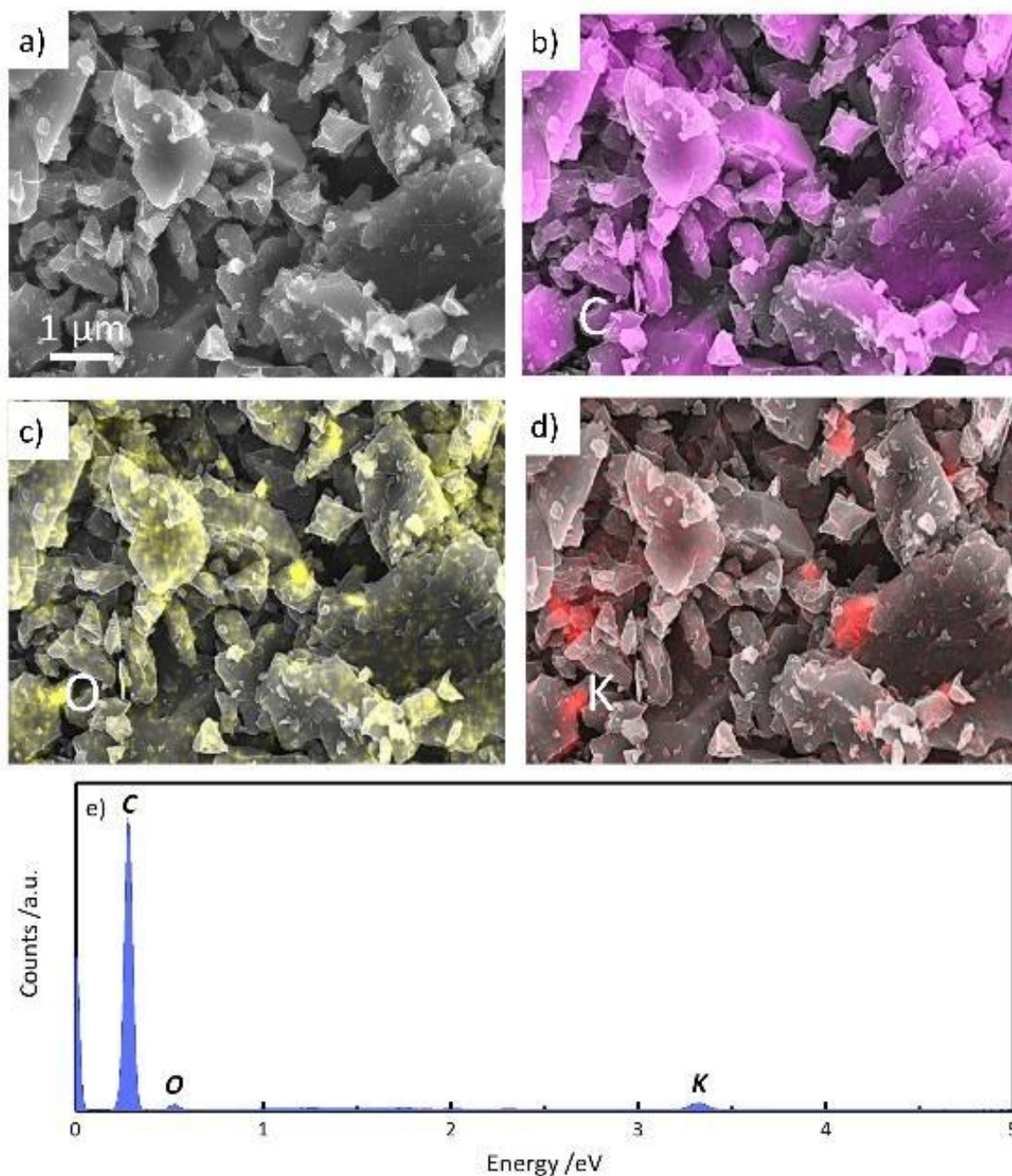
Figure 28 *(a) SEM image of CCDHC; EDX elemental mapping of (b) carbon; (c) oxygen; (d) potassium; Magnification = 5000x. (e) EDX analysis of CCDHC.*

The structure of CCDHC was evaluated by XRD, as shown in **Figure 29 a**. Two broad peaks can be observed at 2θ values of 23° and 43°, which correspond to the crystallographic planes of (002) and (100) in the disordered carbon structure, respectively. No impurity peaks were observed from XRD pattern. Crystallographic parameters acquired by XRD analysis are presented in Table 1. According to the Bragg's Law, the d_{002} interplanar spacing is calculated as 0.387 nm, which is higher than that of graphite (0.335 nm), facilitating the sodium insertion/de-insertion

between graphene layers.[261] The staked plane height (L_c) can be approximately estimated as 0.78 nm from XRD peaks, respectively, which are close to those of the reported sp^2 carbon.[123,262] The number of interlayers stacked in the graphitic domains n can be roughly estimated using d_{002} (0.387 nm) and L_c (0.780 nm) values. According to the calculation (n = 0.780/0.387 + 1) the graphitic domain of CCDHC is made up of 3 stacked graphene layers.[263] To further investigate the carbon textural characteristics, the Raman spectrum of CCDHC powder was performed. As shown in **Figure 29 b**, the powder shows two peaks at around 1344 cm^{-1} (D-band) and 1587 cm^{-1} (G-band), which are characteristic for all layered carbon materials. The D-band originates from disordered and defective sp^3 carbons while the G-band corresponds to graphitic in-plane sp^2 carbons.[264] The intensity ratio between the G band over the D band (I_G/I_D) reflects the disordered degree of hard carbon materials, which is calculated to be 0.996, indicating the low degree of graphitic ordering of CCDHC powder (**Table 3**).[119] Moreover, two broad and small peaks are located at $\sim$ 2690 cm^{-1} and 2900 cm^{-1}, which correspond to 2D and D+G bands, respectively. The 2D band is associated with the degree of graphitization and the D+G band is associated with defect activated process for an elastic scattering.[132,265] An L_a value of 19.14 nm is calculated from Raman band analysis, according to **Eq. (15)**. To fully understand the pore structures of CCDHC, two different probing molecules (N_2 and CO_2) were used. Firstly, N_2 adsorption-desorption measurement was conducted and the obtained isotherm is showed in **Figure 29 c**. According to the International Union of Pure and Applied Chemistry (IUPAC) classification, this graph is the consistent with a type IV isotherm typical of mesoporous materials with a hysteresis loop at a relative pressure in the range 0.15-1 p/p^0. Moreover, the sharp rise at low relative pressure (< 0.14 p/p^0) denotes the presence of micropores.[266,267] The Brunauer-Emmett-Teller (BET) surface area was determined to be 124.4 m^{2}g^{-1}. Considering that N_2 is not suitable for the determination of small size pores (<0.7 nm), the ultramicroporosity determination was achieved using CO_2 at higher temperature (273 K) favoring the gas diffusion into the narrowest pores.[268] The CO_2 adsorption isotherm is showed in **Figure 29 d**. The results showed that the CO_2 BET surface area is significantly higher respect to N_2 BET (427.2 m^{2}g^{-1} vs 124.4 m^{2}g^{-1}) suggesting an extra-porosity coming from the ultramicropores. The same behavior was observed on other types of hard carbons.[268,269] The DFT pore size distributions confirm the presence of micropores with peaks at 0.47, 0.60, 0.77 and 0.85 nm and a total volume of micropores of 0.11 cm^3 g^{-1}.

Table 3 *Crystallographic parameters of CCDHC powder.*

Sample	d$_{002}$ (nm)	L$_c$ (nm)	L$_a$(nm)	I$_G$/I$_D$	*n*
CCDHC	0.387	0.78	19.14	0.996	3.01
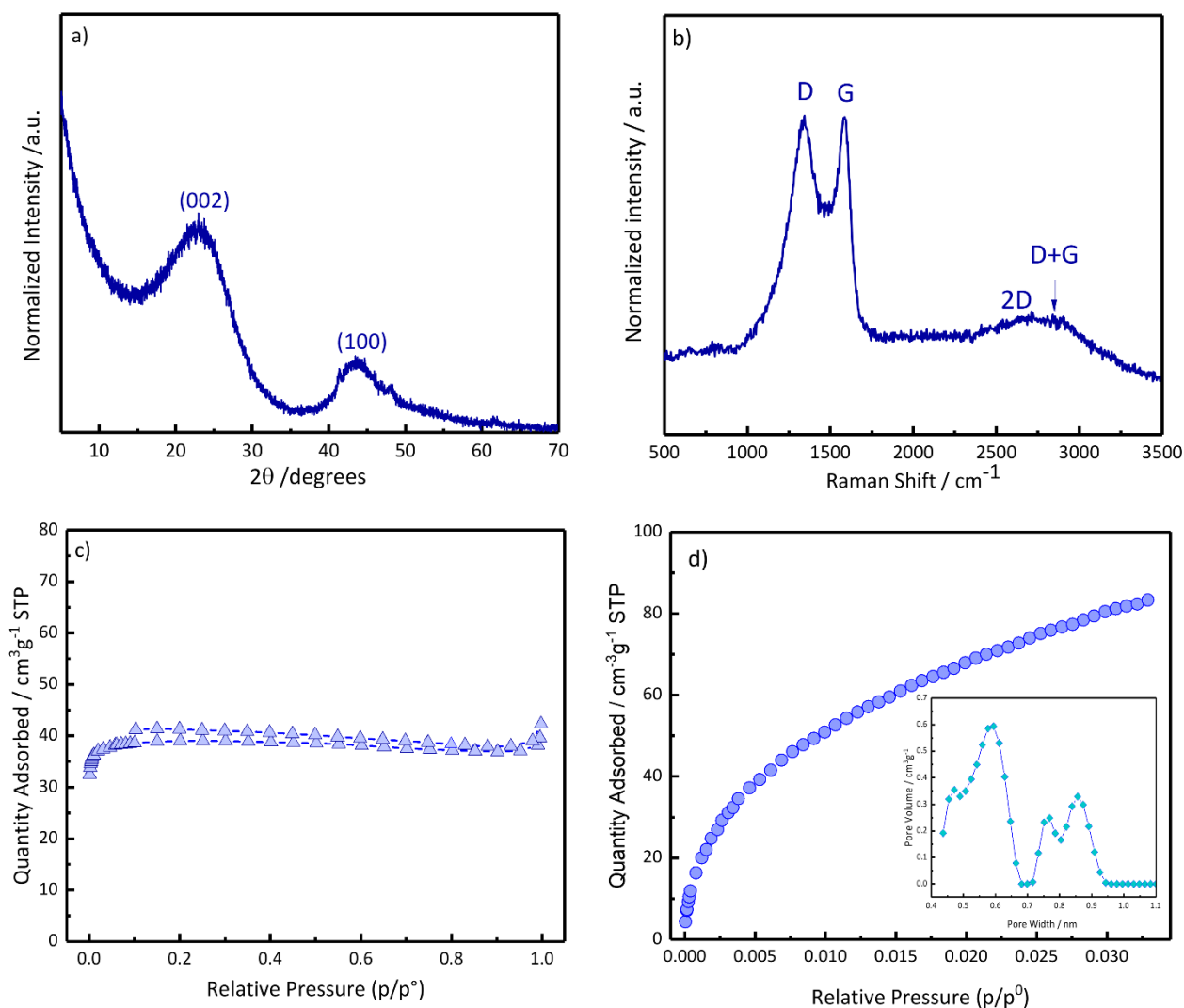
Figure 29 *Chemical and physical characterization of CCDHC powder: (a) XRD pattern; (b) Raman spectra; (c) N$_2$ adsorption-desorption isotherm; (d) CO$_2$ adsorption isotherm and pore size distribution.*

2.2.3 Electrochemical Measurements - SIBs

The galvanostatic charge/discharge E vs. Q profiles of the CCDHC/CC-CMC composite electrodes, cycled at a current density of 300 mAg^{-1} between 0.01 and 2.00 V in Na half-cell, are displayed

in **Figure 30 a**, and reveal the typical features of Na storage by amorphous carbon, i.e. a potential sloping region extending down to 0.10 V followed by a low potential plateau below 0.10 V. During the first discharge process, a pseudo plateau starting at 0.9 V evidence electrolyte decomposition and solid electrolyte interphase (SEI) formation, which lead to an irreversible capacity loss of 165.43 mAhg^{-1}. This pseudo plateau disappears in the subsequent cycles suggesting that a relatively stable SEI is formed.[270] The CCDHC electrode shows a reversible specific capacity above 200 mAhg^{-1} for more than 400 cycles, confirming the high reversibility of the sodiation processes. To investigate the contribution of the sloping region and of the low-voltage plateau to the overall Na storage, dQ/dV curves at different cycles were plotted (**Figure 30 b**). As shown, E_{we} = 0.10 V can be considered as the discrimination point during sodiation between sloping (above 0.10 V) and plateau (below 0.10 V) regions. Thus, the discharge capacities of selected cycles were separated in these two regions, as shown in **Figure 30 c**. It is interesting to note that the contribution of the low-voltage plateau to the capacity remains practically constant through cycling (around 120 mAhg^{-1}), representing a high reversibility of the Na storage processes occurring at the low-voltage plateau. On the other side, the contribution of the sloping region progressively decreases upon cycling (it passes from 136.7 mAhg^{-1} of the 2nd cycle to 85.9 mAhg^{-1} of the 400th cycle), suggesting a partial irreversibility of the step. The charge/discharge capability and capacity retention of three different cells cycled at 1C, 2C, 5C, respectively, are shown in **Figure 30 d**, as well as the corresponding Coulombic efficiencies. The electrodes cycled at 1C, 2C, and 5C evidence initial discharge capacity of 429.7, 366.0, and 350.2 mAhg^{-1}, with corresponding initial Coulombic efficiencies (ICE) of 59.4%, 54.7%, and 43.2%, respectively (see **Table 4**). Caution has to be taken in interpreting this apparently strange ICE trend, since the complete formation of the SEI requires more than one cycle, making the definition of a trend quite difficult. Nonetheless, the CCDHC exhibit ICE in line with most hard carbon materials, which have ICE in the range 40-70%.[271] However, in full-cell configuration the irreversible loss of cyclable sodium must be compensated by the cathode material, reducing the energy density of cell and limiting the practical applications of SIBs. Therefore, improving the ICE is a key issue for the development of commercial sodium-ion batteries.[248] During the second cycle, the electrodes exhibit discharge capacities of 264.3, 206.6, and 147.5 mAhg^{-1} with an excellent capacity retention of 84.0%, 80.4%, and 82.9% after 100 cycles at 1C, 2C, and 5C, respectively. **Figure 30 e** shows the contribution of capacity above and below 0.10 V at different current rates. The low-voltage contribution increases slightly slower (so that the percentage contributions increase from 48.26% at 1C to 50.16% at 2C and 50.85% at 5C), suggesting that, due to the increasing of cell polarization at higher current rates, there is a possible contribution of the fast surface-controlled processes of sodium storage also in the low-voltage plateau. To further evaluate the charge/discharge capability of the electrode at various currents, a fresh cell was subjected to rate capability measurements in the cycling rate from C/5 to 5C, as shown in **Figure 30 f**. The CCDHC electrode exhibits a promising rate capability with a low-capacity fade when the current is boosted, ranging from 273.9 mAhg^{-1} at

C/5 to 179.2 mAhg^{-1} at 5C. Afterwards, the capability to recover pristine performances was investigated by cycling the electrode at 1C up to 100 overall cycles. The cell yields a specific capacity above 200 mAhg^{-1} after 100 cycles, suggesting outstanding reversibility and stability even in demanding conditions. Comparing these results with others found in literature, CCDHC shown superior or comparable performances in terms of specific capacity and rate capability respect to other biomass-derived HCs (**Table 5**).[100,121,260,262,272,273] Moreover, the synthesis of the CMC binder from the same abundant raw material, which has a high cellulose content,[242] can additionally improve the sustainability of the electrode manufacture especially through aqueous electrode processing. However, it is worth to note that testing materials in half-cell configuration may be not truly representative and can eventually underrate the performances of active materials due to the high reactivity of sodium metal counter and reference electrodes in organic electrolytes, which can influence the electrode/electrolyte interface stability and resistance and thus the cycle life.[274,275]
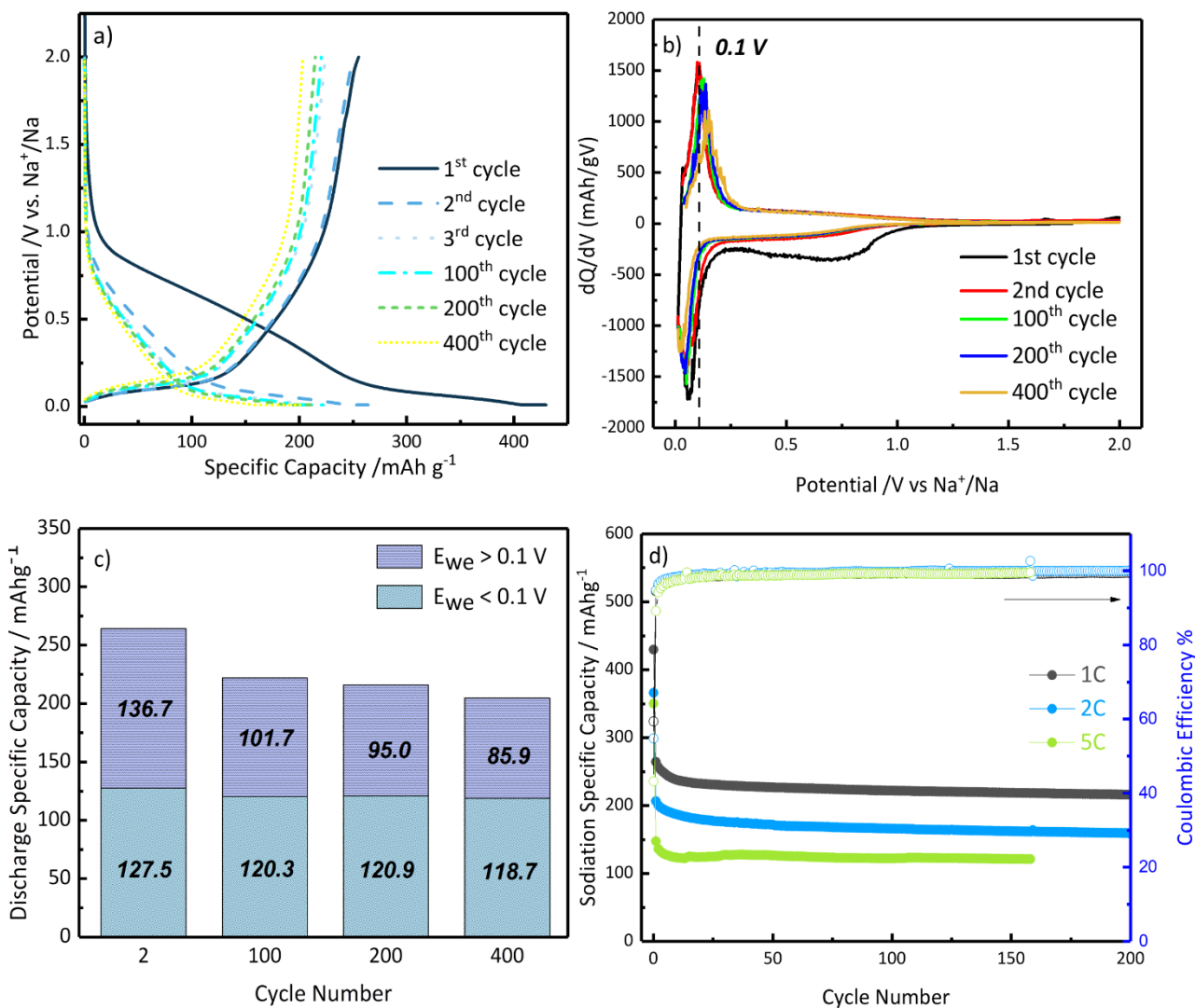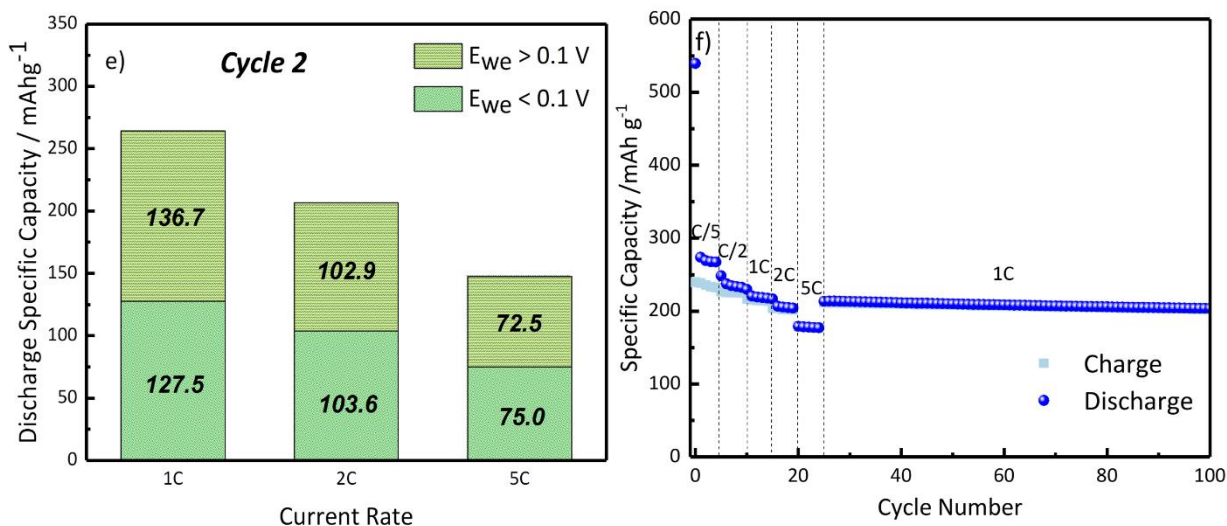
Figure 30 Electrochemical performances of CCDHC-based SIB electrode prepared with CC-CMC binder and 1M NaClO₄ EC:PC 1:1 (v/v) as electrolyte : (a) Galvanostatic discharge/charge voltage profile at 1C; (b) dQ/dV vs Ewe curves at different cycles; (c) Contribution to capacity above and below 0.10 V as a function of cycle number; (d) Long cycling at different scan rates (1C, 2C and 5C); (e) Contribution to capacity above and below 0.10 V as a function of current density at 2nd cycle; (f) Rate capability.

Table 4 First-cycle irreversible capacity, initial coulombic efficiency (ICE), second-cycle reversible discharge capacity, and capacity retention of CCDHC-based SIB electrodes at different current rates.

Current Rate	Discharge Capacity 1st cycle (mAhg⁻¹)	ICE (%)	Discharge Capacity 2nd cycle (mAhg⁻¹)	Capacity Retention after 100 cycles (%)
1C	429.7	59.4	264.3	84.0
2C	366.0	54.7	206.6	80.4
5C	350.2	43.2	147.5	82.9

Table 5 *Comparison of sodium storage performance of various biomass-derived HC in SIBs.*

Precursor	Temperature of pyrolysis	ICE	Specific Capacity
Cotton[100]	1000 °C	26 %	88 mAh g^{-1} at 30 mA g^{-1}
Sugarcane bagasse[121]	950 °C	70 %	234 mAh g^{-1} at 100 mA g^{-1}
Cocoa Pod Husk[262]	1300 °C	-	225 mAh g^{-1} at 250 mA g^{-1}
Shaddock Peel[272]	1000 °C	63 %	230 mAh g^{-1} at 200 mA g^{-1}
Peanut Shells[119]	600 °C	-	193 mAh g^{-1} at 250 mA g^{-1}
Olive Leaves[122]	970 °C	52 %	265 mAh g-1 at 300 mA g^{-1}
Pomelo Peels[112]	700 °C	-	214 mAh g^{-1} at 200 mA g^{-1}
Seaweed[276]	750 °C	21 %	192 mAh g^{-1} at 200 mA g^{-1}
Wood[277]	1000 °C	-	122 mAh g^{-1} at 100 mA g^{-1}
Corncob (this work)	950 °C	59 %	264 mAh g^{-1} at 300 mA g^{-1}

In order to investigate the nature of Na storage processes in the CCDHC electrode, cyclic voltammetry (CV) experiments were performed. Firstly, CV of the initial three cycles was run at a scan rate of 0.10 mVs^{-1} between 0.01 and 2.00 V in a half cell *vs.* Na$^+$/Na, as shown in **Figure 31 a**. The irreversible broad peak at the first cathodic scan centered at 0.57 V (A) can be assigned mostly to the decomposition of the electrolyte and the formation of the SEI.[91] In the following scans, the contribution from irreversible SEI formation disappears, leaving a broad feature (B) due to the "high-potential" (E > 0.10 V) Na storage. This is a reversible process, as confirmed by the symmetrical B' feature revealed during anode scans. The sharp reversible peak near 0.01 V is attributed to the Na$^+$ insertion/extraction into hard carbon.[123] After the 1st cycle, the CV curves are overlapped, indicating a reversible electrochemical behavior. To provide a deeper understanding of the Na storage surface-related pseudocapacitive and bulk-related diffusive behaviors, cyclic voltammetries were also recorded at different scan rates between 0.10 mVs^{-1} and 1.00 mVs^{-1} (**Figure 31 b**). All the CV curves show similar shapes at various sweep rates, and a small polarization of the anodic and cathodic peaks are evidenced during the charge and discharge.[278] In order to determine the sodium storage mechanism, the power-law

relationship between scanning rate and peak currents was calculated by fitting the experimental data to the following equations **Eq. (19)** and **Eq. (20)**:[279]

$$i = av^b \qquad\qquad \textbf{Eq. 19}$$

$$log\,i = b\,log\,v + log\,a \qquad\qquad \textbf{Eq. 20}$$

Where i and v show the peak current and the scanning rate, respectively, while a and b are the parameters to be determined. Typically, a value of b close to 0.5 indicates a diffusion-controlled reaction, such as insertion/extraction between graphene layers, while a value of b close to 1 indicates that the current is governed by a surface-controlled reaction.[279] Two peaks were selected for the kinetic analysis: the first one is the broad peak at 0.50 V (i_j) corresponding to the sloping region, while the second one is the sharp peak in the low potential region at 0.01 V (i_p). The current peaks as a function of the scan rate in logarithmic scale are shown in **Figure 31 c**, representing an excellent linear relationship with $R^2 = 0.99$ for both curves, with a slope of 0.97 for i_j and 0.58 for i_p, respectively. Thus, these results suggests that the current in the sloping region (i_j) arises mostly from the surface controlled reactions (i.e. adsorption on active sites) while the current at low-potentials (i_p) originates from the diffusion-controlled reaction (i.e. sodium insertion/extraction between graphene layers).[92,280–282] Additionally, the capacitive contribution to the current response can be determined according to the following equation **Eq. (21)**:

$$i(V) = k_1 v + k_2 v^{1/2} \qquad\qquad \textbf{Eq. 21}$$

where the current response at a fixed potential can be distinguished in surface-controlled ($k_1 v$) and diffusion-dependent ($k_2 v^{1/2}$) contributions. By counting k_1 and k_2, the split of the contribution of the two mechanisms to the current response can be determined.[281,283] **Figure 31 d** shows the excellent linear relationship of $i(V)/v^{1/2}$ against $v^{1/2}$ at different potentials during the sodiation process, which were used for the determination of k_1 (slope) and k_2 (intercept). **Figure 31 e** shows the trends of capacitive contribution (%) at different scan rates (v) as a function of potential (V), as calculated from **Eq. (21)**. As expected, increasing the sweeping rate leads to a higher capacitive contribution at each potential step, meaning that the current response comes from the fast surface-induced capacitive process, such as adsorption.[267,269] It is interesting to note that starting from 0.15 V, the capacitive contribution increases reaching a maximum at 0.55 V (91.9 % at 0.1 mVs^{-1} and 98.9 % at 1.0 mVs^{-1}) and then decreases rapidly reaching a minimum at 1.35 V (6.2 % at 0.1 mVs^{-1} and 17.8 % at 1.0 mVs^{-1}) at each scan rate. These results confirm that at $E_{we} \leq 0.15$ V the uppermost process is the diffusion-controlled intercalation of sodium into carbon framework, however there is a small contribution of capacitive process especially at high current density; at $0.25 \leq E_{we} \leq 0.75$ V the surface-controlled processes are predominant.

The kinetics of Na$^+$ diffusion in CCDHC was investigated by Galvanostatic Intermittent Titration Technique (GITT), applying a current pulse of 30 mAg^{-1} for 0.5 h followed by 3 h of relaxation for each current pulse. According to the Fick's second law, the diffusion coefficient D$_{Na+}$ values were calculated using the following equation **Eq. (22)**:

$$D_{Na^+} = \frac{4}{\pi t}\left(\frac{m_b \cdot V_m}{M_b \cdot S}\right)^2 \left(\frac{\Delta E_s}{\Delta Et}\right)^2$$

Eq. 22

Where t is the current pulse time (s), m$_b$ is the mass of the active material (g), V$_m$ and M$_b$ represent the molar volume (cm^{3}mol^{-1}) and molar mass (gmol^{-1}) of carbon, respectively, S is the contact surface area of the electrode (cm^2), ΔE_s is the steady-state voltage change during a single step of GITT and ΔE_t is the voltage change during a single current pulse.[262] The calculated diffusion coefficient during sodiation (D$_{Na}^+$) was plotted as a function of voltage, as shown in **Figure 31f**. The high values of D$_{Na}^+$ of CCDHC in the high part of the sloping region (E$_{we}$ > 0.30 V) mimic the rapid adsorption of sodium ions on surface active sites, which are gradually occupied during sodiation leading to a progressive decrease of D$_{Na}^+$. In the lower part of the sloping region (0.30 < E$_{we}$ < 0.10 V), the saturation of the surface accessible sites forces the remaining sodium ions to increase the diffusion length to find vacant adsorption sites, decreasing the apparent diffusion coefficient to values in the order of 10^{-11} cm^{2}s^{-1}.[267] Finally, in the low-voltage plateau (E$_{we}$ < 0.10 V), the apparent diffusion coefficient rapidly decreases reaching a minimum at E$_{we}$ = 0.06 V because the sodium ions have to overcome the energy barrier to intercalate between graphene layers. After that, since the interlayer spacing is enhanced by the intercalated sodium ions, the diffusion coefficient rapidly recovers before the cutoff potential, indicating an easier diffusion kinetics.[284]
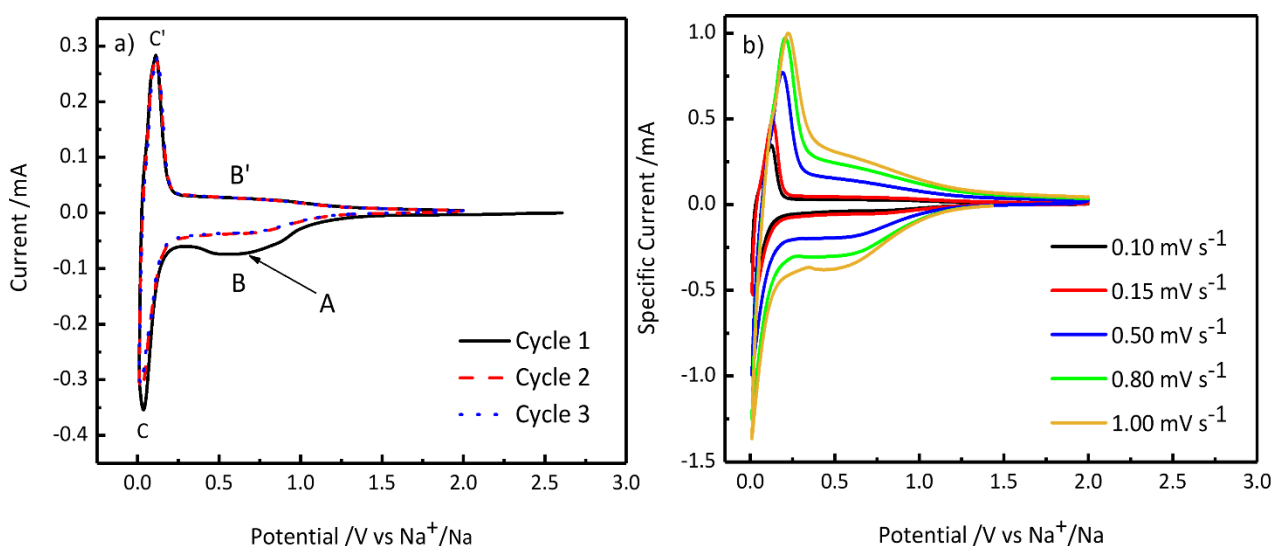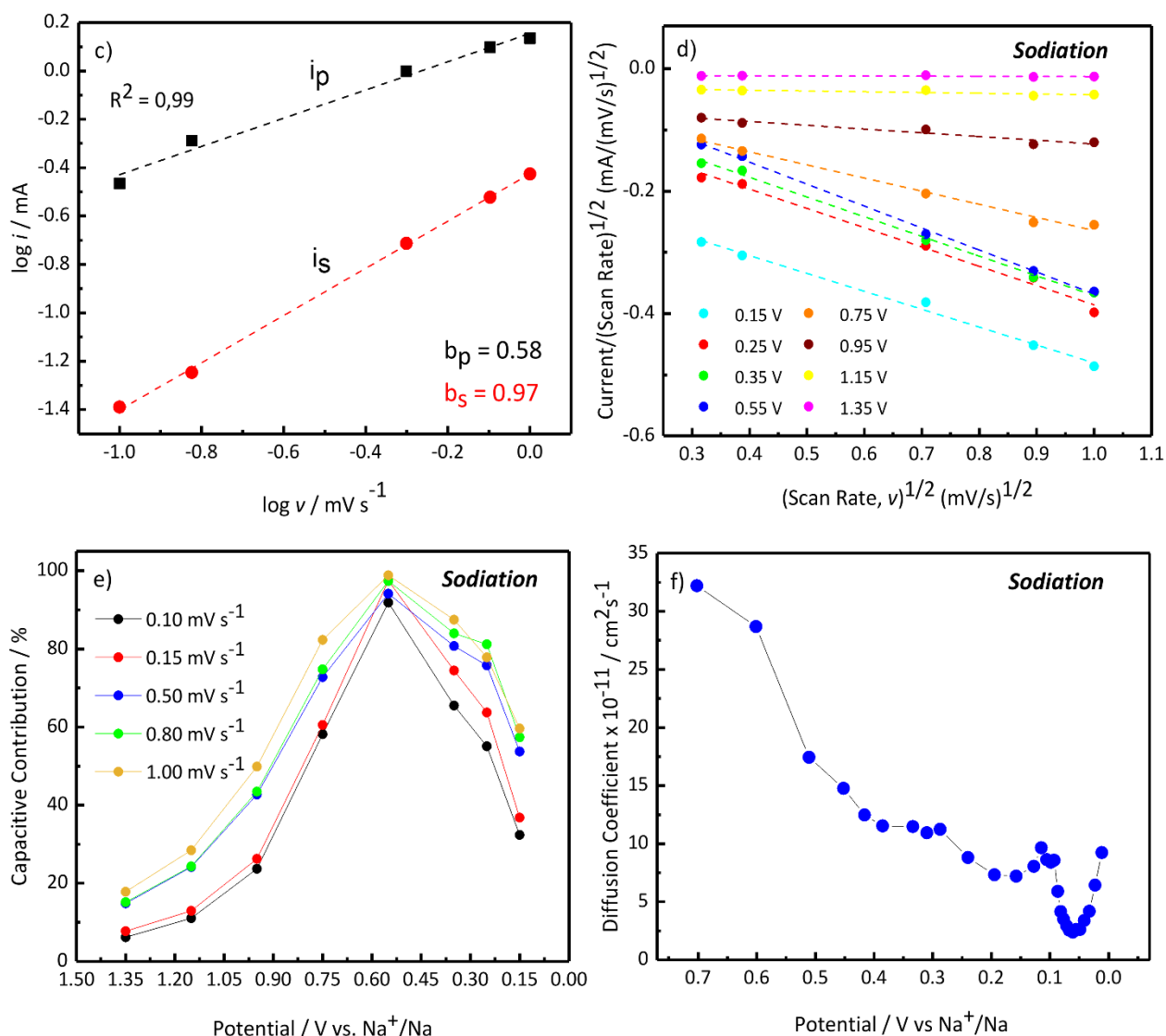
Figure 31 *Electrochemical performances of CCDHC-based SIB electrode prepared with CC-CMC binder and 1M NaClO₄ EC:PC 1:1 (v/v) as electrolyte: (a) Cyclic Voltammetry upon the first three cycles, scan rate 0.1 mV s⁻¹; (b) CV curves at different sweep rates (between 0.1 mV s⁻¹ and 1 mV s⁻¹); (c) Relationship between log i and log v; (d) i(V)/v^(1/2) against v^(1/2) at different potentials during sodiation; (e) capacitive contribution % during sodiation as a function of the potential at different scan rates; (f) Diffusion coefficient at different potentials during sodiation.*

A deeper study of the kinetics of the charge/discharge processes as well as the interfacial behavior of the electrode have been performed through electrochemical impedance spectroscopy (EIS) measurements every 10th cycle at E_{we} = 0.50 V. The Nyquist plots are shown in **Figure 32 a**. All the impedance spectra present similar features: (i) a semicircle in the high-frequency region related to sodium migration through SEI film, which is partially overlapped by (ii) a semicircle in the middle-frequency region correlated with the interfacial charge-transfer process;[285] (iii) a straight line in the low-frequency region corresponding to the Na⁺ ion diffusion in the bulk of electrode material.[278] EIS data were fitted through an equivalent circuit model,

noted as $R_{el}(R_{SEI}C_{SEI})(R_{ct}C_{dl})WC_i$ in the notation of Boukamp. The calculated values of R_{SEI} and R_{ct} are shown in **Figure 32 b** and reported in **Table 6**. The R_{el}, R_{SEI} and R_{ct} are the resistances associated with electrolyte, SEI passivation layer and charge-transfer process, while C_{SEI}, C_{ct} and C_i are the SEI film capacity, electric double layer capacity and differential intercalation capacity, respectively. W is the Warburg element, describing Na^+ diffusion.[265] For the fitting procedure, the pure capacitive elements were replaced by constant phase elements Q to take into account the non-ideal capacitive behavior given by the electrode surface roughness and inhomogeneity.[286] The electrode exhibits low resistance (R_{SEI} and R_{ct}) values upon cycling, indicating high reaction kinetics and interfacial stability. As regards the passivation layer, the calculated R_{SEI} values slightly increase during the first 30 cycles, and then remain almost unchanged during the subsequent ones, suggesting strong interactions of the CC-CMC binder with carbon substrate[203,209] and SEI products. However, the dynamic nature of the SEI formation leads to continuous partial dissolution and re-formation of the outer layer of the SEI, which is soluble in carbonate electrolytes.[238,287] Therefore, the formation of a stable passivation layer requires some cycles. As regards the charge-transfer resistance, during the first cycles the electrode shows higher R_{ct} values with respect to subsequent cycles, probably because of an electrode activation due to progressive pore surface wetting by the electrolyte. The calculated R_{ct} values decrease after 20 cycles and remain unchanged up to 100 cycles, evidencing the stabilization of the electrode/electrolyte interface.
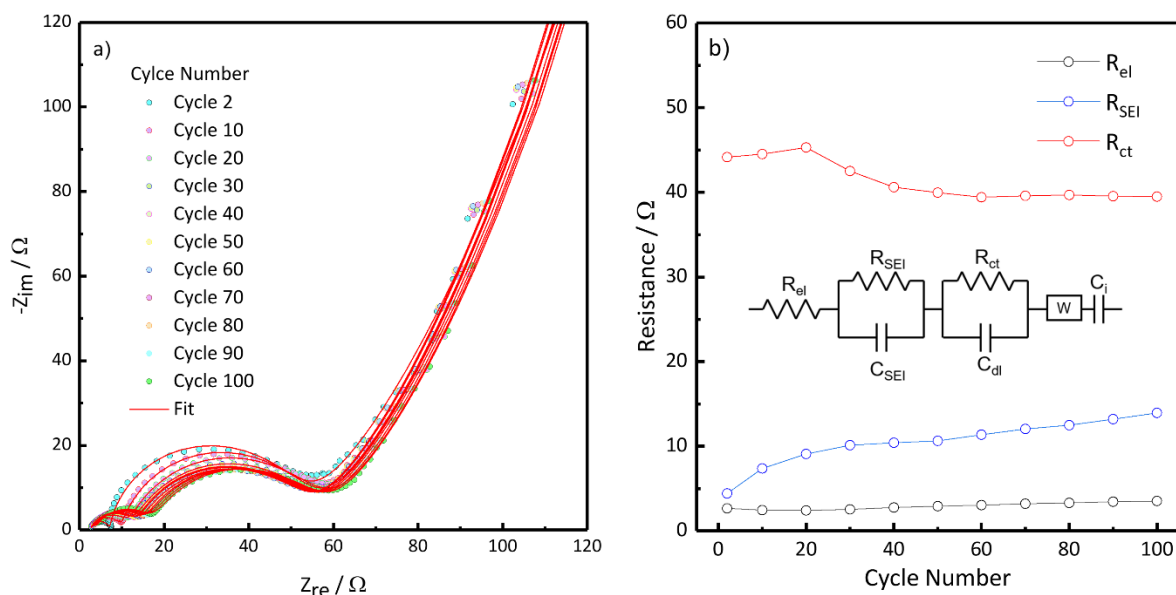
Figure 32 *(a) Nyquist plot of CCDHC-based SIB electrode prepared with CC-CMC binder and 1M NaClO$_4$ EC:PC 1:1 (v/v) as electrolyte, acquired every 10th cycle, E = 0.5 V, 10 mHz < f < 100 kHz; (b) Values of R_{el}, R_{SEI} and R_{ct} upon cycling, as obtained by EIS data analysis; Equivalent circuit used to simulate the data.*

Table 6 *SEI and charge transfer resistances, capacitances and phase angles (α) as a function of cycle number for CCDHC-based SIB electrode prepared with CC-CMC binder and 1M NaClO₄ EC:PC 1:1 (v/v) as electrolyte.*

Cycle	R_{SEI} / Ω	Capacitance / F	α	R_{CT} / Ω	Capacitance / F	α
2	4.43	8.99×10^{-6}	0.91	44.15	8.65×10^{-4}	0.90
10	7.38	1.71×10^{-5}	0.83	44.51	6.86×10^{-4}	0.85
20	9.09	3.15×10^{-5}	0.78	45.30	7.36×10^{-4}	0.80
30	10.13	3.15×10^{-5}	0.77	42.51	7.91×10^{-4}	0.78
40	10.42	2.39×10^{-5}	0.79	40.61	8.07×10^{-4}	0.78
50	10.64	2.50×10^{-5}	0.78	39.96	8.09×10^{-4}	0.78
60	11.37	2.74×10^{-5}	0.77	39.43	8.26×10^{-4}	0.77
70	12.04	2.88×10^{-5}	0.76	39.58	8.25×10^{-4}	0.77
80	12.49	3.20×10^{-5}	0.75	39.68	8.11×10^{-4}	0.77
90	13.20	3.47×10^{-5}	0.74	39.55	8.13×10^{-4}	0.77
100	13.94	3.71×10^{-5}	0.73	39.49	8.16×10^{-4}	0.77

To further evaluate the redox processes occurring at Hard Carbon, distribution of relaxation times analysis (DRT) was applied to the impedance spectra collected during sodiation and desodiation (5th cycle). The raw spectra evidenced the same features observed in **Figure 32**. However, the Nyquist plots here reported (**Figures 33 a,b**) lack the low-frequency, diffusion-related line, since it was subtracted prior the DRT analysis, satisfying the boundary condition of convergence of the impedance toward the real axis when ω tends to 0, which is not guaranteed with the divergent low-frequency Warburg diffusion.[286,288] The spectra have been fitted by a resistor R_{el}, which represents the resistance of the electrolyte and two parallels (RQ) in series, which model the resistance of the passivation layer and the charge transfer resistance, respectively. The calculated DRT functions (**Figures 33 c,d**) show three main peaks, and an additional peak marked as P*, which is the residual artifact retained after the removal of the low-frequency line. The peak P_1, with a time constant of approximatively τ = 1.25×10^{-5} s (i.e. high-frequencies) can be attributed to the contact impedance as already reported for graphite in other study.[289] The peak P_2, with a time constant of approximatively τ = 2.51×10^{-4} s, which is consistent with the resistance of the passivation layer (R_{SEI}), increases during sodiation and decreases during desodiation as well, consistently with the behavior of the high-frequency semicircle in the Nyquist plots. This behavior suggests that SEI is not completely formed and stabilized after 5 cycles. At 1.00 V, the most intense peak is P_3 with a low time constant of τ =

0.49 s, corresponding to the medium-frequency semicircle in the Nyquist plot, which can be related to the resistance of charge transfer processes, which is maximum at high potential since no electrochemical reactions occur. Lowering the potential and approaching the sloping region, P_3 peak decreases in height and area, and shifts to faster time constant (during sodiation it passes from 0.49 s at 1 V to 1.23×10^{-2} s at 0.5 V). Simultaneously, the second semi-circle decreases its diameter in the corresponding Nyquist plots. This means that the resistance associated with the charge transfer R_{ct} progressively decreases upon sodiation and vice versa. Thus, approaching the low voltage plateau, the P_3 peaks continue to shift toward lower time constant, reaching a value of approximatively $\tau = 4.05 \times 10^{-3}$ s, and eventually splitting into two contributions, with a new peak P_4 appearing below 0.30 V with a higher time constant of $\tau = 5.55 \times 10^{-2}$ s. It is assumed that both peaks are related to the charge transfer process of Hard Carbon. Similar results have been reported for Li-graphite half-cells.[290] Consistently with the cyclic voltammetries, since P_4 only appears at low potential upon sodiation, and it is also present upon desodiation at the same potential, it is likely that P_4 is related to the intercalation of Na^+ ions into the carbon host, while P_3 can be assigned to the capacitive adsorption of Na^+ ions onto active sites. This is furtherly supported by the fact that the intercalation is expected to be kinetically sluggish compared to the adsorption process, hence occurring at higher time constants. In order to better investigate the DRT peaks at the low-voltage plateau, EIS was applied at different temperatures (T = -10, +2, +10, +25 °C) at E_{we} = 0.01 V. The corresponding Nyquist plots and the calculated DRT functions are reported in **Figures 33 e,f**. The overall impedance increases, and the DRT peaks increase and shift to the right, when the temperature decreases. The peak P_2 shows a moderate temperature dependance, confirming that it describes the SEI polarization. On the other hand, P_3 is strongly affected by the temperature, with its intensity rapidly growing as the temperature is lowered. This behavior is typical of an activated charge-transfer process. The peak P_4, which is visible below 0.30 V for DRT collected at 25 °C (**Figures 33 c,d**), is not detectable in the graphs of the lower-temperature DRTs because it is probably overlapped by the large-polarization P_3 feature.
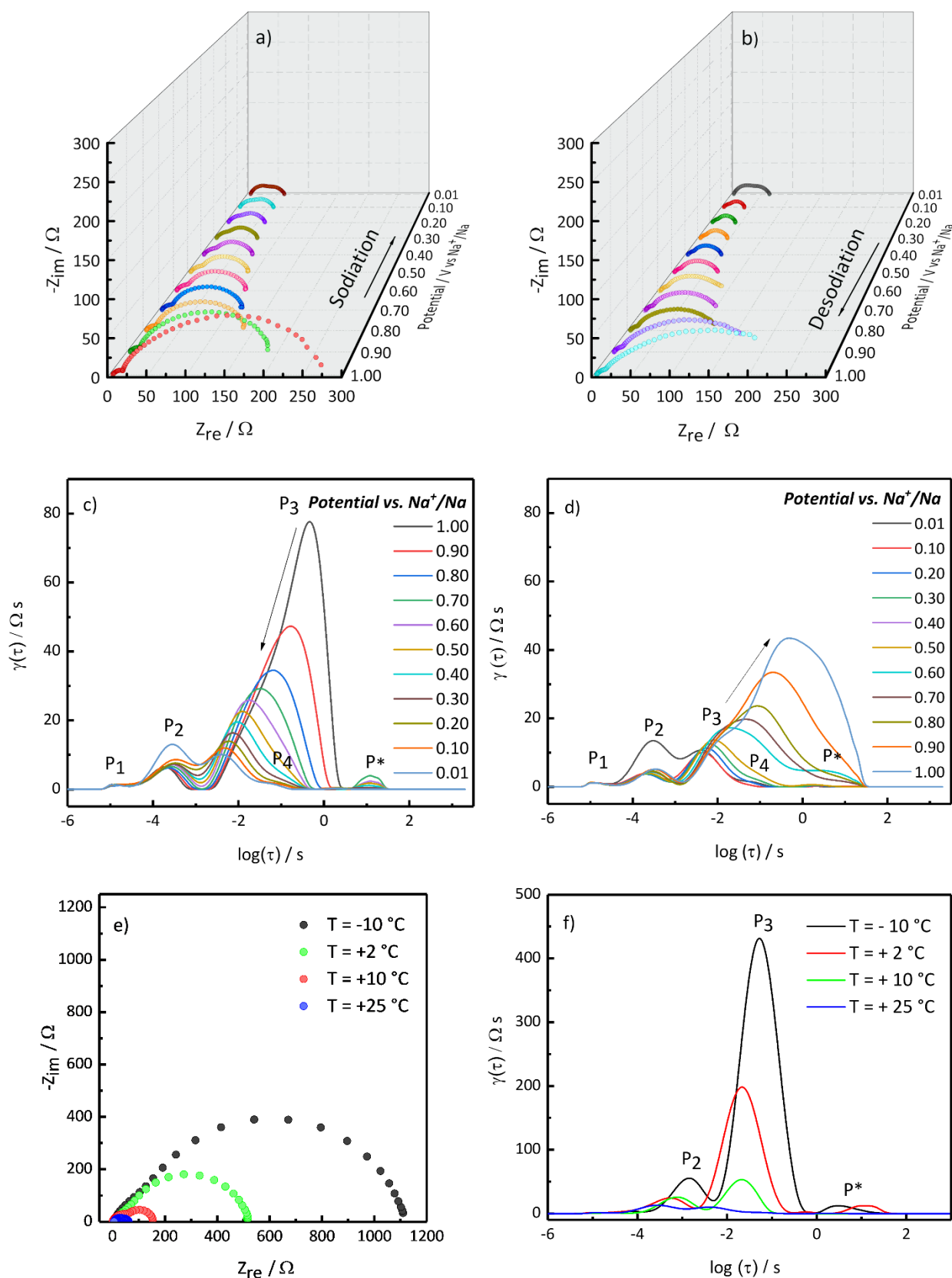
Figure 33 *Nyquist plot of CCDHC-based SIB electrode prepared with CC-CMC binder and 1M NaClO₄ EC:PC 1:1 (v/v) as electrolyte, acquired during (a) sodiation and (b) desodiation every 100 mV, 50 mHz < f < 100 kHz. Calculated DRT functions during (c) sodiation and (d) desodiation. (e) Nyquist plot acquired at E = 0.01 V at different temperatures, 50 mHz < f < 100 kHz; (f) Calculated DRT function at different temperatures.*

2.2.4 Electrochemical Measurements – LIBs

2.2.4.1 CCDHC/CC-CMC Electrode as Active Materials and Binder

CV of the initial three cycles was run at a scan rate of 0.1 mVs^{-1} between 0.01 and 2.00 V in a half cell *vs.* Li$^+$ /Li to examine the nature of Li storage processes, as shown in **Figure 34 a**. As for SIBs, an irreversible peak at the first cathodic scan centered at 0.60 V (A) is due to the irreversible reactions of the electrolyte with electrode surface. In the following scans, the peak A disappears, leaving the CV curves overlapped, indicating that most of the irreversible processes were completed during the first discharge.[265] Subsequent cycles show two reversible processes of Li storage described by a broad feature (B/B') extending up to high-potentials (0.10 < E < 1.00 V) and a sharp reversible peak with an onset potential below 0.10 V (C/C') at low-potential. The galvanostatic E vs. Q profiles of the CCDHC/CC-CMC composite electrodes, cycled at a current density of 300 mAg^{-1} between 0.01 and 2.00 V in Li half-cell*,* are shown in **Figure 34 b**. During the first lithiation, a pseudo plateau starting at around 0.90 V confirms the SEI formation, leading to an irreversible capacity loss of 329.5 mAh g^{-1} which correspond to an ICE of 53.3 %. This huge irreversible capacity loss ICL % (55.9 %) represent the main disadvantage of HC over graphite, which usually has ICL % in the range 10-20 %.[291] From the second cycle, the typical pattern of Hard Carbon is displayed, with a sloping region followed by a low potential plateau area, evidencing again two different storage behaviors in these two regions. As for SIBs, the discrimination between sloping and plateau regions has been confirmed by dQ/dV plots (**Figure 34 c**), where the threshold during lithiation can be fixed at E$_{we}$ = 0.10 V vs Li$^+$/Li. Taking into account the deep analysis conducted in SIBs, it is reasonable to hypothesize that CCDHC exhibit the same electrochemical processes of charge storage in Li-system: the adsorption of Li$^+$ into active sites occurs in the sloping region at high-potentials (E$_{we}$ > 0.10 V) while the the intercalation/de-intercalation of Li$^+$ into carbon host occurs in the low-voltage plateau at low-potential (E$_{we}$ < 0.10 V). In order to assess the voltage hysteresis between charge and discharge, the normalized voltage curves of CCDHC in lithium and sodium cells at 2nd cycle were compared in **Figure 34 d**. As expected, there is a slightly larger voltage hysteresis for Li-system respect to Na-analogue: although in the literature the explanation of this result has been correlated to the residual hydrogens at edges of graphene domains, which could react with lithium atoms to form a complex C, H, Li bond,[292,293] thus requiring higher energy for the removal of Li$^+$ ions from these sites,[111] it was recently pointed out that this phenomenon should be extended to defects/heteroatoms in general, where Li$^+$ displays stronger interactions due to its smaller ionic radius respect to Na$^+$.[82] Beyond the difference between Li- and Na- systems, a large voltage hysteresis decreases the round-trip energy efficiency. The electrochemical performance of CCDHC/CC-CMC were evaluated performing charge/discharge galvanostatic cycling at different current rates (1C, 2C, 5C), as shown in **Figure 34 e**. The cells cycled at 1C, 2C, and 5C evidence

initial discharge capacity of 705.5, 749.0, and 704.2 mAh g^{-1}, with corresponding Initial Coulombic efficiencies (ICE) of 53.3 %, 42.4 %, and 44.8%, respectively (**see Table 7**). The ICE values of Li half-cells are lower to those obtained in Na half-cells except for cell cycled at 5C: taking into account that also in Li-ion system the complete formation of a stable SEI on Hard Carbon-based electrodes requires more than one cycle, this result can be ascribed to a more irreversible Li$^+$ ions trapping into the HC matrix as a consequence of the stronger interactions already mentioned. Nonetheless, huge efforts are required toward higher ICE and more stable SEI layers for the practical application of HC anodes also in lithium-ion cells. During the second cycle, the electrodes exhibit discharge capacities of 394.4, 334.8, and 328.2 mAh g^{-1} with capacity retentions of 79.3 %, 77.7 %, and 80.2 % after 100 cycles at 1C, 2C, and 5C, respectively. As for SIBs, the reported results of CCDHC/CC-CMC electrodes are superior or comparable to other biomass-derived HC for LIBs (**Table 8**). To further evaluate the charge/discharge capability of the electrode at various currents, a fresh cell was subjected to rate capability measurements in the cycling rate from C/5 to 5C, as shown in **Figure 34 f**. The CCDHC electrode exhibits a promising rate capability with a low-capacity fade when the current is boosted, ranging from 343.2 mAh g^{-1} at 5th cycle at C/5 to 269.2 mAh g^{-1} at 2nd cycle at 5C. Afterwards, the capability to recover pristine performances was investigated by restoring the current to 1C and cycling the electrode up to 100 overall cycles. The cell holds a specific capacity above 260 mAhg^{-1} after 100 cycles, suggesting outstanding reversibility and stability even in demanding conditions.
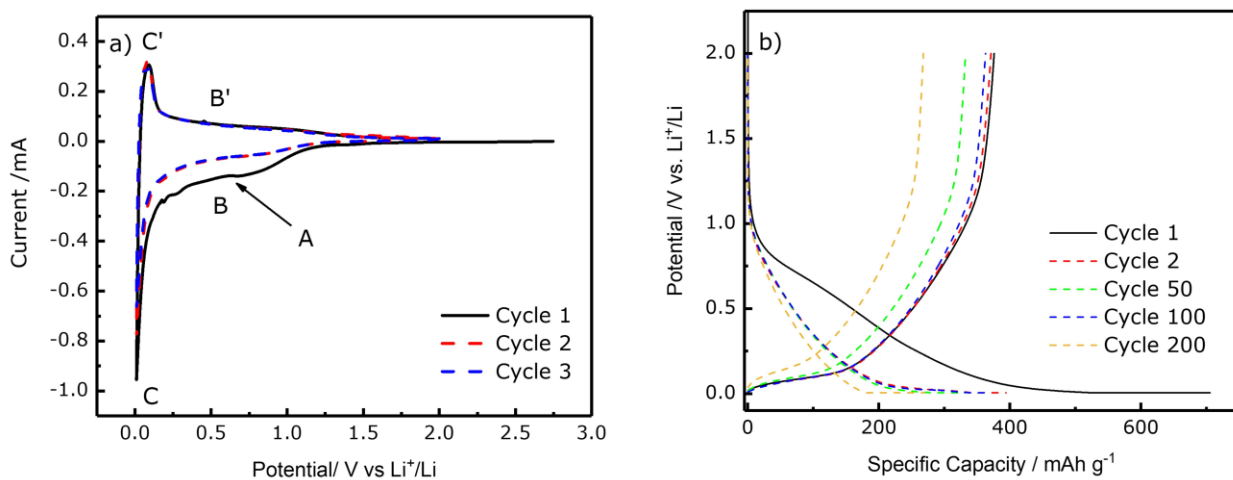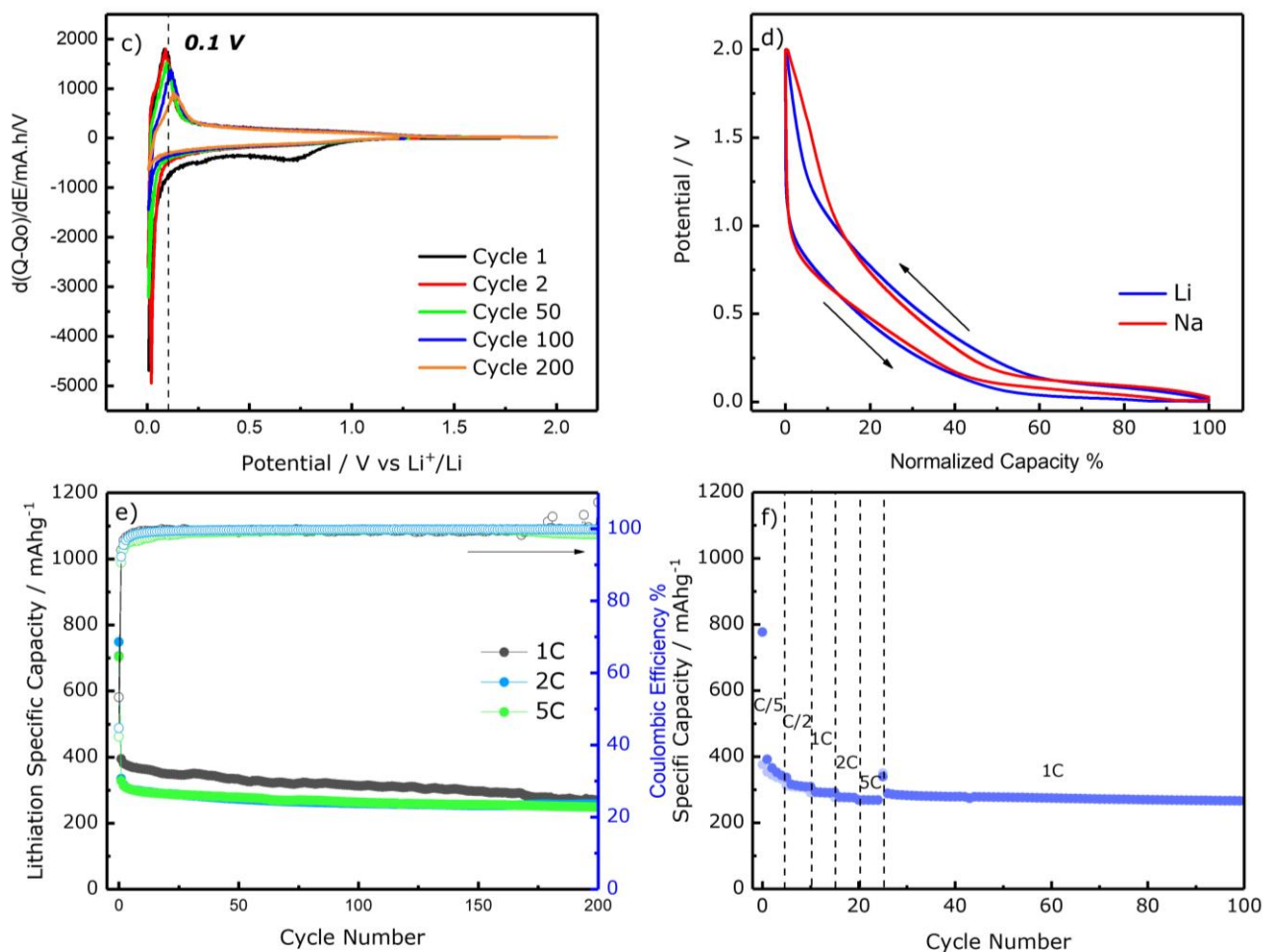
Figure 34 *Electrochemical performances of CCDHC-based LIB electrode prepared with CC-CMC binder and 1M LiPF$_6$ EC:DMC 1:1 (v/v) as electrolyte: (a) Cyclic Voltammetry upon the first three cycles, scan rate 0.1 mV s^{-1}; (b) Galvanostatic discharge/charge voltage profile at 1C; (c) dQ/dV vs E$_{we}$ curves at different cycles; (d) Voltage curves of lithium and sodium cells at 2nd cycle as a function of normalized capacity; (e) Long cycling at different scan rates (1C, 2C and 5C); (f) Rate capability.*

Table 7 *First-cycle irreversible capacity, initial coulombic efficiency (ICE), second-cycle reversible discharge capacity, and capacity retention of CCDHC-based LIB electrodes at different current rates.*

Current Rate	Discharge Capacity 1st cycle (mAhg^{-1})	ICE (%)	Discharge Capacity 2nd cycle (mAhg^{-1})	Capacity Retention after 100 cycles (%)
1C	705.5	53.3	394.4	79.3
2C	749.0	42.4	334.8	77.7
5C	704.2	44.8	328.2	80.2

Table 8 Comparison of lithium storage performance of various biomass-derived HC in LIBs.

Precursor	Temperature of pyrolysis	ICE	Specific Capacity
Coffee Ground[265]	970 °C	56 %	422 mAh g^{-1} at 60 mA g^{-1}
Sweet Gum[294]	1000 °C	54 %	375 mAh g^{-1} at 50 mA g^{-1}
Lignin[295]	1000 °C	-	329 mAh g^{-1} at 50 mA g^{-1}
Olive Pits[296]	800 °C	-	290 mAh g^{-1} at 30 mA g^{-1}
Olive Leaves[122]	970 °C	48 %	331 mAh g^{-1} at 300 mA g^{-1}
Corncob (this work)	950 °C	53 %	394 mAh g^{-1} at 300 mA g^{-1}

EIS analysis have been performed to study the kinetics of the charge/discharge processes as well as the interfacial behavior of the electrode. As for SIBs, the measurements have been conducted every 10th cycle at E$_{we}$ = 0.50 V. The Nyquist plots and the resistance values as a function of cycles are shown in **Figure 35 a,b**, respectively. Numerically, the SEI and charge transfer resistances, capacitances and α values as a function of cycle number are reported in **Table 9**. All the impedance spectra present similar features already described for CCDHC sodium half-cells. The intercept on the real axis at high frequencies represents the migration of Li$^+$ ions through the electrolyte, and hence it was modeled as a pure resistive element (R_{el}). The semicircle (i) at high frequencies is related to the migration of Li$^+$ ions through the SEI layers with charges accumulating onto the passivation layer surface and was modeled as a resistive element (R_{SEI}) in parallel with a capacitor element (C_{SEI}). The semicircle (ii) at middle frequencies can be ascribed to the faradaic charge transfer process with charges accumulating onto the surface of the active material particles, modeled as a resistive element (R_{ct}) in parallel with a capacitor element (C_{dl}). Finally, the line (iii) at low frequency describes a semi-infinite diffusion to a blocking electrode, which was modeled with a Warburg impedance (W) in series with a capacitor describing the intercalation capacitance (C_i).[297] For the fitting procedure, the pure capacitive elements were replaced by constant phase elements Q to take into account the non-ideal capacitive behavior given by the electrode surface roughness and inhomogeneity.[286] Overall, the magnitude of impedance is significantly lower compared to the Na-analogue, as already reported by Linsenmann et al.[298] Apart for the electrolyte resistance (R_{el}), which is stable throughout the cycling, the R_{SEI} decreases during the first 30 cycles, and then remains almost unchanged during the subsequent ones, indicating that the formation of a stable SEI requires several cycles. On the other hand, the charge-transfer resistance R_{ct} increases during

the first 30 cycles and then tends to stabilize, evidencing the stabilization of the electrode/electrolyte interface. Nevertheless, the electrode exhibits low resistance values of R_{SEI} and R_{ct}, indicating high reaction kinetics and interfacial stability, which explain the good rate capability and cycling stability obtained for CCDHC/CC-CMC electrodes. These results also confirm the ability of the CC-CMC binder to form strong interactions with the hard carbon material, providing a stable conductive network with a low interparticle charge transfer resistance upon cycling.[299,300] Comparing the resistance values obtained in Li- and Na- half-cells for CCDHC/CC-CMC electrodes, a lower SEI and charge transfer resistances have been experimented for Li-system. The former can be ascribed to the formation of a more stable and thinner SEI, considering also that in Na-ion system the magnitude of the SEI impedance increases during cycling, while the latter can be related to the higher ionic transport of Li$^+$ compared to Na$^+$ into Hard Carbon.
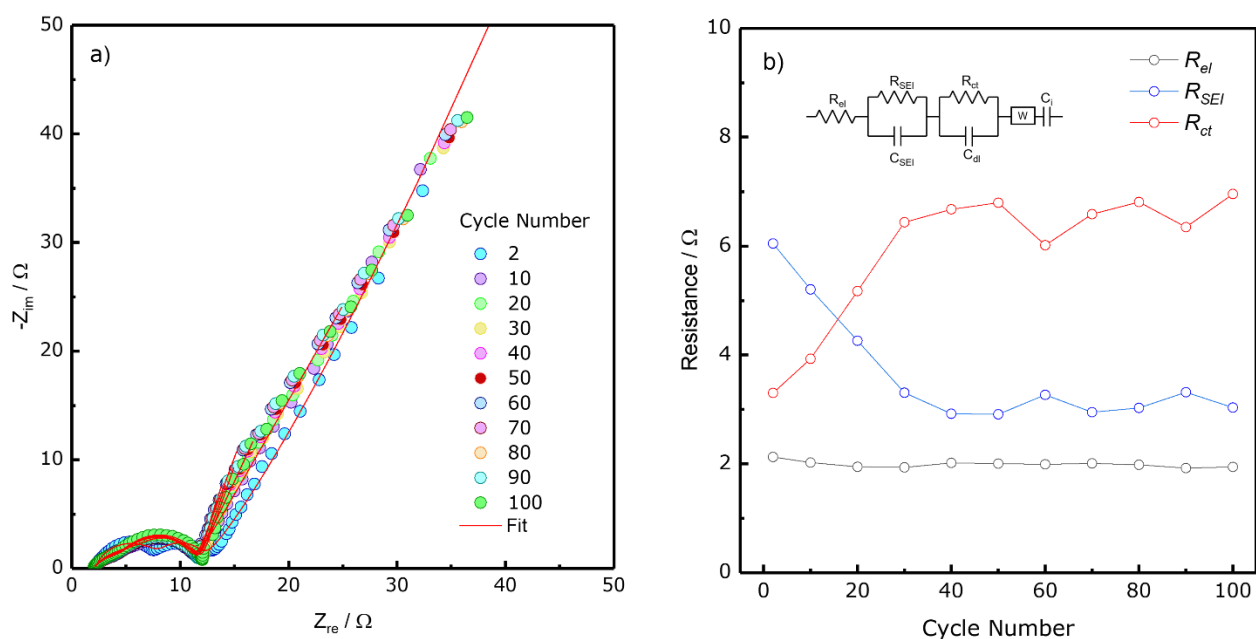
Figure 35 (a) Nyquist plot of CCDHC-based LIB electrode prepared with CC-CMC binder and 1M LiPF$_6$ EC:DMC 1:1 (v/v) as electrolyte, acquired every 10th cycle, E = 0.5 V, 10 mHz < f < 100 kHz; (b) Values of R_{el}, R_{SEI} and R_{ct} upon cycling, as obtained by EIS data analysis; Equivalent circuit used to simulate the data.

Table 9 *SEI and charge transfer resistances, capacitances and α values as a function of cycle number for CCDHC-based LIB electrode prepared with CC-CMC binder and 1M LiPF₆ EC:DMC 1:1 (v/v) as electrolyte.*

Cycle	R_{SEI} / Ω	Capacitance / F	α	R_{CT} / Ω	Capacitance / F	α
2	6.05	1.35×10^{-4}	0.78	3.30	1.27×10^{-3}	1
10	5.20	1.25×10^{-3}	0.62	3.93	1.02×10^{-3}	0.97
20	4.26	2.00×10^{-3}	0.56	5.17	1.00×10^{-3}	0.89
30	3.31	1.59×10^{-3}	0.57	6.44	8.89×10^{-4}	0.85
40	2.92	9.77×10^{-4}	0.61	6.68	8.74×10^{-4}	0.84
50	2.91	9.11×10^{-4}	0.61	6.80	8.24×10^{-4}	0.84
60	3.27	1.01×10^{-3}	0.60	6.02	7.58×10^{-4}	0.88
70	2.95	7.71×10^{-4}	0.63	6.59	7.57×10^{-4}	0.86
80	3.03	7.33×10^{-4}	0.63	6.81	6.43×10^{-4}	0.86
90	3.32	9.82×10^{-4}	0.60	6.35	6.59×10^{-4}	0.88
100	3.03	5.81×10^{-4}	0.66	6.96	5.06×10^{-4}	0.88

2.2.4.2 CCDHC as Buffer Matrix for SnO₂ Anode Material

Since graphite is well-established anode materials for LIBs and the research is focused on the improvement of LIBs energy density through high-capacity electrode materials, Hard Carbon can play a more crucial role in the development of the alloying-type materials such as SnO₂. Indeed, the creation of SnO₂/carbon composites is one of the best strategies to improve the cyclability of tin (IV) oxide since carbon matrix is able to mitigate the mechanical stress coming from the volume variations and thus tackling the rapid cell failure typical of the alloying materials. In this context, SnO₂/CCDHC composite electrodes were prepared and the electrode parameters (formulation, mechanical pressure) as well as the electrolyte compatibility were screened through electrochemical measurements, expanding the efforts for the development of this anode material. Firstly, the effect of the mechanical pressure over the electrochemical performance, especially the cycling stability, was investigated. The comparison has been made using SnO₂/CCDHC composite electrodes with a formulation of SnO₂:CCDHC equal to 3:1, which corresponds to 60 % and 20 % of electrode net weight % of SnO₂ and CCDHC, respectively. **Figure 36 a** shows three different electrodes cycled at 500 mA g^{-1} in the voltage range 0.01 < E$_{we}$ < 3.00 V using the standard electrolyte LP30. As displayed, the pressure does not seem to significantly influence the performance of the material, which in all cases suffers of a severe

capacity loss, where all the electrodes reach capacities below 100 mAh g^{-1} (87 % of capacity fading) in around 70 cycles: these trends can be ascribed to the pulverization phenomenon resulting from the volume variations during the lithiation/delithiation processes.[301] Moreover, in the first 35 cycles, where the main capacity losses are observed for all the cells, the coulombic efficiencies % tends to decrease, indicating that the pulverization is inevitably accompanied by the exposition of "fresh" particle material surface toward the electrolyte decomposition, further consuming cyclable lithium. In addition, the higher pressure actually seems to be slightly detrimental in terms of long-term stability, causing a non-negligible decrease in efficiency in the last charge/discharge cycles. According to these results, next experiments were performed with no-applied pressure over the electrodes. In order to evaluate the buffer ability of CCDHC at different SnO$_2$ content in the electrode, charge and discharge performance were evaluated for different formulations of SnO$_2$/CCDHC composite electrodes, varying the ratio between the two components of the active material, which overall represents 80% of the weight of the electrode. Herein, three different SnO$_2$/CCDHC formulations were prepared. The details are summarized in **Table 10**, while **Figure 36 b** shows the results obtained. All the formulations undergo considerable capacity losses between the first and second lithiation: these results can be associated to the irreversible processes, i.e, either electrolyte decomposition or the conversion of SnO$_2$ to Sn.[302] As expected, Formulation 1 with higher SnO$_2$ content shows a greater specific capacity at the first cycle, while it displays poor capacity retention within 100 cycles (~ 8 %): this rapid cell failure indicates that this low amount of CCDHC is not able to buffer the volume variations of tin (IV) oxide and ensure the electrode integrity. Formulation 2 exhibits the lowest average specific capacity over 100 cycles (240 mAh g^{-1}) with capacity retention comparable to that of Formulation 1. On the other hand, Formulation 3, with the lower SnO$_2$ content, shows the higher capacity retention within 100 cycles (~ 26 %) and higher ICE %. Moreover, its average specific capacity value is close to that of Formulation 1: 285 mAh g^{-1} for Formulation 3 vs 300 mAh g^{-1} for formulation 1. Overall, Formulation 3 appears to be the best formulation, also taking into account the reduced SnO$_2$ content compared to the others. Therefore, the higher amount of CCDHC in the electrode formulation seems to be beneficial for the suppression of the volume strains.
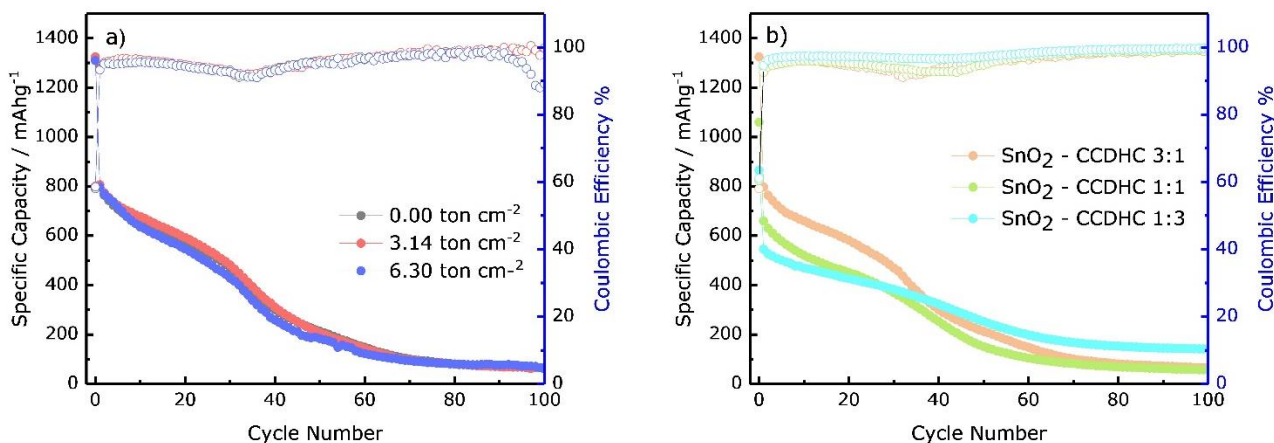
Figure 36 *Electrochemical performances of SnO$_2$/CCDHC electrode in Li half-cells cycled at 500 mA g^{-1} between 0.01 < E$_{we}$ < 3.0 V using 1M LiPF$_6$ EC:DMC 1:1 (v/v) as electrolyte: (a) Comparison of the pressure applied over the electrodes; (b) Comparison of different formulations of SnO$_2$-CCDHC composite electrodes.*

Table 10 *First-cycle discharge capacity, initial coulombic efficiency (ICE), 100th reversible discharge capacity and capacity retention of SnO$_2$/CCDHC-based LIB electrodes as a function of SnO$_2$:CCDHC ratios.*

Formulation	Discharge Capacity 1st cycle (mAhg^{-1})	ICE (%)	Discharge Capacity 100th cycle (mAhg^{-1})	Capacity Retention after 100 cycles (%)
1) SnO$_2$ – CCDHC 3:1 w:w	1324	58.0	65.3	8.2
2) SnO$_2$ – CCDHC 1:1 w:w	1060	60.5	57.0	8.6
3) SnO$_2$ – CCDHC 1:3 w:w	865	61.0	141.5	25.9

Subsequently, the electrochemical stability of the best performing CCDHC/SnO$_2$ composite (SnO$_2$:CCDHC equal to 1:3) was investigated comparing the performance obtained using the standard electrolyte LP30 with those obtained using electrolytes with the addition of different percentages of VC (2% and 5%) and FEC (10 %), which are common additives used for the promotion of the formation of a more stable SEI.[239] The results obtained are shown in **Figure 37 a** and **Table 11**. All additives used clearly prevent rapid deterioration of the working electrode, with significantly better capacity retention than the standard LP30: it passes from the ~26 % of LP30 to more than 70 % for all the cell cycled with an additive in the electrolyte. This means that the stabilization of electrode/electrolyte interface play a crucial role in the determination of the cycling stability of the SnO$_2$/CCDHC composite. Among them, LP30 + 2% VC shows the best electrochemical performance in terms of average capacity (~ 691 mAh g^{-1})

93

and capacity retention (~ 78 %). These results confirm the benefits for the cycling stability of alloying anode materials of the use of small amounts of vinylene carbonate as SEI-forming additive, which is able to produce a thin and stable SEI with an enhanced conductivity. In turn, the SEI layer formed in VC-containing electrolyte provides constant and reduced SEI impedance, which results in long cycling stability.[303,304]
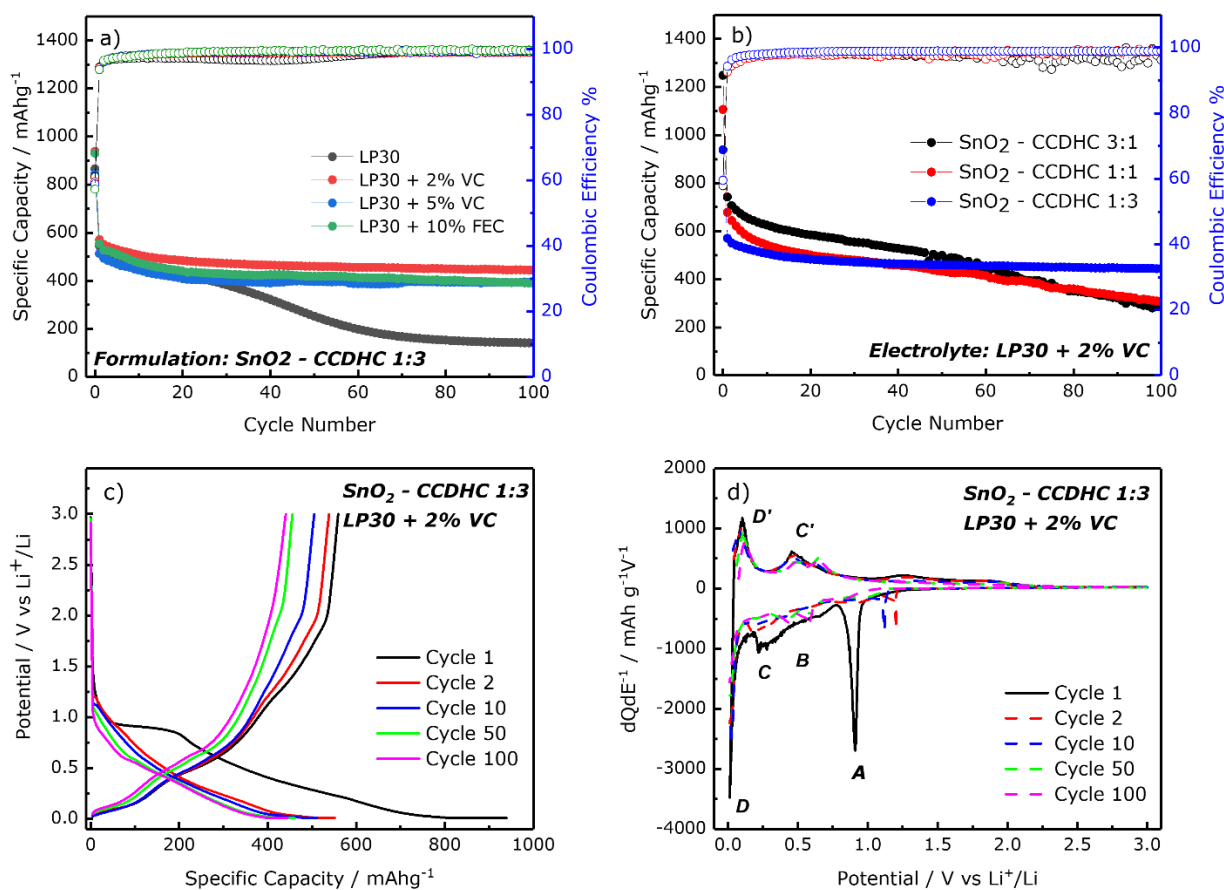
Figure 37 *Comparison of the electrochemical performances of (a) SnO₂/CCDHC 1:3 electrode cycled at 500 mA g⁻¹ with different electrolytes; (b) Comparison of different formulations of SnO₂/CCDHC with LP30 + 2% VC; (c) Voltage profiles and (d) Differential analysis of cycles of SnO₂/CCDHC 1:3 electrode cycled at 500 mA g⁻¹ with LP30 + 2% VC as electrolyte.*

Table 11 *First-cycle discharge capacity, initial coulombic efficiency (ICE), 100th reversible discharge capacity and capacity retention of SnO₂/CCDHC-based LIB electrodes as a function of the electrolyte.*

Electrolyte	Discharge Capacity 1st cycle (mAhg⁻¹)	ICE (%)	Discharge Capacity 100th cycle (mAhg⁻¹)	Capacity Retention after 100 cycles (%)
LP30	865.4	61.0	141.49	25.9
LP30 + 2% VC	939.0	59.5	443.87	77.8
LP30 + 5% VC	845.7	58.9	394.93	77.0
LP30 + 10% FEC	930.7	57.3	389.72	70.3

In order to have a counter evidence of the benefits coming from the use of the electrolyte additives, LP30 + 2 % VC was also tested with higher quantities of SnO_2 in the active material (Formulation 1 and 2). As displayed in **Figure 37 b**, the addition of 2% VC in the electrolyte reflects in a general improvement in the capacity retentions of the cells, although the capacity fade in Formulation 1 and 2 are not completely suppressed: the capacity retentions are still unsatisfactory although they increase to 38.40 % and 45.30 % for Formulation 1 and 2, respectively. This means that the improvement of SnO_2 cycling stability arises from both the buffer effect of volume variations by higher amount of carbon matrix CCDHC and the improvement of electrode/electrolyte interface coming from the formation of a more stable SEI. In order to deeper study the SnO_2/CCDHC 1:3 composite electrode with LP30 + 2% VC as electrolyte, voltage profiles and differential analysis of cycles are reported in **Figure 37 c,d**, respectively. During the first lithiation, the SnO_2/CCDHC 1:3 composite exhibits a plateau at around 0.9 V, corresponding to the peak A in the $dQdE^{-1}$ vs E curve, which is due to the conversion reaction between Li^+ and SnO_2 to form Sn^0 and Li_2O. This reaction is largely irreversible since this peak disappears in the subsequent cycles. The second potential region in the voltage profile (0.8 - 0.1 V) is consistent with the broad feature B between 0.8 V and 0.4 V and the bump C centered at around 0.25 V in the differential analysis of cycles; the former can be mainly ascribed to the SEI formation and Li^+ adsorption storage into CCDHC, while the latter corresponds to the alloying reaction between lithium and tin with the formation of Li-Sn alloy.[159,161] This region is the major responsible of the SnO_2/CCDHC 1:3 composite specific capacity during the whole cycling. In the low voltage plateau (E_{we} < 0.1 V) the intercalation of lithium in the Hard Carbon occurs, leading to a narrow and reversible peak D in the $dQdE^{-1}$ vs E curve. Although the peak of intercalation of lithium into CCDHC is distinguishable from the

others, it is unfeasible and unreliable split the contribution of the two materials over the specific capacity of the composite electrode since the sloping region 0.8-0.1 V meet both the contribution of CCDHC pseudocapacitive processes and tin alloying reaction with lithium.

2.3 CONCLUSIONS

High-performance Hard Carbon has been successfully synthesized from biowaste corncobs through a simple one-step carbonization process at 950° C in inert atmosphere. This process is relatively simple and industrially applicable. Regarding the sustainability, the non-use of acid pre- and post-treatments is, in principle, beneficial for the economic and environmental sustainability, although the electricity consumption during pyrolysis is the most impactful step in Hard Carbon synthesis.[305] In this context, the use of renewable energy derived-electricity can play a crucial role in the sustainability of Hard Carbon production. In parallel, an aqueous binder has been successfully produced from corncob extracted cellulose, by $NaOH:ClCH_2COOH$ etherification, thus obtaining a Na-CMC sample with an estimated degree of substitution of 0.59. By studying the structural and morphological behaviors of the active material, CCHC showed a suitable interlayer spacing and a good surface area for partial bulk insertion and interfacial adsorption of both lithium and sodium. When they are combined in an anode for SIBs, CCDHC active material with CC-CMC binder exhibits good electrochemical performances delivering a specific capacity of 264 mAh g^{-1} at 1C with a promising capacity retention and good rate capability. These performances are superior or comparable to other Hard Carbon found in literature. Moreover, the electrode shows a fast reaction kinetics, while interfacial stability arises from the strong interactions between hard carbon and Na-CMC. According to the experimental observations, the sodium storage arises from the surface-controlled reactions in the sloping region (E_{we} > 0.10 V), while the diffusion-controlled intercalation is the predominant process approaching the low-voltage plateau (E_{we} < 0.10 V). The reported results represent a relevant contribution both to the in-depth understanding and optimization of the sodium storage mechanisms at carbonaceous hosts, and to the development of high-performing, sustainable anodes for SIBs. In LIBs, CCDHC/CC-CMC composite electrodes show the same features of charge storage of sodium, while it possesses a larger voltage hysteresis due to the stronger interactions between lithium and Hard Carbon heteroatoms and defects. Nonetheless, CCDHC delivers a specific capacity of 394 mAh g^{-1} at 1C with a promising capacity retention and good rate capability. These results can be explained by low SEI and charge transfer resistances, indicating fast reaction kinetics and enhanced interfacial stability. Knowing that the graphite is a consolidated anode material for lithium-ion batteries, this work represents an approach toward the investigation of an affordable alternative for less-demanding applications. Finally, the preliminary evaluations of CCDHC as a buffer matrix for SnO_2 reveals that the mitigation of capacity fade typical of alloying-type materials is remarkable when the ratio between SnO_2 and

CCDHC is set at 1:3 and 2% of VC is added to the standard electrolyte, promoting the formation of a thin and stable electrode/electrolyte, which increases the capacity retention after 100 cycles from around 26 % to around 78 %.

Overall, further optimizations are still needed for practical applications in both lithium- and sodium-ion batteries, especially those regarding the improvements of the initial coulombic efficiency of Hard Carbon.

3. Valorization Of Forestry-Waste as Electrode Materials for Na-Ion Batteries

Herein, forestry-waste were used as raw materials for the preparation of electrode materials for sodium-ion batteries. Firstly, Hard Carbon were synthesized from different forestry sources while cellulose and lignin components were extracted from the same feedstocks for the preparation of bio-based binders. Cellulose was isolated with a bleaching process with hydrogen peroxide and then converted into Na-CMC, while lignin was isolated through an organosolv method, using the bio-based polar aprotic solvents γ-Valerolactone (GVL) and Dihydrolevoglucosenone (Cyrene), which have recently attracted great attentions respect to the traditional solvents such as low-molecular weight primary alcohol (methanol and ethanol), polyols (glycerol and ethylene glycol), acetone and acetic acid.[306] Then, Hard Carbons and bio-based binder (i.e. Na-CMC and lignin) were combined and used for the fabrication of composite SIB anodes. The electrochemical performances of the obtained electrodes were investigated in Na half-cells, especially comparing the performance of lignin-containing electrodes with those of CMC-containing electrodes. Finally, the best Hard Carbons have been evaluated in full-cell application with a NASICON-type cathode, evaluating the electrochemical performance in terms of specific capacity and capacity retention especially at high-current rates, where this kind of cathode find its most important application. Additionally, sodium mesoxalate $Na_2C_3O_5$ was preliminary evaluated as sacrificial salt to overcome the drawback of low initial coulombic efficiency of Hard Carbon.

Part of the activities herein reported was carried out in the framework of LEAF project funded by University of Camerino under the FAR 2019 funding scheme, while part of the experiments was conducted in the laboratories at the University of Basque Country (UPV/EHU).

3.1 Experimental Section

In this section, the details about synthetic procedures, electrode processing, structural, chemical, morphological and electrochemical characterizations are summarized.

3.1.1 Synthesis of Forestry-Waste Derived Hard Carbon

The forestry waste utilized in the experiments were collected from the Alte Valli of Rivers Potenza and Chienti, a wooded area in Marche Apennines (Italy). The air-dried samples were sieved to particle size < 1 mm. Then the ground biomasses were submitted to a preliminary water leaching to remove impurities. In details, the samples were put in deionized water (sample:water ratio 1:50) and heat to 60 °C for 12 h under stirring. After that, the biomasses were filtered, washed

two times with fresh water and dried at 80° C overnight. Then the dried raw materials were ground to a fine powder with an automatic ball mill at 300 rpm for 4h in a steel jar (ball to powder ratio 1:50 in weight) and carbonized in a horizontal cylindrical furnace at 1000 °C for 2 h under nitrogen flow after a heating ramp of 5 °C/min. The samples were cooled down inside the furnace, under nitrogen flow as well. Additionally, the holm-oak and willow derived hard carbons were submitted to an acid leaching after the pyrolysis in HCl 3M (sample:solution ratio 1:20) for 3 days under vigorous stirring at room temperature. After that, the samples were filtered and washed with deionized water until a neutral pH was obtained and stored at 80° C overnight. The fabricated hard carbons were labelled as listed in **Table 8**.

3.1.2 Isolation of Cellulose and Synthesis of CMC

The bleaching of cellulose was conducted following a different procedure respect to that used for corncob-derived cellulose written in **Subsection 2.1.2**. In details, the raw materials were first dried and ground to remove the excess of water, then they underwent to one-step treatment with an aqueous solution of NaOH (5% w/w) and H_2O_2 (5% w/w) at 80 °C for 2 h under vigorous agitation. The products were filtered and washed several times until neutral pH was reached. The products were dried, collected and labelled as shown in **Table 12**. For the carboxymethylation of cellulose, the extracted cellulose was submitted to the same procedure used for corncob-derived CMC, increasing only the reaction time for the etherification. In fact, after the preliminary step in a 15 % NaOH aqueous solution for 1h at room temperature, the samples were mixed with chloroacetic acid (NaOH:$ClCH_2COOH$ molar ratio of 1.6) already dissolved in ethanol (96% v/v) for 4 h at 70 °C. The alkali excess was neutralized with 1 M HCl and the Na-carboxymethyl cellulose (Na-CMC) were obtained by filtration, followed by washing with ethanol and drying. The synthesized CMCs were prepared only from holm-oak and willow bleached cellulose samples and were labelled as H-CMC and W-CMC, respectively.

3.1.3 Extraction of Lignin

The extractions of lignin-rich fractions were performed using an organosolv method. Firstly, the biomasses were dried and milled to a particle size < 1 mm and suspended into a mixture GVL or Cyrene with H_2O in the ratio 1:1 w/w using a solid-to-solvent ratio 1:10 w:w. The resulting mixture was put into a microwave reactor and heated for 2h at 170 °C under vigorous stirring. Subsequently the solution was cooled down below 50 °C. The heating-up time for all experiments was relatively short (within 2 min). After that, the mixture was filtered and the solid residue was washed, dried and weighted to determine the pulp yield. The lignin contained in the filtrate ("organosolv liquor") was precipitated using fresh water and collected using centrifugation. The extracted lignin-rich fractions were dried in an oven overnight.

3.1.4 Synthesis of Na$_3$(VO)$_2$(PO$_4$)$_2$F

The cathode active material was synthesized by the research group of Prof. Verónica Palomares at the University of Basque Country using a not reported microwave process. VO(C$_5$H$_2$O$_2$), H$_3$PO$_4$ and NaF with a molar ratio of 1:1.5:1.7 and a 6 wt. % of Ketjen black carbon were used as the precursors during the synthesis. VO(C$_5$H$_2$O$_2$) was added to 3 mL of ethanol and 1 mL of acetone followed by H$_3$PO$_4$, NaF and Ketjen black. The mixture was ultrasonicated for 10 minutes until it was completely homogeneous, then 20 mL of water was added. The prepared solution was heated at 200 °C for 2 h in a microwave reactor.

3.1.5 Electrode Processing and Cell Assembling

Anode electrodes were made with forestry-waste derived HCs as the active materials, Super-P carbon (Imerys) as the conductive agent, and commercial CMC, synthesized CMCs and extracted lignins as the binders. HC:Super-P:Binder (80:10:10 w/w) slurries were prepared in high purity deionized water, coated onto Cu foil using the doctor blade technique (thickness of wet coating = 100 μm), and left to dry at room temperature. After calendaring, circular electrodes (9- and 12-mm diameters) were cut and further dried at 120 °C under vacuum for 12 h. The loadings of active materials were in the range 0.5-1.5 mg cm^{-2} for all the electrodes. For the Na half-cells, three-electrode Swagelok-type cells were assembled in an argon-filled glove box (Jacomex GP-campus, oxygen and moisture content less than 0.8 ppm) using forestry-waste derived HCs as working electrode and metallic sodium (Sigma-Aldrich) as reference and counter electrodes. A 1 M solution of NaClO$_4$ (Sigma-Aldrich) in ethylene carbonate (EC)/ polycarbonate (PC) (1:1 in volume) (Sigma-Aldrich) was selected as the electrolyte (400 μl) and 12 mm glass fiber disks (Whatman GF/A) as separator. For the full-cells, the cathode slurries without the sacrificial salt was obtained by mixing the different components in the formulation of 80:10:10 w/w (Na$_3$(VO)$_2$(PO$_4$)$_2$F:PVdF:Super C-65). All the components were firstly ground together in an agate mortar, added to NMP and left stirring for 3 h to form a homogeneous dispersion. On the other hand, cathode slurries with sodium mesoxalate as sacrificial salt, commercially available as Na$_2$C$_3$O$_5$·5H$_2$O, were prepared as reported by Fernández-Ropero and co-workers.[307] Firstly, the ground sodium-salt was heat-treated to 200 °C under vacuum for 12 h to remove the water molecules and then leave dry overnight at 50 °C under vacuum as well. Then, the cathode additive was obtained mixing the dried sodium mesoxalate with Ketjen Black (KJ600) in the ratio 70:30 w/w %. Finally, the cathode slurries were obtained mixing the cathode active material Na$_3$(VO)$_2$(PO$_4$)$_2$F, the cathode additive Na$_2$C$_3$O$_5$/KJ600, the binder PVDF and the conductive carbon Super C-65 in the ratio of 65:15:10:10 w/w %. All obtained cathode slurries were coated onto Al foil (150 μm thickness) through doctor blade technique and left drying for 2 h at room temperature and then at 80 °C in a vacuum oven. Finally, circular electrodes of Ø = 12 mm and Ø = 16 mm were cut by using an electrode puncher with the proper diameter and pressed at

4.42 ton cm^{-2} through a hydraulic press. Two-electrode coin cells (CR2032) were used for the electrochemical measurements and assembled in an argon-filled glovebox (MBraun) with O$_2$ and H$_2$O content < 0.1 ppm. The electrolyte employed was 1M NaPF$_6$ dissolved in a 1:1 v/v mixture of ethylene carbonate and propylene carbonate (EC:PC) for all full-cells tested. Prior to the full-cell assembling without cathode additive, the anode electrodes were submitted to electrochemical presodiation through half-cell cylcling vs metallic sodium in order to reach a % of coulombic efficiency higher than 98.0 %, while the cathode electrodes were submitted to electrochemical desodiation through one cycle in half-cell vs Na$^+$/Na. After that, the half-cells were disassembled in glovebox and the full-cell assembled with fresh electrolyte. After the assembly, all the cells were removed from the glove box for the electrochemical characterization. For full cell measurements, the wet thicknesses of the cathodic and anodic coatings were adjusted to provide charge balancing between positive and negative electrode (without considering SEI contribution), maintaining a slight excess of the latter to prevent plating effects. The mass loadings of the electrodes employed in the full cells ranged from 0.8 to 2.0 mg cm^{-2} for Na$_3$(VO)$_2$(PO$_4$)$_2$F and 0.5 to 1.5 mg cm^{-2} for holm-oak derived Hard Carbon (LHC).

3.1.6 Material Characterization

Infrared spectra of the standard CMC (ST-CMC), extracted cellulose, synthesized CMC and lignins powders were recorded by means of a Perkin-Elmer Spectrum Two FTIR spectrometer within the wave number range of 400 to 4000 cm^{-1}. Thermogravimetric analysis (TGA) of CMC and lignin-rich fractions were carried out using a Perkin-Elmer STA 6000 Thermal Analyzer. The nitrogen flow rate at the powder was set to 50 mL min^{-1} and an alumina crucible was used to hold the sample. After equilibration, the powder was heated up to 800 °C at a rate of 10 °C min^{-1}. ^{1}H-Nuclear Magnetic Resonance spectroscopy (NMR) was used to estimate the degree of substitution (DS) of CMC, according to the method proposed by Klosiewict[250] and described in **Subsection 2.1.4**. Before the analysis, the H-CMC and W-CMC samples were dissolved in deuterium oxide at a concentration of 15 mg/ml heating to 70 °C for 2h. The spectra were recorded using a Varian Mercury 400 spectrometer operating at 400 MHz. The chemical shifts were quoted in ppm and calibrated from the residual protons signal of deuterated solvent as internal standard.

Scanning Electron Microscopy (SEM) and Energy Dispersive X ray analysis (EDX) of the Hard Carbons samples were acquired using a FESEM Cambridge Stereo scan 360 electron microscope equipped with QUANTAX EDX detector (at an accelerating voltage of 15 kV). The structure of the Hard Carbons powders were characterized by X-ray diffraction (XRD) (Bragg–Brentano geometry, Cu-Kα, λ = 1.54059Å) and Raman spectroscopy (Horiba IHR 320, wavelength 532 nm). The interplanar spacing (d$_{002}$), the crystallite size along c-axis (L$_c$) and the average width of graphene domain (L$_a$) were calculated according to the already mentioned equations **Eq. (13), Eq. (14)** and **Eq. (15)**, respectively. Pore characteristics of holm-oak and willow derived HCs

were evaluated by CO_2 adsorption measurement at 273 K using a Micromeritics ASAP 2020 instrument. Prior both adsorptions, the samples have been outgassed for 12 h at 150 °C. The specific surface area was calculated by the BET model over the classical range p/p^0 = 0.05 - 0.3.

3.1.7 Electrochemical Characterization

All electrochemical tests were carried out using a VMP-2Z multichannel electrochemical workstation by Bio-Logic Science Instruments (France). Cyclic voltammetry of forestry-waste derived HCs electrodes in Na half-cell were performed at scanning rate of 0.10 mV s^{-1} in the voltage range 0.01 to 2 V vs Na$^+$/Na. Galvanostatic charge/discharge and rate capability tests of the Hard Carbon electrodes in Na half-cells were collected with the voltage ranging between 0.01 and 2 V, assuming for all the experiments that 1C rate corresponds to 300 mA g^{-1} with respect to active material mass. In addition, C-rate capability of the forestry-waste derived HC electrodes were evaluated in the C/5 to 5C range (5 cycles at every rate). In order to evaluate the interfacial behavior of electrodes, electrochemical impedance spectroscopy (EIS) was carried out at the first cycle and then at each tenth cycle at E = 0.5 V, with an AC amplitude of 5 mV, in a frequency range 100 kHz > f > 10 mHz. For $Na_3(VO)_2(PO_4)_2F$ half-cell characterization, cyclic voltammetry was performed at scanning rate of 0.10 mV s^{-1} in the voltage range 3.00 to 4.30 V vs Na$^+$/Na. Galvanostatic charge/discharge and rate capability tests were collected in the same voltage range of cyclic voltammetry, applying different current rate with respect to active material mass. EIS measurements were carried out at the first cycle and then at each tenth cycle at E = 3.82 V, with an AC amplitude of 5 mV, in a frequency range 200 kHz > f > 100 mHz. For full-cell characterizations, cyclic voltammetries were performed at scanning rate of 0.10 mV s^{-1} in the voltage range 1.00 < E_{cell} < 4.30 V, as well as galvanostatic charge/discharge and rate capability tests.

3.2 RESULTS AND DISCUSSION

3.2.1 Chemical, Structural and Morphological Characterizations of the Forestry Waste-Derived Hard Carbons Active Materials

The yield % of forestry waste pyrolysis to produce Hard Carbon and the corresponding sample labelling are listed in **Table 12**. The values of yield % were obtained making a ratio between the mass of the obtained Hard Carbon over the mass of the dry raw material putted in the furnace.

Forest waste	Yield %	HC Label
Holm Oak (*Quercus Ilex*)	22.4	LHC
Pubescent Oak (*Quercus Pubescens*)	21.5	RHC
Hop-hornbeam (*Ostrya Carpinifolia*)	18.4	OHC
Ash (*Fraxinus*)	17.1	FHC
Willow (*Salix*)	17.8	SHC

The yields % of the pyrolysis products can be justified considering that lignin has an higher carbon content (approximatively 60 % wt)[226] respect to cellulose ($\sim$ 44 % wt)[308], thus leading to higher yields % for samples which are expected to have higher lignin content. However, the ash content in biomasses, i.e. mineral content and inorganic substances,[309] should be taken into account since it is still present in the samples after pyrolysis. Thus, the observed yields % are not only related to carbon but also to the inorganic part. Therefore, to estimate the amount of inorganic impurities, EDX analysis were performed (**Figure 38 a-e**).
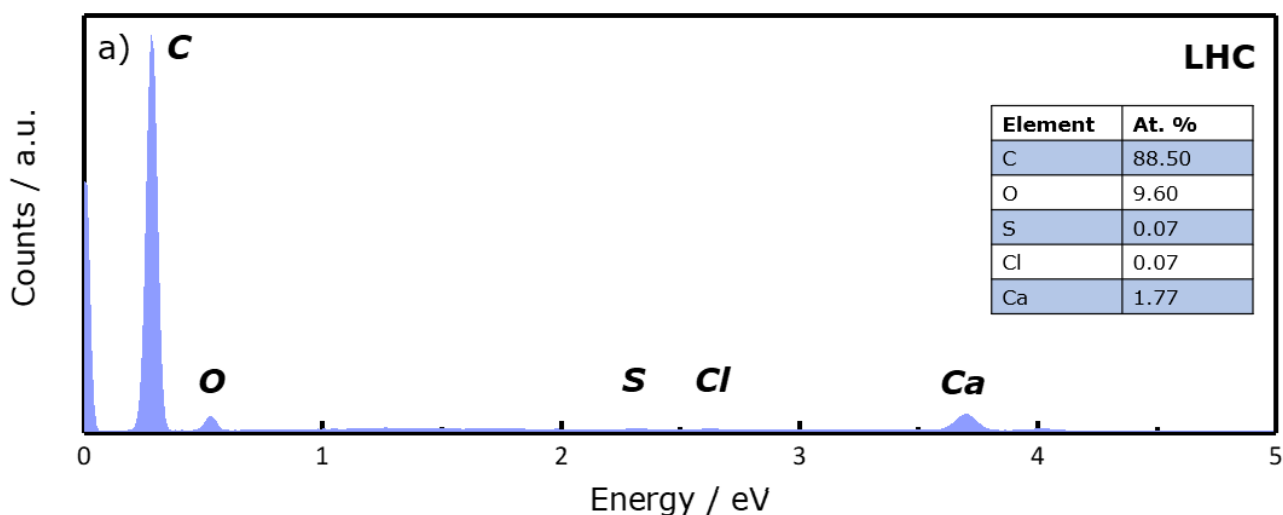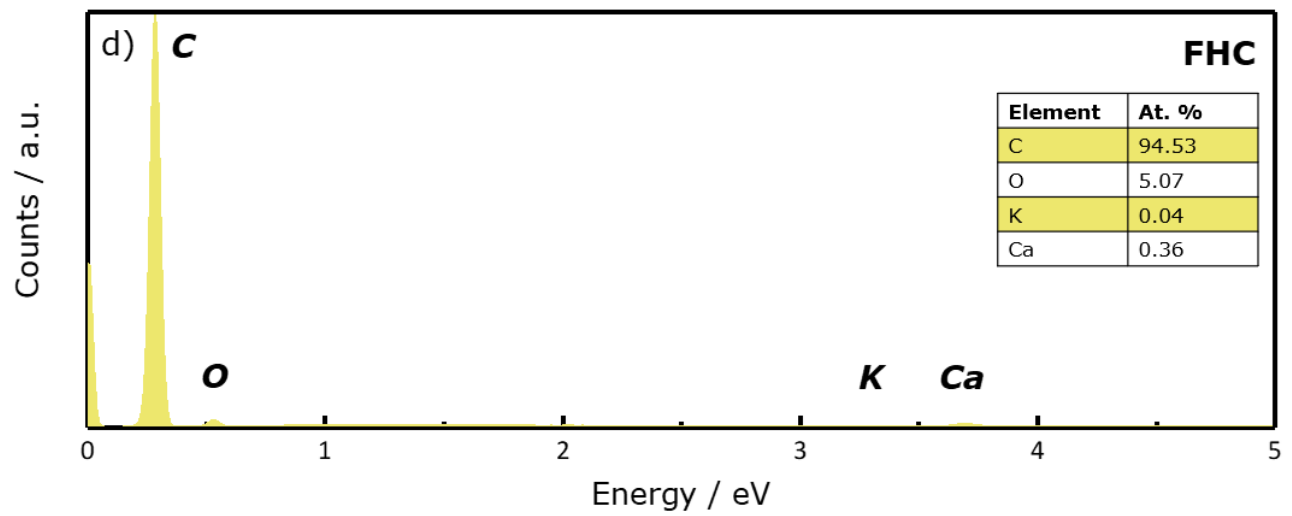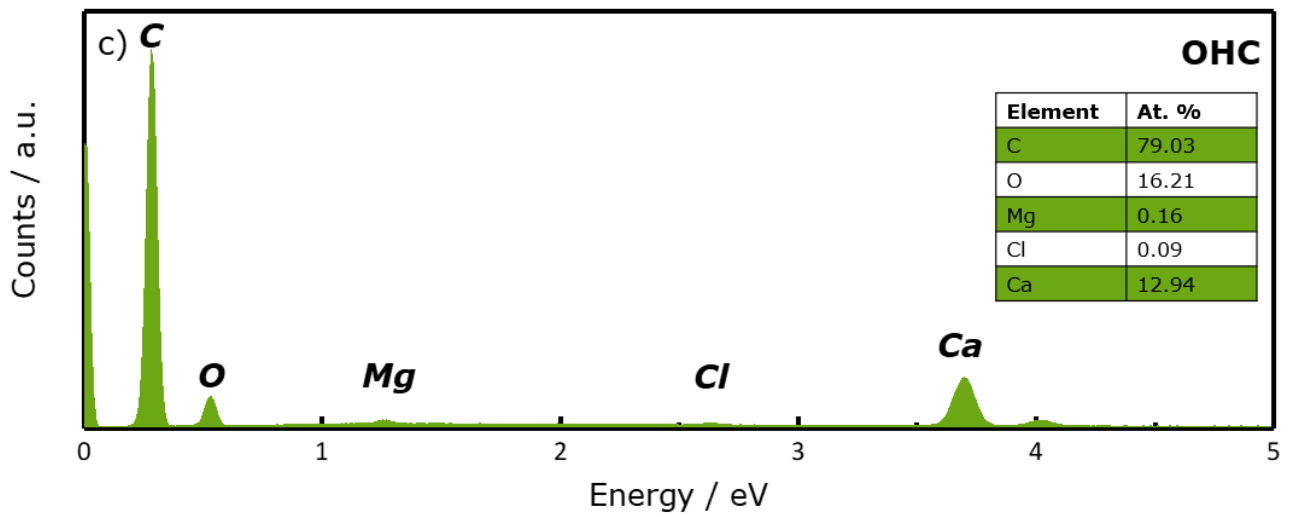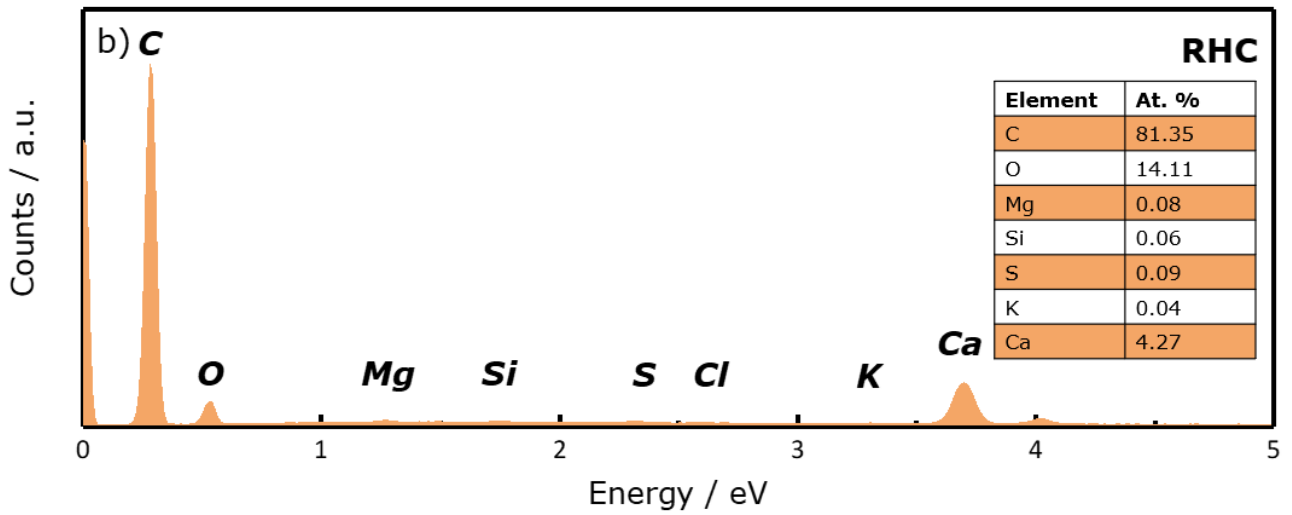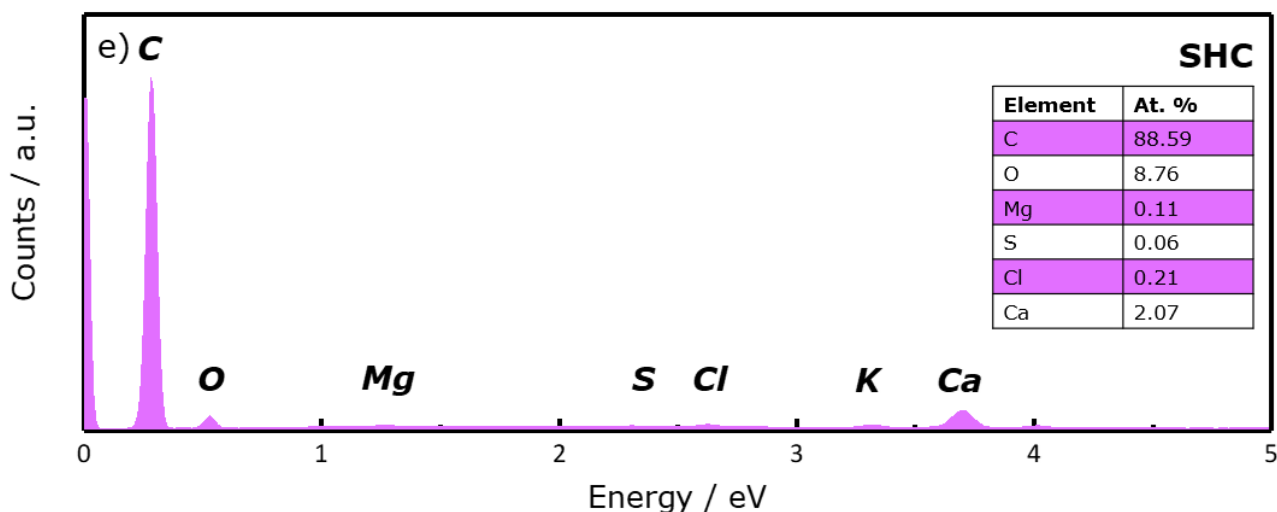
Figure 38 *EDX analysis of: (a) Holm-Oak (b) Pubescent-Oak (c) Hop-Hornbeam (d) Ash (e) Willow derived HCs.*

In addition to carbon and oxygen, all the Hard Carbons have residual inorganic elements coming from the biomass, ranging from the 0.40 at. % of Ash derived HC (FHC) to the 13.19 at. % of Hop-Hornbeam derived HC (OHC). However, it is important to consider that EDX does not measure hydrogen and nitrogen, leading to a possible overestimation of the other elements.

Simultaneously, a screening of the electrochemical performance was performed to preliminary compare the HCs specific capacities and focus the next experiments on the two samples with the best results in Na half-cells. As shown in **Figure 39**, the best specific capacities were delivered by LHC and SHC, which are also the Hard Carbons fabricated from the expected higher lignin containing precursor, i.e., holm-oak (reported lignin content ∼ 30 %),[310] and from the expected higher cellulose containing precursor, i.e., willow (reported cellulose content between 36-65 %).[311]
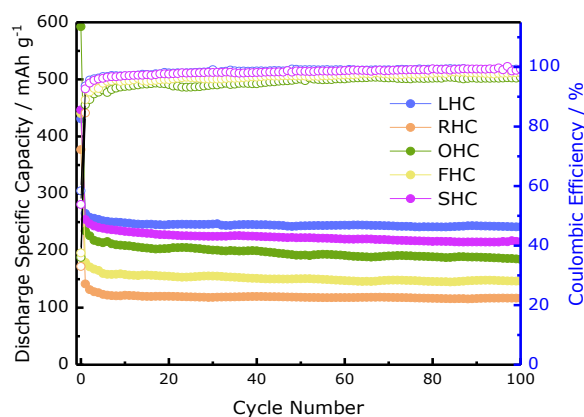
Figure 39 *Comparison of different forestry-waste derived HCs in Na half-cells with 1M NaClO₄ in EC:PC 1:1 (v/v) as electrolyte.*

Since the inorganic impurities strongly affect the structural, textural and electrochemical properties of hard carbons,[312] acid leaching was performed on holm-oak derived HC (LHC) and willow derived HC (SHC). In order to evaluate the effectiveness of the leaching to remove the inorganic fraction, EDX and XRD analysis were performed. **Figure 40 a,b** shows LHC and SHC diffraction patterns before and after acid leaching. The characteristic peaks of Hard Carbon are located at ~ 22-23° and 43°, which can be assigned to the (002) and (100) crystallographic planes,[133] while the presence of impurities is indicated by several sharp peaks clearly visible for no-washed materials. The peaks marked with the * present both in non-leached and acid-leached samples belong to the sample holder, which is made of brass. Considering that the impurities identification based on XRD is rather difficult due to phase complexity and also unnecessary due to the effectiveness of acid leaching to remove them, it has not been performed. On the other hand, the determination of structural parameters from XRD spectra of acid-leached materials was carried out and will be proposed later.
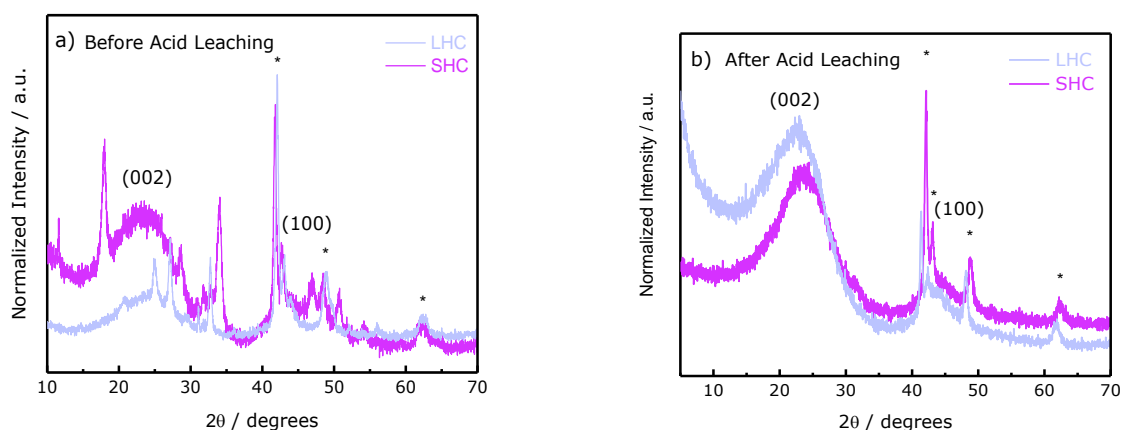
Figure 40 *XRD diffractogram of LHC and SHC (a) before and b) after acid leaching.*

EDX analysis performed on acid-leached holm-oak and willow derived HCs are shown in **Figure 41 a,b**, respectively. The atomic percentage of carbon increases in both samples passing from around 88 % to 96 at. % for both samples, while the oxygen content decreases from around 9 % to 2.5 at. %. The decrease in the atomic percentage of oxygen suggests that inorganic impurities in the form of oxides or carbonates are dissolved in HCl and removed during the filtration. Additionally, the sum of atomic percentage of heteroelements decreases in both samples (1.91 vs 0.58 at. % for LHC and 2.45 vs 1.58 at. % for SHC), especially for calcium. The removal of these inorganic compounds might be beneficial for the electrochemical performance, since they can otherwise occupy available active sites for Na uptake, as well as decrease the electronic conductivity or affect the electrode surface chemistry.[247] In SHC, the EDX shows the presence of very small amounts of potassium K and phosphorous P which are not present in the unwashed SHC sample: this difference in terms of the type of impurities may

be explained by local investigation range of the EDX technique.[128] For the sake of clarity, one could argue that the intensity of S, Cl and Ca peaks seems to be much higher than that of O in both EPMA spectra, thus indicating a much higher amount of these heteroelements respect to O. However, in the absence of a flat and highly polished surface standard, a proper quantification of O cannot be performed: lighter elements (i.e., O and C) generally yield low-energy photons that are susceptible to self-absorption phenomena when an energy beam $E_0 > 3$ keV is employed for the measurement. This phenomenon can lead to a lowering of the intensity of the O peak relative of other heavier elements, thus underestimating the amount of O when considering relative intensities.[313]
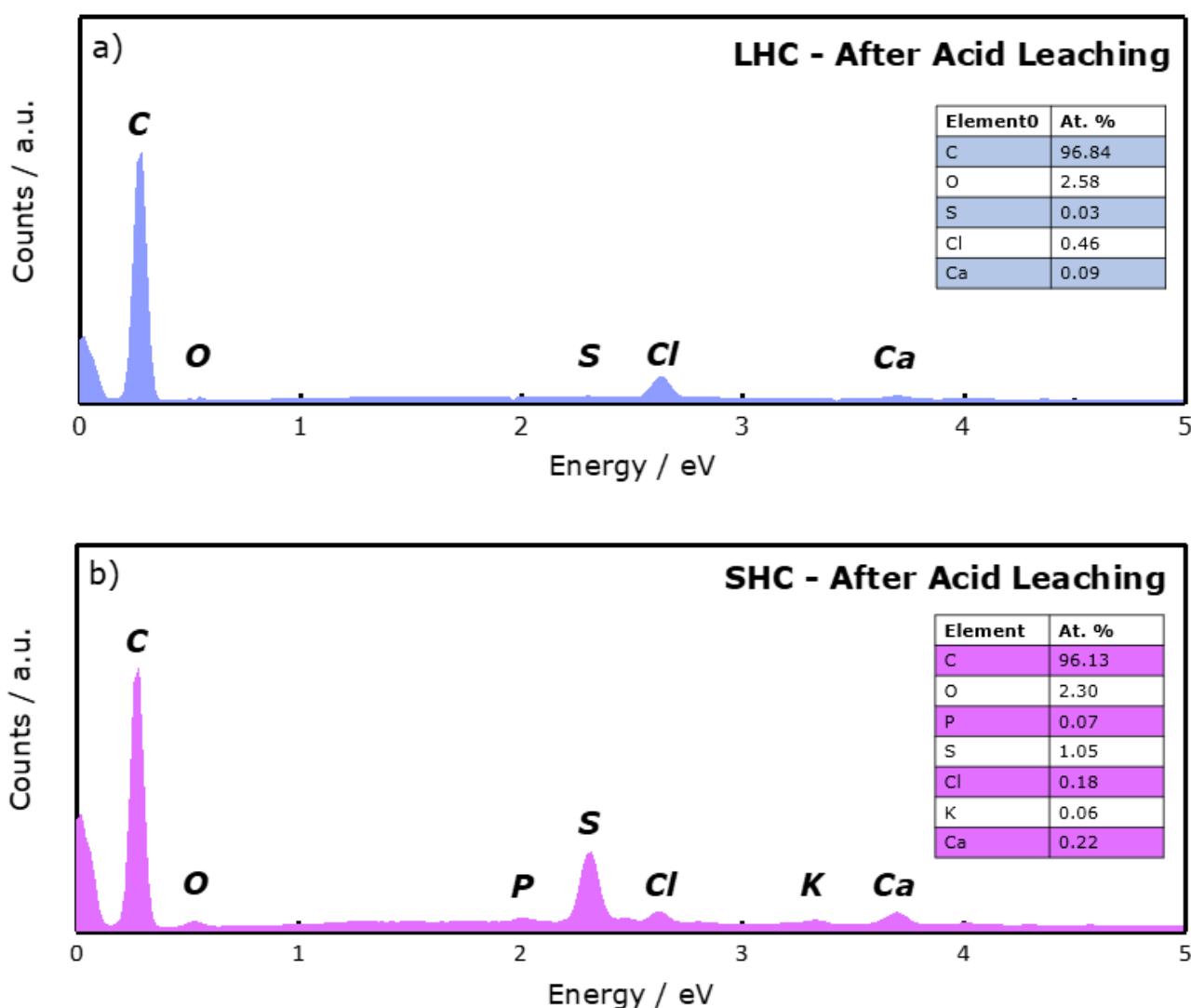
Figure 41 *EDX analysis of acid-leached (a) Holm-Oak (b) Willow derived HCs.*

The structure and porosity of LHC and SHC were evaluated by XRD, Raman and CO_2 adsorption as shown in **Figure 42 a, b, c**, while all the structural parameters acquired are presented in **Table 13**. As already mentioned, the two broad diffraction peaks of Hard Carbon can be

observed at 2θ values of ∼ 22-23° and 43°, which correspond to the crystallographic planes of (002) and (100), respectively.[127] The (002) band indicates the spacing between graphene layers and the broadening of the signal is consistent with the presence of short-range structures composed of a random layer lattice with defective sites and crystalline graphitic domains.[270,286] The maximum of this bump is located at higher angles for SHC respect to LHC, implying a lower interlayer distance:[124] according to the Bragg's Law (**Eq.(13)**) the d_{002} interplanar spacing are calculated to be 0.392 nm for LHC and 0.379 nm for SHC, which are both higher than that of graphite (0.335 nm), facilitating the sodium insertion/de-insertion between graphene layers.
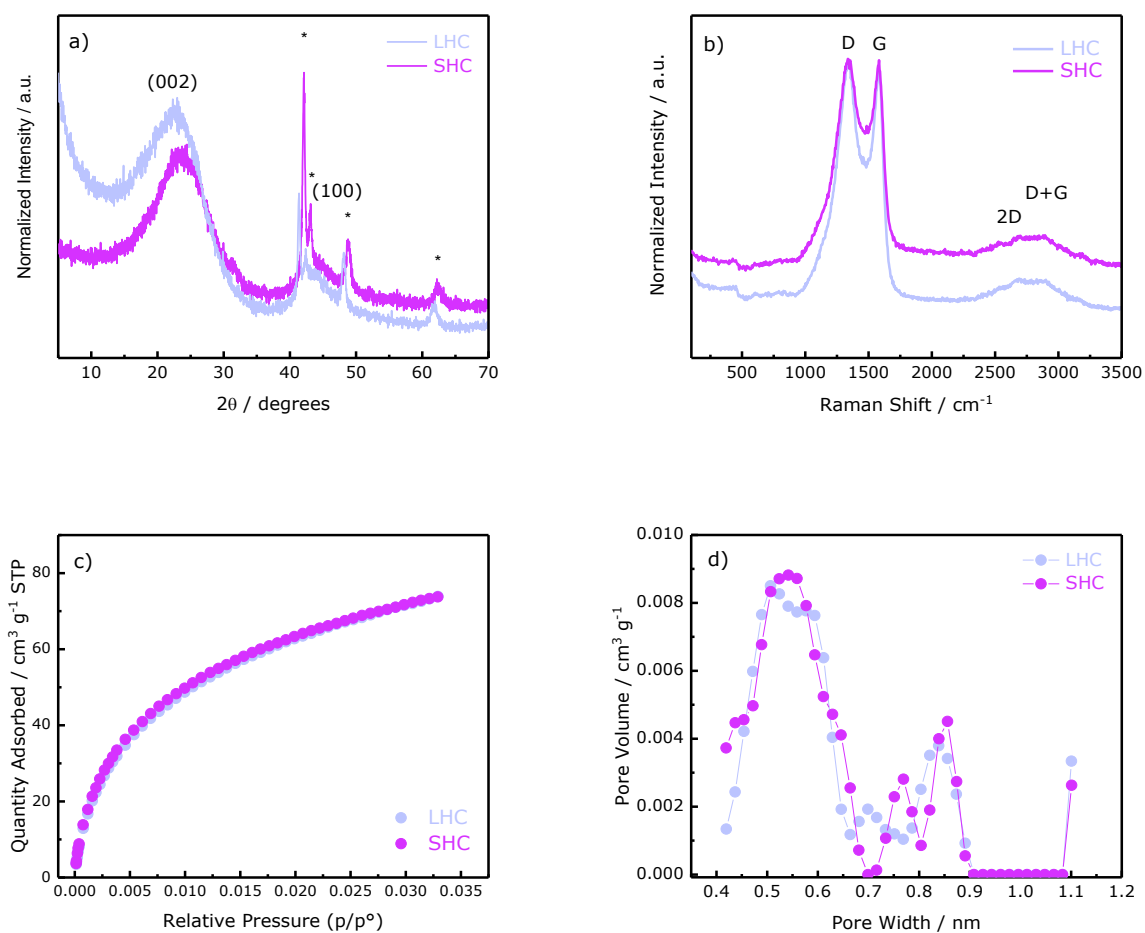
Figure 42 *Chemical and physical characterization of acid-leached LHC and SHC powders: (a) XRD pattern; (b) Raman spectra; (c) CO_2 adsorption isotherm; (d) DFT pore size distribution.*

Table 13 *Crystallographic parameters of LHC and SHC powders;*

Sample	d_{002} (nm)	L_c (nm)	L_a (nm)	I_G/I_D	*n*
LHC	0.392	0.760	18.46	0.96	2.93
SHC	0.378	0.937	19.03	0.99	3.48

The higher interlayer distance of LHC respect to SHC may be ascribed, in part, to the expected higher content of lignin in holm-oak raw material respect to willow. Indeed, the highly cross-linked structure of lignin is able to prevent graphitization during the carbonization and thus reflecting in higher interlayer spacing between graphene layers. Although a recent article by del Mar Saavedra Rios and co-workers state that the interlayer spacing d_{002} of Hard Carbon is not generally affected by cellulose, lignin, extractives or ash content of the biomass precursors,[247] the forestry residues-derived Hard Carbons that they tested shows the same correlation between the lignin content and the interlayer distance d_{002}. Moreover, the impact of heteroelements (H, O, N, Ca, Cl, Mg, etc.), both in the form of mineral impurities and/or bounded to the carbon of cellulose, hemicellulose and lignin,[106] in determining the Hard Carbon structure, must be also taken into account.[247] Regarding the other lattice parameters, the staked plane height L_c is smaller for LHC respect to SHC, 0.760 nm vs 0.937 nm, respectively. Both values are close to those of other reported hard carbon with similar interplanar distance d_{002}.[261] The number of interlayers stacked in the graphitic domains *n* are estimated according to the calculation $n = L_c/d_{002} + 1$, revealing approximatively 3 stacked graphene layers in the graphitic domains (2.93 and 3.48 for LHC and SHC, respectively).[263] Additional information about materials structure were obtained using Raman spectroscopy on Hard Carbon powders. As shown in **Figure 42 b**, the two typical bands of layered carbon are located at around 1336 cm^{-1} (D-band) and 1580 cm^{-1} (G-band). Moreover, two broad and low intensity peaks are located at ~ 2680 cm^{-1} and 2880 cm^{-1}, which correspond to the second-order bands 2D and D+G, respectively. From the intensity ratio between the G band and the D band (I_G/I_D), the disordered degree of hard carbon materials is calculated to be 0.96 for LHC and 0.99 for SHC, indicating a lower degree of graphitic ordering for LHC powder respect to SHC. The values of the average width of the graphitic domains L_a, as calculated from Raman bands according to **Eq. (15)**, are of 18.46 nm for LHC and 19.03 nm for SHC. To investigate the Hard Carbons porosity, CO_2 adsorption measurement of LHC and SHC were conducted. The obtained isotherms are shown in **Figure 42 c**, while the corresponding DFT pore size distributions are displayed in **Figure 42 d**. The values of CO_2 BET surface area are almost identical (320.3 m^{2}g^{-1} for LHC vs 321.7 m^{2}g^{-1} for SHC) and in line with other Hard Carbons synthesized at the same temperature of annealing.[314] Generally, increasing the temperature of the pyrolysis, the porosity will be significantly reduced as a consequence of the pore closure phenomena:[251] it is reported that Hard Carbons synthesized at temperature higher than 1300

°C exhibit very low surface area,[128,247,251] which is beneficial for the reduction of electrolyte decomposition and irreversible Na^+ ions trapping into pores, improving the initial coulombic efficiency %. On the other hand, higher surface areas should increase the capacity from Na^+ adsorption, which is characterized by a fast reaction kinetic and, thus, is particularly appealing for high-current applications. The DFT pore size distributions confirm the presence of micropores in both samples, with most of the pores having size described by a gaussian-type curve in the range 0.4 - 0.7 nm, representing around the 78 % of the total volume created by micropores with size ≤ 1.1. These so-called "ultramicropores" have been recently pointed out that are involved in the Na^+ storage, providing extra sites for sodium adsorption and thus increasing the sloping capacity of Hard Carbon.[268]

3.2.2 Synthesis, Chemical and Structural Characterizations of the Forestry Waste-Derived Cellulose and Carboxymethylcellulose Binder

The bleaching of cellulose was conducted by a chlorine-free procedure, using the nontoxic and safe bleaching agent hydrogen peroxide in alkaline environment.[315] Although the mechanism of the isolation is not completely elucidated, it is generally accepted that the perhydroxyl ions are the main responsible of bleaching. These perhydroxyl anions are generated through the dissociation of H_2O_2 which occurs at a pH of around 10-12 because it is a very weak acid,[316] as described by the following equation **Eq. (23)**:

$$H_2O_2 \rightleftarrows H^+ + HO_2^-$$ **Eq. 23**

The debate is still ongoing about how the reactions proceeds, the role of free radicals and oxygen.[317] Nonetheless, H_2O_2 promotes the solubilization of hemicellulose and the depolymerization of lignin with a strong pH dependence.[318] The yields % of forestry waste cellulose extractions and the corresponding sample labelling are listed in **Table 14**.

Table 14 *Yield % of cellulose extractions.*

Forest waste	Yield %	Sample Name
Holm Oak (*Quercus Ilex*)	23.4	LC
Pubescent Oak (*Quercus Pubescens*)	35.1	RC
Hop-hornbeam (*Ostrya Carpinifolia*)	40.1	OC
Ash (*Fraxinus*)	51.2	FC
Willow (*Salix*)	52.3	SC

The extraction yields % suggest that the holm-oak may be the sample with lowest content of cellulose (23 %) while willow should be the sample with the highest content of cellulose (52.3 %). The characterizations of all the cellulose samples extracted, compared with a reference sample (MC), were conducted using FT-IR as displayed in **Figure 43 a**. The wide peaks at around 3335 cm^{-1} are attributed to the stretching vibration of O-H groups in glycosidic units and intermolecular hydrogen bonds in cellulose.[319] The peaks at around 2880-2890 cm^{-1} are related to C-H group stretching.[320] The peaks at around 1320 cm^{-1} present in all the samples are ascribed to the rocking vibrations of -CH$_2$-. The bands at 1130 cm^{-1} are ascribed to the C-O-C asymmetric stretching.[321] In the region of -O- vibrations (1200-1000 cm^{-1}), there are two main peaks at around 1047 cm^{-1} and 1023 cm^{-1}, attributed to C-O stretching of ether and alcohol in glucose units.[254] Overall, the spectra are very similar each other and to the reference sample, indicating that the isolations was successful for all the samples.
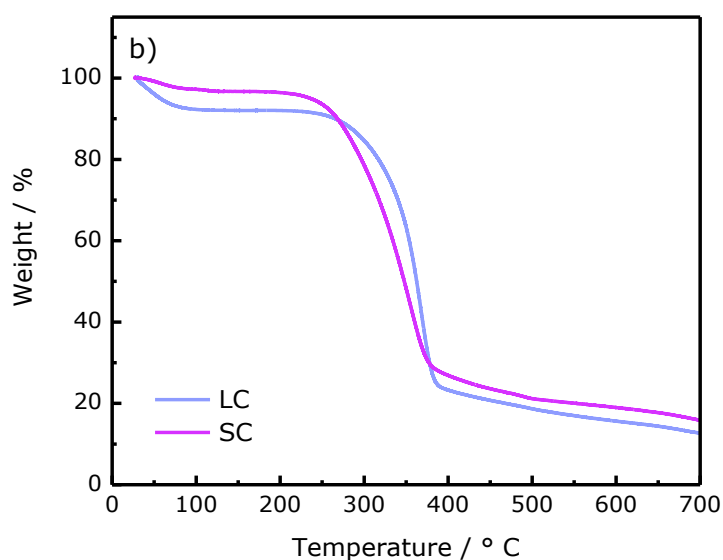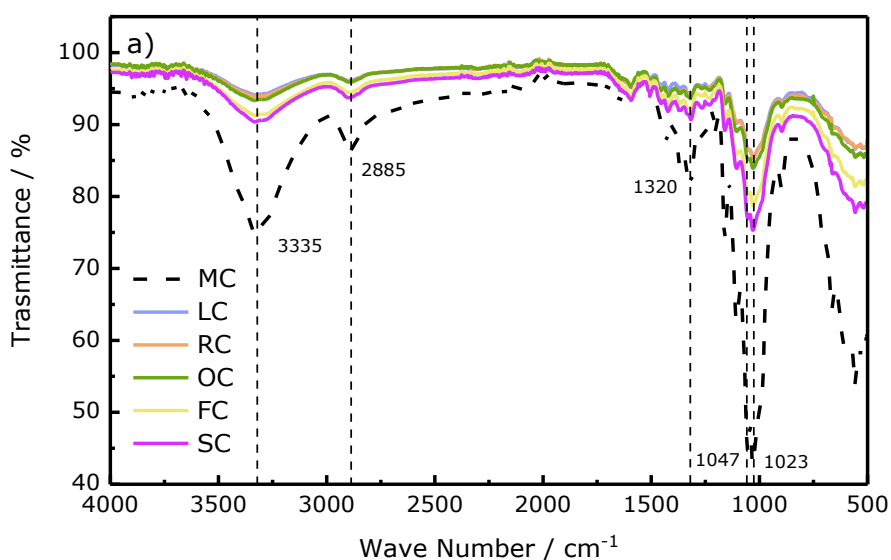
Figure 43 *(a) FT-IR spectra of forestry waste derived cellulose compared with a reference cellulose sample; (b) TGA of holm-oak and willow derived cellulose compared with reference.*

Thermograms of extracted cellulose from holm-oak and willow are shown in **Figure 43 b**. The first weight drops at around 100 °C, which is more pronounced for LC, indicate the evaporation of water. Both samples present a quite similar thermogram profile, although willow shows a lower onset temperature of thermal degradation (around 250 °C) respect to the holm-oak (around 290 °C). The major weight losses continue until ~380 °C and is mainly due to the degradation of cellulose chains through subsequent steps involving depolymerisation, dehydration and disruption of glycosidic units. The second weight losses between 380-700 °C

are more gentle and correspond to the decomposition of carbonic residue into low molecular weight products.[322]

The derivatized carboxymethyl cellulose samples have been produced from LC and SC by the method detailed in the Experimental Section, where the etherification synthesis follows the reactions describe previously by the **Eq. (16)**, **(17)**, **(18)**. The products were labelled as H-CMC and W-CMC, indicating respectively holm-oak derived CMC and willow derived CMC. **Figure 44 a** shows the FT-IR spectra of CMC samples compared with a commercial CMC (ST-CMC), while **Figure 44 b** shows the FT-IR spectra of the respective cellulose precursors. The stretching bands of O-H, C-H and C-O are still distinguishable in CMCs samples at 3330 cm^{-1}, 2890 cm^{-1} and 1051 cm^{-1}, respectively. In addition, the presence of a strong absorption band at 1587 cm^{-1} in CMC samples confirms that the carboxymethylation took place, since it is ascribed to the carboxyl stretching COO$^-$.[255,256] The peaks at 1418 and 1324 cm^{-1} presents in CMC samples are related to the -CH$_2$ scissoring[259] and -OH bending vibration, respectively.[257]
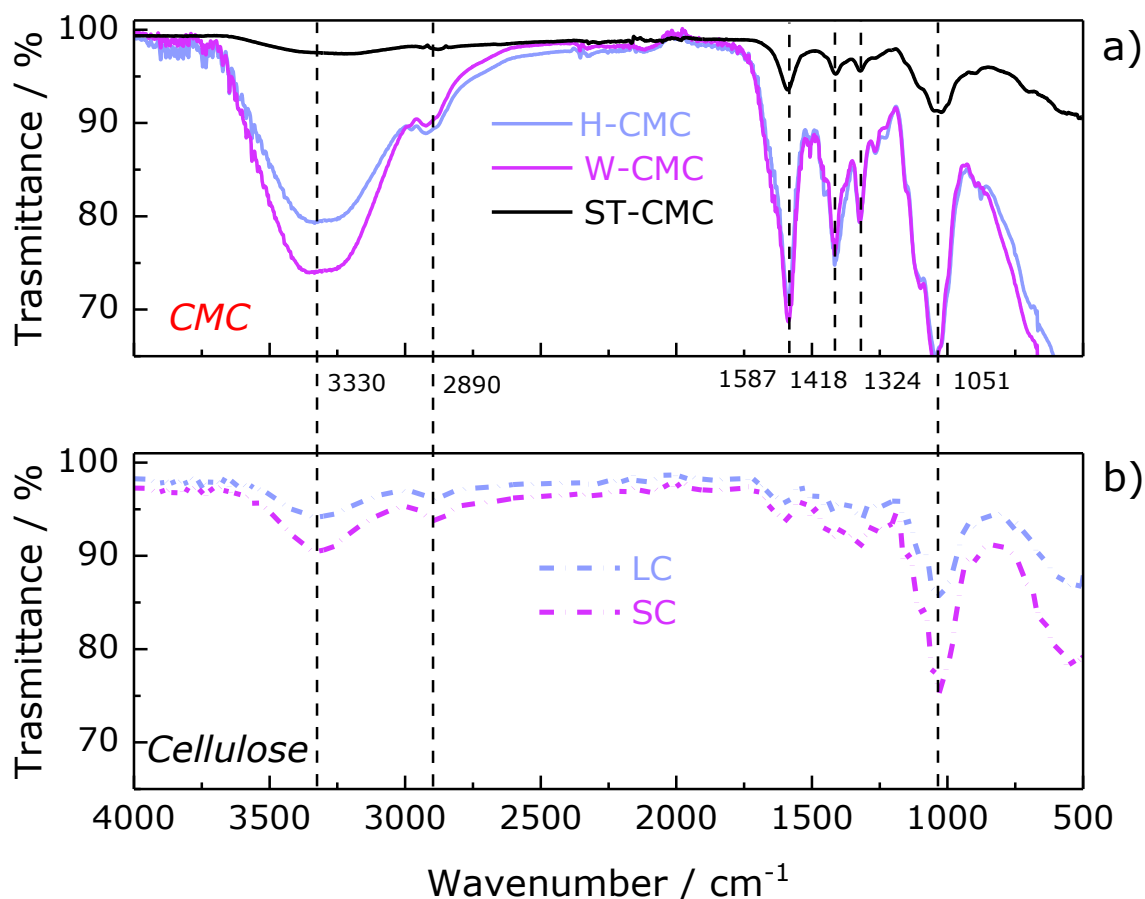
Figure 44 *FT-IR spectra of holm-oak and willow (a) derived CMC compared with a reference sample and (b) cellulose precursors.*

Figure 45 a show the TGA curves of biomass-derived CMCs compared with a standard CMC (ST-CMC). The CMCs have similar trends of thermal degradation respect to the reference compound. In both CMC the first degradation step around 100 °C is associated to the evaporation of water. The main weight losses (~ 30 %) for CMCs start at the onset temperature of 230 °C and continued until 305 °C. This step has been related in the previous chapter (see **Subsection 2.2.1**) mainly to the decarboxylation of cellulose[208,258,259] followed by the start of cellulose chains break down. However, according to the work of Casaburi et al.[207], where the thermogram of CMCs with different DS are compared with the cellulose precursor, the weight loss of samples in the range 230-305 °C are more pronounced as the DS decrease and become the highest for unsubstituted cellulose. These results clearly indicate that there is a strong contribution of unmodified cellulose backbone decomposition in this temperature range and also that the functionalization increases the thermal stability of the cellulose since the weight loss decrease as the DS of the samples increase. Therefore, since the weight loss in this temperature range was found to be ~ 41 % for the CC-CMC samples described in **Chapter 2** which has an estimated DS of 0.59, it can be hypothesize that the DS of H-CMC and W-CMC are closely each other and both are higher than CC-CMC sample. On the other hand, the third weight losses in the temperature range 305-700 °C are around 15 % of samples weights and originate from the CMC backbone decomposition to form carbon residues.
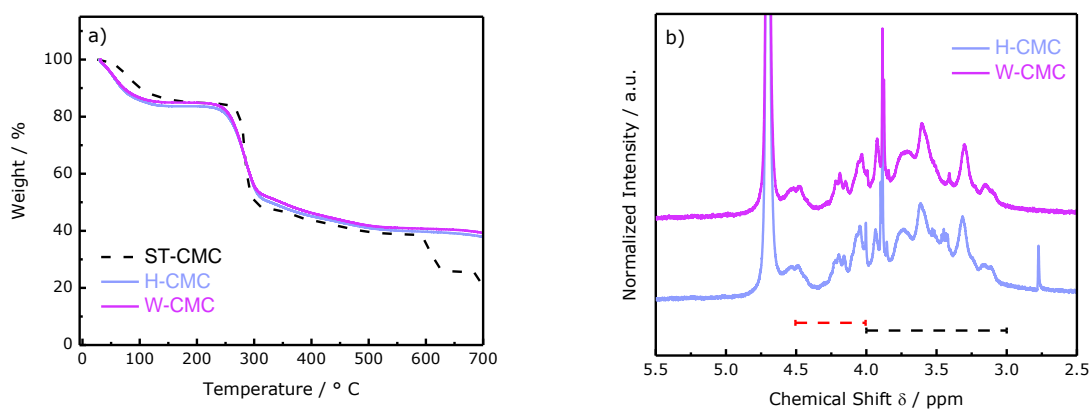
Figure 45 *(a) TGA of H-CMC and W-CMC compared to a reference sample (ST-CMC); (b) ^{1}H-NMR spectra of H-CMC and W-CMC.*

Since the physical-chemical properties of CMC are strongly affected by the DS, the latter has been estimated using ^{1}H-NMR spectroscopy according to the method proposed by Klosiewicz[250] and described in **Subsection 2.1.4**. **Figure 45 b** illustrates ^{1}H-NMR spectrum of H-CMC and W-CMC in D_2O. The two spectra are almost similar with overlapped peaks in the region 3.0-4.5 ppm, which disallow the extrapolation of structural informations from the ^{1}H-NMR spectrum. However, the peaks positions and shape of ^{1}H-NMR spectra of H-CMC and W-CMC are similar to those reported in the literature by previous researchers.[206,208,255,323,324] The DS values were

estimated to be 1.08 and 1.05 for H-CMC and W-CMC, respectively. These values are relatively high, indicating a high solubility in water.

3.2.3 Extraction, Chemical and Structural Characterizations of the Forestry Waste-Derived Lignin-Rich Binder

The extractions of lignin were performed using the organosolv separation method described in **Subsection 3.1.3**. Basically, the organosolv-based biomass fractionation involves the break of lignin-carbohydrate complexes (LCC) linkages followed by the hydrolysis of glycosidic bonds of hemicellulose and dissolution of lignin through the cleavage of ether bonds, promoting the depolymerization of the lignin.[221,325] In this way, an insoluble cellulose-rich fraction in the solid residue, a lignin-rich fraction in the organosolv liquor and a water soluble fraction containing mainly hemicellulose sugars monomers are obtained.[306] The insoluble cellulose-rich fraction, known as pulp, can be further treated to purify the cellulose, while the lignin-rich fraction and the water soluble fraction in the filtrate are separated through the addition of fresh water which promotes the precipitation of the lignin.[326] The extraction mechanism is quite complicated since it involves several simultaneous reactions schematized in **Figure 46 a**. Firstly, the breakdown of LCC bonds to free lignin from carbohydrate includes the acid-catalyzed hydrolysis of eight main different ether and ester bonds between lignin and hemicellulose but also between lignin and cellulose.[327,328] In the organsolv process carried out at elevated temperature (> 150° C) the addition of the acid catalysts is not required, since acetic acid and other organic acids released from hemicellulose, coupled with, to a small extent, the autoionization of water, autocatalyze LCCs degradation.[306,328] Simultaneously to the LCC bonds cleavage, the lignin is isolated mainly through the cleavage of α- and β-aryl ether bonds present in lignin, which leads to lignin depolymerization and the dissolution of the fragments.[329] The reactions pathways for the cleavage of α-aryl linkages includes solvolytic cleavage (i) by quinone intermediate or (ii) via nucleophilic substitution and (iii) direct breakage with the formation of resonance-stabilized benzyl carbocation which can undergo condensation reactions with other units.[330] On the other hand, the cleavage of β-aryl ether bonds, which is enhanced by the addition of acid catalyst,[306,330,331] proceeds following three different pathways: (i) solvolytic cleavage and elimination of formaldehyde, (ii) homolytic and solvolytic cleavage for the formation of Hibbert ketones and (iii) benzyl carbocation formation.[330,331] Unfortunately, at this stage, condensation reactions of the lignin fragments through the benzyl carbocations which can readily form a covalent bond with an electron-rich carbon atom in the aromatic ring of another lignin fragment are already taking place.[332] Therefore, lignin is counterproductively repolymerized through condensation reactions which forms new bonds of the type β-1', β-β' and β-5', 5-5' (**Figure 46 b**).[332,333]
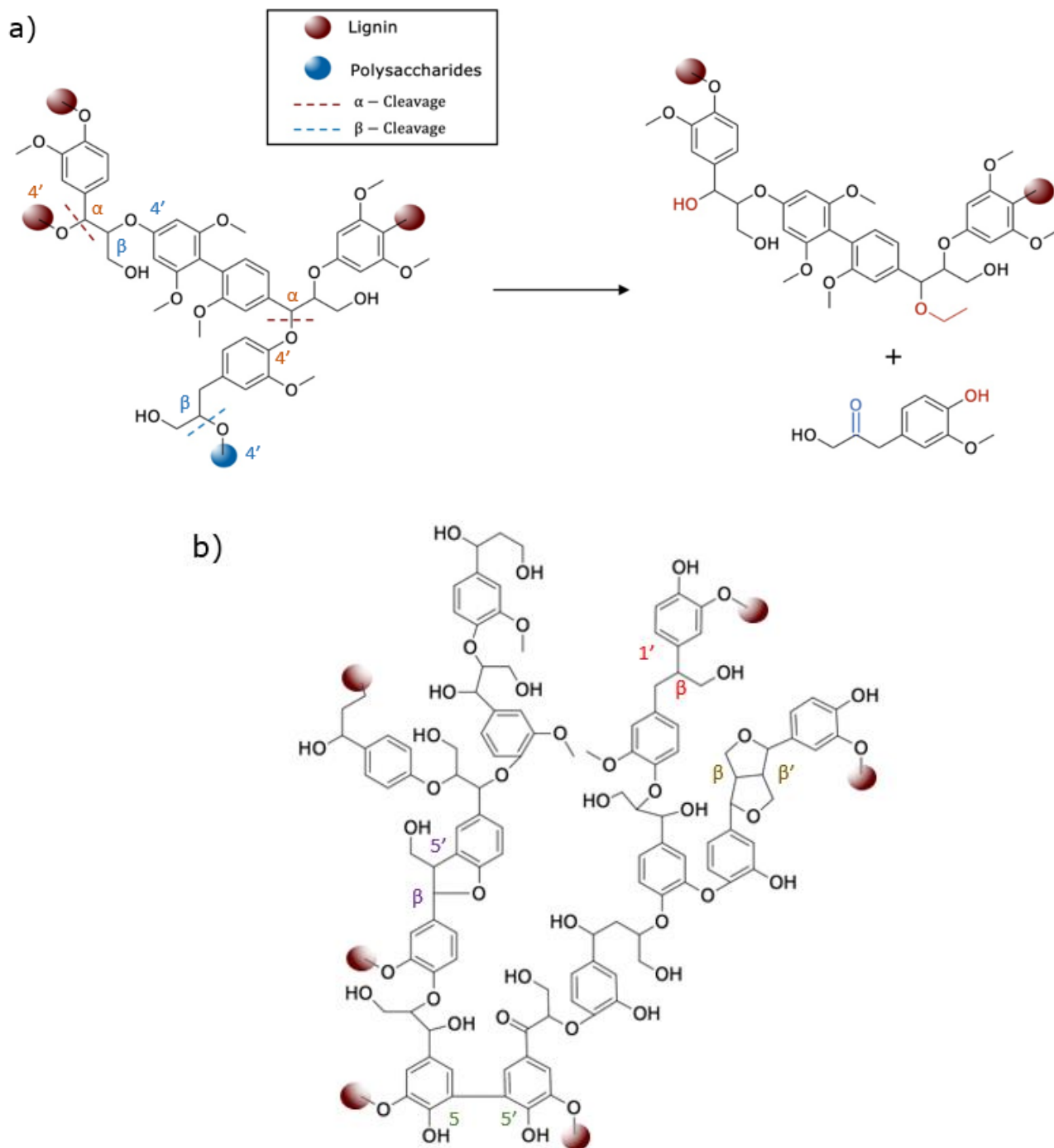
Figure 46 *Schematic representation of (a) α- and β-cleavage[332] and (b) condensation reactions during organosolv process;*

Overall, during the organosolv process the native structure of lignin is modified by a combination of depolymerization and condensation reactions, which of these concurrent reactions occur can be a matter of thermodynamic or kinetic control. Theoretical chemical modeling supported by

experimental observations state that depolymerization reaction is under thermodynamic control while condensation reaction is regulated by kinetic control since the average bond dissociation energies of the typical condensation products are larger than those of the depolymerization products. Moreover, the average activation energies of the condensation products are smaller than those of the depolymerization products.[223,332]

Table 15 illustrates the extraction yields % obtained using Cyrene:H_2O and GVL:H_2O mixtures:

Table 15 Pulp and lignin yields % of Cyrene:H_2O and GVL:H_2O extractions.

Forest waste	Cyrene : H_2O*		GVL : H_2O*	
	Pulp Yield %	Lignin Yield %	Pulp Yield %	Lignin Yield %
Holm Oak	44.9	44.2	39.0	13.9
Pubescent Oak	56.3	39.2	52.0	7.6
Hop-hornbeam	52.6	45.9	-	-
Ash	43.1	27.4	-	-
Willow	68.7	9.4	41.8	13.1

*The percentage of pulp and lignin yield are calculated over the weight of the starting biomass

Several parameters such as solvent used, temperature, process time, catalyst, solvent concentration, solid-liquid ratio, particle size control the organsolv process concerning the extent of delignification and the properties of the lignin obtained. The latter is influenced especially in terms of Klason lignin content and molecular weight, but also the proportion of aliphatic and phenolic OH groups.[332]

Using Cyrene as organic solvent, % yields of lignin-rich fractions lie in a wide range, from the impressively high value of 45.9 % for Hop-hornbeam to the 9.4 % of Willow, while % yields of lignin-rich fractions obtained using GVL as organic solvent are more restrained are lower than 14 % for the three biomasses tested. Looking at these extraction results, although the lignin content shows a large variability in biomass and in hardwoods it generally ranges between 15 and 30 %,[218] the extraction yields % obtained using Cyrene suggest that the lignin-rich fraction samples are probably biased by a considerable amount of impurities. On the other hand, although using the mixture GVL:H_2O lower % yields of lignin-rich fraction are obtained, the effectiveness of delignification performed with GVL shall not be considered lower respect to the ones done with Cyrene, because the purity of lignin obtained must be evaluated and taken into account. Therefore, before making any kind of assumptions, in order to compare the purity of

lignin-rich fractions obtained with the two solvents mixtures, the Klason lignin content in the holm-oak derived lignin-rich fractions were determined according to the Laboratory Analytical Procedure of National Renewable Energy Laboratory (NREL) – Determination of Structural Carbohydrates and Lignin in Biomass.[334] As shown in **Table 16**, the Klason Lignin content, which corresponds to the residue after acid hydrolysis of the carbohydrate portion, is considerably higher for GVL extraction respect to that of Cyrene. These results confirm the hypothesis of large amount of impurities present in the Cyrene-extracted lignin-rich fraction, while the purity of lignin obtained with GVL is in the range of other organosolv lignin-rich fractions isolated using different raw materials and solvents.[335–337]

Table 16 *Klason Lignin % of Holm Oak extracted lignin-rich fractions from Cyrene:H_2O and GVL:H_2O mixtures.*

Forest waste	Cyrene : H_2O	GVL : H_2O
	Klason Lignin %	Klason Lignin %
Holm Oak (*Quercus Ilex*)	58.4	73.7

These results can be explained, in part, considering the Hildebrand and especially the Hansen solubility parameters (δ), which basically describe the ability of a solvent to dissolve a solute: the more the δ values of solvent and solute are similar, the more is the extent of dissolution. The Hildebrand δ of lignin ranges between 22.5 and 24.5 MPa$^{1/2}$[223,306,333] while that of GVL is 23.1 MPa$^{1/2}$[338] and that of Cyrene is, to the best of my knowledge, not reported in the literature. Therefore, according to the Hildebrand parameters, GVL is able to dissolve lignin with a high effectiveness. However, for polar and complicated molecules such as GVL and Cyrene, Hansen Solubility Parameters (HSP) are more realistic since they take into account the contribution of hydrogen bond ability and polar nature of the molecules.[306] According to the theory, a practical way to evaluate how close the solubility parameters of two substances to each other is the calculation of the Hansen Relative Energy Difference (RED), which is a parameter that describes the compatibility between solvent and solute: a good solvent has a RED value lower than 1 while bad solvent have a RED value higher than 1.[339] In this context, the Hansen relative energy difference between lignin and Cyrene was estimated to be 0.89,[340] while between lignin and GVL is 0.83,[341] indicating that both solvents are able to solubilize lignin and GVL has a slightly higher affinity for lignin respect to Cyrene. Moreover, the RED value of Cyrene decreases to approximately 0.60 when a mixture of around 90 % Cyrene and 10 % water is considered,[342] while RED of GVL reaches 0.58 when a mixture 80 % GVL and 20 % of H_2O is used.[343] These results are the consequence of the enhanced hydrogen bonding capability of the solvent system, which allows easier and stronger hydrogen bonding interactions between solvent system and lignin, replacing the intermolecular hydrogen bonds in lignin and therefore promoting the dissolution.[344,345] Typically, a high hydrogen bond acceptor (HBA) ability of the solvent system

is required for the solubilization of lignin, and Cyrene has a relatively high HBA capacity (0.61)[340] and comparable with that of GVL (0.60).[306] However, with a mixture 50 % Cyrene and 50 % H_2O, the RED reaches values slightly higher than 1.0,[346] indicating that the solvent system lost is effectiveness toward lignin solubilization. Although Cyrene forms a geminal diol when it reacts with water (**Figure 47 a**), establishing additional polarity and amplifying the hydrogen bonding capacity of the system,[342] thus improving, in principle, the lignin dissolution, molecular simulations show that using a Cyrene:H_2O 1:1 system results in a collapsed-like structure of lignin, while it adopts a more extended structure in Cyrene:H_2O 4:1 mixture (**Figure 47 b**). The collapsed-like structure inevitably leads to more intramolecular H-bonds within the lignin molecules, disfavoring lignin dissolution.[346] On the other hand, the extended-structure is more prone to form favorable interactions with the solvent system, facilitating the solubilization. Overall, taking into account the purity of lignin-fraction obtained with Cyrene:H_2O mixture and the above considerations, the solvent system is not selective toward the lignin but it extracts also a considerable amount of carbohydrates, which can be mainly related to the hemicellulose still connected with lignin, but also to hydrolyzed neutral sugars such as xylose, glucose, galactose and arabinose.[347]

a)

b)

Cyrene:H_2O 1:1   Cyrene:H_2O 4:1
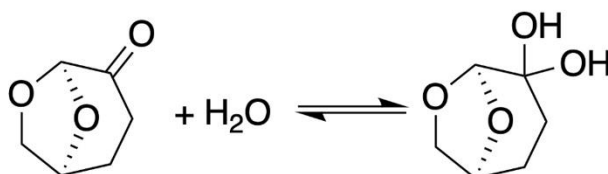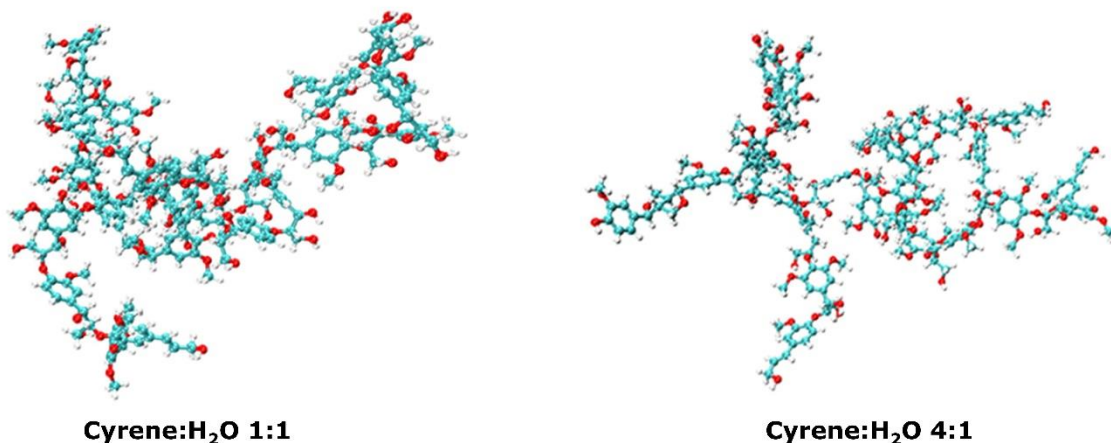
Figure 47 *(a) Formation of geminal diol from Cyrene and H_2O;[342] (b) Representations of lignin structure in Cyrene:H_2O mixture 1:1 and 4:1;* [346]

On the other hand, GVL:H_2O binary system exhibit an higher selectivity toward lignin solubilization respect to Cyrene:H_2O system due to the higher affinity of GVL for lignin. Although according to the Hansen relative energy difference RED the optimal solubility should be reached

at GVL 80 % and H_2O 20 %,[343] experimental results show that the maximum extent of delignification was obtained using water content in the range 35-50 %.[326,338] These results can be related to the higher H-bonding ability, which is maximum at GVL concentration between 50-60 %, providing more hydrogen bonds respect to pure GVL, but excessive water made the interaction between γ-valerolactone and water molecules stronger, hindering the formation of hydrogen bonds with lignin.[348,349]

FT-IR spectra of lignin-rich fractions extracted with Cyrene:H_2O and GVL:H_2O mixtures from holm-oak and willow are shown in **Figure 48 a,b**. The profiles of the spectra are similar each other when the same solvent is used, while is different when the mixtures is changed even if the raw material is the same: this trend confirms that the solvents influence the chemical structure of the lignin obtained. In all the spectra, the broad bands between 3550–3100 cm^{-1} are attributed to the O-H stretching of phenolic and alcoholic groups.[227] The peaks between 2940-2935 cm^{-1} and 2896-2840 cm^{-1} are attributed to C-H stretching in -CH_2- and -CH_3, respectively. The bands with two ticks at around 1730 cm^{-1} can be assigned to the C=O stretching of the unconjugated carbonyl group[336] and also to the residual acetyl group of hemicellulose:[341] this band is particularly pronounced for Cyrene extracted lignin-rich fractions, which can be explained by the presence of hemicellulose impurities into the samples. In the region of aromatic backbone vibrations (~ 1600-1250 cm^{-1}), different peaks with different intensities are present. Syringyl units (S) of lignin show typical bands at 1600 cm^{-1}, 1326-1324 cm^{-1} and 1125 cm^{-1}, which are assigned to the aromatic skeletal vibrations (S > G), S ring breathing and aromatic C-H in plane deformation of S units, respectively. On the other hand, guaiacyl units (G) of lignin exhibit the above-mentioned vibrations with bands at 1511 cm^{-1}, 1257 cm^{-1} and 1031 cm^{-1}, respectively.[337] The bands at approximatively 1210 cm^{-1} are attributed to the C-O stretching of characteristic aryl and alkyl ether linkages of lignin.
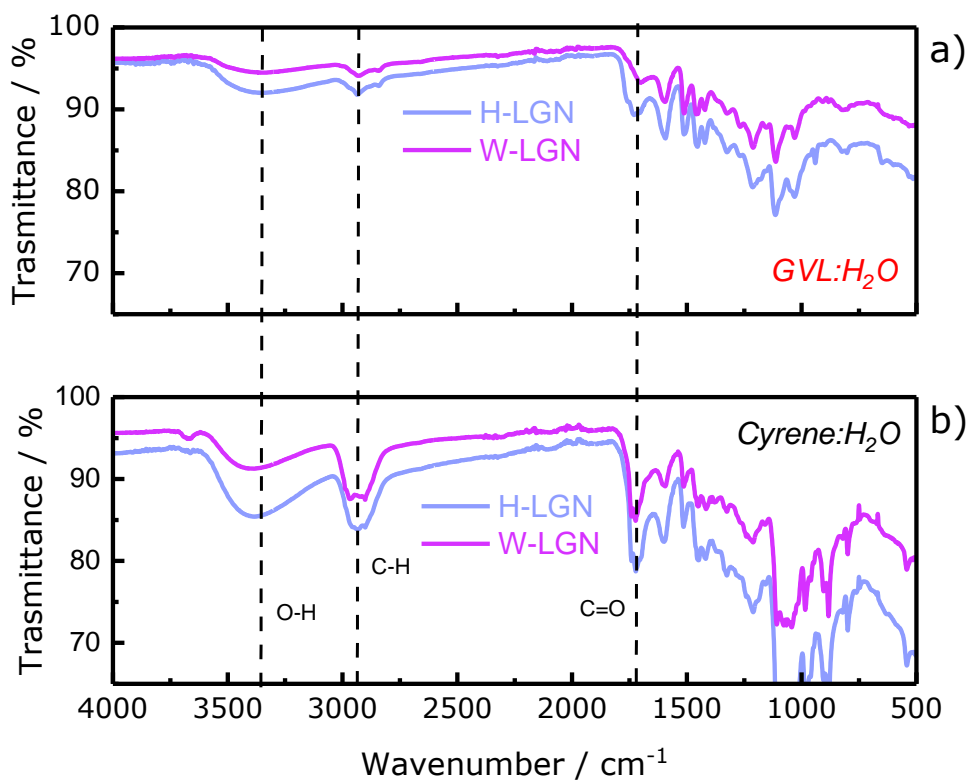
Figure 48 *FT-IR spectra of Holm-Oak derived lignin-rich fractions extracted with (a) GVL:H₂O and (b) Cyrene:H₂O mixtures;*

Table 17 *Assignment of FTIR peaks for lignin-rich fractions extracted from Holm-Oak and Willow*

Assignment	Vibration	Wavenumber / cm^{-1}
Phenolic + alcoholic OH	O-H stretching	3550-3100
CH$_2$ + CH$_3$	C-H stretching	2940-2935/2896-2840
Unconjugated + Acetyl Carbonyls	C=O stretching	1730
Aromatic backbone vibrations (S > G)	C-C stretching	1600
Aromatic backbone vibrations (G > S)	C-C stretching	1511
S ring breathing	C-C breathing	1326-1324
G ring breathing	C-C breathing	1257
Aryl + alkyl ether bonds	C-O stretching	1210
Aromatic in plane deformation (S)	In plane C-H deformation	1125
Aromatic in plane deformation (G)	In plane C-H deformation	1031

The thermal behaviors of the isolated lignin-rich fractions were characterized using thermogravimetric analysis (**Figure 49 a,b**). Generally, lignin has an high thermal stability and decompose slowly under the whole temperature range from ambient to 800 °C, leaving a considerable amount of solid residue.[350] Nonetheless, in thermal decomposition behavior of isolated lignin-rich fractions, different stages of degradation can be distinguished. At the first stage (around 100 °C), the weight losses were attributed to the moisture retained in the samples.[341] The next stage, which occurred in the temperature range 180-300 °C, can be mainly attributed to the degradation of carbohydrates components in the lignin samples, which converted to volatile gases such as CO, CO_2, and CH_4.[351] This stage leads to weight losses comparable between GVL and Cyrene extracted lignin-rich fractions, both in the range 12-17 % wt. The main weight losses occurred between 300-450 °C, where the fragmentation of inter-unit linkages release monomers and low-molecular weight derivatives of phenol into the vapor phase.[351,352] As the temperature was further increased (over 450 °C), the decomposition and condensation of aromatic rings occurred leading to the formation of char, which gives a solid residues, are all above 32 %.[341,351]
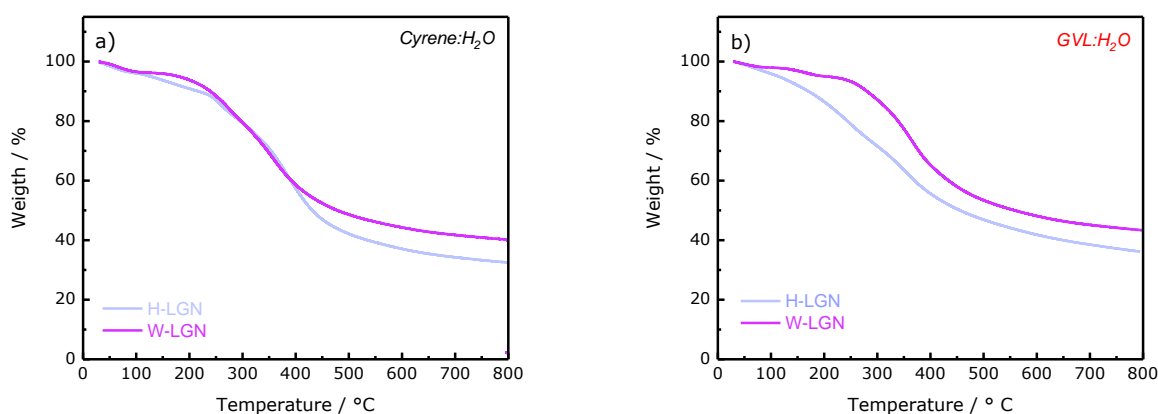
Figure 49 TGA of H-LGN and W-LGN extracted with (a) Cyrene:H_2O and (b) GVL:H_2O;

3.2.4 Electrochemical Characterization

3.2.4.1 Half-Cell Characterizations

- *Hard Carbon*

Cyclic Voltammetries (CVs) during the initial three cycles were performed on holm-oak and willow derived Hard Carbon (LHC and SHC) in order to assess the topotactical reaction of Na^+ in the synthetized materials. The analysis were perfomed at a scanning rate of 0.10 mV s^{-1} in the potential range 0.01 < E_{we} < 2.00 V using metallic sodium as reference and counter electrodes. As shown in **Figure 50 a,b**, both Hard Carbons show the same CV shape. During the first

cathodic scan, an irreversible broad peak (A), which extends from approximatively 1.00 V to 0.20 V, can be assigned mainly to the decomposition of the electrolyte and the formation of the SEI, which is the main responsible of low ICE.[264] In the following scans, the contribution from irreversible SEI formation disappears, leaving a reversible broad peak (B) due to the "high-potential" ($E_{we} > 0.10$ V) Na storage associated to the adsorption of sodium ions into surface active sites,[123] and a sharp peak (C) centered at around 0.02 V, which is mainly attributed to the Na$^+$ intercalation into hard carbon graphene layers, although the contribution of pseudocapacitive processes related to the internal pores filling by Na$^+$ ions must be taken into account especially at potentials approaching the cut-off of 0.01 mV.[353,354] During the anodic scans, the oxidation peaks (C') and the broad feature (B') indicate the reversibility of the electrochemical processes. After the 1st cycle, the CV curves are overlapped, indicating a reversible electrochemical reaction between active materials and sodium ions.
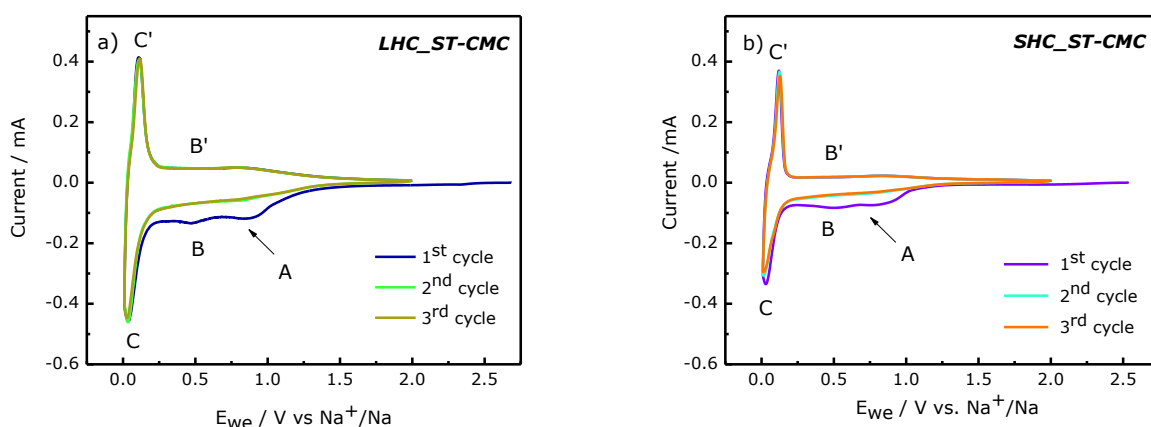
Figure 50 *Cyclic Voltammetries upon the first three cycles of (a) LHC and (b) SHC-based electrodes prepared with ST-CMC binder and cycled with 1M NaClO$_4$ in EC:PC 1:1 (v/v) as electrolyte.*

To compare the cycling performance of Holm-oak and Willow derived-Hard Carbon with ST-CMC as binder, charge and discharge cycling were performed in the voltage range 0.01 < E_{we} < 2.00 V applying a current of 300 mA g^{-1}. A constant voltage step was applied during sodiation until the current drops to 30 mA g^{-1} in order to ensure that the electrodes reach the maximum state of charge. As displayed in **Figure 51 a,b** and summarized in **Table 18**, hard carbons show comparable initial coulombic efficiency as a consequence of the similar surface area of the Hard Carbons accessible to the electrolyte, leading to a similar extension of SEI formation and irreversible capacity loss at first cycle.[247] Anyway, the complete formations of the SEI require several cycles in both cells until coulombic efficiencies of 99 % are reached, then leaving flat and stable profiles of charge and discharge specific capacities over cycling. The capacity retentions after 100 cycles are equal to 91.1 % and 85.0 % for LHC and SHC, respectively. However, both cells underwent to cycling instability probably as a consequence of partial

solubilization and reformation of the SEI, which causes further consumption of the electrolyte.[238] Overall, the performances of Hard Carbons are comparable, although holm-oak derived hard carbon exhibits the best performance in terms of ICE, specific capacity and capacity retention after 100 cycles.
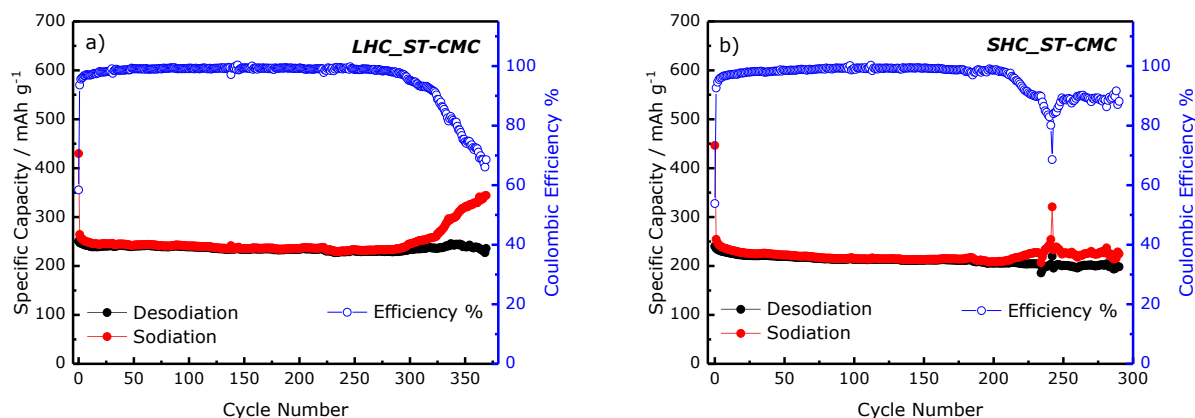
Figure 51 *Charge and discharge performances of (a) LHC and (b) SHC electrodes in Na half-cells cycled at 300 mA g^{-1} between 0.01 < E$_{we}$ < 2.00 V using commercial CMC as binder and 1M NaClO$_4$ in EC:PC 1:1 (v/v) as electrolyte.*

Table 18 *First-cycle irreversible capacity, initial coulombic efficiency (ICE), second-cycle reversible discharge capacity and capacity retention after 100 cycles of LHC and SHC-based SIB electrodes with commercial CMC as binder.*

Electrode	Discharge Capacity 1st cycle (mAhg^{-1})	ICE (%)	Discharge Capacity 2nd cycle (mAhg^{-1})	Capacity Retention after 100 cycles (%)
LHC_ST-CMC	429.85	58.40	264.44	91.11
SHC_ST-CMC	446.50	53.82	254.43	84.97

After that, the two Hard Carbons were tested using synthesized CMCs as binders, as shown in **Figure 52**. Compared to the commercial CMC, the ICEs % were decreased probably as a consequence of the higher DS of synthesized CMCs, which corresponds to a higher amount of carboxylic groups COO$^-$ in the binder and in the electrode surfaces: the oxygen-containing functional groups are considered to have a catalytic activity toward the decomposition of electrolyte, thus leading to the formation of a thicker SEI layer.[248] Although the capacity retentions after 100 cycles are quite high (**Table 19**), these values might be misleading since the fluctuations of charge and discharge specific capacity profiles, especially in LHC_H-CMC electrode, reflect the instability and the dynamic nature of the SEI layers formed in both cells,

which leads to coulombic efficiencies never exceeding 98.9 % in both cells during the whole cycling and inevitably consuming the electrolyte.
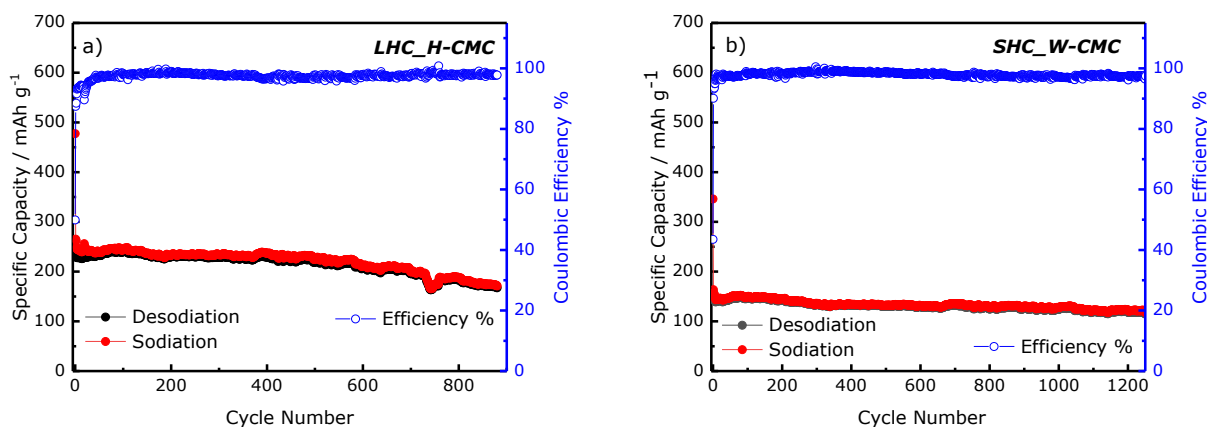
Figure 52 Charge and discharge performances of (a) LHC and (b) SHC electrodes in Na half-cells cycled at 300 mA g^{-1} between 0.01 and 2.00 V using synthesized CMCs as binders and 1M NaClO$_4$ in EC:PC 1:1 (v/v) as electrolyte.

Table 19 First-cycle irreversible capacity, initial coulombic efficiency (ICE), second-cycle reversible discharge capacity and capacity retention after 100 cycles of LHC and SHC-based SIB electrodes with synthesized CMCs as binders.

Electrode	Discharge Capacity 1st cycle (mAhg^{-1})	ICE (%)	Discharge Capacity 2nd cycle (mAhg^{-1})	Capacity Retention after 100 cycles (%)
LHC_H-CMC	477.29	49.92	265.30	92.30
SHC_W-CMC	346.05	43.52	163.65	91.55

In order to evaluate the feasibility of lignin-rich fractions extracted with Cyrene and GVL as binder materials, galvanostatic cycling were performed using LHC and SHC as active materials and the lignin-rich fractions as binder. As displayed in **Figure 53 a,b** and **Table 20**, the electrodes made with Cyrene show an improvement of ICE % compared to those made with standard and synthesized CMC as well as lignin extracted with GVL as binders. Additionally, the coulombic efficiencies % of both cells overcome 99.0 % in around 10 cycles, indicating the formation of a stable solid electrolyte interface. One explanation of these results can be found in the hydrogen bonding ability of the binder, which benefits from the polar functional groups of both lignin and carbohydrates residues, which in turn hinder the ability of oxygen-containing functional groups of HCs to promote the decomposition of the electrolyte, by establishing hydrogen bonds with them. In this way, the irreversible decomposition of the electrolyte may be reduced and a thin and stable SEI is formed.[240] Moreover, electrodes made with lignin extracted

125

with Cyrene show good specific capacities and impressively long cycling stability: LHC electrode retains the 76.0 % of capacity after 1000 cycles and 66.6 % after 3000 cycles, while SHC electrode still has 86.6 % capacity after 1000 cycles. The capacity fades around 1000 cycles, present in both cells, are due to an anomaly in the electrochemical workstation. In fact, the cells restore their specific capacities in few cycles.

On the other hand, electrodes made with lignin extracted with γ-valerolactone as binder exhibit coulombic efficiencies that fluctuate around 98 %, indicating the instability of the SEI layers which underwent partial solubilization and reformation. Moreover, both Hard Carbons experiment a considerable decrease in the specific capacities, which decrease from around 261 to 202 mAh g^{-1} for LHC and from 212 mAh g^{-1} to 141 mAh g^{-1} for SHC.
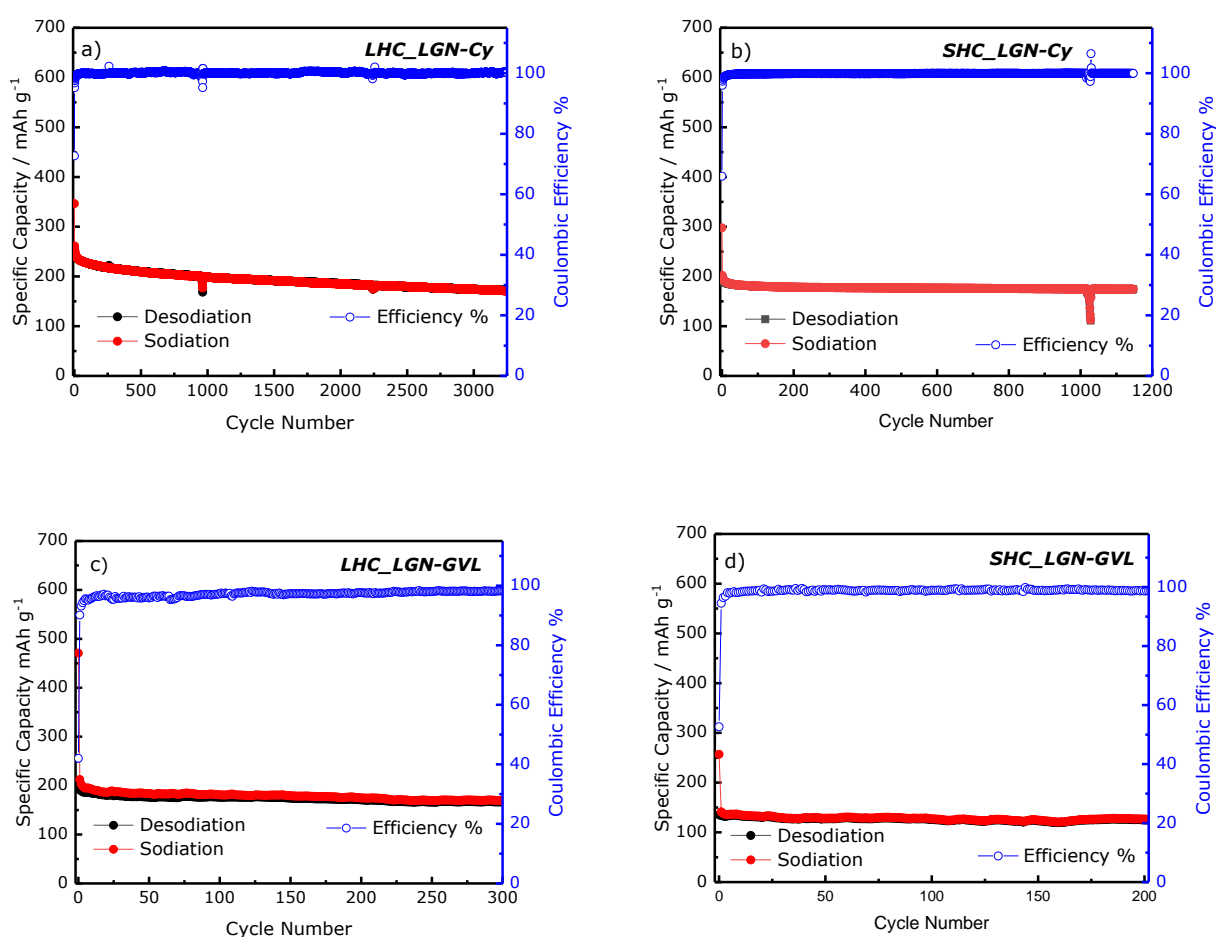
Figure 53 *Charge and discharge performances of Hard Carbon cycled at 300 mA g^{-1} between 0.01 < E_{we} < 2.0 V using lignin as binders and 1M NaClO₄ in EC:PC 1:1 (v/v) as electrolyte.*

Table 20 *First-cycle irreversible capacity, initial coulombic efficiency (ICE), second-cycle reversible discharge capacity and capacity retention after 100 cycles of LHC and SHC-based SIB electrodes with extracted lignin as binders.*

Electrode	Discharge Capacity 1st cycle (mAhg^{-1})	ICE (%)	Discharge Capacity 2nd cycle (mAhg^{-1})	Capacity Retention after 100 cycles (%)
LHC_LGN-Cy	346.48	72.70	261.32	86.70
SHC_LGN-Cy	297.71	65.97	202.10	89.27
LHC_LGN-GVL	470.89	42.00	212.52	85.21
SHC_LGN-GVL	256.87	52.66	141.26	90.05

To fully assess the electrochemical performances of holm-oak and willow derived hard carbons with the different bio-based binders, rate capability tests were performed at selected cycling rates in the range C/10 to 5C, as shown in **Figure 54 a,b**. Overall, the holm-oak and willow derived Hard Carbons exhibit a promising rate capability with low-capacity fades when the currents are boosted. In details, holm-oak derived HC electrodes produced with Cyrene- and GVL- extracted lignin as binder deliver capacities higher than 250 mAh g^{-1} at C/5 and higher than 195 mAh g^{-1} at 5C, both comparable with those obtained with commercial CMC. Afterwards, the capability to recover pristine performances was investigated by cycling the electrode at 1C up to 50 overall cycles. The cells yield a specific capacity above 220 mAhg^{-1} after 50 cycles, suggesting reversibility of the electrochemical processes. On the other hand, willow derived HC electrodes produced with Cyrene extracted lignin as binder shows promising rate capability with capacities around 235 mAh g^{-1} at C/5 and around 185 mAh g^{-1} at 5C, while LGN-GVL based electrode experiments the same capacity decrease as that observed during long cycling with the same binder (**Figure 53 d**).
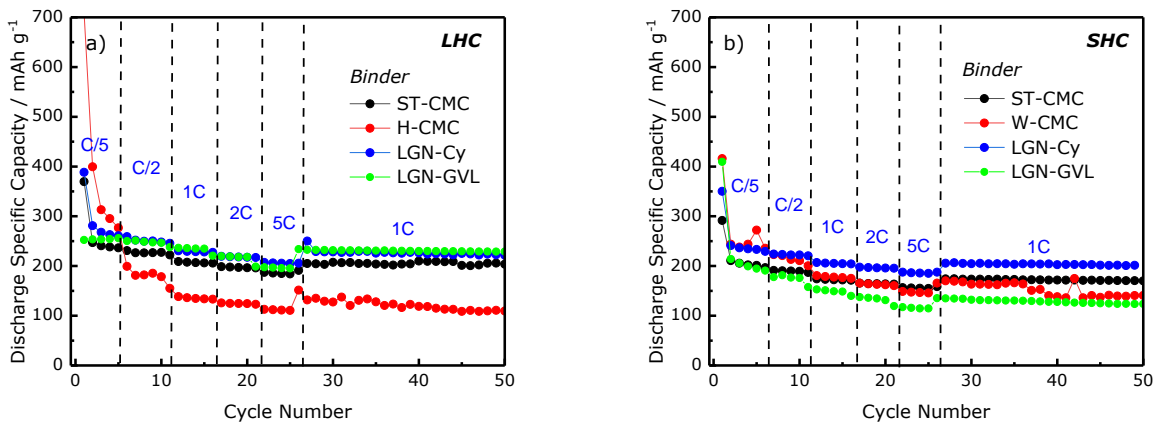
Figure 54 *Rate capability of (a) LHC and (b) SHC electrodes prepared with different binders and 1M NaClO₄ in EC:PC 1:1 (v/v) as electrolyte.*

To better investigate the electrode/electrolyte interface of the two Hard Carbons electrodes made with Cyrene extracted lignins as binder, as well the kinetics of the charge/discharge processes, potentiostatic impedance spectroscopy measurements were performed every 10th cycle at E_{we} = 0.5 V on Holm-Oak and Willow derived Hard Carbon electrodes. The Nyquist plots are shown in **Figure 55 a,b**. All the impedance spectra present similar features: (i) a semicircle in the high-frequency region related to sodium migration through SEI film, which is partially overlapped by (ii) a semicircle in the middle-frequency region correlated with the interfacial charge-transfer process;[285] (iii) a straight line in the low-frequency region corresponding to the Na⁺ ion diffusion in the bulk of electrode material.[278] EIS data were fitted through an equivalent circuit model, noted as $R_{el}(R_{SEI}C_{SEI})(R_{ct}C_{dl})WC_i$ in the notation of Boukamp.[265] The calculated values of R_{el}, R_{SEI} and R_{ct} are shown in **Figure 55 c,d**, while the respective numerical values of resistances, capacitance and phase angles are reported in **Table 21** and **22**. The R_{el}, R_{SEI} and R_{ct} are the resistances associated with electrolyte, SEI passivation layer and charge-transfer process, while C_{SEI}, C_{ct} and C_i are the SEI film capacity, electric double layer capacity and differential intercalation capacity, respectively. W is the Warburg element, describing Na⁺ diffusion.[265] For the fitting procedure, the pure capacitive elements were replaced by constant phase elements Q to take into account the non-ideal capacitive behavior given by the electrode surface roughness and inhomogeneity.[286] Apart for the electrolyte resistance (R_{el}), which is stable and negligible throughout the cycling for both cells, the holm-oak derived Hard Carbon electrodes show a constant SEI resistance indicating that a stable electrode/electrolyte interface is formed, while the R_{SEI} of willow-derived Hard Carbon electrode is very low but progressively increases during cycling. On the other hand, the charge-transfer resistance R_{ct} is considerably lower for LHC respect to SHC, suggesting a faster reaction kinetics, which reflects in the the good rate capability and cycling stability obtained especially for LHC electrodes. Nevertheless, the

magnitude of the impedance spectra of the two Hard Carbons are almost similar with almost constant values of R_{SEI} and R_{ct}. Overall, these results also confirm the ability of the lignin binder to provide good adhesion forming strong interactions with the hard carbon materials, which in turn reflects both in the interfacial stability and in the constant interparticle charge transfer resistance upon cycling.
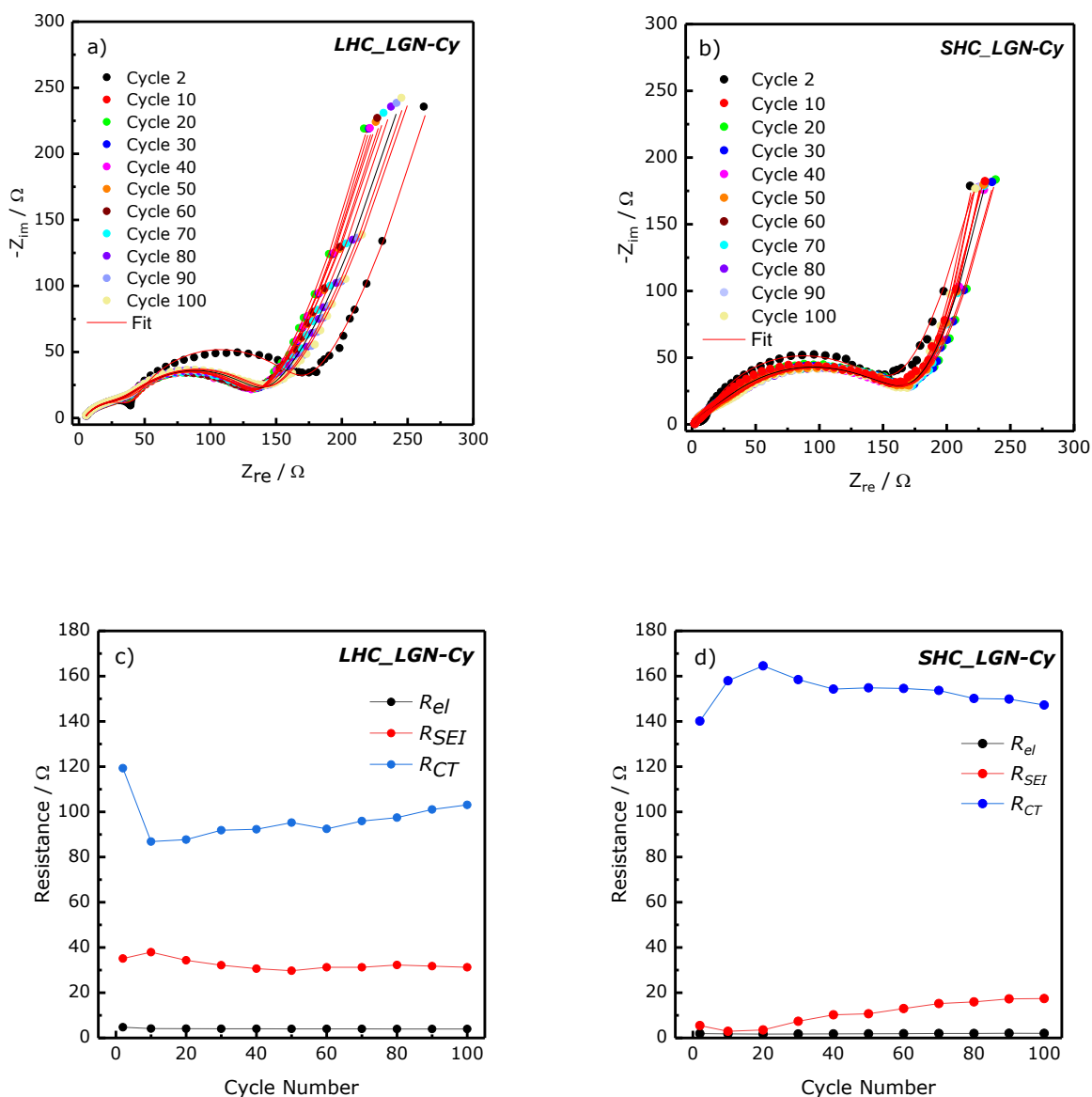
Figure 55 *Nyquist plot of (a) LHC and (b) SHC electrodes prepared with Cyrene extracted lignin as binder and 1M NaClO₄ in EC:PC 1:1 (v/v) as electrolyte, acquired every 10th cycle, E = 0.5 V, 10 mHz < f < 100 kHz; (b) Values of R_{el}, R_{SEI} and R_{ct} upon cycling, as obtained by EIS data analysis; Equivalent circuit used to simulate the data.*

Table 21 SEI and charge transfer resistances, capacitances and α values as a function of cycle number for LHC-based SIB electrode prepared with LGN-Cy binder and 1M NaClO$_4$ EC:PC 1:1 (v/v) as electrolyte.

	LHC_LGN-Cy					
Cycle	R$_{SEI}$ / Ω	Capacitance / F	α	R$_{CT}$ / Ω	Capacitance / F	α
2	35.14	5.17×10^{-5}	0.69	119.28	4.55×10^{-4}	0.84
10	37.95	1.30×10^{-4}	0.61	86.85	4.09×10^{-4}	0.79
20	34.33	1.22×10^{-4}	0.61	87.70	3.74×10^{-4}	0.77
30	32.18	1.20×10^{-4}	0.62	91.87	3.72×10^{-4}	0.75
40	30.63	1.15×10^{-4}	0.62	92.26	3.67×10^{-4}	0.75
50	29.73	1.09×10^{-4}	0.62	95.23	3.80×10^{-4}	0.73
60	31.27	1.13×10^{-4}	0.62	92.47	3.70×10^{-4}	0.74
70	31.26	1.13×10^{-4}	0.62	95.93	3.75×10^{-4}	0.73
80	32.25	1.22×10^{-4}	0.62	97.43	3.64×10^{-4}	0.73
90	31.75	1.15×10^{-4}	0.62	101.02	3.57×10^{-4}	0.72
100	31.24	1.11×10^{-4}	0.62	103.08	3.59×10^{-4}	0.72

Table 22 SEI and charge transfer resistances, capacitances and α values as a function of cycle number for SHC-based SIB electrode prepared with LGN-Cy binder and 1M NaClO$_4$ EC:PC 1:1 (v/v) as electrolyte.

	SHC_LGN-Cy					
Cycle	R$_{SEI}$ / Ω	Capacitance / F	α	R$_{CT}$ / Ω	Capacitance / F	α
2	5.46	4.88×10^{-5}	0.77	140.13	8.06×10^{-4}	0.75
10	2.96	3.85×10^{-5}	0.89	157.96	6.00×10^{-4}	0.62
20	3.56	3.35×10^{-5}	0.93	164.54	5.17×10^{-4}	0.60
30	7.36	8.96×10^{-5}	0.82	158.46	5.15×10^{-4}	0.61
40	10.22	1.25×10^{-4}	0.77	154.30	5.68×10^{-4}	0.61
50	10.67	1.01×10^{-4}	0.78	154.82	5.99×10^{-4}	0.61
60	13.02	1.15×10^{-4}	0.76	154.56	6.13×10^{-4}	0.61
70	15.21	1.13×10^{-4}	0.75	153.69	6.25×10^{-4}	0.61
80	15.93	9.75×10^{-5}	0.75	150.14	6.36×10^{-4}	0.62
90	17.26	1.05×10^{-4}	0.74	149.87	6.34×10^{-4}	0.62
100	17.41	9.68×10^{-5}	0.75	140.13	8.06×10^{-4}	0.75

- **Na₃(VO)₂(PO₄)₂F**

Na$_3$(VO)$_2$(PO$_4$)$_2$F cathode material was characterized by CV for the first three cycles at a scanning rate of 0.10 mV s^{-1} in the potential range 3.00 < E$_{we}$ < 4.30 V vs Na$^+$/Na. As shown in **Figure 56 a**, NVOPF exhibit two couples of redox peaks A/A' and B/B' at 3.60-3.70 V and 4.00 V, respectively, which corresponds to the two plateaus in the galvanostatic profiles (**Figure 56 b**). The shapes of the CV curves are similar to those reported by Chao and co-workers.[355] The reaction mechanism of this type of cathode has been studied by Sharma and co-workers[356], evidencing an asymmetric behavior in cathode structural evolution during charge and discharge. During charge, a two-phase transition from a Na-rich phase P to a Na-poor phase P'' through an intermediate phase P' has been attributed to the lower potential plateau (A), while a single-phase region characterized by sodium extraction with a solid-solution reaction has been assigned to the higher potential plateau (B).[357] Close to the cut-off potential, another two-phase reaction is observed before reaching the final Na-poor phase P''', producing a small bump in the cyclic voltammetry curves. During discharge, the reaction mechanism evolution is distinctly different, with the phase P''' undergoing solid-solution reaction to insert sodium into its structure in the higher potential plateau (B'), while a two- phase reaction occurs during the transition from the higher to lower potential plateaus and finally a solid solution followed by a two-phase reaction for the lower potential plateau (A') to obtain the Na-rich phase P. Despite the asymmetry in the reaction mechanism between sodiation and desodiation of NVOPF, the structural motif is maintained throughout the whole cycling and the transition reactions lead to phases with varying sodium content and/or distribution within the same structural framework.[356]

Regarding the electrochemical performances, galvanostatic cycling at 130 mA g^{-1} within 3.00 < E$_{we}$ < 4.30 V was performed in order to evaluate the charge/discharge performance over 100 cycles and the cycling stability of NVOPF. As shown in **Figure 56 c**, a small irreversibility is observed during the first desodiation, leaving a coulombic efficiency of around 77 %, indicating that the electrode requires activation cycles. After the first cycle, the electrode delivers a specific capacity of 87 mAh g^{-1} at second sodiation, however, a progressive capacity fade and a persistent gap between desodiation and sodiation specific capacities lead to poor capacity retention (around 80 % after 100 cycles) and low coulombic efficiency (around 97 %), respectively. This situation can be ascribed to side reactions involving the irreversible extraction of Na$^+$ from NVOPF active material as well as electrolyte decomposition.[358] Also the rate capability (**Figure 56 d**) of NVOPF was evaluated in order to assess low- and high-current tolerance of the cathode material from 30 mA g^{-1} to 300 mA g^{-1}. The specific capacities of NVOPF during sodiation ranges between 91 mAh g^{-1} at 30 mA g^{-1} and 78 mAh g^{-1} at 300 mA g^{-1}. Also in this case a gap between specific capacities during sodiation and desodiation is clearly visible, which reflects in low coulombic efficiency during cycling, however, when the current is boosted to 300 mA g^{-1}, this gap is considerably reduced. The low coulombic efficiency at low C-rate typical of vanadium

fluorophosphate has not been fully understood, although the optimization of the electrolyte formulation is reported to be an effective strategy to solve this issue.[359]

Figure 56 *Electrochemical performances of NVOPF_PVDF electrode in Na half-cells cycled between 3.00 < E_{we} < 4.30 V using 1M NaPF$_6$ in EC:PC 1:1 (v/v) as electrolyte: (a) Cyclic Voltammetry; (b) Galvantostatic profile; (c) Cycling at 130 mA g^{-1}; (d) Rate capability.*

In order to study the kinetics of NVOPF, EIS measurements were performed every 10th cycle at E_{we} = 3.82 V in the frequency range 100 mHz < f < 200 kHz. The Nyquist plots shown in **Figure 57 a** were composed of an intercept with the real axis in the high frequency region, a depressed semicircle in the medium-frequency to low-frequency region and a straight line in the low-frequency region. The obtained EIS spectra have been modeled using the equivalent circuit model shown in the inset of **Figure 57 b**. The intercept at high frequencies was modeled as a pure resistive element (R_{el}), representing the migration of Na$^+$ ions through the electrolyte solution. The semicircle at medium-to-low frequencies has been modeled as a resistive element (R_{ct}) in parallel with a capacitor element (C_{dl}), describing the charge transfer process with double layer formation onto the surface of the active material particles. Finally, the line at low frequency has been modeled with a Warburg impedance (W), describing the diffusion into the bulk-phase

132

of the material,[360] in series with a capacitor element (C_i) indicating the intercalation capacitance. The resulting equivalent circuit, written according to Boukamp's notation, is $R_{el}(R_{ct}C_{dl})WC_i$. For the fitting procedure, the pure capacitive elements were substituted by constant phase elements (P), in order to consider the non-ideal, capacitive behavior given by electrode inhomogeneity and surface roughness. The resistance values obtained are displayed in **Figure 57 b**. The electrolyte resistance R_{el} is low and stable throughout the whole cycling, while the charge transfer resistance R_{ct} progressively increases during cycling coherently with the capacity fading experimented during NVOPF electrodes cycling and rate capability tests.
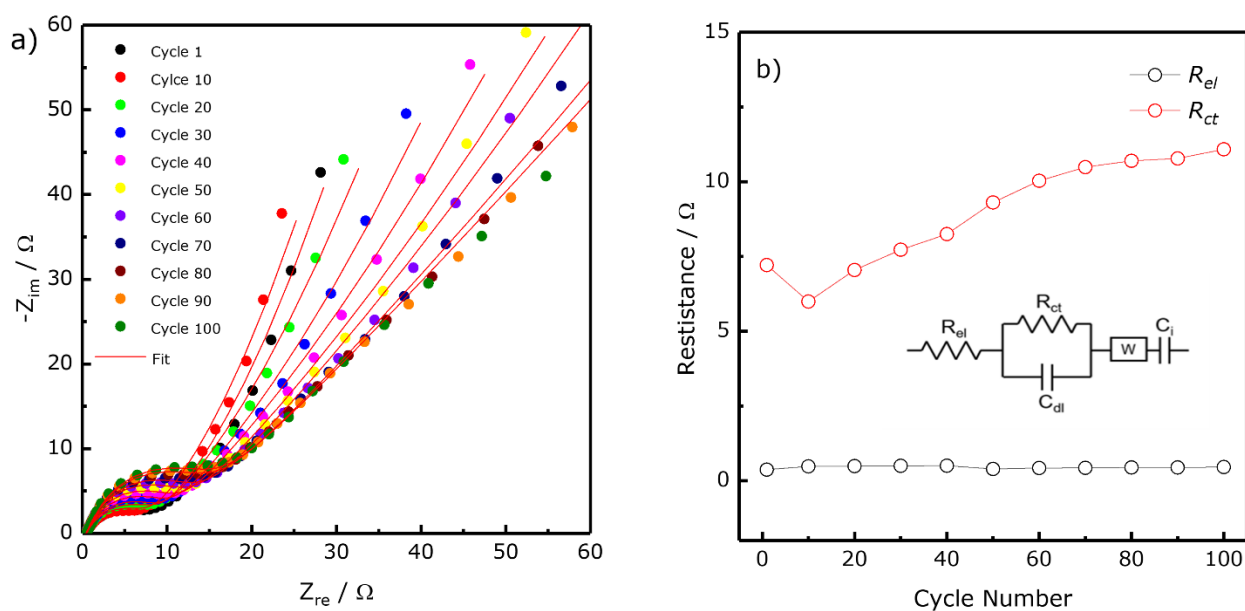
Figure 57 *(a) Nyquist plot of NVOPF-based SIB electrode prepared with PVDF binder and tested in Na half-cell using 1M NaPF$_6$ in EC:PC 1:1 (v/v) as electrolyte. Data acquisition performed every 10th cycle, E = 3.82 V, 100 mHz < f < 200 kHz; (b) Values of R$_{el}$ and R$_{ct}$ upon cycling, as obtained by EIS data analysis; Equivalent circuit used to simulate the data.*

Table 23 *SEI and charge transfer resistances, capacitances and α values as a function of cycle number for SHC-based SIB electrode prepared with LGN-Cy binder and 1M NaClO$_4$ EC:PC 1:1 (v/v) as electrolyte.*

Cycle	R$_{CT}$ / Ω	Capacitance / F	α
1	7.21	1.23 x 10^{-3}	0.77
10	5.99	1.49 x 10^{-3}	0.78
20	7.05	8.13 x 10^{-4}	0.83
30	7.72	5.67 x 10^{-4}	0.87
40	8.24	4.11 x 10^{-4}	0.91
50	9.31	3.64 x 10^{-4}	0.91
60	10.03	3.31 x 10^{-4}	0.91
70	10.49	2.97 x 10^{-4}	0.93
80	10.70	2.89 x 10^{-4}	0.93
90	10.78	2.68 x 10^{-4}	0.95
100	11.08	2.50 x 10^{-4}	0.95

Due to the good performance obtained by Cyrene-extracted lignin as binder material for Hard Carbon electrode, its binding ability was tested also with NVPOF cathode material during long cycling (**Figure 58 a**) and rate capability (**Figure 58 b**). Before making any kind of assumptions, it is worth mentioning that the mass loadings of the electrodes made with lignin as binder are very low compared to those made with PVDF (~ 0.4 mg cm^{-2} for lignin-based electrodes vs ~ 0.9 mg cm^{-2} for PVDF-based electrodes), hindering a fair comparison between the two binders. Unfortunately, it has not been possible to increase the mass loading of lignin-based electrode due to adhesion problems which can be ascribed to the low molecular weight of Cyrene-extracted lignin. Nonetheless, the cycling stability of the cathode is impressively improved as well as the coulombic efficiency %: after few cycles of activation the NVOPF reaches the coulombic efficiency of 99 % with an excellent capacity retention of 95.8 % after 100 cycles and 88.5 % after 1000 cycles. The specific capacity of the cell is slightly lower respect to that observed for PVDF-based NVOPF electrode, suggesting a possible minor dissolution of the low-molecular weight fraction of the Cyrene-extracted lignin in the electrolyte solvents, which in turn leads to loss of the active material. The results obtained during galvanostatic cycling are confirmed by the rate capability test, where the low coulombic efficiency % experimented in PVDF-based NVOPF electrode is improved also at low current rates, as well as the cycling stability. These results suggest that

the binder plays a crucial role in the stabilization of electrode/electrolyte interface also at cathode side.
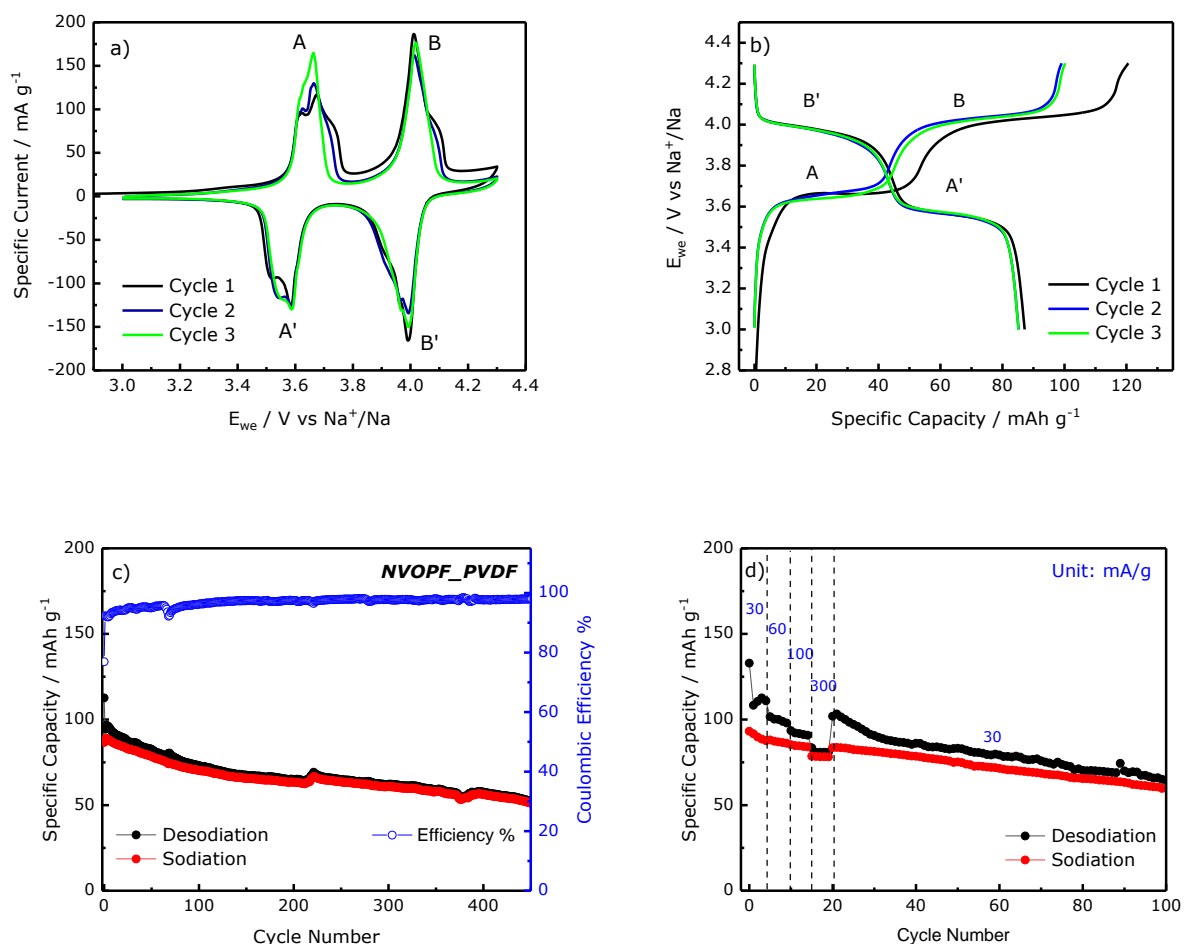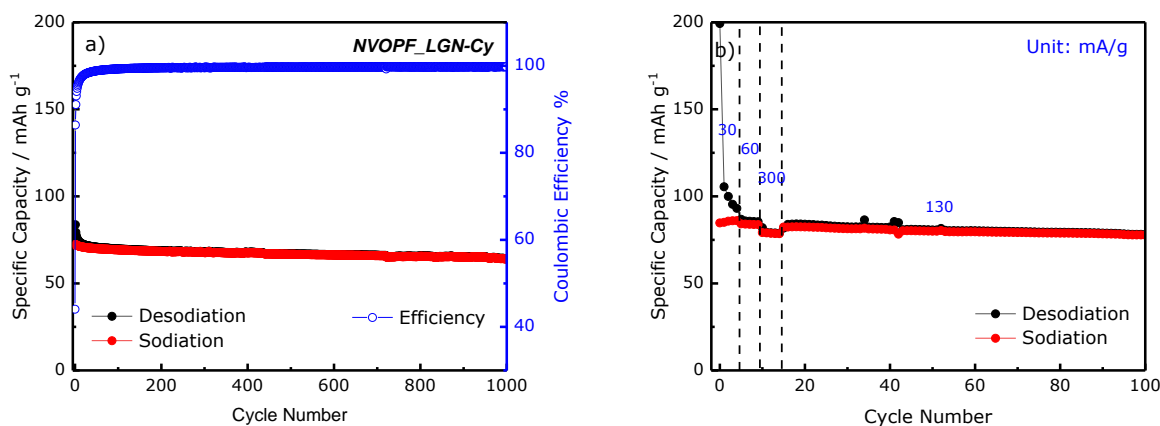

Figure 58 *Electrochemical performances of NVOPF_LGN-Cy electrode in Na half-cells cycled between 3.00 < E_{we} < 4.3 V using 1M $NaPF_6$ in EC:PC 1:1 (v/v) as electrolyte: (a) Cycling at 130 mA g^{-1} and (b) Rate capability.*

3.2.4.2 LHC//Na₃(VO)₂(PO₄)₂F Full-Cell Characterizations

In order to fully address the use of forestry-waste and demonstrate its practical feasibility in sodium-ion batteries, full-cells using holm oak-derived Hard Carbon as anode material and vanadium fluorophosphate $Na_3(VO)_2(PO4)_2F$ as cathode material were assembled. Prior to the full-cell assembly, the LHC anodes were electrochemically passivated in half-cells and then brought to two different voltages: 2 V vs Na^+/Na, where the anode can be considered fully desodiated (State of Charge 0 %), and 0.01 V vs Na^+/Na, where the anode can be considered fully sodiated (State of Charge 100 %). After the pretreatment, in order to balance the charge, the full-cells were assembled using untreated cathode ($SoC_{cathode}$ 100 %) for anode at SoC_{anode} 0 % and desodiated cathode ($SoC_{cathode}$ 0 %) in half-cell configuration for fully sodiated anode (SoC_{anode} 100 %). To better clarify the initial state of the electrodes, the cell set-ups 1 and 2 are schematized in **Table 24** and **Table 25**, while the cyclic voltammetries and galvanostatic charge and discharge are shown in **Figure 59 a,b** for Cell 1 and **60 a,b** for Cell 2, respectively. Firstly, the CV measurements were performed to compare the electrochemical behaviour of LHC//NVOPF systems. At the open circuit, the LHC//NVOPF_1 in **Figure 59 a** is completely discharged (SoC_{cell} 0 %), thus the open circuit voltage (OCV) of the cell is E_{cell} = 0.9 V. During the first oxidation, three redox peaks can be observed which disappear during the reduction leaving a broad feature centered at around E_{cell} = 3.47 V. Although a clear explanation of this behavior is not given, similar results were reported by Pi and co-workers using Hard Carbon and sodium vanadium fluorophosphate $Na_3V_2(PO_4)_2F_3$ as cathode: they found that the resistance of the charge transfer strictly depends on the cut-off voltage (i.e. State of Charge) at which the presodiation of the

anode is concluded. In other words, the charge transfer resistance decreases as the state of charge of pretreated anode increases.[361] On the other hand, at the open circuit, the LHC//NVOPF_2 in **Figure 60 a** exhibit an open circuit voltage of around E_{cell} = 3.60 V. The CV curves shows redox peaks similar to those of NVOPF half-cell indicating the goodness of the system. Moreover, the CV curves of the second and third cycles are overlapped, suggesting a high reversibility of the full-cell charge and discharge processes. After the CVs, the same LHC//NVOPF cells were cycled in the potential range 1.00 V < E_{cell} < 4.30 V applying a current of 30 mA g^{-1}. As shown in **Figures 59 b** and **60 b**, the system LHC//NVOPF_2 exhibit a superior specific capacity (around 88 mAh g^{-1} at the second charge) and coulombic efficiency, which overcomes 97.8 % after some cycles due to the solid electrolyte interPHASE stabilization. On the other hand, the LHC//NVOPF_1 system delivers an initial specific capacity of around 56 mAh g^{-1} which initially decreases and then tends to progressively stabilize around that value. The coulombic efficiency of the cell is always lower than 97.0 % indicating a poorer reversibility of the charge/discharge process. Overall, it can be concluded that the state of charge of the pretreated hard carbon can determine the electrochemical performance of the full cells. Therefore, all the subsequent experiments were carried out using the cell set-up with presodiated anode at SoC$_{anode}$ 100 % and desodiated cathode at SoC$_{cathode}$ 0 %.

Table 24 *Schematization of LHC//NVOPF_1 full-cell properties and initial state.*

Cell Set-Up 1	Active Material	Binder	Pre-treatment	Initial State
Anode	LHC	ST-CMC	Presodiation	Desodiated (SoC 0 %)
Cathode	$Na_3(VO)_2(PO_4)_2F$	PVDF	Untreated	Sodiated (SoC 100 %)
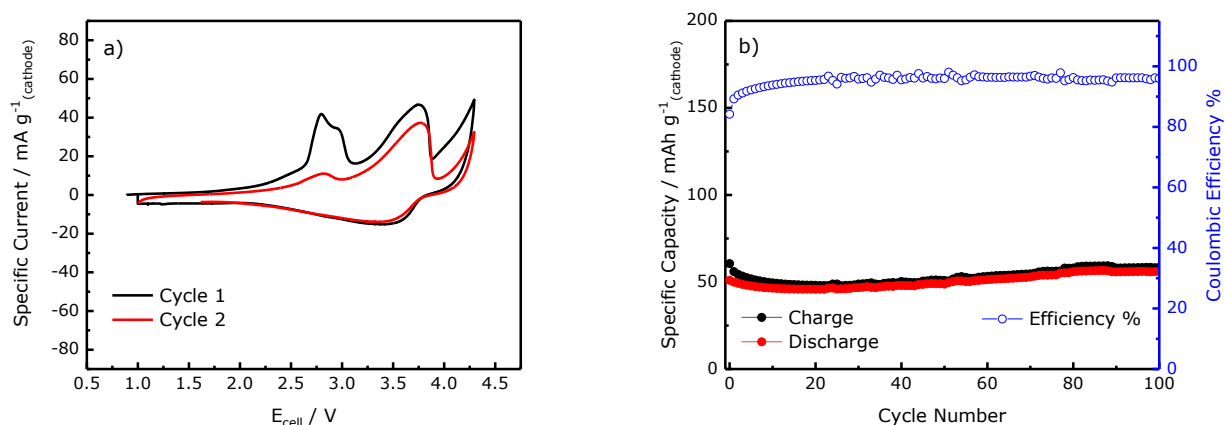
Figure 59 *Electrochemical performances of LHC//NVOPF_1 full-cell in the voltage range 1.00 < E_{cell} < 4.30 V using 1M NaPF$_6$ in EC:PC 1:1 (v/v) as electrolyte: (a) Cyclic Voltammetry and (b) Cycling at 30 mA g^{-1}. Specific capacity and current are normalized to the cathode active mass.*

136

Cell Set-Up 2	Active Material	Binder	Pre-treatment	Initial State
Anode	LHC	ST-CMC	Presodiation	Sodiated (SoC 100 %)
Cathode	$Na_3(VO)_2(PO_4)_2F$	PVDF	Untreated	Desodiated (SoC 0 %)
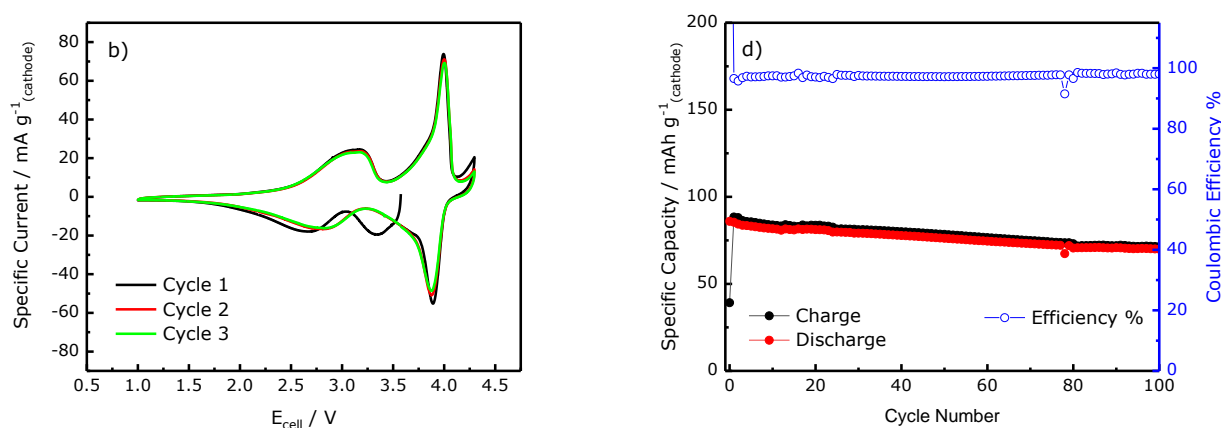
Figure 60 *Electrochemical performances of LHC//NVOPF_2 full-cell in the voltage range 1.00 < E_{cell} < 4.30 V using 1M NaPF$_6$ in EC:PC 1:1 (v/v) as electrolyte: (a) Cyclic Voltammetry and (b) Cycling at 30 mA g^{-1}. Specific capacity and current are normalized to the cathode active mass.*

To fully evaluate the cycling performances of the LHC//NVOPF full-cell, different cells were assembled and cycled at different current rates as shown in **Figure 61 a,b,c,d**. Cells cycled at lower current rates (i.e. 30 mA g^{-1} and 130 mA g^{-1}) deliver initial specific capacities higher than 100 mAh g^{-1} although the cell cycled at 30 mA g^{-1} exhibit the typical low coulombic efficiency (~ 96-97 %) of vanadium fluorophosphate cathode already experimented in half-cell. This behavior disappears in the cell cycled at 130 mA g^{-1}, which has a coulombic efficiency higher than 99 %. The capacity retentions of the cells cycled at low-current rates are higher than 80 % for both cells, indicating a good reversibility of the sodium shuttling between anode and cathode. Regarding the cells cycled at 300 mA g^{-1} and 500 mA g^{-1}, the specific capacities at first charge considerably decrease to values around 60 mAh g^{-1} for both cells, suggesting that there is a considerable loss of cyclable sodium. Several aspects can contribute to these results, such as the wetness of the electrodes and the stabilization of the system. This situation can be overcome or mitigated, in principle, with some cycles of activation at low-current rate. However, the more plausible explanation relies in a imperfect mass/charge balance between anode and cathode which implies that the full-cell reach the cut-off voltages before the complete sodiation or desodiation of the cathode, which is the limiting electrode in terms of specific capacity. This

situation happens mostly in the cells cycled at higher currents because the specific capacity of the Hard Carbon anode electrodes are calculated during the presodiation steps, which were done at 30 mA g^{-1}, therefore, considering that the gap in the specific capacity between low-current and high-current rates of Hard Carbon is larger than that of NVOPF, the mass/charge balance between anode and cathode may be incorrect leading to the poor specific capacities of LHC//NVOPF cycled at 300 mA g^{-1} and 500 mA g^{-1}. Unfortunately, the potential profile of anode and cathode cannot be separated without reference electrode, thus not allowing the identification of which components doesn't reach its cut-off voltages during cycling. Nonetheless, the cells exhibit very high coulombic efficiencies % (> 99.5 % for both cells) although the capacity retentions after 100 cycles are limited to 80.2 % and 70.9 % for cell cycled at 300 mA g^{-1} and 500 mA g^{-1}, respectively.
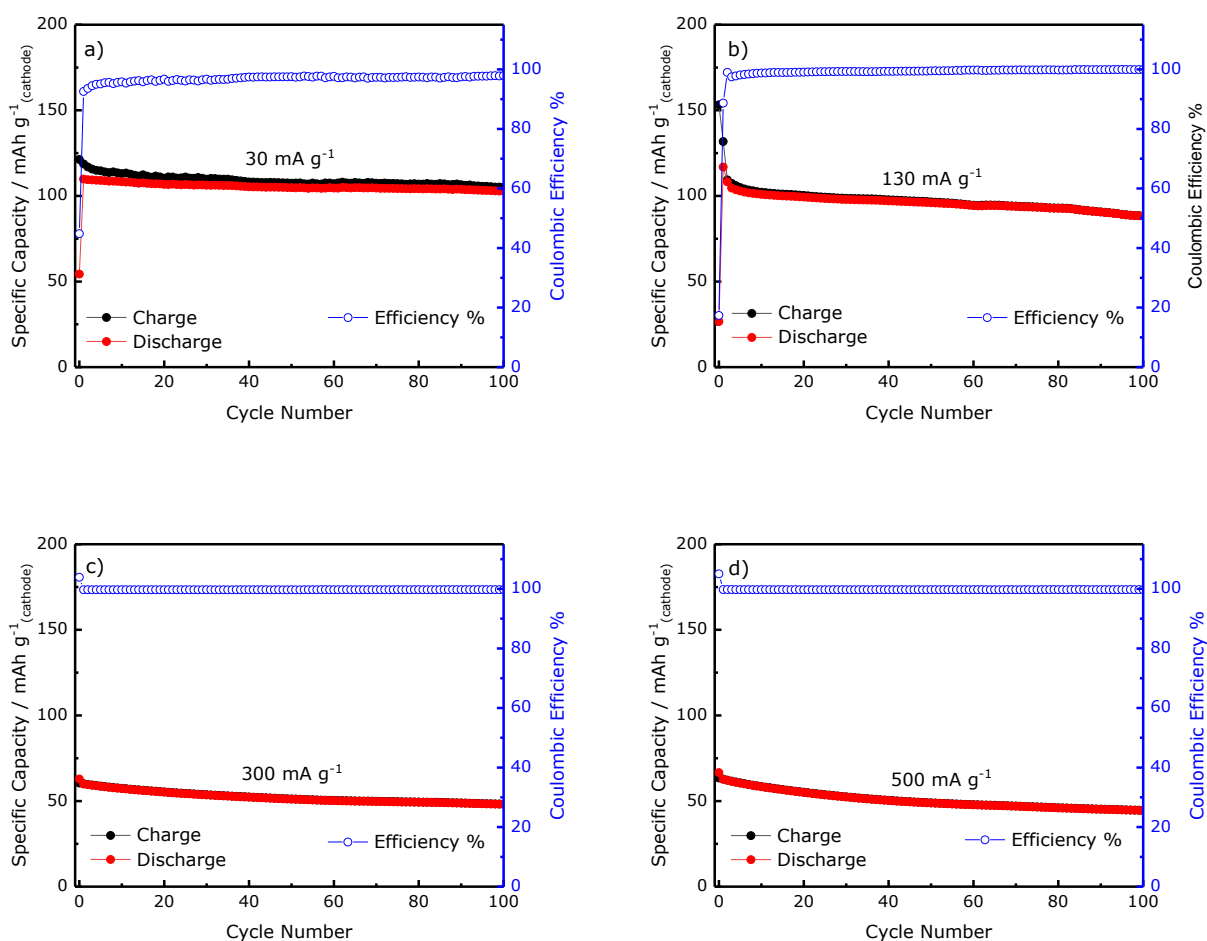
Figure 61 *Cycling performances of LHC//NVOPF full-cell in the voltage range 1.00 < E$_{cell}$ < 4.30 V at different current rates using 1M NaPF$_6$ in EC:PC 1:1 (v/v) as electrolyte: (a) 30 mA g^{-1}; (b) 130 mA g^{-1}; (c) 300 mA g^{-1} and (d) 500 mA g^{-1}. Specific capacity and current are normalized to the cathode active mass.*

Table 26 *First-cycle and 100th-cycle charge capacities and capacity retention after 100 cycles of LHC//NVOPF full-cell.*

Current (mA g^{-1})	Charge Capacity 1st cycle (mAhg^{-1})	Charge Capacity 100th cycle (mAhg^{-1})	Capacity Retention after 100 cycles (%)
30	118.65	105.01	88.50
130	107.27	87.46	81.53
300	60.08	48.21	80.24
500	62.84	44.54	70.88

To deeply evaluate the tolerance of the LHC//NVOPF full-cell toward low- and high-current rates, rate capability tests were performed in two different cells in the current range from 60 mA g^{-1} to 1000 mA g^{-1} in the first cell (**Figure 62 a**) and from 60 mA g^{-1} to 4000 mA g^{-1} in the second cell (**Figure 62 b**). The first LHC//NVOPF full-cell exhibits a promising rate capability with a low-capacity fade when the current is boosted, ranging from around 105 mAhg^{-1} at 60 mA g^{-1} to around 83 mAhg^{-1} at 1000 mA g^{-1}. Afterwards, the capability to recover pristine performances was investigated by cycling the electrode at cathode 1C current (i.e. 130 mA g^{-1}) up to 1000 overall cycles. The cell yields a specific capacity above 86.3 mAh g^{-1} after 100 cycles and 72.5 mAhg^{-1} after 1000 cycles, suggesting outstanding reversibility and stability even in demanding conditions. On the other hand, the second LHC//NVOPF full-cell cycled at higher current rates shows limited specific capacities at high current rates: approximatively 35 mAh g^{-1} at 2500 mA g^{-1} around 28 mAh g^{-1} at 4000 mA g^{-1}. These results can be again ascribed to an improper mass

balance between anode and cathode in the second cell since the specific capacity at 1000 mA g^{-1} is quite lower with respect to that of the first cell at the same current.
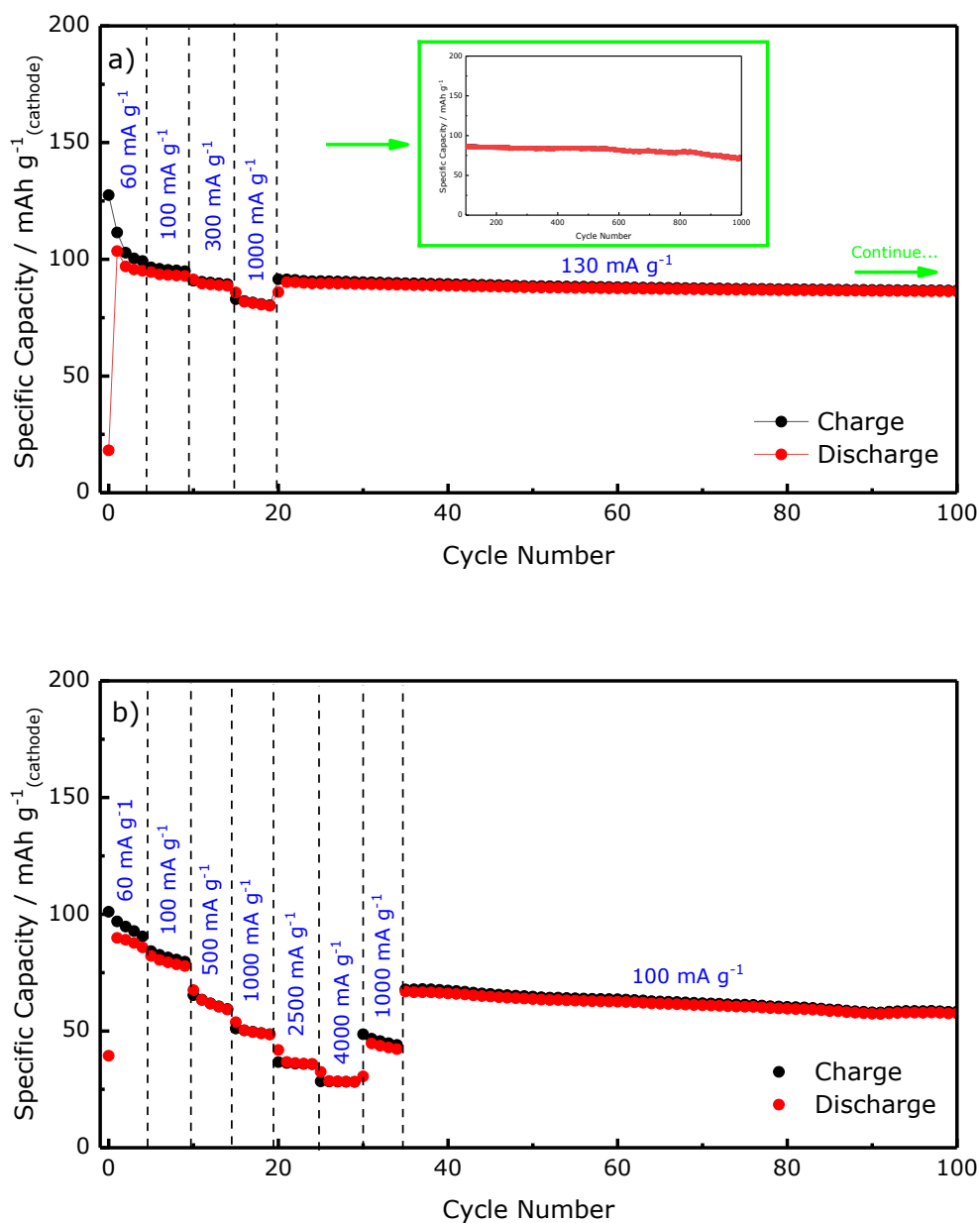
Figure 62 *Rate Capability of LHC//NVOPF full-cell in the voltage range 1.00 < E$_{cell}$ < 4.30 V using 1M NaPF$_6$ in EC:PC 1:1 (v/v) as electrolyte: (a) from 60 mA g^{-1} to 1000 mA g^{-1} and (b) from 60 mA g^{-1} to 4000 mA g^{-1}. Specific capacity and current are normalized to the cathode active mass.*

Taking into account the good results obtained by lignin-based Hard Carbon electrodes, LHC//NVOPF full-cell with Cyrene extracted lignin as binder at anode side were assembled and cycled at different current rates (**Figure 63 a,b,c**). As for the full-cells assembled with traditional binders (CMC for anode electrode and PVDF at cathode electrode), cells cycled at lower current

rates (i.e. 30 mA g^{-1} and 130 mA g^{-1}) deliver initial specific capacities higher than 100 mAh g^{-1} with low coulombic efficiency (~ 95 %) which increases to ~ 99 % in the cell cycled at 130 mA g^{-1}. However, in this case, the capacity retention of the cell cycled at 130 mA g^{-1} is lower with respect to the CMC-containing analogue, suggesting that the anode active material can undergo to a disconnection from the current collector and dissolution in the electrolyte during cycling. Regarding the cell cycled at 1000 mA g^{-1}, the performance are good in terms of specific capacity (83.3 mAh g^{-1} at first charge) and capacity retention (77.2 % after 100 cycles); these results are even better that those obtained in CMC-containing analogue cycled at lower current (**Figure 61 c,d**), indicating, again, that the correct mass balance between anode and cathode plays a crucial role in determining the performance of the resulting full-cell. Finally, the rate capability test (**Figure 63 d**) LHC//NVOPF full-cell with lignin-based anode exhibits a promising rate capability with a low-capacity fade when the current is boosted, ranging from around 108 mAhg^{-1} at 30 mA g^{-1} to around 77 mAhg^{-1} at 300 mA g^{-1}.
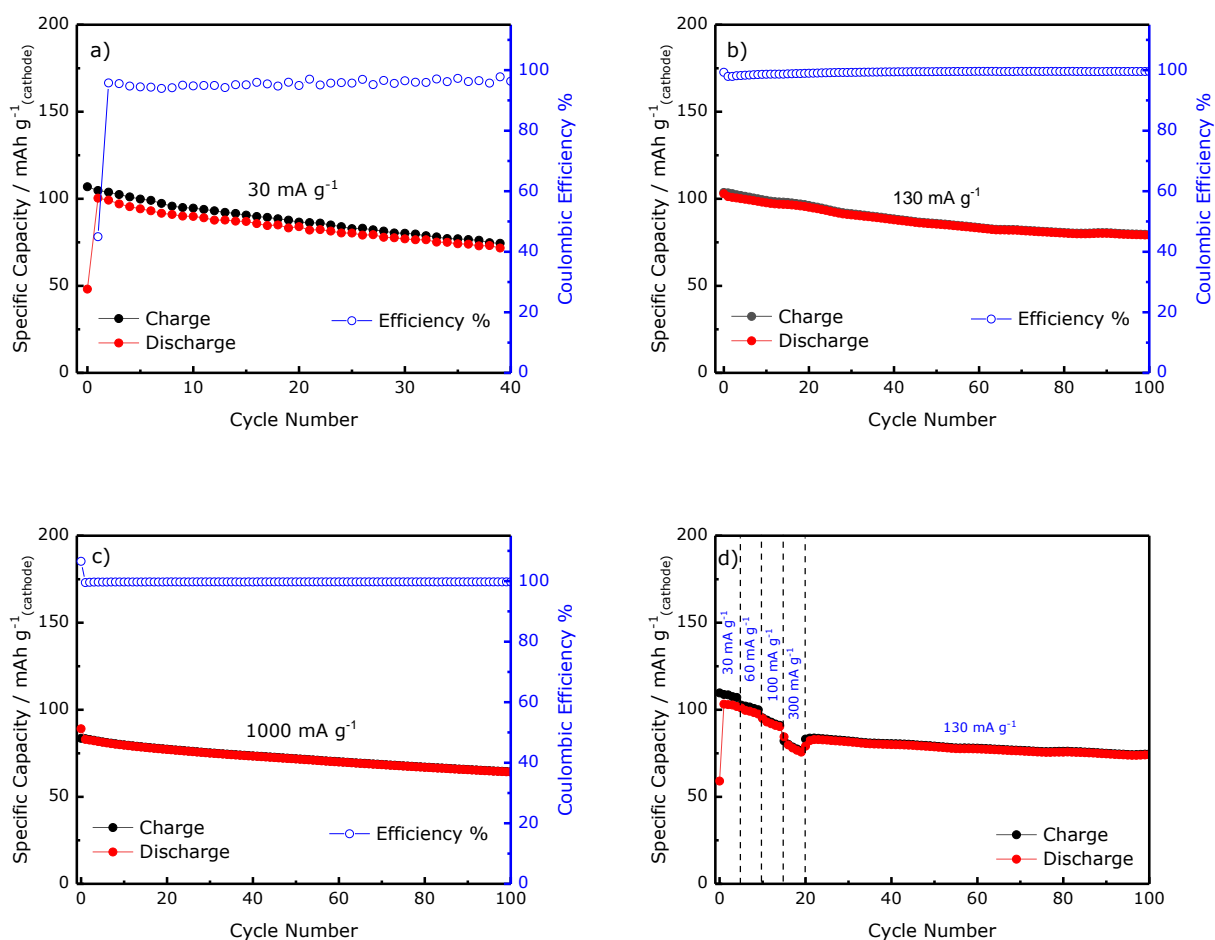
Figure 63 *Cycling performances of LHC//NVOPF full-cell using lignin as binder at anode side, in the voltage range 1.00 < E$_{cell}$ < 4.30 V at different current rates: (a) 30 mA g^{-1}; (b) 130 mA g^{-1}; (c) 1000 mA g^{-1}; (d) Rate Capability. Specific capacity and current are normalized to the cathode active mass.*

Table 27 *First-cycle and 100th-cycle charge capacities and capacity retention after 100 cycles of LHC//NVOPF full-cell with lignin as binder at anode side.*

Current (mA g⁻¹)	Charge Capacity 1st cycle (mAhg⁻¹)	Charge Capacity 100th cycle (mAhg⁻¹)	Capacity Retention after 100 cycles (%)
30	104.75	-	-
130	103.39	79.46	76.83
1000	83.35	64.40	77.26

Since the electrochemical presodiation of the anode is not a suitable strategy at industrial level due to the complicated disassembling and reassembling of the battery required,[362] the use of a cathode additive to compensate the sodium loss during the first charge, avoiding the spent of Na⁺ ions from the cathode, is a well-accepted approach to overcome this drawback. This strategy involves the oxidative decomposition at high-voltage of the sacrificial salt at the first charge, providing extra Na⁺ ions to the anode for the formation of the SEI and for the irreversible trapping at the defective sites of Hard Carbon.[363] Sodium mesoxalate monohydrate $Na_2C_3O_5 \cdot H_2O$ was chosen as sacrificial salt since it couples all the aspects of safety, low cost, ease of synthesis and environmental friendliness with optimum technical aspects of suitable oxidation potential ($\sim$ 4.0 V vs Na⁺/Na) and the major extent of the decomposition during the first cycle.[307] Additionally, the decomposition of this salt is reported to proceed following the general reaction mechanism of dicarboxylic acid family described in **Eq. (24)** which become **Eq. (25)** when sodium mesoxalate is considered with a theoretical capacity of 331 mAh g⁻¹:[307,364]

$$Na_2C_xO_y \rightarrow 2Na^+ + \frac{y}{2}CO_2 + \left(x - \frac{y}{2}\right)C + 2e^- \qquad \textbf{Eq. 24}$$

$$Na_2C_3O_5 \rightarrow 2Na^+ + \frac{5}{2}CO_2 + \left(3 - \frac{5}{2}\right)C + 2e^- \qquad \textbf{Eq. 25}$$
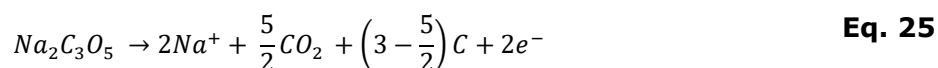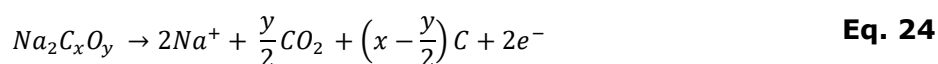
This means that the decompositions product are carbon dioxide and carbon, which do not negatively affect the formation of a stable solid electrolyte interphase. Firstly, the $Na_2C_3O_5$/KJ600 cathode additive (SS) was cycled versus sodium metal anode up to 4.3 V vs Na⁺/Na to determine the practical capacity that could be derived from the additive, then by knowing the amount of charge provided by $Na_2C_3O_5$ and the charge needed to address the SEI formation at the anode during the first charge, cathode additive was mixed with cathode active material in a way that the sacrificial cathode additive constitutes only 15 % (w/w) of the cathode electrode composition. **Figure 64** show the comparison between the cyclic voltammetries vs Na⁺/Na of the first two cycles of the cathode with (NVOPF + SS) and without the sacrificial salt (NVOPF) in the potential

range 3.00 V < E_{we} < 4.30 V. During the oxidation, both cells exhibit the two typical current peaks (A and B) of NVOPF already shown in **Figure 56 a**. However, the presence of the sacrificial salt is responsible of the appearance of another small and enlarged peak (C) around 4.2 V during the first cycle, which can be attributed to the decomposition of sodium mesoxalate. The decomposition seems to be irreversible since no additional peaks can found during the reduction scan except for the two peaks A' and B' of NVOPF reduction. Moreover, the cathode electrochemical processes are reversible in the second cycle with apparently no cell polarization.
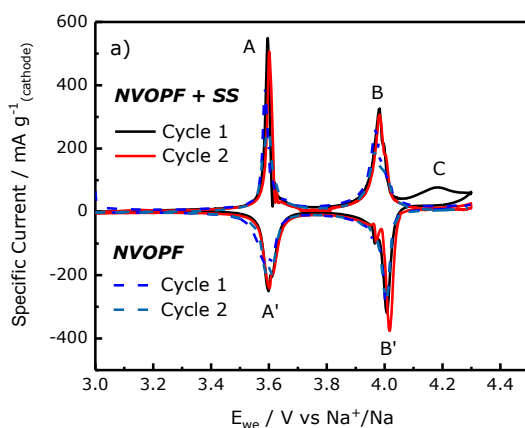
Figure 64 *Cylic voltammetries of the first two-cycles of NVOPF and NVOPF + SS in the potential range 3.00 < E_{we} < 4.30 V vs Na+/Na using 1M NaPF₆ in EC:PC 1:1 (v/v) as electrolyte. Specific current is normalized to the cathode active mass.*

When the NVOPF + SS cathode is combined in a full cell with LHC, the situation dramatically changes. **Figure 65 a** shows the galvanostatic profiles E vs Q of electrochemical presodiated LHC//NVOPF full-cell with LHC//NVOPF + SS full-cell during the first two cycles. A constant-voltage step during the first charge at E_{cell} = 4.30 V was applied only to the cell with the cathode additive to favor the complete oxidation of the sacrificial salt. In the first charge the cathode additive provides an extra capacity leading the initial capacity to around 250 mAh g^{-1} as a consequence of the decomposition of sodium mesoxalate and the formation of the SEI at anode side. Comparing the potential profiles of the two full cells, at first charge, the cell without the cathode additive exhibits the two typical plateaus located at approximatively at 3.50 and 4.00 V, [365] while the cell with the cathode additive displays a considerable decrease in the average voltage of the two plateau, which are located at approximatively 2.70 V and 3.50 V. This decrease in the voltage plateau reflects the poor power density of the resulting full cell. The small bump in the NVOPF + SS potential profile at E_{cell} = 3.73 V at first charge may indicate that the irreversible mesoxalate decomposition starts. In the following discharge, contrarily to the half-cell, a very high polarization of the cell is experimented, with apparently inhibited reaction processes, hence causing a dramatically decrease in the specific capacity to 42 mAh g^{-1}, which

is lower than the reversible capacity of bare NVOPF when used in full cell with LHC. The very high polarization can be attributed to the CO_2 evolution during sacrificial salt decomposition. Moreover, the cell rapidly loses capacity with a coulombic efficiency slowly rising to values around 95 % (**Figure 65 b**).
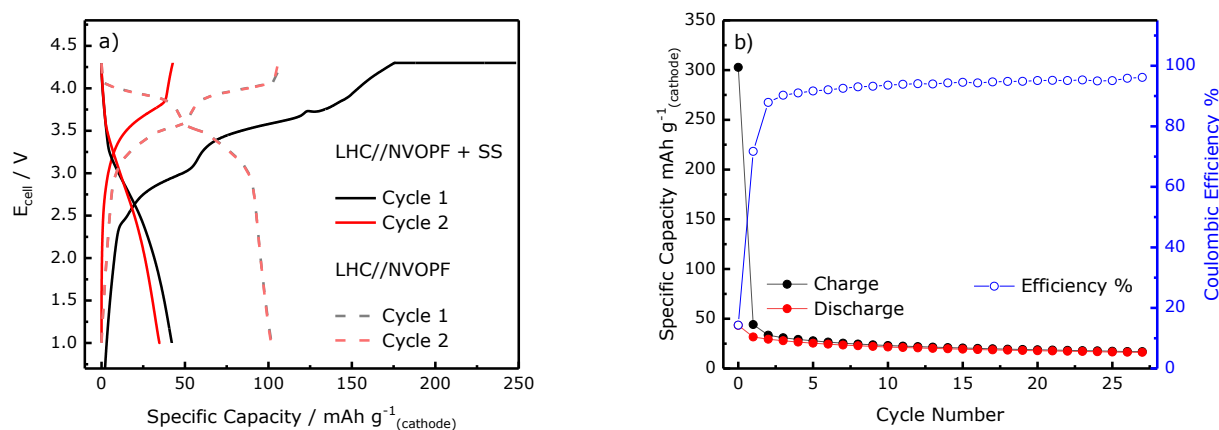
Figure 65 *Electrochemical performances of LHC//NVOPF + $Na_2C_3O_5$/KJ full-cell in the voltage range 1.00 < E_{cell} < 4.30 V using 1M $NaPF_6$ in EC:PC 1:1 (v/v) as electrolyte: (a) Galvanostatic profiles and (b) Cycling at 30 mA g^{-1}. Specific capacity and current are normalized to the cathode active mass.*

3.3 CONCLUSIONS

In this chapter, the feasibility of forestry-waste as raw materials for the preparation of electrode materials for sodium-ion have been demonstrated. High-performance Hard Carbons have been successfully synthesized either from lignin-rich and cellulose rich-precursors by a pyrolysis at 1000 °C followed by acid leaching to remove the inorganic impurities present in Hard Carbon samples. Contrarily to the corncob-derived HC shown in previous chapter, the acid leaching of HC powders has been unavoidable since an high ash content has been found in all the samples. Taking into account that the achieved specific capacities of LHC and SHC are comparable to that of CCDHC, the use of acid leaching inevitably reduce the economic and environmental sustainability. In parallel, the aqueous binder Na-CMC has been produced from holm-oak and willow extracted cellulose samples. Simultaneously, lignin samples were extracted by organosolv methods using either Cyrene or γ-valerolactone, and the extraction methods were compared. Regarding the sustainability, a recent Life Cycle Assessment study reveals that the organic solvent, in that case GVL, account for the major portion of environmental impact during the organosolv delignification.[366] Therefore, the optimization of the extraction must be carefully addressed toward the optimization of organic solvent:water ratio as a function of extraction yield and purity. The structural and morphological characterizations of the Hard Carbon active materials revealed that holm oak-derived HC has an higher interlayer distance and lower

graphitization degree respect to willow-derived analogue. These results can be ascribed, in part, to the higher content of lignin in the holm-oak raw material, which can prevent short-range ordering through the highly cross-linked structure of lignin. Nonetheless, both Hard Carbons exhibit quite similar porosity and BET surface areas, indicating that the synthesis conditions play a major role over the precursor composition in determining the textural properties of the final Hard Carbon. Regarding the characterization of the synthesized carboxymethylcellulose, the degree of substitution values were estimated to be 1.08 and 1.05 for holm oak-derived CMC and willow-derived CMC, respectively, indicating a high solubility in water. About the characterization of lignin-rich fraction, the determination of the Klason lignin % of the extracted lignin-rich fractions with Cyrene:H_2O and GVL:H_2O shows that the GVL:H_2O mixture is more selective toward lignin solubilization with respect to Cyrene analogue mixture, since the purities were determined to be 58.4 % and 73.7 % for Cyrene:H_2O and GVL:H_2O, respectively. When the two Hard Carbons are combined in an anode for SIBs with commercial CMC as binder, they exhibit good electrochemical performances delivering specific capacities of around 264 mAh g^{-1} and 254 mAh g^{-1} at 300 mA g^{-1}, with capacity retentions over 100 cycles of approximatively 91 % and 85 % for LHC and SHC, respectively. When synthesized CMC is used as binder, both Hard Carbons experimented fluctuations in the specific capacities and coulombic efficiencies profile, probably due to the increased catalytic activity toward the electrolyte decomposition originated from the higher amount of carboxylic groups present in the electrode surface as a consequence of the higher DS of the binder.

When extracted lignin is used as binder, the electrodes made with lignin extracted with Cyrene show good specific capacities (261 mAh g^{-1} for LHC and 202 mAh g^{-1} for SHC at 300 mA g^{-1}) and impressively long cycling stability: LHC electrode retains 76.0 % capacity after 1000 cycles, while SHC electrode still retains 86.6 % capacity after 1000 cycles. These long cycling stabilities can be ascribed to the high hydrogen bonding ability of the binder, which benefits from the polar functional groups of both lignin and carbohydrates residues, establishing strong interactions with the Hard Carbons materials. The long cycling stability as well as the coulombic efficiency is enhanced when Cyrene extracted lignin is used also in NVOPF cathode.

On the other hand, anode electrodes made with lignin extracted with γ-valerolactone as binder exhibit a considerable decrease in the specific capacities (202 mAh g^{-1} for LHC and 212 mAh g^{-1} for SHC at 300 mA g^{-1}) and larger instability of the electrode/electrolyte interphase. Overall, the holm oak-derived HC exhibit better electrochemical performance respect to willow-derived HC. When LHC is employed with $Na_3(VO)_2(PO_4)_2F$ cathode in full-cell application, the system delivers good specific capacities at different current rates and promising rate capability. These results are confirmed also when the commercial CMC is replaced with Cyrene extracted lignin as binder at anode side, where LHC//NVOPF full-cell delivers a specific capacity of 83.3 mAh g^{-1} with capacity fade lower than 13 % after 100 cycles. Nonetheless, the accuracy of the mass balance between anode and cathode plays a crucial role in determining the electrochemical performance of the cell. Concerning the use of cathode additive for SEI formation, the sodium mesoxalate

could be a promising sacrificial salt for this purpose, however other attempts are required to obtain better results.

Overall, further optimizations are still needed for practical applications of forestry-waste derived Hard Carbon anode coupled with $Na_3(VO)_2(PO_4)_2F$ cathode in sodium-ion batteries, especially those regarding the improvements of the initial coulombic efficiency of Hard Carbon, either by optimizing the Hard Carbon synthesis conditions or by tuning the use of the sacrificial salt such as sodium mesoxalate.

4. GENERAL CONCLUSION

In this thesis work, the aim of circular economy and sustainability have been pursued by investigating the lignocellulosic waste as raw materials for the production of electrode materials for lithium- and sodium-ion batteries. In details, the valorization of bio-waste has been divided into two sub-projects, the first one focused on one of the most abundant agricultural by-products, i.e. corncob, the second one focused on the forestry residues of the local areas.

Regarding the first study, the core of an ear of maize have been used as precursor for the synthesis of high performances Hard Carbon (CCDHC) through a simple, sustainable and industrially-scalable carbonization process at 950 °C in inert atmosphere. By studying the structural and morphological behaviors of the active material, CCHC showed small amount of potassium impurities coming from the biomass matrix, a suitable interlayer spacing for sodium insertion/extraction, and a high surface area beneficial for interfacial adsorption of both lithium and sodium but deleterious for the initial coulombic efficiency of the Hard Carbon. Simultaneously, the aqueous binder sodium carboxymethylcellulose has been produced from cellulose extracted from the same corncob feedstock and derivatized by $NaOH:ClCH_2COOH$ etherification, obtaining a Na-CMC sample with an estimated degree of substitution of 0.59. When corncob-derived Hard Carbon and binder are combined in an anode for SIBs, they exhibit good electrochemical performances delivering a specific capacity of 264 mAh g^{-1} at 1C with a promising capacity retention and good rate capability. Moreover, the electrode shows a fats reaction kinetics, while outstanding electrode/electrolyte interphase stability arises from the strong interactions between hard carbon and Na-CMC. The bio-based composite anode was used to study the mechanism of sodium storage into Hard Carbon, which is an interesting topic in the field of Hard Carbon. According to the experimental results, in the so-called "sloping-region" ($E_{we} > 0.1$ V), the sodium storage arises from the pseudocapacitive-controlled adsorption on surface active sites, while in the so-called "low- voltage plateau" ($E_{we} < 0.1$ V) the diffusion-controlled intercalation between graphene layers is the predominant process. These results represent another relevant contribution both to the understanding of the sodium storage mechanisms into carbonaceous hosts, which is beneficial for the structural design of carbonaceous active materials, but also to the development of high-performing and sustainable bio-based anodes for SIBs. Concerning the lithium-ion batteries, CCDHC/CC-CMC delivers a specific capacity of 394 mAh g^{-1} at 1C with a promising capacity retention and good rate capability as consequence of the fast kinetics and good interfacial stability demonstrated by EIS measurements. On the other hand, the buffer ability of CCDHC for SnO_2 is effective for low tin (IV) oxide content in the electrode formulation and with 2% of vinylene carbonate as SEI-forming additive in the electrolyte, highlighting that a stable and conductive solid electrolyte interphase plays a crucial role in the capacity retention of alloying materials.

As regards the second project, taking into account the good results obtained with corncobs-derived Hard Carbon, a larger and more systematic study about another important class of bio-waste, i.e. forestry scraps, have been conducted in order to assess the feasibility of using this feedstock for the production of carbonaceous materials and bio-based binders. In this context, high-performances Hard Carbons have been successfully synthesized both from lignin-rich and cellulose rich-precursors, and the structural characterizations revealed that the lignin-rich precursor Holm-oak lead to an Hard Carbon with higher interlayer distance and lower graphitization degree respect to cellulose-rich precursor willow. These results can be in part associated with the role of lignin in preventing short-range ordering through its highly cross-linked structure. Nonetheless, both Hard Carbons exhibit quite similar porosity and BET surface areas, indicating that the synthesis conditions play a major role over the precursor composition in determining the porosity of the Hard Carbon. As regards the extraction of cellulose and lignin, the extraction yields suggest that the holm-oak is the sample with the lowest content of cellulose (around 23 %) while willow is the sample with the highest content of cellulose (around 52 %). The Na-CMC produced from holm oak- and willow- extracted cellulose samples have a relatively high DS (1.08 and 1.05 for holm-oak and willow derived CMCs, respectively), which is higher to that of corncob derived CMC due to the higher reaction time with chloroacetic acid. When these CMC samples are used as binder for Hard Carbon anodes, the high DS reflects in the fluctuations of the specific capacities and coulombic efficiencies profiles, deteriorating the performance of the same Hard Carbons with respect to the use of commercial CMC as binder. Concerning the lignin, the extractions with Cyrene and γ-valerolactone display that holm oak apparently has a higher lignin content with respect to willow, however, further validation of this result is required. Moreover, γ-valerolactone has shown to be more selective with respect to Cyrene toward lignin extraction, since the Klason lignin % of holm oak-extracted lignin-rich fractions have been estimated to be 58.4 % and 73.7 % for Cyrene:H_2O and GVL:H_2O, respectively. These results can be ascribed to a more pronounced hydrogen bonding ability of the GVL mixture. When extracted lignin is used as binder, the electrodes made with lignin extracted with Cyrene show impressively long cycling stability (around 76 % and 87 % of capacity after 1000 cycles for LHC and SHC, respectively), which can be attributed to the strong interactions between binder and carbonaceous active materials given by the high amount of hydrogen bonding sites offered by the functional groups of the binder. On the other hand, the electrodes made with GVL extracted lignin binder exhibit worse electrochemical performance in terms of specific capacities and SEI stabilities. Thanks to its better electrochemical performance, the holm-oak derived HC has been employed with $Na_3(VO)_2(PO_4)_2F$ cathode in full-cell application, delivering good specific capacities at different current rates and promising rate capability, either when it is coupled with commercial CMC or with Cyrene extracted lignin as binder. Finally, the preliminary investigation of sodium mesoxalate as sacrificial salt to compensate the irreversibility at the first cycle has been conducted (although important experiments are still going on). Overall, further optimizations are still needed for practical applications of this sodium-ion cell-chemistry,

especially those regarding the improvements of the initial coulombic efficiency of Hard Carbon as well as the use of cathode additive for anode preconditioning.

In conclusion, both lithium- and sodium-ion batteries represent two key technologies for the ongoing energy transition since they are the most realistic options to store electricity generated by renewable energy sources. In particular, SIBs are going to be the more appealing device for large-scale stationary energy storage system, thus play a complementary role with respect to LIBs and decongesting the increasing pressure over the LIBs market. In my opinion, SIB will be readily able to penetrate LFP-based LIBs market such as stationary energy storage, industrial traction and short-range transportation applications. However, the success of SIBs is strictly related to the cost-competitiveness in terms of $ kWh^{-1} by the different cell chemistries. To do this, high-energy density and/or low-cost electrode materials are required. In this context, Hard Carbons are considered the optimal candidate anode hosts for SIBs, both for their electrochemical performance and for the possibility to be synthesized from low-cost bio-waste precursors. However, the requirement of high-temperature pyrolysis as well as pre- or post-pyrolysis treatment can dramatically break down the economical and environmental sustainability of the final product. Although LCA studies recently conducted state that, compared with commercial graphite for LIBs, bio-waste derived Hard Carbon displays a significant reduction in terms of economical[54] and environmental impact,[130] additional reduction can be obtained if: the electricity for the pyrolysis is produced by clean energy sources; the electrochemical performance of Hard Carbon is improved; the use of pre- and post-treatments is avoided. Overall, all the environmental and economic analysis must be done considering the final application of the material and thus, normalizing the values of $ and CO_2-eq over the specific capacity of the obtained Hard Carbon (mAh of Na$^+$). In this context, another industrially relevant problem is represented by the poor reproducibility of biomass-derived Hard Carbon in terms of achievable specific capacity since they are affected by considerable variability in the composition of different feedstock. More in-depth and large studies in terms of biomass composition are required to evaluate the feasibility of producing Hard Carbon with reproducible performance even from complex incoming streams of precursors. Concerning the lithium-ion batteries, the state-of-the-art graphite anode material will probably face two important issues, one related to its relatively low theoretical specific capacity (372 mAh g^{-1}) which is unable to meet the required energy densities for powering EVs, and the other related to the fact that China produces most of the world's graphite, posing serious concerns about the LIBs supply chain in the rest of the world. Therefore, Hard Carbons can be an affordable alternative either as active materials themselves or as a low-cost and sustainable buffer matrix for high-energy density alloying anode materials. Nonetheless, further optimizations are still needed for the application in both lithium- and sodium-ion batteries, especially those regarding the improvements of the initial coulombic efficiency of Hard Carbon.

5. REFERENCES

[1]   U. Nations, "What Is Climate Change?," can be found under https://www.un.org/en/climatechange/what-is-climate-change, **2022**.

[2]   US EPA, "Causes of Climate Change," can be found under https://www.epa.gov/climatechange-science/causes-climate-change#2foot, **2022**.

[3]   NASA, "How Do We Know Climate Change Is Real?," can be found under https://climate.nasa.gov/evidence/, **2023**.

[4]   NASA, "NASA Says 2022 Fifth Warmest Year on Record, Warming Trend Continues," can be found under https://climate.nasa.gov/news/3246/nasa-says-2022-fifth-warmest-year-on-record-warming-trend-continues/, **2023**.

[5]   U.S. Global Change Research Program, "Highlights of the Findings of the U.S. Global Change Research Program Climate Science Special Report," **2017**.

[6]   NASA, "Global Temperature," can be found under https://climate.nasa.gov/vital-signs/global-temperature/, **2023**.

[7]   IPCC, *Climate Change 2014: Synthesis Report*, Geneva, Switzerland, **2014**.

[8]   IPCC, *Climate Change 2022 - Mitigation of Climate Change - Full Report*, **2022**.

[9]   UNFCCC, *The Paris Agreement*, **2015**.

[10]   International Energy Agency, *World Energy Outlook 2022*, **2022**.

[11]   International Energy Agency, *Net Zero by 2050: A Roadmap for the Global Energy Sector*, **2021**.

[12]   EMBER, *Global Electricity Review: Global Trends*, **2023**.

[13]   T. Liu, Y. Zhang, Z. Jiang, X. Zeng, J. Ji, Z. Li, X. Gao, M. Sun, Z. Lin, M. Ling, J. Zheng, C. Liang, *Energy Environ. Sci.* **2019**, *12*, 1512–1533.

[14]   G. Coppez, S. Chowdhury, S. P. Chowdhury, *IEEE Proc.* **2010**.

[15] T. M. Gür, *Energy Environ. Sci.* **2018**, *11*, 2696–2767.

[16] H. Ibrahim, A. Ilinca, J. Perron, *Renew. Sustain. Energy Rev.* **2008**, *12*, 1221–1250.

[17] H. Pan, Y. S. Hu, L. Chen, *Energy Environ. Sci.* **2013**, *6*, 2338–2360.

[18] B. Dunn, H. Kamath, J. M. Tarascon, *Science (80-.).* **2011**, *334*, 928–935.

[19] D. Linden, T. B. Reddy, *Handbook Of Batteries*, New York, **2002**.

[20] A. Van Der Ven, Z. Deng, S. Banerjee, S. P. Ong, *Chem. Rev.* **2020**, *120*, 6977–7019.

[21] S. Y. Hong, Y. Kim, Y. Park, A. Choi, N. S. Choi, K. T. Lee, *Energy Environ. Sci.* **2013**, *6*, 2067–2081.

[22] D. Lin, Y. Liu, Y. Cui, *Nat. Nanotechnol.* **2017**, *12*, 194–206.

[23] M. S. Whittingham, *Science (80-.).* **1976**, *192*, 1126–1127.

[24] B. Scrosati, *J. Solid State Electrochem.* **2011**, *15*, 1623–1630.

[25] M. Lazzari, B. Scrosati, *J. Electrochem. Soc.* **1980**, *127*, 773–774.

[26] J. O. Besenhard, G. Eichinger, *J. Electroanal. Chem.* **1976**, *68*, 1–18.

[27] S. Basu, C. Zeller, P. J. Flanders, C. D. Fuerst, W. D. Johnson, J. E. Fischer, *Mater. Sci. Eng.* **1979**, *38*, 275–283.

[28] R. Yazami, P. Touzain, *J. Power Sources* **1983**, *9*, 365–371.

[29] D. Deng, *Energy Sci. Eng.* **2015**, *3*, 385–418.

[30] J.-M. Tarascon, M. Armand, *Nature* **2001**, *414*, 359–367.

[31] K. Mizushima, P. C. Jones, P. J. Wiseman, J. B. Goodenough, *Solid State Ionics* **1981**, *3–4*, 171–174.

[32] J. B. Goodenough, K. S. Park, *J. Am. Chem. Soc.* **2013**, *135*, 1167–1176.

[33] A. M. Divakaran, M. Minakshi, P. A. Bahri, S. Paul, P. Kumari, A. M. Divakaran, K. N. Manjunatha, *Prog. Solid State Chem.* **2021**, *62*, 100298.

[34] S. Passerini, D. Bresser, A. Moretti, A. Varzi, *Batteries*, Wiley-Vch, Weinheim, **2020**.

[35] J. Janek, W. G. Zeier, *Nat. Energy* **2016**, *1*, 1–4.

[36] K. W. Beard, T. B. Reddy, *Linden's Handbook of Batteries*, McGraw-Hill, New York, **2019**.

[37] B. Nykvist, M. Nilsson, *Nat. Clim. Chang.* **2015**, *5*, 329–332.

[38] Z. P. Cano, D. Banham, S. Ye, A. Hintennach, J. Lu, M. Fowler, Z. Chen, *Nat. Energy* **2018**, *3*, 279–289.

[39] C. P. Grey, D. S. Hall, *Nat. Commun.* **2020**, *11*, 2–5.

[40] J. Deng, C. Bae, A. Denlinger, T. Miller, *Joule* **2020**, *4*, 511–515.

[41] McKinsey & Company, *Battery 2030: Resilient, Sustainable and Circular*, **2023**.

[42] European Commission, *Study on the Critical Raw Materials for the EU*, **2023**.

[43] J. Neumann, M. Petranikova, M. Meeus, J. D. Gamarra, R. Younesi, M. Winter, S. Nowak, *Adv. Energy Mater.* **2022**, *12*, DOI 10.1002/aenm.202102917.

[44] K. Chayambuka, G. Mulder, D. L. Danilov, P. H. L. Notten, *Adv. Energy Mater.* **2018**, *8*, DOI 10.1002/aenm.201800079.

[45] P. T. Moseley, D. A. J. Rand, *High-Temperature Sodium Batteries for Energy Storage*, Elsevier B.V., **2015**.

[46] G. H. Newman, L. P. Klemann, *J. Electrochem. Soc.* **1980**, *127*, 2097–2099.

[47] C. Delmas, *Adv. Energy Mater.* **2018**, *8*, 1–9.

[48] M. M. Doeff, Y. Ma, S. J. Visco, L. C. De Jonghe, *J. Electrochem. Soc.* **1993**, *140*, 169–170.

[49] D. A. Stevens, J. R. Dahn, *J. Electrochem. Soc.* **2000**, *147*, 4428.

[50] V. Palomares, P. Serras, I. Villaluenga, K. B. Hueso, J. Carretero-González, T. Rojo, *Energy Environ. Sci.* **2012**, *5*, 5884–5901.

[51] D. Kundu, E. Talaie, V. Duffort, L. F. Nazar, *Angew. Chemie - Int. Ed.* **2015**, *54*, 3432–3448.

[52] Y. Liu, X. Liu, T. Wang, L. Z. Fan, L. Jiao, *Sustain. Energy Fuels* **2017**, *1*, 986–1006.

[53] "TRADING ECONOMICS," can be found under https://tradingeconomics.com/, **2023**.

[54] J. F. Peters, A. P. Cruz, M. Weil, *Batteries* **2019**, *5*, DOI 10.3390/batteries5010010.

[55] K. Chayambuka, G. Mulder, D. L. Danilov, P. H. L. Notten, *Adv. Energy Mater.* **2020**, *10*, 1–11.

[56] J. Y. Hwang, S. T. Myung, Y. K. Sun, *Chem. Soc. Rev.* **2017**, *46*, 3529–3614.

[57] L. Zhao, T. Zhang, W. Li, T. Li, L. Zhang, X. Zhang, Z. Wang, *Engineering* **2023**, DOI 10.1016/j.eng.2021.08.032.

[58] K. M. Abraham, *ACS Energy Lett.* **2020**, *5*, 3544–3547.

[59] I. Hasa, J. Barker, G. Elia, S. Passerini, *Sodium-Ion Batteries: History, Development, and Overview on Market and Application*, Elsevier B.V., **2023**.

[60] S. L. Chou, Y. Pan, J. Z. Wang, H. K. Liu, S. X. Dou, *Phys. Chem. Chem. Phys.* **2014**, *16*, 20347–20359.

[61] A. Wang, S. Kadam, H. Li, S. Shi, Y. Qi, *npj Comput. Mater.* **2018**, *4*, DOI 10.1038/s41524-018-0064-0.

[62] H. Adenusi, G. A. Chass, S. Passerini, K. V. Tian, G. Chen, *Adv. Energy Mater.* **2023**, *13*, DOI 10.1002/aenm.202203307.

[63] M. Á. Muñoz-Márquez, D. Saurel, J. L. Gómez-Cámer, M. Casas-Cabanas, E. Castillo-Martínez, T. Rojo, *Adv. Energy Mater.* **2017**, *7*, 1–31.

[64]   R. Raccichini, U. Ulissi, *Nanomaterials for Electrochemical Energy Storage*, Elsevier, **2021**.

[65]   R. A. Huggins, *Advanced Batteries*, Springer, Stanford, **2009**.

[66]   D. D. L. Chung, *J. Mater. Sci.* **2002**, *37*, 1475–1489.

[67]   A. Zubiarrain-Laserna, P. Kruse, *J. Electrochem. Soc.* **2020**, *167*, 037539.

[68]   Z. Wang, S. M. Selbach, T. Grande, *RSC Adv.* **2014**, *4*, 4069–4079.

[69]   Y. Li, Y. Lu, P. Adelhelm, M. M. Titirici, Y. S. Hu, *Chem. Soc. Rev.* **2019**, *48*, 4655–4687.

[70]   R. Korthauer, *Lithium-Ion Batteries: Basics and Applications*, **2018**.

[71]   A. Senyshyn, O. Dolotko, M. J. Mühlbauer, K. Nikolowski, H. Fuess, H. Ehrenberg, *J. Electrochem. Soc.* **2013**, *160*, A3198–A3205.

[72]   J. Asenbauer, T. Eisenmann, M. Kuenzel, A. Kazzazi, Z. Chen, D. Bresser, *Sustain. Energy Fuels* **2020**, *4*, 5387–5416.

[73]   D. Allart, M. Montaru, H. Gualous, *J. Electrochem. Soc.* **2018**, *165*, A380–A387.

[74]   A. Shellikeri, V. Watson, D. Adams, E. E. Kalu, J. A. Read, T. R. Jow, J. S. Zheng, J. P. Zheng, *J. Electrochem. Soc.* **2017**, *164*, A3914–A3924.

[75]   H. Kim, J. Hong, G. Yoon, H. Kim, K. Y. Park, M. S. Park, W. S. Yoon, K. Kang, *Energy Environ. Sci.* **2015**, *8*, 2963–2969.

[76]   H. Kim, J. Hong, Y. U. Park, J. Kim, I. Hwang, K. Kang, *Adv. Funct. Mater.* **2015**, *25*, 534–541.

[77]   P. Bai, Y. He, P. Xiong, X. Zhao, K. Xu, Y. Xu, *Energy Storage Mater.* **2018**, *13*, 274–282.

[78]   P. Engels, F. Cerdas, T. Dettmer, C. Frey, J. Hentschel, C. Herrmann, T. Mirfabrikikar, M. Schueler, *J. Clean. Prod.* **2022**, *336*, 130474.

[79]   B. Xiao, T. Rojo, X. Li, *ChemSusChem* **2019**, *12*, 133–144.

[80] P. Bai, X. Han, Y. He, P. Xiong, Y. Zhao, J. Sun, Y. Xu, *Energy Storage Mater.* **2020**, *25*, 324–333.

[81] X. Dou, I. Hasa, D. Saurel, C. Vaalma, L. Wu, D. Buchholz, D. Bresser, S. Komaba, S. Passerini, *Mater. Today* **2019**, *23*, 87–104.

[82] Y. Huang, Y. Wang, P. Bai, Y. Xu, *ACS Appl. Mater. Interfaces* **2021**, *13*, 38441–38449.

[83] X. Chen, C. Liu, Y. Fang, X. Ai, F. Zhong, H. Yang, Y. Cao, *Carbon Energy* **2022**, 1–18.

[84] P. Bai, Y. He, X. Zou, X. Zhao, P. Xiong, Y. Xu, *Adv. Energy Mater.* **2018**, *8*, 1–9.

[85] F. Xie, Z. Xu, Z. Guo, M. M. Titirici, *Prog. Energy* **2020**, *2*, DOI 10.1088/2516-1083/aba5f5.

[86] W. Shao, H. Shi, X. Jian, Z.-S. Wu, F. Hu, *Adv. Energy Sustain. Res.* **2022**, *3*, 2200009.

[87] D. A. Stevens, J. R. Dahn, *J. Electrochem. Soc.* **2000**, *147*, 1271.

[88] D. A. Stevens, J. R. Dahn, *J. Electrochem. Soc.* **2001**, *148*, A803.

[89] S. Komaba, W. Murata, T. Ishikawa, N. Yabuuchi, T. Ozeki, T. Nakayama, A. Ogata, K. Gotoh, K. Fujiwara, *Adv. Funct. Mater.* **2011**, *21*, 3859–3867.

[90] Y. Cao, L. Xiao, M. L. Sushko, W. Wang, B. Schwenzer, J. Xiao, Z. Nie, L. V. Saraf, Z. Yang, J. Liu, *Nano Lett.* **2012**, 3783–3787.

[91] J. Ding, H. Wang, Z. Li, A. Kohandehghan, K. Cui, Z. Xu, B. Zahiri, X. Tan, E. M. Lotfabad, B. C. Olsen, D. Mitlin, *ACS Nano* **2013**, *7*, 11004–11015.

[92] S. Qiu, L. Xiao, M. L. Sushko, K. S. Han, Y. Shao, M. Yan, X. Liang, L. Mai, J. Feng, Y. Cao, X. Ai, H. Yang, J. Liu, *Adv. Energy Mater.* **2017**, *7*, 1–11.

[93] L. Xiao, H. Lu, Y. Fang, M. L. Sushko, Y. Cao, X. Ai, H. Yang, J. Liu, *Adv. Energy Mater.* **2018**, *8*, 1–7.

[94] H. Lu, F. Ai, Y. Jia, C. Tang, X. Zhang, Y. Huang, H. Yang, Y. Cao, *Small* **2018**, *14*, 1–8.

[95] X. Chen, Y. Fang, J. Tian, H. Lu, X. Ai, H. Yang, Y. Cao, *ACS Appl. Mater. Interfaces*

2021, *13*, 18914–18922.

[96] X. Chen, Y. Fang, H. Lu, H. Li, X. Feng, W. Chen, X. Ai, H. Yang, Y. Cao, *Small* **2021**, *17*, 1–9.

[97] C. Bommier, T. W. Surta, M. Dolgos, X. Ji, *Nano Lett.* **2015**, *15*, 5888–5892.

[98] Y. Jin, S. Sun, M. Ou, Y. Liu, C. Fan, X. Sun, J. Peng, Y. Li, Y. Qiu, P. Wei, Z. Deng, Y. Xu, J. Han, Y. Huang, *ACS Appl. Energy Mater.* **2018**, *1*, 2295–2305.

[99] B. Zhang, C. M. Ghimbeu, C. Laberty, C. Vix-Guterl, J. M. Tarascon, *Adv. Energy Mater.* **2016**, *6*, 1–9.

[100] Y. Li, Y. S. Hu, M. M. Titirici, L. Chen, X. Huang, *Adv. Energy Mater.* **2016**, *6*, DOI 10.1002/aenm.201600659.

[101] U. Mittal, L. Djuandhi, N. Sharma, H. L. Andersen, *JPhys Energy* **2022**, *4*, DOI 10.1088/2515-7655/ac8dc1.

[102] J. Górka, C. Vix-Guterl, C. Matei Ghimbeu, *C* **2016**, *2*, 24.

[103] J. Deng, T. Xiong, H. Wang, A. Zheng, Y. Wang, *ACS Sustain. Chem. Eng.* **2016**, *4*, 3750–3756.

[104] P. K. Nayak, L. Yang, W. Brehm, P. Adelhelm, *Angew. Chemie - Int. Ed.* **2018**, *57*, 102–120.

[105] M. Thompson, Q. Xia, Z. Hu, X. S. Zhao, *Mater. Adv.* **2021**, *2*, 5881–5905.

[106] C. del M. Saavedra, A. B. Rios, L. Simonin, C. M. Ghimbeu, in *Na-Ion Batter.* (Ed.: Wiley), **2021**, pp. 101–146.

[107] H. S. Hirsh, B. Sayahpour, A. Shen, W. Li, B. Lu, E. Zhao, M. Zhang, Y. S. Meng, *Energy Storage Mater.* **2021**, *42*, 78–87.

[108] Y. Wan, Y. Liu, D. Chao, W. Li, D. Zhao, *Nano Mater. Sci.* **2022**, *5*, 189–201.

[109] H. Hou, X. Qiu, W. Wei, Y. Zhang, X. Ji, *Adv. Energy Mater.* **2017**, *7*, 1–30.

[110] Z. Tang, S. Zhou, P. Wu, H. Wang, Y. Huang, Y. Zhang, D. Sun, Y. Tang, H. Wang, *Chem. Eng. J.* **2022**, *441*, 135899.

[111] L. Xie, C. Tang, Z. Bi, M. Song, Y. Fan, C. Yan, X. Li, F. Su, Q. Zhang, C. Chen, *Adv. Energy Mater.* **2021**, *11*, DOI 10.1002/aenm.202101650.

[112] K. L. Hong, L. Qie, R. Zeng, Z. Q. Yi, W. Zhang, D. Wang, W. Yin, C. Wu, Q. J. Fan, W. X. Zhang, Y. H. Huang, *J. Mater. Chem. A* **2014**, *2*, 12733–12738.

[113] S. V. Vassilev, D. Baxter, L. K. Andersen, C. G. Vassileva, *Fuel* **2010**, *89*, 913–933.

[114] F. Wang, D. Ouyang, Z. Zhou, S. J. Page, D. Liu, X. Zhao, *J. Energy Chem.* **2021**, *57*, 247–280.

[115] J. Bettles, D. S. Battisti, S. C. Cook-Patton, T. Kroeger, J. T. Spector, N. H. Wolff, Y. J. Masuda, *For. Policy Econ.* **2021**, *130*, 102538.

[116] L. J. R. Nunes, T. P. Causer, D. Ciolkosz, *Renew. Sustain. Energy Rev.* **2020**, *120*, 109658.

[117] J. Gupta, M. Kumari, A. Mishra, Swati, M. Akram, I. S. Thakur, *Chemosphere* **2022**, *287*, 132321.

[118] F. Shen, W. Luo, J. Dai, Y. Yao, M. Zhu, E. Hitz, Y. Tang, Y. Chen, V. L. Sprenkle, X. Li, L. Hu, *Adv. Energy Mater.* **2016**, *6*, 1–7.

[119] W. Lv, F. Wen, J. Xiang, J. Zhao, L. Li, L. Wang, Z. Liu, Y. Tian, *Electrochim. Acta* **2015**, *176*, 533–541.

[120] T. Zhang, J. Mao, X. Liu, M. Xuan, K. Bi, X. L. Zhang, J. Hu, J. Fan, S. Chen, G. Shao, *RSC Adv.* **2017**, *7*, 41504–41511.

[121] P. C. Rath, J. Patra, H. T. Huang, D. Bresser, T. Y. Wu, J. K. Chang, *ChemSusChem* **2019**, *12*, 2302–2309.

[122] H. Darjazi, L. Bottoni, H. R. Moazami, S. J. Rezvani, L. Balducci, L. Sbrascini, *Mater. Today Sustain.* **2023**, 100313.

[123] N. Zhang, Q. Liu, W. Chen, M. Wan, X. Li, L. Wang, L. Xue, W. Zhang, *J. Power Sources*

2018, *378*, 331–337.

[124] V. Simone, A. Boulineau, A. de Geyer, D. Rouchon, L. Simonin, S. Martinet, *J. Energy Chem.* **2016**, *25*, 761–768.

[125] X. Lin, Y. Liu, H. Tan, B. Zhang, *Carbon N. Y.* **2020**, *157*, 316–323.

[126] M. Chen, F. Luo, Y. Liao, C. Liu, D. Xu, Z. Wang, Q. Liu, D. Wang, Y. Ye, S. Li, D. Wang, Z. Zheng, *J. Electroanal. Chem.* **2022**, *919*, 116526.

[127] B. Yang, J. Wang, Y. Zhu, K. Ji, C. Wang, D. Ruan, Y. Xia, *J. Power Sources* **2021**, *492*, 229656.

[128] A. M. Escamilla-Pérez, A. Beda, L. Simonin, M.-L. Grapotte, J. M. Le-Meins, C. Matei Ghimbeu, *ACS Appl. Energy Mater.* **2023**, DOI 10.1021/acsaem.3c00640.

[129] J. Conder, C. Vaulot, C. Marino, C. Villevieille, C. M. Ghimbeu, *ACS Appl. Energy Mater.* **2019**, *2*, 4841–4852.

[130] H. Liu, Z. Xu, Z. Guo, J. Feng, H. Li, T. Qiu, M. Titirici, *Philos. Trans. R. Soc. A Math. Phys. Eng. Sci.* **2021**, *379*, DOI 10.1098/rsta.2020.0340.

[131] Q. Wang, C. Zhao, Y. Lu, Y. Li, Y. Zheng, Y. Qi, X. Rong, L. Jiang, X. Qi, Y. Shao, D. Pan, B. Li, Y. S. Hu, L. Chen, *Small* **2017**, *13*, 1–32.

[132] A. Beda, P. L. Taberna, P. Simon, C. Matei Ghimbeu, *Carbon N. Y.* **2018**, *139*, 248–257.

[133] A. Kamiyama, K. Kubota, T. Nakano, S. Fujimura, S. Shiraishi, H. Tsukada, S. Komaba, *ACS Appl. Energy Mater.* **2020**, *3*, 135–140.

[134] J. Zhu, C. Chen, Y. Lu, Y. Ge, H. Jiang, K. Fu, X. Zhang, *Carbon N. Y.* **2015**, *94*, 189–195.

[135] L. Xiao, Y. Cao, W. A. Henderson, M. L. Sushko, Y. Shao, J. Xiao, W. Wang, M. H. Engelhard, Z. Nie, J. Liu, *Nano Energy* **2016**, *19*, 279–288.

[136] J. Peters, D. Buchholz, S. Passerini, M. Weil, *Energy Environ. Sci.* **2016**, *9*, 1744–1751.

[137] J. F. Peters, M. Abdelbaky, M. Baumann, M. Weil, *Mater. Tech.* **2019**, *107*, DOI

10.1051/mattech/2019029.

[138] H. Zhang, I. Hasa, S. Passerini, *Adv. Energy Mater.* **2018**, *8*, DOI 10.1002/aenm.201702582.

[139] C. Wu, S. X. Dou, Y. Yu, *Small* **2018**, *14*, 1–20.

[140] J. Cabana, L. Monconduit, D. Larcher, M. R. Palacín, *Adv. Mater.* **2010**, *22*, 170–192.

[141] J. Lu, Z. Chen, F. Pan, Y. Cui, K. Amine, *Electrochem. Energy Rev.* **2018**, *1*, 35–53.

[142] M. R. Palacín, *Chem. Soc. Rev.* **2009**, *38*, 2565–2575.

[143] D. Puthusseri, M. Wahid, S. Ogale, *ACS Omega* **2018**, *3*, 4591–4601.

[144] L. Wang, J. Świątowska, S. Dai, M. Cao, Z. Zhong, Y. Shen, M. Wang, *Mater. Today Energy* **2019**, *11*, 46–60.

[145] K. Song, C. Liu, L. Mi, S. Chou, W. Chen, C. Shen, *Small* **2021**, *17*, DOI 10.1002/smll.201903194.

[146] M. Lao, Y. Zhang, W. Luo, Q. Yan, W. Sun, S. X. Dou, *Adv. Mater.* **2017**, *29*, 1–23.

[147] W. J. Zhang, *J. Power Sources* **2011**, *196*, 877–885.

[148] W. J. Zhang, *J. Power Sources* **2011**, *196*, 13–24.

[149] J. Y. Li, Q. Xu, G. Li, Y. X. Yin, L. J. Wan, Y. G. Guo, *Mater. Chem. Front.* **2017**, *1*, 1691–1708.

[150] F. Wang, G. Chen, N. Zhang, X. Liu, R. Ma, *Carbon Energy* **2019**, *1*, 219–245.

[151] X. Su, Q. Wu, J. Li, X. Xiao, A. Lott, W. Lu, B. W. Sheldon, J. Wu, *Adv. Energy Mater.* **2014**, *4*, 1–23.

[152] L. Zhang, X. Liu, Q. Zhao, S. Dou, H. Liu, Y. Huang, X. Hu, *Energy Storage Mater.* **2016**, *4*, 92–102.

[153] S. C. Jung, D. S. Jung, J. W. Choi, Y. K. Han, *J. Phys. Chem. Lett.* **2014**, *5*, 1283–1288.

[154] Y. Xu, E. Swaans, S. Basak, H. W. Zandbergen, D. M. Borsa, F. M. Mulder, *Adv. Energy Mater.* **2016**, *6*, 1–5.

[155] J. M. Buriak, S. Y. Sayed, W. Peter Kalisvaart, E. J. Luber, B. C. Olsen, *ACS Appl. Energy Mater.* **2020**, *3*, 9950–9962.

[156] H. Tan, D. Chen, X. Rui, Y. Yu, *Adv. Funct. Mater.* **2019**, *29*, 1–32.

[157] L. D. Ellis, T. D. Hatchard, M. N. Obrovac, *J. Electrochem. Soc.* **2012**, *159*, A1801–A1805.

[158] S. Liang, Y. J. Cheng, J. Zhu, Y. Xia, P. Müller-Buschbaum, *Small Methods* **2020**, *4*, DOI 10.1002/smtd.202000218.

[159] F. Zoller, D. Böhm, T. Bein, D. Fattakhova-Rohlfing, *ChemSusChem* **2019**, *12*, 4140–4159.

[160] Y. Deng, C. Fang, G. Chen, *J. Power Sources* **2016**, *304*, 81–101.

[161] V. M. H. Ng, S. Wu, P. Liu, B. Zhu, L. Yu, C. Wang, H. Huang, Z. J. Xu, Z. Yao, J. Zhou, W. Que, L. B. Kong, *Electrochim. Acta* **2017**, *248*, 440–448.

[162] M. A. Kebede, *Curr. Opin. Electrochem.* **2020**, *21*, 182–187.

[163] J. Xu, S. Dou, H. Liu, L. Dai, *Nano Energy* **2013**, *2*, 439–442.

[164] W. Zuo, A. Innocenti, M. Zarrabeitia, D. Bresser, Y. Yang, S. Passerini, *Acc. Chem. Res.* **2023**, *56*, 284–296.

[165] G.-A. Nazri, G. Pistoia, *Lithium Batteries: Science and Technology*, Kluwer Academic Publishers, Boston, **2004**.

[166] A. Chakraborty, S. Kunnikuruvan, S. Kumar, B. Markovsky, D. Aurbach, M. Dixit, D. T. Major, *Chem. Mater.* **2020**, *32*, 915–952.

[167] N. Nitta, F. Wu, J. T. Lee, G. Yushin, *Mater. Today* **2015**, *18*, 252–264.

[168] A. K. Stephan, *Joule* **2020**, *4*, 1632–1633.

[169] A. Manthiram, *Nat. Commun.* **2020**, *11*, 1–9.

[170] W. Li, E. M. Erickson, A. Manthiram, *Nat. Energy* **2020**, *5*, 26–34.

[171] Y. Zhao, Q. Liu, X. Zhao, D. Mu, G. Tan, L. Li, R. Chen, F. Wu, *Mater. Today* **2023**, *62*, 271–295.

[172] C. Delmas, J.-J. Braconnier, C. Fouassier, P. Hagenmuller, *Solid State Ionics* **1988**, *3–4*, 165–169.

[173] N. Yabuuchi, K. Kubota, M. Dahbi, S. Komaba, *Chem. Rev.* **2014**, *114*, 11636–11682.

[174] P. Gupta, S. Pushpakanth, M. A. Haider, S. Basu, *ACS Omega* **2022**, *7*, 5605–5614.

[175] P. A. Maughan, A. B. Naden, J. T. S. Irvine, A. R. Armstrong, *Commun. Mater.* **2023**, *4*, 4–10.

[176] A. Kanwade, S. Gupta, A. Kankane, M. K. Tiwari, A. Srivastava, J. A. Kumar Satrughna, S. Chand Yadav, P. M. Shirage, *RSC Adv.* **2022**, *12*, 23284–23310.

[177] O. K. Park, Y. Cho, S. Lee, H. C. Yoo, H. K. Song, J. Cho, *Energy Environ. Sci.* **2011**, *4*, 1621–1633.

[178] R. Schmuch, R. Wagner, G. Hörpel, T. Placke, M. Winter, *Nat. Energy* **2018**, *3*, 267–278.

[179] C. Zuo, Z. Hu, R. Qi, J. Liu, Z. Li, J. Lu, C. Dong, K. Yang, W. Huang, C. Chen, Z. Song, S. Song, Y. Yu, J. Zheng, F. Pan, *Adv. Energy Mater.* **2020**, *10*, 1–10.

[180] C. M. Julien, A. Mauger, *Review of 5-V Electrodes for Li-Ion Batteries: Status and Trends*, **2013**.

[181] Q. Ni, Y. Bai, F. Wu, C. Wu, *Adv. Sci.* **2017**, *4*, DOI 10.1002/advs.201600275.

[182] P. Barpanda, L. Lander, S. I. Nishimura, A. Yamada, *Adv. Energy Mater.* **2018**, *8*, 1–26.

[183] J. Li, Z.-F. Ma, *Chem* **2019**, *5*, 3–6.

[184] Z. Gong, Y. Yang, *Energy Environ. Sci.* **2011**, *4*, 3223–3242.

[185] Y. Z. Dong, Y. M. Zhao, H. Duan, *Mater. Chem. Phys.* **2011**, *129*, 756–760.

[186] N. Lyczko, A. Nzihou, P. Sharrock, A. Germeau, C. Toussaint, *Ind. Eng. Chem. Res.* **2012**, *51*, 292–300.

[187] Y. Liu, Y. Zhou, J. Zhang, S. Zhang, P. Ren, *J. Power Sources* **2016**, *314*, 1–9.

[188] Z. Jian, Y. Hu, X. Ji, W. Chen, *Adv. Mater.* **2017**, *29*, 1601925.

[189] T. Jin, H. Li, K. Zhu, P.-F. Wang, P. Liu, L. Jiao, *Chem Soc Rev* **2020**, *49*, 2342.

[190] H. Zhang, B. Qin, D. Buchholz, S. Passerini, *ACS Appl. Energy Mater.* **2018**, DOI 10.1021/acsaem.8b01390.

[191] S. Chen, C. Wu, L. Shen, C. Zhu, Y. Huang, K. Xi, *Adanced Mater.* **2017**, *29*, 1700431.

[192] P. Serras, J. Alonso, N. Sharma, J. Miguel, P. Kubiak, *Chem. Mater.* **2013**, *25*, 4917–4925.

[193] V. Palomares, P. Serras, H. E. A. Brand, T. Rojo, N. Sharma, *J. Mater. Chem. A* **2015**, *3*, 23017–23027.

[194] R. A. Shakoor, D. H. Seo, H. Kim, Y. U. Park, J. Kim, S. W. Kim, H. Gwon, S. Lee, K. Kang, *J. Mater. Chem.* **2012**, *22*, 20535–20541.

[195] Y. U. Park, D. H. Seo, H. S. Kwon, B. Kim, J. Kim, H. Kim, I. Kim, H. I. Yoo, K. Kang, *J. Am. Chem. Soc.* **2013**, *135*, 13870–13878.

[196] P. Serras, V. Palomares, A. Goni, I. G. de Muro, P. Kubiak, L. Lezama, T. Rojo, *J. Mater. Chem.* **2012**, 22301–22308.

[197] M. T. Ahsan, Z. Ali, M. Usman, Y. Hou, *Carbon Energy* **2022**, *4*, 776–819.

[198] J. Peng, W. Zhang, Q. Liu, J. Wang, S. Chou, H. Liu, S. Dou, *Adv. Mater.* **2022**, *34*, 1–20.

[199] A. Zhou, W. Cheng, W. Wang, Q. Zhao, J. Xie, W. Zhang, H. Gao, L. Xue, J. Li, *Adv. Energy Mater.* **2021**, *11*, 1–35.

[200] B. Xie, B. Sun, T. Gao, Y. Ma, G. Yin, P. Zuo, *Coord. Chem. Rev.* **2022**, *460*, 214478.

[201] P. S. Salini, S. V. Gopinadh, A. Kalpakasseri, B. John, M. Thelakkattu Devassy, *ACS Sustain. Chem. Eng.* **2020**, *8*, 4003–4025.

[202] N. Lingappan, L. Kong, M. Pecht, *Renew. Sustain. Energy Rev.* **2021**, *147*, 111227.

[203] D. Bresser, D. Buchholz, A. Moretti, A. Varzi, S. Passerini, *Energy Environ. Sci.* **2018**, *11*, 3096–3127.

[204] V. A. Nguyen, C. Kuss, *J. Electrochem. Soc.* **2020**, *167*, 065501.

[205] X. Lim, *Nature* **2023**, *620*.

[206] H. Kono, K. Oshima, H. Hashimoto, Y. Shimizu, K. Tajima, *Carbohydr. Polym.* **2016**, *146*, 1–9.

[207] A. Casaburi, Ú. Montoya Rojo, P. Cerrutti, A. Vázquez, M. L. Foresti, *Food Hydrocoll.* **2018**, *75*, 147–156.

[208] M. Yáñez-S, B. Matsuhiro, S. Maldonado, R. González, J. Luengo, O. Uyarte, D. Serafine, S. Moya, J. Romero, R. Torres, M. J. Kogan, *Cellulose* **2018**, *25*, 2901–2914.

[209] J.-H. Lee, U. Paik, V. A. Hackley, Y.-M. Choi, *J. Electrochem. Soc.* **2005**, *152*, A1763.

[210] R. R. Li, Z. Yang, X. X. He, X. H. Liu, H. Zhang, Y. Gao, Y. Qiao, L. Li, S. L. Chou, *Chem. Commun.* **2021**, *57*, 12406–12416.

[211] I. Kovalenko, B. Zdyrko, A. Magasinski, B. Hertzberg, Z. Milicev, R. Burtovyy, I. Luzinov, G. Yushin, *Science (80-.).* **2011**, *334*, 75–79.

[212] F. Bigoni, F. De Giorgio, F. Soavi, C. Arbizzani, *J. Electrochem. Soc.* **2017**, *164*, A6171–A6177.

[213] Z. P. Cai, Y. Liang, W. S. Li, L. D. Xing, Y. H. Liao, *J. Power Sources* **2009**, *189*, 547–551.

[214] J. Chong, S. Xun, H. Zheng, X. Song, G. Liu, P. Ridgway, J. Q. Wang, V. S. Battaglia, *J. Power Sources* **2011**, *196*, 7707–7714.

[215] L. Zhang, L. Chai, Q. Qu, L. Zhang, M. Shen, H. Zheng, *Electrochim. Acta* **2013**, *105*, 378–383.

[216] C. Luo, L. Du, W. Wu, H. Xu, G. Zhang, S. Li, C. Wang, Z. Lu, Y. Deng, *ACS Sustain. Chem. Eng.* **2018**, *6*, 12621–12629.

[217] J. M. Yuan, W. F. Ren, K. Wang, T. T. Su, G. J. Jiao, C. Y. Shao, L. P. Xiao, R. C. Sun, *ACS Sustain. Chem. Eng.* **2022**, *10*, 166–176.

[218] A. Lourenço, H. Pereira, H. Pereira, in *Lignin - Trends Appl.* (Ed.: M. Poletto), IntechOpen, **2018**, p. 308.

[219] Y. Zhang, M. Naebe, *ACS Sustain. Chem. Eng.* **2021**, *9*, 1427–1442.

[220] W. J. Chen, C. X. Zhao, B. Q. Li, T. Q. Yuan, Q. Zhang, *Green Chem.* **2022**, *24*, 565–584.

[221] Y. Liu, W. Chen, Q. Xia, B. Guo, Q. Wang, S. Liu, Y. Liu, J. Li, H. Yu, *ChemSusChem* **2017**, *10*, 1692–1700.

[222] Q. Xia, Y. Liu, J. Meng, W. Cheng, W. Chen, S. Liu, Y. Liu, J. Li, H. Yu, *Green Chem.* **2018**, *20*, 2711–2721.

[223] R. Rinaldi, R. Jastrzebski, M. T. Clough, J. Ralph, M. Kennema, P. C. A. Bruijnincx, B. M. Weckhuysen, *Angew. Chemie - Int. Ed.* **2016**, *55*, 8164–8215.

[224] A. Beaucamp, M. Muddasar, I. S. Amiinu, M. Moraes Leite, M. Culebras, K. Latha, M. C. Gutiérrez, D. Rodriguez-Padron, F. del Monte, T. Kennedy, K. M. Ryan, R. Luque, M. M. Titirici, M. N. Collins, *Green Chem.* **2022**, *24*, 8193–8226.

[225] W. Zhang, X. Qiu, C. Wang, L. Zhong, F. Fu, J. Zhu, Z. Zhang, Y. Qin, D. Yang, C. C. Xu, *Carbon Res.* **2022**, *1*, 1–39.

[226] T. C. Nirmale, B. B. Kale, A. J. Varma, *Int. J. Biol. Macromol.* **2017**, *103*, 1032–1043.

[227] H. Lu, A. Cornell, F. Alvarado, M. Behm, S. Leijonmarck, J. Li, P. Tomani, G. Lindbergh, *Materials (Basel).* **2016**, *9*, 1–17.

[228] T. Chen, Q. Zhang, J. Pan, J. Xu, Y. Liu, M. Al-Shroofy, Y. T. Cheng, *ACS Appl. Mater.*

Interfaces **2016**, *8*, 32341–32348.

[229] R. Gond, H. D. Asfaw, O. Hosseinaei, K. Edström, R. Younesi, A. J. Naylor, *ACS Sustain. Chem. Eng.* **2021**, DOI 10.1021/acssuschemeng.1c05263.

[230] Q. Wang, H. Wang, J. Wu, M. Zhou, W. Liu, H. Zhou, *Nano Energy* **2021**, *80*, 105516.

[231] J. Motavalli, *Nature* **2015**, *526*, 96–97.

[232] J. Li, C. Ma, M. Chi, C. Liang, N. J. Dudney, *Adv. Energy Mater.* **2015**, *5*, 1–6.

[233] W. Teng, J. Wu, Q. Liang, J. Deng, Y. Xu, Q. Liu, B. Wang, T. Ma, D. Nan, J. Liu, B. Li, Q. Weng, X. Yu, *Energy Environ. Mater.* **2023**, *6*, 1–28.

[234] E. Bekaert, L. Buannic, U. Lassi, A. Llordés, J. Salminen, *Electrolytes for Li- and Na-Ion Batteries: Concepts, Candidates, and the Role of Nanotechnology*, Elsevier Inc., **2017**.

[235] K. Xu, *Chem. Rev.* **2004**, *104*, 4303–4417.

[236] Y. Wu, X. Liu, L. Wang, X. Feng, D. Ren, Y. Li, X. Rui, Y. Wang, X. Han, G. L. Xu, H. Wang, L. Lu, X. He, K. Amine, M. Ouyang, *Energy Storage Mater.* **2021**, *37*, 77–86.

[237] H. Kumar, E. Detsi, D. P. Abraham, V. B. Shenoy, *Chem. Mater.* **2016**, *28*, 8930–8941.

[238] R. Mogensen, D. Brandell, R. Younesi, *ACS Energy Lett.* **2016**, *1*, 1173–1178.

[239] Y. K. Liu, C. Z. Zhao, J. Du, X. Q. Zhang, A. B. Chen, Q. Zhang, *Small* **2023**, *19*, DOI 10.1002/smll.202205315.

[240] W. Li, X. Guo, K. Song, J. Chen, J. Zhang, G. Tang, C. Liu, W. Chen, C. Shen, *Adv. Energy Mater.* **2023**, *13*, 1–10.

[241] A. Paiano, G. Lagioia, *Energy Policy* **2016**, *91*, 161–173.

[242] J. A. Elegbede, V. A. Ajayi, A. Lateef, *Environ. Technol. Innov.* **2021**, *24*, 102073.

[243] P. K. Gandam, M. L. Chinta, A. P. Gandham, N. P. P. Pabbathi, S. Konakanchi, A. Bhavanam, S. R. Atchuta, R. R. Baadhe, R. K. Bhatia, *Fermentation* **2022**, *8*, DOI 10.3390/fermentation8120704.

[244] M. Trninić, L. Wang, G. Várhegyi, M. Grønli, Ø. Skreiberg, *Energy and Fuels* **2012**, *26*, 2005–2013.

[245] S. Bobba, S. Carrara, J. Huisman, F. Mathieux, C. Pavel, *Critical Raw Materials for Strategic Technologies and Sectors in the EU - A Foresight Study*, **2020**.

[246] R. Millati, R. B. Cahyono, T. Ariyanto, I. N. Azzahrani, R. U. Putri, M. J. Taherzadeh, *Agricultural, Industrial, Municipal, and Forest Wastes: An Overview*, Elsevier B.V., **2019**.

[247] C. del Mar Saavedra Rios, L. Simonin, C. M. Ghimbeu, C. Vaulot, D. da Silva Perez, C. Dupont, *Fuel Process. Technol.* **2022**, *231*, 107223.

[248] M. Zhang, Y. Li, F. Wu, Y. Bai, C. Wu, *Nano Energy* **2021**, *82*, DOI 10.1016/j.nanoen.2020.105738.

[249] C. Liu, B. Li, H. Du, D. Lv, Y. Zhang, G. Yu, X. Mu, H. Peng, *Carbohydr. Polym.* **2016**, *151*, 716–724.

[250] D. W. Klosiewict, **1980**, 913–916.

[251] C. Nita, B. Zhang, J. Dentzer, C. Matei Ghimbeu, *J. Energy Chem.* **2021**, *58*, 207–218.

[252] J. S. Kim, Y. Y. Lee, T. H. Kim, *Bioresour. Technol.* **2016**, *199*, 42–48.

[253] L. Brinchi, F. Cotana, E. Fortunati, J. M. Kenny, *Carbohydr. Polym.* **2013**, *94*, 154–169.

[254] T. Shui, S. Feng, G. Chen, A. Li, Z. Yuan, H. Shui, T. Kuboki, C. Xu, *Biomass and Bioenergy* **2017**, *105*, 51–58.

[255] G. Joshi, S. Naithani, V. K. Varshney, S. S. Bisht, V. Rana, P. K. Gupta, *Waste Manag.* **2015**, *38*, 33–40.

[256] M. S. Yeasmin, M. I. H. Mondal, *Int. J. Biol. Macromol.* **2015**, *80*, 725–731.

[257] N. Haleem, M. Arshad, M. Shahid, M. A. Tahir, *Carbohydr. Polym.* **2014**, *113*, 249–255.

[258] M. Akram, I. Taha, M. M. Ghobashy, *Cellulose* **2016**, *23*, 1713–1724.

[259] C. M. Obele, M. E. Ibenta, J. L. Chukwuneke, S. C. Nwanonenyi, *Cellulose* **2021**, *28*,

2615–2633.

[260] Y. Li, Y. S. Hu, H. Li, L. Chen, X. Huang, *J. Mater. Chem. A* **2015**, *4*, 96–104.

[261] X. Zhu, X. Jiang, X. Liu, L. Xiao, Y. Cao, *Green Energy Environ.* **2017**, *2*, 310–315.

[262] R. F. Susanti, S. Alvin, J. Kim, *J. Ind. Eng. Chem.* **2020**, *91*, 317–329.

[263] S. Puravankara, Nagmani, *ACS Appl. Energy Mater.* **2020**, *3*, 10045–10052.

[264] K. Wang, Y. Jin, S. Sun, Y. Huang, J. Peng, J. Luo, Q. Zhang, Y. Qiu, C. Fang, J. Han, *ACS Omega* **2017**, *2*, 1687–1695.

[265] H. Darjazi, A. Staffolani, L. Sbrascini, L. Bottoni, R. Tossici, F. Nobili, *Energies* **2020**, *13*, 6216.

[266] S. Ghosh, R. Santhosh, S. Jeniffer, V. Raghavan, G. Jacob, K. Nanaji, P. Kollu, S. K. Jeong, A. N. Grace, *Sci. Rep.* **2019**, *9*, 1–15.

[267] C. Chen, Y. Huang, Y. Zhu, Z. Zhang, Z. Guang, Z. Meng, P. Liu, *ACS Sustain. Chem. Eng.* **2020**, *8*, 1497–1506.

[268] C. Matei Ghimbeu, J. Górka, V. Simone, L. Simonin, S. Martinet, C. Vix-Guterl, *Nano Energy* **2018**, *44*, 327–335.

[269] A. Beda, F. Rabuel, M. Morcrette, S. Knopf, P. L. Taberna, P. Simon, C. Matei Ghimbeu, *J. Mater. Chem. A* **2021**, *9*, 1743–1758.

[270] V. Velez, G. Ramos-Sánchez, B. Lopez, L. Lartundo-Rojas, I. González, L. Sierra, *Carbon N. Y.* **2019**, *147*, 214–226.

[271] M. Liu, J. Zhang, S. Guo, B. Wang, Y. Shen, X. Ai, H. Yang, J. Qian, *ACS Appl. Mater. Interfaces* **2020**, *12*, 17620–17627.

[272] N. Sun, H. Liu, B. Xu, *J. Mater. Chem. A* **2015**, *3*, 20560–20566.

[273] X. Li, X. Zeng, T. Ren, J. Zhao, Z. Zhu, S. Sun, Y. Zhang, *J. Alloys Compd.* **2019**, *787*, 229–238.

[274] M. Zarrabeitia, M. Á. Muñoz-Márquez, F. Nobili, T. Rojo, M. Casas-Cabanas, *Batteries* **2017**, *3*, 1–13.

[275] J. Conder, C. Villevieille, *Chem. Commun.* **2019**, *55*, 1275–1278.

[276] C. Senthil, J. W. Park, N. Shaji, G. S. Sim, C. W. Lee, *J. Energy Chem.* **2022**, *64*, 286–295.

[277] W. Jing, M. Wang, Y. Li, H. Li, H. Zhang, S. Hu, H. Wang, Y. He, *Electrochim. Acta* **2021**, *391*, 139000.

[278] Q. Jin, K. Wang, P. Feng, Z. Zhang, S. Cheng, K. Jiang, *Energy Storage Mater.* **2020**, *27*, 43–50.

[279] V. Augustyn, J. Come, M. A. Lowe, J. W. Kim, P. L. Taberna, S. H. Tolbert, H. D. Abruña, P. Simon, B. Dunn, *Nat. Mater.* **2013**, *12*, 518–522.

[280] J. Yang, Z. Ju, Y. Jiang, Z. Xing, B. Xi, J. Feng, S. Xiong, *Adv. Mater.* **2018**, *30*, DOI 10.1002/adma.201700104.

[281] Y. Liu, H. Dai, L. Wu, W. Zhou, L. He, W. Wang, W. Yan, Q. Huang, L. Fu, Y. Wu, *Adv. Energy Mater.* **2019**, *9*, 1–9.

[282] N. Sun, Z. Guan, Y. Liu, Y. Cao, Q. Zhu, H. Liu, Z. Wang, P. Zhang, B. Xu, *Adv. Energy Mater.* **2019**, *9*, 1–14.

[283] T. Brezesinski, J. Wang, S. H. Tolbert, B. Dunn, *Nat. Mater.* **2010**, *9*, 146–151.

[284] J. Wang, L. Yan, Q. Ren, L. Fan, F. Zhang, Z. Shi, *Electrochim. Acta* **2018**, *291*, 188–196.

[285] F. Nobili, S. Dsoke, M. Mancini, R. Tossici, R. Marassi, *J. Power Sources* **2008**, *180*, 845–851.

[286] L. Sbrascini, A. Staffolani, L. Bottoni, H. Darjazi, L. Minnetti, M. Minicucci, F. Nobili, *ACS Appl. Mater. Interfaces* **2022**, DOI 10.1021/acsami.2c07888.

[287] L. A. Ma, A. J. Naylor, L. Nyholm, R. Younesi, *Angew. Chemie - Int. Ed.* **2021**, *60*, 4855–4863.

[288] K. Pan, F. Zou, M. Canova, Y. Zhu, J. H. Kim, *J. Power Sources* **2020**, *479*, 229083.

[289] P. Shafiei Sabet, G. Stahl, D. U. Sauer, *J. Power Sources* **2020**, *472*, DOI 10.1016/j.jpowsour.2020.228189.

[290] X. Chen, L. Li, M. Liu, T. Huang, A. Yu, *J. Power Sources* **2021**, *496*, 229867.

[291] Y. Lin, Z. Liu, K. Leung, L. Chen, P. Lu, Y. Qi, *J. Power Sources* **2016**, *309*, 221–230.

[292] E. Buiel, A. E. George, J. R. Dahn, *J. Electrochem. Soc.* **1998**, *145*, 2252–2257.

[293] P. Thomas, D. Billaud, *Electrochim. Acta* **2002**, *47*, 3303–3307.

[294] K. Wang, Y. Xu, H. Wu, R. Yuan, M. Zong, Y. Li, V. Dravid, W. Ai, J. Wu, *Carbon N. Y.* **2021**, *178*, 443–450.

[295] S. Alvin, H. S. Cahyadi, J. Hwang, W. Chang, S. K. Kwak, J. Kim, *Adv. Energy Mater.* **2020**, *10*, 1–16.

[296] J. Ajuria, E. Redondo, M. Arnaiz, R. Mysyk, T. Rojo, E. Goikolea, *J. Power Sources* **2017**, *359*, 17–26.

[297] J. Feng, L. Wang, D. Li, P. Lu, F. Hou, J. Liang, *Prog. Nat. Sci. Mater. Int.* **2018**, *28*, 205–211.

[298] F. Linsenmann, D. Pritzl, H. A. Gasteiger, *J. Electrochem. Soc.* **2021**, *168*, 010506.

[299] J. Nam, E. Kim, R. K.K, Y. Kim, T. H. Kim, *Sci. Rep.* **2020**, *10*, 1–12.

[300] A. Cholewinski, P. Si, M. Uceda, M. Pope, B. Zhao, *Polymers (Basel).* **2021**, *13*, 1–20.

[301] B. Zhou, S. Yang, L. Wu, W. Wu, W. Wei, L. Chen, H. Zhang, J. Pan, X. Xiong, *RSC Adv.* **2015**, *5*, 49926–49932.

[302] R. Hu, D. Chen, G. Waller, Y. Ouyang, Y. Chen, B. Zhao, B. Rainwater, C. Yang, M. Zhu, M. Liu, *Energy Environ. Sci.* **2016**, *9*, 595–603.

[303] L. Chen, K. Wang, X. Xie, J. Xie, *J. Power Sources* **2007**, *174*, 538–543.

[304] P. G. Kitz, M. J. Lacey, P. Novák, E. J. Berg, *J. Power Sources* **2020**, *477*, 0–8.

[305] H. Moon, A. Innocenti, H. Liu, H. Zhang, M. Weil, M. Zarrabeitia, S. Passerini, *ChemSusChem* **2023**, *16*, DOI 10.1002/cssc.202201713.

[306] Z. Zhang, M. D. Harrison, D. W. Rackemann, W. O. S. Doherty, I. M. O'Hara, *Green Chem.* **2016**, *18*, 360–381.

[307] A. J. Fernández-Ropero, M. Zarrabeitia, G. Baraldi, M. Echeverria, T. Rojo, M. Armand, D. Shanmukaraj, *ACS Appl. Mater. Interfaces* **2021**, *13*, 11814–11821.

[308] Suhas, V. K. Gupta, P. J. M. Carrott, R. Singh, M. Chaudhary, S. Kushwaha, *Bioresour. Technol.* **2016**, *216*, 1066–1076.

[309] J. A. Lacey, J. E. Aston, V. S. Thompson, *Front. Energy Res.* **2018**, *6*, 1–6.

[310] F. M. Yedro, D. A. Cantero, M. Pascual, J. García-Serna, M. J. Cocero, *Bioresour. Technol.* **2015**, *191*, 124–132.

[311] P. Baker, A. Charlton, C. Johnston, J. J. Leahy, K. Lindegaard, I. Pisano, J. Prendergast, D. Preskett, C. Skinner, *Ind. Crops Prod.* **2022**, *189*, 115823.

[312] A. Beda, J. M. Le Meins, P. L. Taberna, P. Simon, C. Matei Ghimbeu, *Sustain. Mater. Technol.* **2020**, *26*, DOI 10.1016/j.susmat.2020.e00227.

[313] D. E. Newbury, N. W. M. Ritchie, *Scanning* **2013**, *35*, 141–168.

[314] K. Yu, X. Wang, H. Yang, Y. Bai, C. Wu, *J. Energy Chem.* **2021**, *55*, 499–508.

[315] K. Li, B. Tang, W. Zhang, Z. Shi, X. Tu, K. Li, J. Xu, J. Ma, L. Liu, H. Zhang, *ACS Omega* **2020**, *5*, 22551–22559.

[316] S. H. Zeronian, M. K. Inglesby, *Cellulose* **1995**, *2*, 265–272.

[317] R. E. Brooks, S. B. Moore, *Cellulose* **2000**, *7*, 263–286.

[318] J. M. Fang, R. C. Sun, J. Tomkinson, *Cellulose* **2000**, *7*, 87–107.

[319] F. Hemmati, S. M. Jafari, M. Kashaninejad, M. Barani Motlagh, *Int. J. Biol. Macromol.*

2018, *120*, 1216–1224.

[320] A. Y. Melikoğlu, S. E. Bilek, S. Cesur, *Carbohydr. Polym.* **2019**, *215*, 330–337.

[321] R. A. Ilyas, S. M. Sapuan, M. R. Ishak, *Carbohydr. Polym.* **2018**, *181*, 1038–1051.

[322] S. Bano, Y. S. Negi, *Carbohydr. Polym.* **2017**, *157*, 1041–1049.

[323] H. Kono, *Carbohydr. Polym.* **2013**, *97*, 384–390.

[324] R. Reeves, A. Ribeiro, L. Lombardo, R. Boyer, J. B. Leach, *Polymers (Basel).* **2010**, *2*, 252–264.

[325] Y. Li, Y. Liu, W. Chen, Q. Wang, Y. Liu, J. Li, H. Yu, *Green Chem.* **2016**, *18*, 1010–1018.

[326] W. Fang, H. Sixta, *ChemSusChem* **2015**, *8*, 73–76.

[327] D. Tarasov, M. Leitch, P. Fatehi, *Biotechnol. Biofuels* **2018**, *11*, 1–28.

[328] Y. Zhao, U. Shakeel, M. Saif Ur Rehman, H. Li, X. Xu, J. Xu, *J. Clean. Prod.* **2020**, *253*, 120076.

[329] R. El Hage, N. Brosse, P. Sannigrahi, A. Ragauskas, *Polym. Degrad. Stab.* **2010**, *95*, 997–1003.

[330] T. J. Mcdonough, *TAPPI J.* **1993**, *76*, 186–193.

[331] L. G. Nair, K. Agrawal, P. Verma, *Bioresour. Bioprocess.* **2023**, *10*, DOI 10.1186/s40643-023-00673-0.

[332] J. Bergrath, J. Rumpf, R. Burger, X. T. Do, M. Wirtz, M. Schulze, *Macromol. Mater. Eng.* **2023**, *2300093*, DOI 10.1002/mame.202300093.

[333] D. Wei Kit Chin, S. Lim, Y. L. Pang, M. K. Lam, *Biofuels, Bioprod. Biorefining* **2020**, *14*, 808–829.

[334] A. Sluiter, B. Hames, R. Ruiz, C. Scarlata, J. Sluiter, D. Templeton, D. Crocker, *Natl. Renew. Energy Lab.* **2008**, 17.

[335] I. Cybulska, G. Brudecki, K. Rosentrater, J. L. Julson, H. Lei, *Bioresour. Technol.* **2012**, *118*, 30–36.

[336] X. Erdocia, R. Prado, M. Á. Corcuera, J. Labidi, *J. Ind. Eng. Chem.* **2014**, *20*, 1103–1108.

[337] C. Inkrod, M. Raita, V. Champreda, N. Laosiripojana, *Bioenergy Res.* **2018**, *11*, 277–290.

[338] H. Q. Lê, A. Zaitseva, J. P. Pokki, M. Ståhl, V. Alopaeus, H. Sixta, *ChemSusChem* **2016**, *9*, 2939–2947.

[339] N. AlQasas, A. Eskhan, D. Johnson, *Surfaces and Interfaces* **2023**, *36*, 102594.

[340] X. Meng, *Green Chem.* **2020**, 2862–2872.

[341] X. Tan, Q. Zhang, W. Wang, X. Zhuang, Y. Deng, Z. Yuan, *Fuel* **2019**, *249*, 334–340.

[342] A. Duval, L. Averous, *Green Chem.* **2022**, *24*, 338–349.

[343] X. Xu, K. Wang, Y. Zhou, C. Lai, D. Zhang, C. Xia, A. Pugazhendhi, *Fuel* **2023**, *338*, 127361.

[344] A. Dastpak, T. V. Lourençon, M. Balakshin, S. Farhan Hashmi, M. Lundström, B. P. Wilson, *Ind. Crops Prod.* **2020**, *148*, 112310.

[345] Q. Li, Y. Dong, K. D. Hammond, C. Wan, *J. Mol. Liq.* **2021**, *344*, 117779.

[346] M. Mohan, K. L. Sale, R. S. Kalb, B. A. Simmons, J. M. Gladden, *ACS Sustain. Chem. Eng.* **2022**, DOI 10.1021/acssuschemeng.2c03373.

[347] M. Wu, J. K. Liu, Z. Y. Yan, B. Wang, X. M. Zhang, F. Xu, R. C. Sun, *RSC Adv.* **2016**, *6*, 6196–6204.

[348] E. Jasiukaitytė-Grojzdek, M. Huš, M. Grilc, B. Likozar, *ACS Sustain. Chem. Eng.* **2020**, *8*, 17475–17486.

[349] Y. H. Xu, P. Zeng, M. F. Li, J. Bian, F. Peng, *Sep. Purif. Technol.* **2021**, *279*, 119780.

[350] H. Yang, R. Yan, H. Chen, D. H. Lee, C. Zheng, *Fuel* **2007**, *86*, 1781–1788.

[351] D. Watkins, M. Nuruddin, M. Hosur, A. Tcherbi-Narteh, S. Jeelani, *J. Mater. Res. Technol.* **2015**, *4*, 26–32.

[352] A. Tejado, C. Peña, J. Labidi, J. M. Echeverria, I. Mondragon, *Bioresour. Technol.* **2007**, *98*, 1655–1663.

[353] Z. V. Bobyleva, O. A. Drozhzhin, K. A. Dosaev, A. Kamiyama, S. V. Ryazantsev, S. Komaba, E. V. Antipov, *Electrochim. Acta* **2020**, *354*, 136647.

[354] F. Wang, T. Zhang, F. Ran, *Electrochim. Acta* **2023**, *441*, 141770.

[355] D. Chao, C. H. M. Lai, P. Liang, Q. Wei, Y. S. Wang, C. R. Zhu, G. Deng, V. V. T. Doan-Nguyen, J. Lin, L. Mai, H. J. Fan, B. Dunn, Z. X. Shen, *Adv. Energy Mater.* **2018**, *8*, 1–8.

[356] N. Sharma, P. Serras, V. Palomares, H. E. A. Brand, J. Alonso, P. Kubiak, M. L. Fdez-gubieda, *Chem. Mater.* **2014**, *26*, 3391–3402.

[357] K. Liu, P. Lei, X. Wan, W. Zheng, X. Xiang, *J. Colloid Interface Sci.* **2018**, *532*, 426–432.

[358] Q. Liu, D. Wang, X. Yang, N. Chen, C. Wang, X. Bie, Y. Wei, G. Chen, F. Du, *J. Mater. Chem. A* **2015**, *3*, 21478–21485.

[359] Z. Jian, W. Han, X. Lu, H. Yang, Y. S. Hu, J. Zhou, Z. Zhou, J. Li, W. Chen, D. Chen, L. Chen, *Adv. Energy Mater.* **2013**, *3*, 156–160.

[360] X. Shen, J. Zhao, Y. Li, X. Sun, C. Yang, H. Liu, Y. S. Hu, *ACS Appl. Energy Mater.* **2019**, *2*, 7474–7482.

[361] Y. Pi, Z. Gan, M. Yan, C. Pei, H. Yu, Y. Ge, Q. An, L. Mai, *Chem. Eng. J.* **2021**, *413*, 127565.

[362] Y. Tang, X. Wang, J. Chen, D. Wang, Z. Mao, *Chem. Eng. J.* **2022**, *427*, 131951.

[363] J. H. Jo, J. U. Choi, Y. J. Park, J. K. Ko, H. Yashiro, S. T. Myung, *Energy Storage Mater.* **2020**, *32*, 281–289.

[364] D. Shanmukaraj, S. Grugeon, S. Laruelle, G. Douglade, J. M. Tarascon, M. Armand,

Electrochem. commun. **2010**, *12*, 1344–1347.

[365] B. Shen, Y. You, Y. Niu, Y. Li, C. Dai, L. Hu, B. Guo, J. Jiang, S. Bao, M. Xu, *ACS Appl. Mater. Interfaces* **2018**, *10*, 16581–16587.

[366] G. Cavalaglio, I. Mecca, P. Iodice, T. Giannoni, M. Gelosia, A. Nicolini, R. Barros Lovate Temporim, *Sustainability* **2023**, *15*, 15905.